ANALYSIS OF EXPERIMENTAL PIV/PTV MEASUREMENTS ON A

MATCHED-INDEX-OF-REFRACTION 61-PIN WIRE-WRAPPED HEXAGONAL FUEL

BUNDLE

A Dissertation

by

NOLAN EDWARD GOTH

Submitted to the Office of Graduate and Professional Studies of
Texas A&M University
in partial fulfillment of the requirements for the degree of

DOCTOR OF PHILOSOPHY

Chair of Committee,	Yassin Hassan
Committee Members,	Maria King
	William Marlow
	Rodolfo Vaghetto
Head of Department,	Yassin Hassan

December 2018

Major Subject: Nuclear Engineering

ABSTRACT

In nuclear reactor thermal hydraulics modeling, detailed coolant velocity fields are essential to accurately anticipating flow induced vibrations and temperature distributions in the coolant and pins. Predictive computational tools are under development to produce these coolant velocity fields using computational fluid dynamics. Turbulence modeling validation is a necessary remaining step in the development of such tools. Prior liquid metal fast reactor experimental velocity field data is not suitable for computational fluid dynamics turbulence modeling validation. Therefore, a demand exists for experimental data to be collected using non-intrusive probes with sufficiently high spatiotemporal resolution and of a hydraulically similar fuel bundle.

The primary objective of this research was to produce high spatiotemporal experimental velocity field data on a 61-pin wire-wrapped hexagonal fuel bundle such that commercial sodium fast reactor core design and computational fluid dynamics turbulence modeling validation may be performed. The primary phenomena of interest are the bulk swirl, local swirl, subchannel mixing, and bypass flow. Flow statistics such as ensemble-averaged velocity, root-mean-square fluctuating velocity, Reynolds stresses, Z-vorticity, and integral length scales were presented.

The methodology to meet the primary objective was the utilization of a matched-index-of-refraction experimental flow facility with laser-based optical measurement techniques. A total of 9 different measurement locations at various bundle-averaged Reynolds numbers have been investigated to generate a total of 50 unique datasets.

The scientific value of this work is twofold. It benefits the grand effort of turbulence modeling validation by providing new high spatiotemporal resolution experimental data for which benchmark activities may be performed. It also furthers the research and development of liquid metal fast breeder reactor core thermal hydraulics to progress the U.S Department of Energy's advanced reactor development agenda.

Maybe you think you're fast enough to keep up with us, huh?

A lot faster than you'll ever live to be.

ACKNOWLEDGMENTS

CONTRIBUTORS AND FUNDING SOURCES

Contributors

This work was supervised by a dissertation committee consisting of Dr. Yassin Hassan, Dr. William Marlow, Dr. Thien Nguyen, and Dr. Rodolfo Vaghetto of the Department of Nuclear Engineering as well as Professor Maria King of the Department of Mechanical Engineering.

All work for the dissertation was completed by the student, under the advisement of the dissertation committee.

Funding Sources

NOMENCLATURE

Acronyms

2D2C two-dimension two-component

2D3C two-dimension three-component

3D3C three-dimension three-component

AEC Atomic Energy Commission

AFC Advanced Fuels Campaign

ALMR Advanced Liquid Metal Reactor

ANL Argonne National Laboratory

ART Advanced Reactor Technologies

BOL beginning-of-life

CAD computer-aided design

CCD charge-coupled device

CCW counter-clockwise

CFD computational fluid dynamics

CMOS complementary metal oxide semiconductor

CRBR Clinch River Breeder Reactor

CW clockwise

DAS data acquisition system

DFR Dounreay Fast Reactor

DNS direct numerical simulation

DOD U.S. Department of Defense

DOE U.S. Department of Energy

DP differential pressure

DWO Discrete Window Offset

EBR-II Experimental Breeder Reactor II

EBR-I Experimental Breeder Reactor I

EFL effective focal length

EOL end-of-life

FCMI fuel-cladding mechanical interactions

FFT fast Fourier transform

FFTF Fast Flux Test Facility

FOV field of view

HDD hard disk drive

IFR Integral Fast Reactor

INL Idaho National Laboratory

LANL Los Alamos National Laboratory

LDV laser Doppler velocimetry

LMFBR liquid metal fast breeder reactor

MIR matched-index-of-refraction

NASA National Aeronautics and Space Administration

ORNL Oak Ridge National Laboratory

P/D pitch-to-diameter ratio

PIV particle image velocimetry

PMMA Poly(methyl methacrylate)

PTV particle tracking velocimetry

RAM random access memory

RANS Reynolds-averaged Navier Stokes

RBCB run beyond cladding breach

RMS root-mean-square

ROI region of interest

RPC robust phase correlation

RTD resistance temperature detector

SC-HTGR steam cycle high-temperature gas-cooled reactor

SFR sodium fast reactor

SNR signal-to-noise ratio

SPIV stereoscopic particle image velocimetry

SSD solid state drive

TAMU Texas A&M University

Tomo-PIV tomographic particle image velocimetry

TR-PIV time-resolved particle image velocimetry

TRA technical readiness assessment

TREAT Transient Reactor Test Facility

TRL technical readiness level

UOD universal outlier detection

VFD variable frequency drive

TABLE OF CONTENTS

LIST OF FIGURES

LIST OF TABLES

1. INTRODUCTION

This beginning section opens to six various concepts to establish a platform and direction for the work compiled in this dissertation. Section 1.1 defines the market role of liquid metal fast breeder reactor (LMFBR)s. Section 1.2 compiles a list of the global effort to develop and deploy the reactor design and then discusses various studies quantifying the readiness of the technology. The motivation and demand for modern experimental thermal hydraulic data on the LMFBR fuel bundle is defined in Section 1.3. Research objectives and the scope of experimental data analysis are presented in Section 1.4. Section 1.5 presents a timeline of milestones achieved throughout this endeavor. The organization of the dissertation is given in Section 1.6.

1.1 Market Role of Liquid Metal-cooled Fast Reactors

In the 1950s, well-known uranium resources were inadequate to support anticipated growth of global nuclear power with estimated uranium ores lasting until 2020. At that time, fast spectrum breeder reactors were considered the best solution to maximize resource utilization. Shortly after, the U.S. Atomic Energy Commission (AEC) endorsed the LMFBR over other fast and thermal breeding systems, and therefore directed significant amounts of research funding in that direction. One specific type of LMFBR, the sodium fast reactor (SFR), made substantially further progress during this time period of high demand for breeder reactors. However, between 1970-1990, well-known uranium resources expanded significantly, Three Mile Island and Chernobyl accidents caused a decline in nuclear power demand, and the Integral Fast Reactor (IFR) closed fuel cycle program was canceled.

In the past decade, a resurgence of interest in developing advanced reactor concepts to meet increasing global energy demand while avoiding an exorbitant increase in greenhouse gas emissions. Another selling point of such development has been that such advanced reactor concepts can utilize modern predictive computational tools to improve plant safety

relative to the aging nuclear fleet. It is important to note that well-known uranium resources, consumed in an open fuel cycle manner at the rate equal to the year 2008, would last 100-115 years OECD-NEA (2010). High burnup fuels, breeding, reprocessing, and closed fuel cycles are all techniques to drastically increase resource utilization and last hundreds of years, if not a few thousand OECD-NEA (2008).

As previously mentioned, the LMFBR class of reactor excels at resource utilization in a closed fuel cycle. However, efficient resource utilization is not a heavily marketed trait of advanced reactors. Therefore, society must interpret the 100 to 1000 year supply of uranium as sufficient. Today, highly marketed traits of advanced reactors include minimal capital costs, the ability to produce economically competitive low-carbon electricity, process heat for industry, hydrogen production, and desalination to increase the fresh water supply. Nevertheless, the liquid metal-cooled reactor is regarded as the most technologically developed advanced reactor design.

1.2 Technology Readiness Level

Table 1.1 contains an extensive, but not complete, list of experimental, prototype, and commercial liquid metal-cooled reactors. Several of the first fast reactors were experimental systems to prove conceptual theory and were not focused on fuel performance metrics. Clementine (designed by Los Alamos National Laboratory (LANL)) was the world's first fast spectrum reactor, and it was used primarily to quantify neutron cross sections and better understand reactivity control. Experimental Breeder Reactor I (EBR-I) (designed by Argonne National Laboratory (ANL)), the first nuclear reactor to produce electricity in 1951, was primarily designed to perform limited experiments with the smallest critical mass possible. These systems demonstrated metallic fuel elements could be utilized in a fast spectrum system. They also highlighted the limitations of metallic fuel on burnup and temperature requirements for viable commercial breeder reactors, as both systems had multiple fuel failures during their lifetime. In the UK, Dounreay Fast Reactor (DFR) fuel was designed to mitigate the rod bow observed at EBR-I. It also featured refractory metal cladding, fis-

sion gas venting, and recriticality mitigation via a two-shell cladding design. However, excessive fuel-cladding mechanical interactions (FCMI) were seen at 0.1 at.% burnup. The Experimental Breeder Reactor II (EBR-II) was an engineering demonstration reactor with the primary objective of showcasing the closed-loop fast breeder infrastructure, including a sodium-cooled breeder reactor power plant and co-located pyroprocessing and fuel fabrication facilities. It also tested a plethora of materials and fuel types, including oxide, carbine, and nitrides of U and U-Pu. Per Chang (2007), over 40 different fuel types were irradiated at EBR-II. The culminating discovery from EBR-II irradiations was that managing metallic fuel swelling via allowing room to swell, rather than containment by the cladding, can enable burnups above 20 at.%. Fifteen transient overpower tests were performed at Idaho National Laboratory (INL)'s Transient Reactor Test Facility (TREAT). Fuel performance was hardy with cladding (D9 and HT9) failure thresholds at 4 times the standard operating power level. Failures occurred near the top of the fuel column. As suggested by Planchon et al. (1987), thermal expansion and conduction phenomena matched the behavior seen during the EBR-II inherent safety demonstration test, where pre-failure axial expansion was a significant safety characteristic. The experimental database created by the previously mentioned efforts has been summarized in Table 4.3 of Reckley (2012). The highlights are: 43,000+ driver fuel pin irradiations; the qualification of SS-316, D9, and HT9 claddings in both EBR-II and Fast Flux Test Facility (FFTF); the demonstration of burnup capability to 18.5 at.%; and the excellent stability during run beyond cladding breach (RBCB) and transient testing.

Table 1.1: Liquid metal-cooled fast reactors of experimental, prototype, and commercial design that have either operated or are in conceptual design space.

Reactor	Fuel Form	Coolant	MW_{th}	First Criticality	Location
Experimental					
Clementine	Pu	Hg	0.025	1949	USA
EBR-I	U, U-Zr, Pu-Al	NaK	0.2	1951	USA
SRE	U	Na	20	1957	USA
BR-5/BR-10	PuO_2, UC, UN	Na	8	1959	Russia
LAMPRE-I	Molten Pu-Fe	Pu-Fe	1	1959	USA

Table 1.1 – Continued

Reactor	Fuel Form	Coolant	MW$_{th}$	First Criticality	Location
DFR	U-Cr, U-Mo	Nak	60	1959	UK
EBR-II	U-Fs, UPu-Zr,	Na	62.5	1961	USA
Fermi I	U-10Mo	Na	200	1963	USA
BOR-60	MOX, UN, UC	Na	55	1969	Russia
Rapsodie	MOX, UN, UC	Na	40	1967	France
SEFOR	MOX	Na	20	1969	USA
PEC	MOX	Na	120	Canceled	Italy
KNK-II	UO$_2$, MOX, UC	Na	58	1977	Germany
JOYO	MOX	Na	140	1977	Japan
FFTF	U-Zr, U-Pu-Zr	Na	400	1980	USA
FBTR	UC-PuC	Na	40	1985	India
CEFR	UO$_2$	Na	65	2010	China
MYRRHA	U-Pu-TRU	Pb	100	Concept	EU
Prototype					
BN-350	UO$_2$	Na	750	1972	Russia
Phenix	MOX	Na	350	1973	France
PFR	MOX	Na	650	1974	UK
BN-600	UO$_2$, MOX	Na	1470	1980	Russia
CRBRP	UO$_2$, MOX	Na	975	Canceled	USA
SNR-300	UO$_2$, MOX	Na	750	1985	Germany
MONJU	MOX	Na	715	1994	Japan
PFBR	MOX	Na	1250	Construction	India
BREST300	PuN-UN	Pb	700	Construction	Russia
CFR-600	MOX	Na	1500	Construction	China
ASTRID	MOX	Na	600	Concept	France
SVBR-75/100	UO$_2$	Pb-Bi	265	Concept	Russia
KALIMER-150	U-TRU-Zr	Na	392	Concept	Korea
Commercial					
Superphenix 1	MOX	Na	2990	1985	France
BN-800	MOX	Na	2100	2015	Russia
CDFR-1000	U-Zr	Na	3000	Concept	China
EFR	MOX	Na	3600	Concept	EU
Superphenix 2	MOX	Na	3600	Concept	France
SNR-2	MOX	Na	3420	Concept	Germany
DFBR	MOX	Na	1600	Concept	Japan
4S	U-Zr	Na	135	Concept	Japan
JSFR1500	MOX	Na	3500	Concept	Japan
KALIMER600	U-TRU-Zr	Na	1600	Concept	Korea
KALIMER1200	U-TRU-Zr	Na	3150	Concept	Korea
PGSFR	U-Pu-Zr	Na	392	Concept	Korea
AFR-100	U-Zr	Na	250	Concept	USA

Table 1.1 – Continued

Reactor	Fuel Form	Coolant	MW_{th}	First Criticality	Location
ABTR	U-Pu-Zr	Na	250	Concept	USA
ARC-100	U-Zr	Na	260	Concept	USA
IFR	U-Pu-Zr	Na	840	Concept	USA
PRISM	U-Pu-Zr	Na	840	Concept	USA
SAFR	U-Pu-Zr	Na	1200	Concept	USA
SMFR	U-Pu-Zr	Na	125	Concept	USA
TWR-P	U-Zr, U-Pu-Zr	Na	1475	Concept	USA
TWR-C	U-Zr, U-Pu-Zr	Na	2950	Concept	USA
BN-1200	MOX	Na	3150	Concept	Russia
BN-1800	MOX	Na	4000	Concept	Russia
BREST1200	PuN-UN	Pb	2800	Concept	Russia

As can be seen, extensive R&D and operational experience has been gained on the SFR. It is significantly more than a paper reactor, but the question regarding how technologically developed it is remains. To characterize such a status, The U.S. Department of Energy (DOE) released a technical readiness level (TRL) guide in 2011 Sanchez (2011). The guide is tailored from National Aeronautics and Space Administration (NASA) and U.S. Department of Defense (DOD) technical readiness assessment (TRA) models. The models assist in highlighting elements and processes required to ensure a project satisfies its objectives in a safe and cost-effective manner. The research, design, and deployment process for a nuclear reactor power plant consists of the following steps Strydom et al. (2017): (1) R&D to prove scientific feasibility, (2) engineering demonstration at reduced scale, (3) performance demonstration to prove a scaled-up system, and (4) commercial demonstration. It is important to note that TRLs can be defined for specific systems and components of a given reference plant. The two most relevant TRAs were performed by Reckley (2012) for metallic fuel qualification (the USA's selected SFR fuel form) and by Strydom et al. (2017) for the entire plant.

Reckley (2012) combines TRLs 0-9 into four phases of fuel qualification: (Phase 1, TRL

1-2) fuel candidate selection, (Phase 2, TRL 3-4) concept definition and feasibility, (Phase 3, TRL 5-6) fuel design and improvements evaluation, and (Phase 4, TRL 7-9) fuel qualification and demonstration. Table 6.1 of Reckley (2012) provides visualization of the bounding design space provided by the experimental efforts of metallic fuel irradiations at EBR-II and FFTF. It also presents the operating conditions of 4S, PRISM, and ARC-100 as of 2010. PRISM appears to align most closely with the experimental dataset, while fluence limits are exceed (ARC-100), and fuel dimensions increase for other conceptual designs (4S, TWR). The TRA concluded that the TRL for metallic fuel is Phase 2 (TRL 3-4). The defense of "prototypic" geometry for fuel pins with large deviations from EBR-II/FFTF specifications is expected to be most difficult during the licensing / qualification process.

An options study on demonstration and test reactors was performed jointly by INL, ANL, Oak Ridge National Laboratory (ORNL) in 2017 by Strydom et al. (2017). The TRA utilized the PRISM and AFR-100 for baseline standard and advanced SFR designs. The fuel element subsystem for each design was evaluated at a TRL of 5 and 3, respectively. They recognized the PRISM design selected fuel technologies demonstrated in EBR-II, but anticipated that issues will emerge when scaling the core thermal output by a factor of 8. When analyzing the AFR-100, the fission-gas vented fuel was evaluated at a significantly lower TRL.

Also in 2017, Kim et al. (2017) published an R&D roadmap and TRA for liquid metal-cooled fast reactors. The report recognizes the prior conclusions of Strydom et al. (2017), but revised the TRLs with the following additional criteria: (1) recommendations from industry experts and (2) progress achieved post-EBR-II/FFTF operation, such as the Clinch River Breeder Reactor (CRBR), Advanced Liquid Metal Reactor (ALMR), Advanced Fuels Campaign (AFC), and Advanced Reactor Technologies (ART) programs. Including consideration of said addition criteria, ANL revised the TRL of metallic fuel to 7-8 for standard SFRs. It is suggested that the only remaining R&D needed for commercial demonstration is documentation of irradiation data and previous analyses. For evolutionary concepts (U-TRU-Zr) and revolutionary concepts (sodium-free annular fuel, advanced steels), there is recognition

of a lower, but unquantified, TRL. Table 2 of Kim et al. (2017) summarizes overall design TRLs for each of the six Generation IV advanced reactors. The PRISM SFR and steam cycle high-temperature gas-cooled reactor (SC-HTGR) received the highest TRL of 5.

1.3 Motivation of This Work

As previously mentioned, the role of the LMFBR is less defined when the societal value of maximum uranium resource utilization does not counter the potentially higher capital and $/kWh price of electricity. Nevertheless, optimization of the standard SFR design is possible at the expense of lower TRLs. Such optimizations involve passive safety systems, simplified piping and components, as well as fuel performance. An example of fuel performance optimization is the goal to achieve extremely high burnups (>20 at.%). One aspect of such an optimization involves accurately quantifying the thermal-hydraulic performance of the fuel bundle from beginning-of-life (BOL) to end-of-life (EOL). Detailed descriptions of velocity fields inside the fuel bundle are required to accurately predict flow induced vibrations and temperature distributions in the coolant and pins. This information is crucial for Generation IV LMFBR designs to achieve longer core lives with higher fuel burnups. Predictive computational tools are currently being researched and developed utilizing turbulence modeling methods through computational fluid dynamics (CFD). A necessary step in CFD turbulence modeling development is the validation of computational physics models with experimental measurements. Prior LMFBR experimental velocity field data is not suitable for CFD turbulence modeling validation because prior measurements were performed with intrusive probes, poor spatiotemporal resolution, or contained an insufficient number of pins such that wall effects of the hexagonal duct were significant on flow behavior in the subchannels surrounding the central pin.

Therefore, a demand existed for experimental data to be collected using non-intrusive probes with sufficiently high spatiotemporal resolution and of a hydraulically similar fuel bundle relative to past and future designs such that CFD validation may be performed on the LMFBR fuel bundle. To collect the necessary experimental data, an isothermal experimental

7

flow facility was required. Major project activities are highlighted in Figure 1.1. Tasks up to and including facility shakedown were discussed by Goth (2017). This dissertation will cover the MIR experimental flow tests and analysis of experimental velocity data collected from those tests.
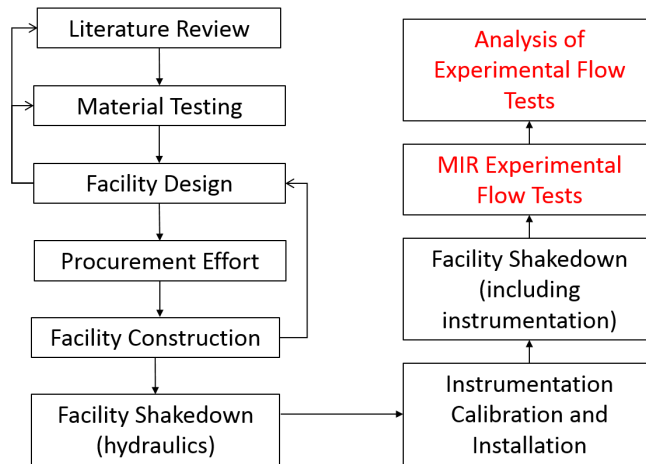
Figure 1.1: Dissertation scope highlighted in red relative to the total project scope

1.4   Research Objectives

The primary objective of this research was to produce experimental velocity field data on a 61-pin wire-wrapped hexagonal fuel bundle such that commercial SFR fuel design and CFD turbulence model validation may be performed. Vertical and transverse velocity fields were quantified using 2D2C PIV, 2D2C particle tracking velocimetry (PTV), and 2D3C SPIV laser-based imaging techniques. The experimental facility and methods applied to meet the primary objective are described in Sections 3 and 4, respectively. The primary phenomena of interest were asymmetric flow, subchannel mixing and cross-flow, recirculation regions, coherent structures, and preferential flow toward the exterior of the bundle (bypass flow). The asymmetric flow is produced by the helical wire spacers. These spacers generate transverse velocity and pressure gradients, along with increased subchannel mixing and

cross-flow. The expected location of recirculation regions are downstream of the wire spacers. This region may result in high local cladding temperatures. Analysis of experimental data includes comparison of first and second order flow statistics for various Reynolds numbers, spatial cross-correlations, integral length scales, along with residual convergence of the data sets.

1.5   Timeline and Milestones

Figure 1.2 presents a timeline highlighting project milestones and deliverables. The timeline is split into six task types: construction, measurement, conference, journal, report, and defense. The following pattern repeated throughout the project: perform a measurement, analyze the collected data, write a conference or journal paper. A total of five journal articles and eight conference papers were produced by Texas A&M University (TAMU)'s Nuclear Engineering Thermal-Hydraulic Research Lab between 2015 and 2018 involving the Wire-Wrapped Flow Facility.

Figure 1.2: Proposed timeline of the research to be conducted for this dissertation. The timeline highlights project milestones and deliverables.
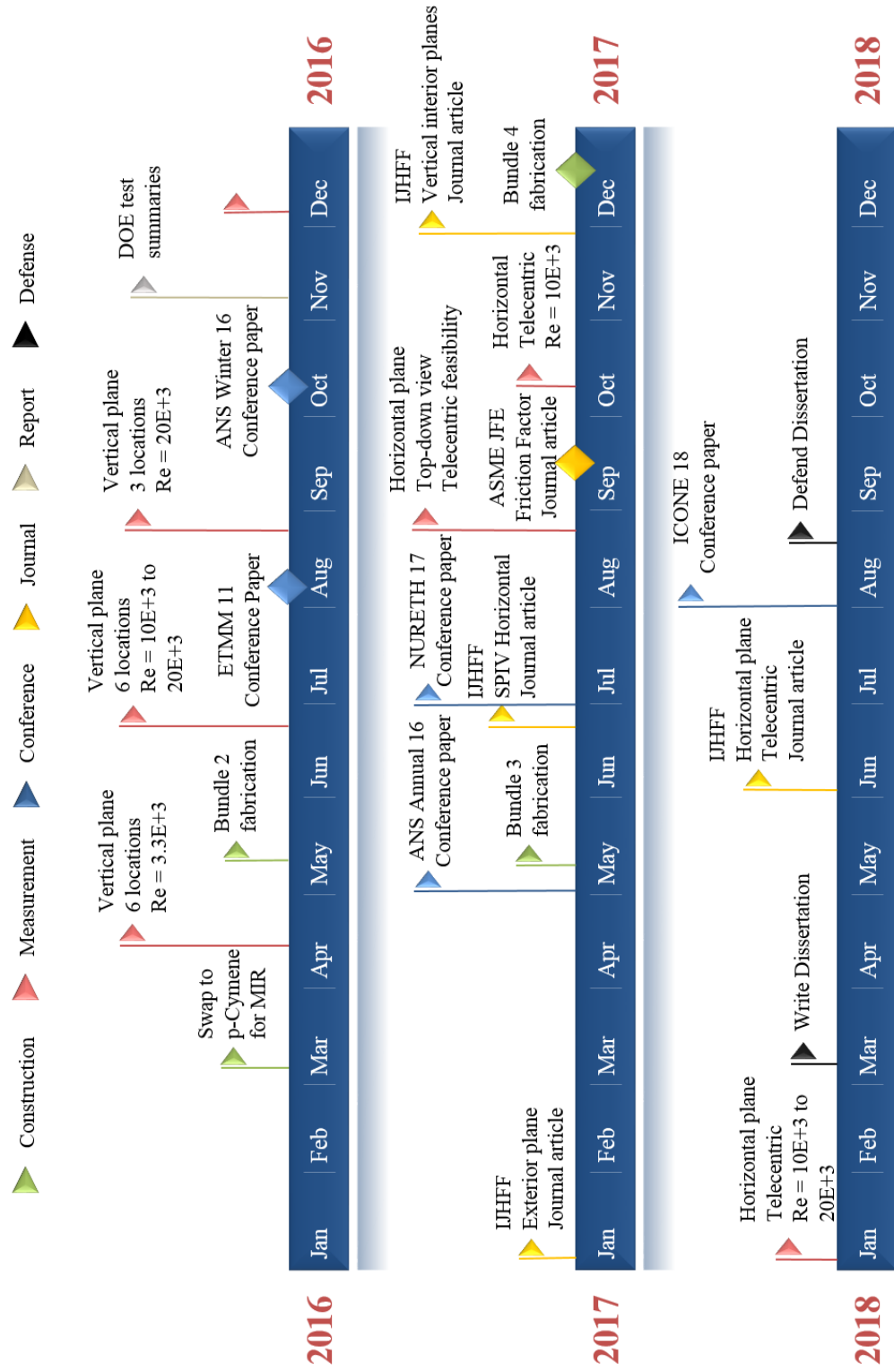
1.6 Dissertation Organization

The structure of this dissertation includes six sections. After this introductory section on the LMFBR background and motivation (Section 1), Section 2 discusses the current state of experimental measurements and simulations on LMFBR fuel bundles. Section 3 highlights the design features of the experimental facility and characterizes the hexagonal duct test section and fuel bundle. Section 4 defines governing equations, the experimental measurement technique, and measurement uncertainties. Section 5 presents results and discussion of the experimental measurements, where each subsection represents a different measurement location inside in the fuel bundle. Finally, Section 6 summarizes the main findings of this work and the direction of future work on the Wire-Wrapped Experimental Facility.

2. LITERATURE REVIEW

A literature review was performed to understand the current state of velocity field experimental measurements and computational simulations on LMFBR fuel bundles. The review covers prior measurement techniques, the motivation for non-intrusive laser-based optical measurements, literature on existing experimental LMFBR MIR facilities, and CFD simulations that are relevant for turbulence modeling validation efforts.

Collingham et al. (1973) were first to present coolant mixing experimental results on a 217-pin wire-wrapped LMFBR bundle utilizing salt injection and conductivity monitoring with over 400 probes. Next, Lorenz and Ginberg (1977) recognized that prior work primarily focused on interior subchannel characterization. Therefore, their work focused on edge subchannels and used electrolytic tracers and isokinetic sampling techniques on a 91-pin bundle. Cheng and Todreas (1986) developed bundle and subchannel friction factor correlations, along with subchannel mixing parameters. These quantities have been extracted from the experimental work of this dissertation and can be compared to the existing literature.

Following those works came advances in digital cameras, laser-based optical techniques for flow visualization, and computational performance for post-processing experimental data and CFD simulations. Grant (1994) compiled the historical development of the modern PIV methodology. The compilation includes the underlying works of Lourenco et al. (1989), Willert and Gharib (1991), Adrian (1991), and Westerweel (1993). Woodhams (1980) and Raffel et al. (2007) were major contributors to applied methods of laser Doppler velocimetry (LDV), PIV, and PTV for flow characterization. With respect to correlation type, multi-pass and multi-grid spatial discretization, velocity interpolation schemes, sub-pixel correlation peak estimation, literature recommendations from Eckstein and Vlachos (2009a), Eckstein and Vlachos (2009b), Westerweel (1994), and Westerweel et al. (1997) will be utilized to justify the image processing methodology for each measurement location.

In 2008, McCreery et al. (2008) designed a 7-pin wire-wrapped hexagonal bundle to

place inside their MIR test section. This was the first experiment capable of measuring velocity fields in interior subchannels of a LMFBR fuel bundle using laser-based optical techniques. Nishimura et al. (2012) performed PIV on a 3-pin bundle to quantify interior subchannel behavior. Sato et al. (2008) used both PIV and LDV to investigate the flow in interior subchannels around the central pin of a 7-pin bundle.

With such a large discrepancy between experimental bundle size (3-,7-,19-pin) and practical bundle size (91- to 271-pin), Brockmeyer et al. (2017) performed a computational study on the dependency of inter-subchannel exchange relative to bundle size. They performed CFD simulations on 19-, 37-, 61-, and 91-pin bundles to estimate the extendibility of small bundle flow behavior to large bundles. They concluded that transverse flow near the central subchannel was very dependent on bundle size, while vortical structure size near the helical wire spacers were nearly independent of bundle size. A recommendation for bundle sizes of 37-pin and greater was given for modeling and experimentation.

3. EXPERIMENTAL FACILITY

This section briefly discusses the design and components of the experimental facility containing a 61-pin hexagonal fuel bundle with helical wire spacers utilized to conduct MIR isothermal flow tests. A detailed description of the experimental facility and lessons learned has been discussed by Goth (2017). The prototypical SFR fuel bundle geometry is displayed in Figure 3.1 as modified from Waltar et al. (2011).
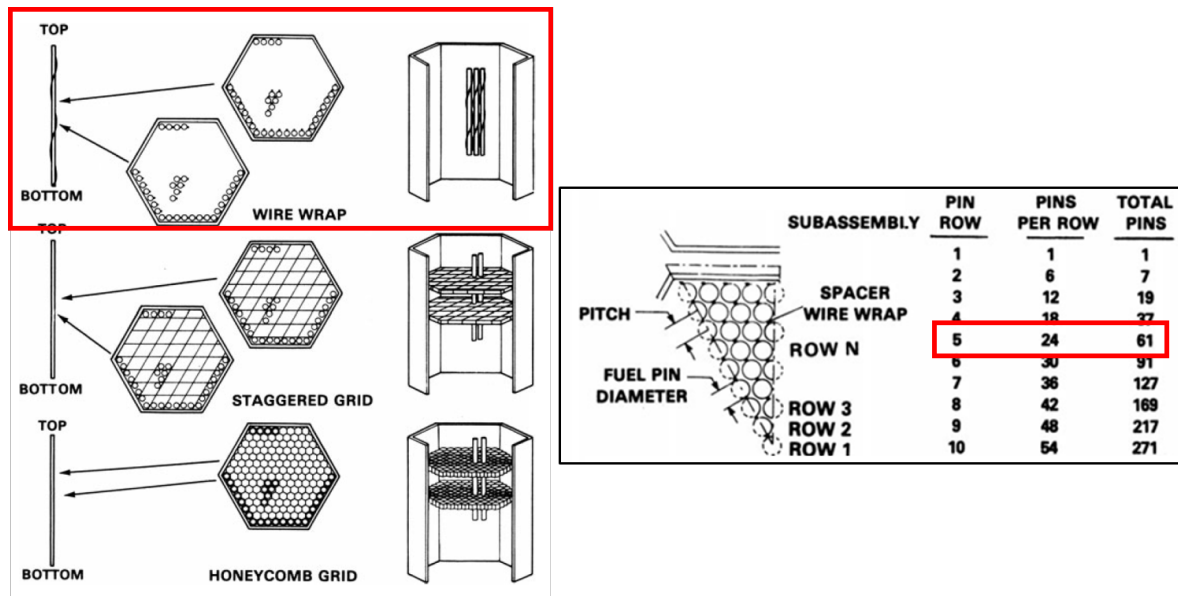
Figure 3.1: Highlighted are the selected spacer method (helical wire-wrap) and bundle size (61-pin) with other spacing and bundle size options presented. Modified from Waltar et al. (2011).

Figure 3.2 presents an overview of the experimental facility. The primary loop contained a centrifugal pump with variable frequency drive (VFD), an in-line turbine flow meter, a resistance temperature detector, an in-line surge reservoir, and a test section which housed the 61-pin bundle. The secondary loop provided inventory control, particulate filtration, and working fluid temperature control. All facility components were made of chemical-

resistant materials, such as Viton seals, cross-linked polyethylene hosing, and 316 stainless steel piping. The test section was structurally isolated from the primary loop utilizing support structures, flexible hoses, and rubber dampeners to reduce the transmission of vibrations.

The experimental facility employed the MIR technique to allow for laser-based optical measurements by matching the refractive index of the pins, wires, and hexagonal duct material to the working fluid. A material's refractive index is both temperature- and wavelength-dependent. For isothermal experimental flow loops, it is beneficial to for the MIR condition to be achievable near room temperature at 295 K. The matching process must also consider the monochromatic light source for the laser-based optical measurement. For PIV, the 532 nm wavelength is most common. For facilities looking to achieve high Re_B flow conditions, it is paramount to consider fluids with low viscosities to avoid large pumping and cooling requirements. Table 3.1 contains two promising solid-fluid pairs for isothermal MIR PIV facilities, as suggested by Campagnole dos Santos et al. (2018) and Hassan and Dominguez-Ontiveros (2008). Both pairs have equivalent potentials for well-matched refractive indicies. However, the selection depends on the fabrication requirements of the solid geometry. Poly(methyl methacrylate) (PMMA) is softer and easier to machine while borosilicate glass is more rigid and chemically compatible with its fluid pair. For the fabrication of the helical wire spacer, PMMA was chosen due to its advantageous machining capabilities. Specific experimental conditions for each measurement location are defined in Section 5.

Table 3.1: Promising solid-fluid pairs for isothermal room temperature (295 K) MIR PIV using 532 nm wavelength light sources for high Re_B applications.

Solid	Refractive Index (n_D)	Fluid	Refractive Index (n_D)	Reference
Borosilicate	1.4726	D-Limonene	1.4727	Works (1987), Arce et al. (2004)
PMMA	1.4908	p-Cymene	1.4912	Bardet et al. (2014)
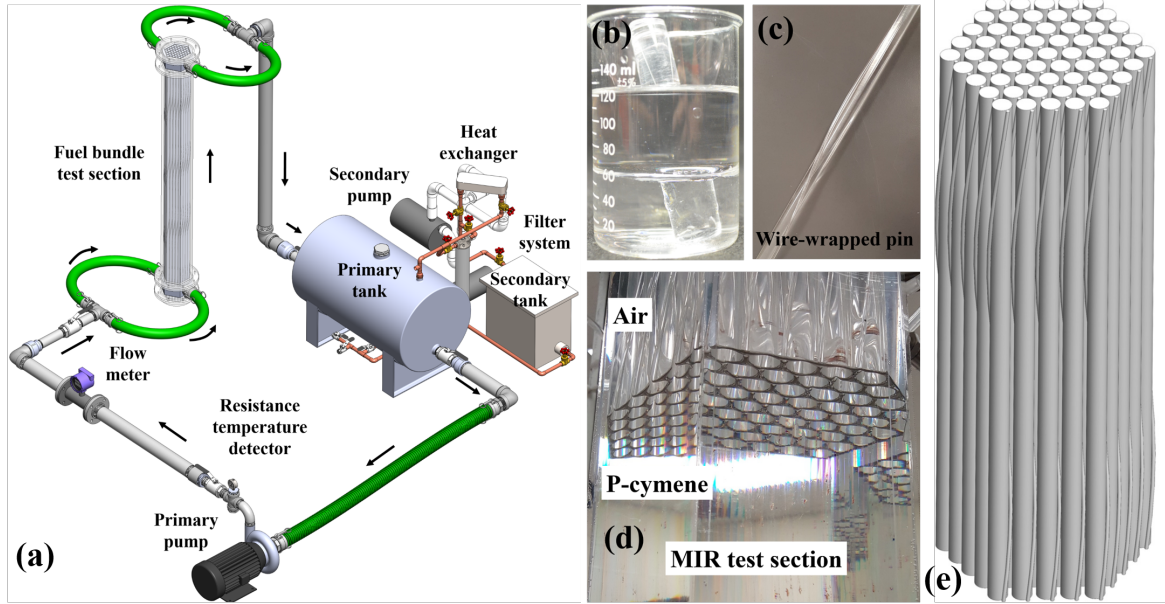
Figure 3.2: *(a)* An overview of the experimental facility primary and secondary loops, *(b)* matched-index-of-refraction technique using PMMA and p-Cymene, *(c)* a fabricated pin, and *(d)* fuel bundle test section half filled with p-Cymene.

Lower and upper guide plates established the triangular lattice and set the wire azimuthal position, as seen in Figure 3.3. Figure 3.4 displays the hexagonal inlet and outlet plena were located upstream and downstream the hexagonal test section, respectively. Flow enters and exits each plena from opposite sides.

3.1 Test Section

Figure 3.5, as modified from Waltar et al. (2011), displays the typical driver fuel bundle for a LMFBR, including the end caps, axial blankets, fission gas plenum, active fuel region, and hexagonal duct enclosure. The experimental bundle in this dissertation only represented the active fuel region of a prototypical bundle.

As seen in Figure 3.6, and as modified from Waltar et al. (2011), the wire wrap, staggered grid, and honeycomb grid are three common methods of minimizing vortex-induced vibrations and avoiding pin-to-pin contact. The experimental bundle in this dissertation only represented the wire-wrap method. The wire wrap method is preferable because it can minimize
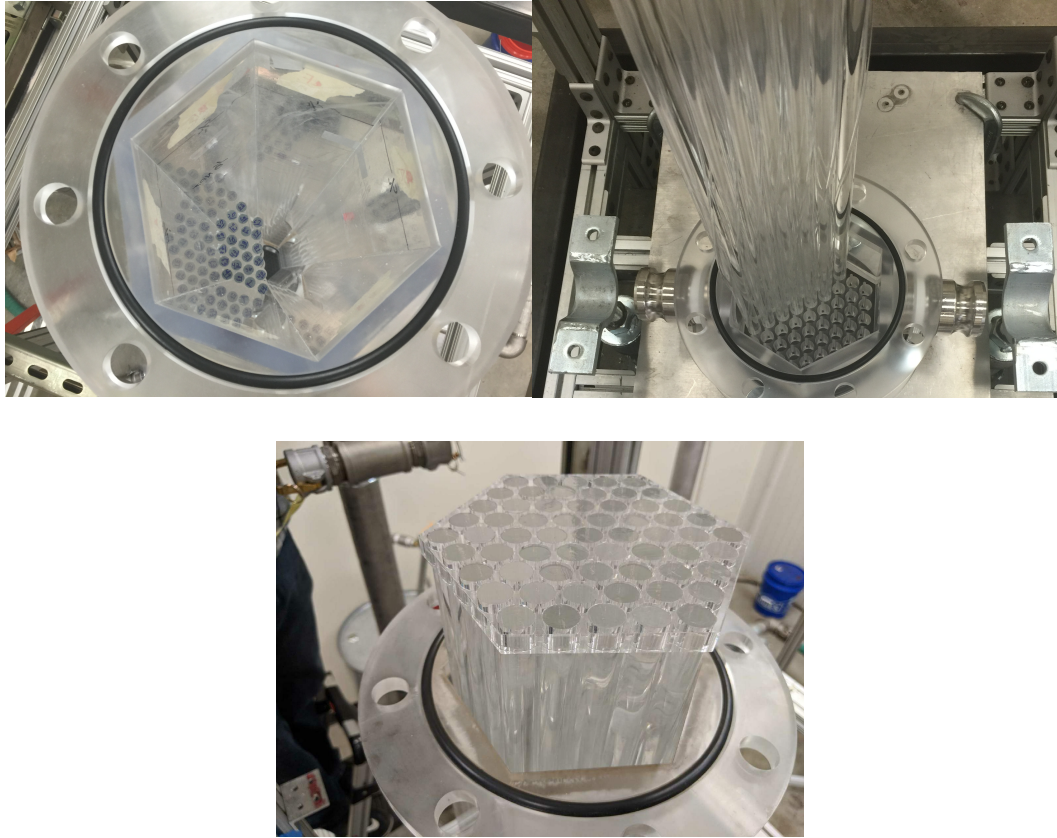
Figure 3.3: Top-down view of a typical core loading showing the lower and upper guide plates used to establish the triangular lattice.

flow induced vibrations while also enhancing subchannel mixing to improve the convective heat transfer ability of the coolant. It also achieves these functions while having a minimal impact on the neutron absorption reaction rate and pressure drop through the core.

The test section housed the experimental fuel bundle, which consisted of 61 pins with helically wrapped wire spacers enclosed in a hexagonal duct. The bundle was arranged in a tightly-packed triangular lattice with the gap between adjacent pins set only by the wire spacer. The triangular lattice is the typical configuration for LMFBRs. The tightly-packed parameter is unique to the SFR, a type of LMFBR, where the pitch-to-diameter ratio (P/D) is reduced to minimize the neutron absorption reaction rate in the sodium coolant.

Figure 3.7 shows a horizontal cross section of the test section. Primary dimensions are presented in Table 3.2. The faces of the hexagonal duct are identified with letters A to F in a
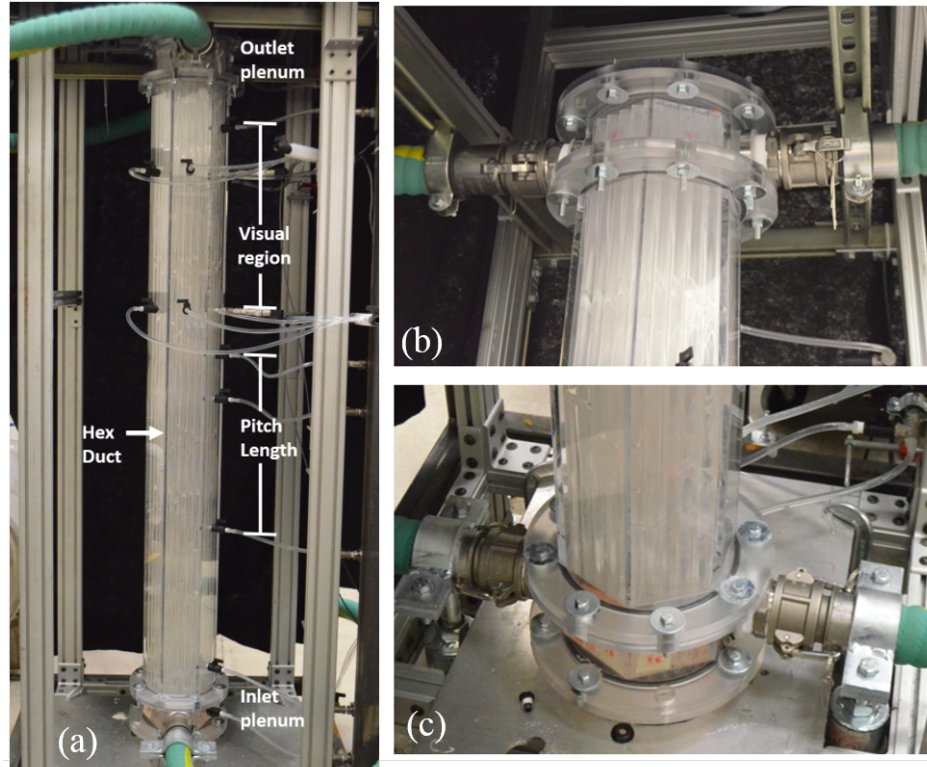
Figure 3.4: *(a)* Test section of the experimental facility with hexagonal duct and *(b)* outlet and *(c)* inlet plena, where fluid exited/entered the test section.

counterclockwise fashion. The flow inlet and outlet are located on Faces B and E. The wire wrap direction is clockwise when looking from the bottom of the fuel bundle toward the top.

As presented by Waltar et al. (2011), the SFR fuel pin P/D typically ranges from 1.06 to 1.29. The P/D of 1.189 was chosen for this experimental investigation to align with the other experimental and simulation efforts of the DOE joint project under DE-NE0008321. Based on typical SFR fuel pin dimensions, the experimental bundle P/D was scaled up by a factor of 2.5 from typical dimensions.

Entrance and exit lengths were selected based on preliminary CFD simulations. The entrance length was 2.25 wire pitches long to achieve fully-developed flow conditions. The exit length was 0.25 wire pitches long to minimize downstream affects. The bundle length in the test section was 3.5 wire pitches. This configuration yielded a fully-developed region with a length equal to 1.0 wire pitches. The wire pitch length compared to the total bundle
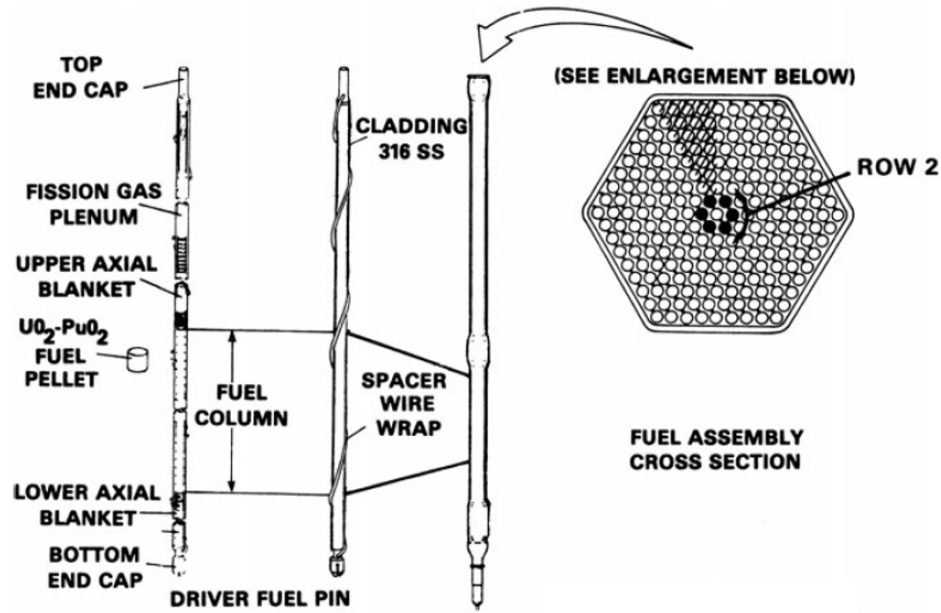
Figure 3.5: Typical LMFBR fuel bundle configuration with axial discretization of the different interior regions for a single pin. Modified from Waltar et al. (2011).

length is presented in Figure 3.4.

Figure 3.8 displays the hexagonal duct and fuel bundle illuminated by vertical and transverse laser sheets. Also visible is an optical prism used to achieve an orthogonal orientation between the vertical laser sheet and camera.

3.2 Volumetric Flowrate Hardware

Quantification of the volumetric flow rate was necessary to estimate the bundle-averaged Reynolds number, which is defined in Section 4.5. Throughout this experimental endeavor, three different instruments were employed to measurement the volumetric flow rate. For the majority duration of the work, a Sponsler in-line precision turbine flowmeter, model SP3-MB-PHL-D-4X, was connected to the data acquisition system (DAS) and its output recorded using LabView. The uncertainty of the flowmeter analog output was 0.025% of full scale at 293 K. The full scale reading was 2271 $\mathrm{L\,min^{-1}}$. A Sponsler IT400 totalizer recorded the analog output from the flowmeter with a digital uncertainty of ± 3.8 $\mathrm{L\,min^{-1}}$. Figure 3.9 displays the meter and totalizer.
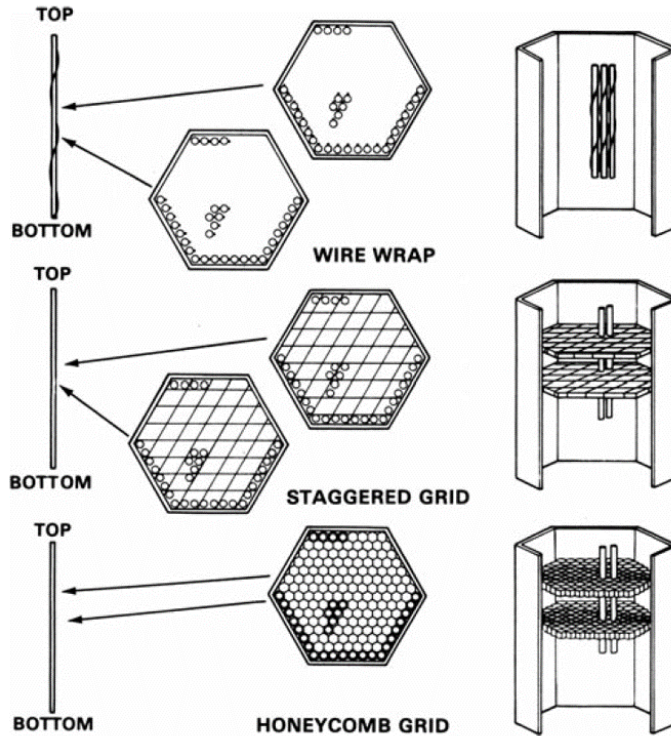
Figure 3.6: The wire wrap, staggered grid, and honeycomb grid methods used to reduce flow induced vibrations of the fuel pin. Modified from Waltar et al. (2011).

The turbine flowmeter was factory calibrated for use in systems with water as the working fluid. Such a calibration was sufficient for water shakedown work conducted in Goth (2017), but required correction when the MIR fluid p-Cymene was introduced. To perform the new calibration, an Omega high accuracy pitot tube, model FPT-6130, was installed into the primary loop of the experimental facility. The pitot tube was connected to three Omega differential pressure (DP) transducers to measure pressure drop across the obstruction caused by the pitot tube over a wide range of flow rates.

The p-Cymene turbine flowmeter calibration involved simultaneously recording the output of the turbine meter and pitot tube at various primary pump speeds between 0% and 100%. Three DP transducers, specified in Table 3.3 were required to measure the range of differential pressure encountered during the flow rate sweep. The sample rate and duration for such recordings was equal to 250 Hz and 15 s. This process was repeated to generate
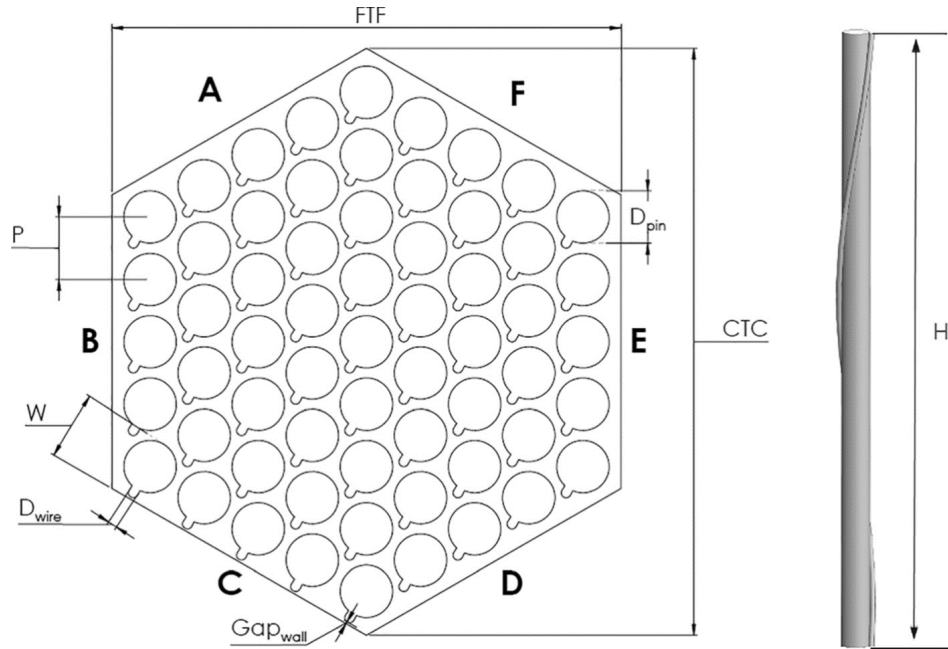
Figure 3.7: Horizontal cross section through the test section and relevant dimensions of the pins, wires, and hexagonal duct enclosure.

two datasets for repeatability analysis. A calibration curve containing 50 data points was generated to applied to the turbine flowmeter output to correct for the different fluid density and kinematic viscosity between water and p-Cymene.

The above mentioned methodology has been applied for all vertical plane PIV flow rate data and subsequent bundle-averaged Re_B number and bulk velocity calculations, which are defined in Section 4.5.

During a restart of the experimental facility after a period of downtime of approximately 2 months, a worker noticed the turbine flowmeter output had drifted from the initial calibration, even though the calibration certificate had not expired. The two variables most likely to influence the turbine flowmeter's behavior were (1) the chemical incompatibility of all wetted surfaces of the turbine meter and (2) the impact of seeding particle deposition in the meter. The manufacturer stated stainless steel was the only wetted surface of the turbine flowmeter. However, p-Cymene is a strong solvent and fabrication tolerances may allow fluid into the bearings of the instrument which could modify its rotational characteristics and

Table 3.2: As-built dimensions and tolerances of the fuel pins, wires, and hexagonal duct used in the experimental facility. The bundle hydraulic diameter, D_h, is equal to 7.728 mm.

Variable	Description	Value (mm)	Value (D_h)
FTF	Flat-to-flat	154.000 ± 0.20	19.93 ± 0.03
P	Rod Pitch	18.875 ± 0.10	2.44 ± 0.01
D_{pin}	Rod Diameter	15.875 ± 0.10	2.05 ± 0.01
D_{wire}	Wire Diameter	3.000 ± 0.05	0.39 ± 0.01
D_h	Hydraulic Diameter	7.728 ± 0.10	1.00 ± 0.01
W	Edge Pitch	19.625 ± 0.10	2.54 ± 0.01
H	Wire Pitch	476.25 ± 2.00	61.63 ± 0.26
CTC	Corner-to-Corner Distance	177.824 ± 0.70	23.00 ± 0.10
Gap_{wall}	Wall Gap Size	0.750 ± 0.10	0.097 ± 0.01
L	Bundle Length	1857 ± 2.00	240.30 ± 0.26
L_{ts}	Bundle Length in Test Section	1667 ± 2.00	215.71 ± 0.26
H/D	Helical Pitch to Pin Diameter Ratio	30 N/A	N/A N/A
P/D	Rod Pitch to Pin Diameter Ratio	1.189 N/A	N/A N/A

Table 3.3: Differential pressure transducers utilized with the Omega model FPT-6130 pitot tube.

Brand	Model	Pressure Range (kPa)	Accuracy (kPa)
Omega	PX409-10WDWUV	0 - 2.49	± 0.02
Omega	PX409-001DWUV	0 - 6.89	± 0.06
Omega	PX409-2.5DWUV	0 - 34.47	± 0.28

result in an out-of-calibration condition.

The corrective action involved replacing the turbine flowmeter with a Sierra InnovaMass 240i in-line vortex shedding flowmeter. Accuracy of the instrument is 0.7% of the volumetric flow rate reading. It also includes a static pressure transducer (± 3.5 kPa) and resistance temperature detector (RTD) (± 1 K). The vortex shedding meter has no moving parts and instead utilizes a pressure transducer to measure vortex shedding frequency caused by a triangular wedge obstruction. Another advantage of the vortex shedding meter is that the
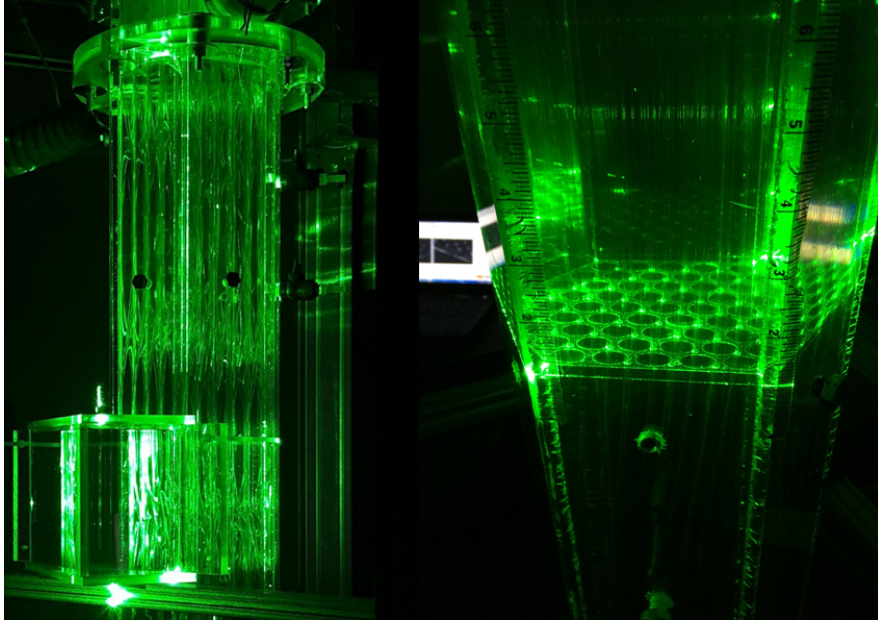
Figure 3.8: (*left*) Vertical laser sheet and optical prism without MIR conditions. (*right*) Transverse laser sheet with MIR conditions.

vortex shedding frequency is not fluid density or viscosity dependent. Therefore, no calibration curve using the Omega high accuracy pitot tube was required, thus reducing another experimental effort and subsequent error propagation. Nevertheless, a primary pump flow sweep from 0% to 100% pump speed was performed while simultaneously recording output from the vortex shedding meter and pitot tube. The two instruments were in agreement with overlapping error bars through the entire measurement range. A summary of volumetric flow rate hardware and instrument accuracy is provided in Table 3.4.

Table 3.4: Volumetric flowrate hardware with DP designating a limit or accuracy dependent on the differential pressure transducer used to perform the measurement

Meter Type	Model	Range ($\mathbf{Lmin^{-1}}$)	Accuracy
Turbine	Sponsler SP3-MB-PHL-D-4X	150 - 2271	1% FS
Pitot Tube	Omega FPT-6130	DP - 2090	1% reading + DP
Vortex Shed	Sierra InnovaMass 240i	80 - 2340	0.7% of reading

Figure 3.9: Sponsler SP3-MB-PHL-D-4X turbine flowmeter and IT 400 totalizer initially used to quantify the volumetric flow rate.

3.3 Temperature Hardware

An RDF Corporation RTD was utilized to measure the fluid temperature during all experimentation. The accuracy of the device was $\pm$ 0.3 K at 273 K with an operating range of 77 K to 753 K. The RTD was connected to the DAS and its output recorded using LabView.

3.4 Fuel Bundle Fabrication

Due to the chemical incompatibility between the working fluid, p-Cymene, and PMMA pins, wires, and hexagonal duct, several experimental bundles were fabricated to address optical and mechanical degradation issues. Cast PMMA pins were procured from PolyOne with a specified cast diameter and fabrication tolerance of 15.875 mm $\pm$ 0.254 mm, respectively. Extruded PMMA pins were procured from Wuxi YanYang International Trading Co. Ltd for the wire spacers with a specified extruded diameter and fabrication tolerance of 3.000 mm $\pm$ 0.15 mm, respectively. Once received by the distributor, pin and wire diameters were quantified at three different axial locations (bottom, middle, and top). Those with the smallest standard deviation about the nominal value were selected. Table 3.5 contains the mean and standard deviation of the pin and wire diameters for Bundles 1 and 2. A total of 5 bundles were fabricated. Bundles 3, 4, and 5 were fabricated with mean and standard deviations

bound by the lower and upper limits of Bundles 1 and 2.

Table 3.5: Experimental fuel pin and wire spacer mean diameter and standard deviation

	Mean D_{rod} (mm)	σ_{rod} (mm)	Mean D_{wire} (mm)	σ_{wire} (mm)
Bundle 1	15.92	0.015	2.97	0.03
Bundle 2	15.88	0.036	3.0	0.03

3.4.1 Wire Attachment Techniques

A thorough pin fabrication process describing the wire attachment technique was out-
lined by Goth (2017). Bundle 1 wires were attached only to the bottom and top of the rods,
similar to how LMFBR fuel pin fabrication is performed. Due to chemical interactions be-
tween the p-Cymene and PMMA, the wires began to elongate slightly and become brittle
over time. Chemical interactions were more severe with the extruded PMMA used for the
wire spacers than the cast PMMA used for the pins. This interaction prompted a more robust
wire attachment technique for Bundle 2. Using a small amount of water-thin cyanoacrylate,
the wires were fully adhered along the entire length of the rod. It is important to recall the
design requirement of MIR throughout the entire bundle. Therefore, cyanoacrylate adhesive
with a very similar refractive index was specified.

The fabrication process for Bundles 2-4 required two people and took approximately two
hours per rod. The process was identical to that of Bundle 1 (Goth (2017)), except for the
following additional steps:

1. With the pin laid horizontally, the wire was tacked with single drops of adhesive at
   eight different axial locations spaced by 0.5 wire pitches.

2. The pin was then rotated vertically.

3. Single drops of adhesive were then applied from the top of the rod to the bottom. The low very viscosity of the adhesive allowed it to run in the joint created by the pin and wire surfaces.

Fabrication tolerances on the wire clocking angle were determined after the bundle was loaded into the facility using a transverse laser sheet. By taking an image of the cross-section and using a centroid estimating algorithm inside ImageJ processing software, the tolerance was calculated as ± 3 degrees.

4. EXPERIMENTAL METHODS

This section includes the governing equations, measurement principles, workflow, practical issues, and measurement uncertainties of the experimental methods utilized to quantify flow behavior in the 61-pin hexagonal bundle. The methods used in this work include PTV, PIV, and SPIV. All approaches are MIR, non-intrusive, laser-based optical measurement techniques to quantify velocity flow fields in exterior and interior subchannels of the fuel bundle. As suggested by Raffel et al. (2007), the measurement concept appeared 34 years ago and has proliferated throughout the fluid mechanics sector. The key attributes to the technique's success are the large amount of data that can be obtained relative to the setup and implementation effort (whole-field methodology), the non-intrusive nature, and the output is instantaneous flow fields rather than averaged quantities. Advances in digital image recording and computational processing power have given these techniques the ability to capture high spatiotemporal resolution image sets and process them with today's modern desktop in reasonable time periods.

4.1 Governing Equations

Claude-Louis Navier and George Gabriel Stokes introduced a system of conservation equations to describe viscous fluid flow via the application of Issac Newton's second law. Conserved quantities in this system are mass, momentum, and energy. Four necessary assumptions for the system include:

- The fluid is continuous for the physical scale of interest

- The flow is steady

- The flow velocity, pressure, temperature, and density are weakly differentiable

- No mass sources or sinks exist in the system

Derivations of the system in the Eulerian reference frame can be found in the works of Temam (2001) and Stokes (1851). Therefore for an incompressible fluid system with the above assumptions, mass conservation may be expressed as,

$$\frac{\partial \rho}{\partial t} + \nabla \cdot (\rho\, \mathbf{u}(\mathbf{x}, t)) + S = \nabla \cdot \mathbf{u}(\mathbf{x}, t) = \frac{du}{dx} + \frac{dv}{dy} + \frac{dw}{dz} = 0 \qquad (4.1)$$

$$(4.2)$$

where ρ is the fluid density, t is time, and $\mathbf{u}(\mathbf{x}, t)$ is the flow velocity vector defined in the Cartesian coordinate system as,

$$\mathbf{u}(\mathbf{x}, t) = (u(\mathbf{x}, t), v(\mathbf{x}, t), w(\mathbf{x}, t)) = \left(\frac{dx}{dt}, \frac{dy}{dt}, \frac{dz}{dt} \right) \qquad (4.3)$$

The general momentum conservation equations simplify significantly for the special case of steady state, viscous, incompressible, Newtonian fluid flow relevant in this dissertation. In the most general form, the momentum conservation equations are,

$$\rho \frac{D\mathbf{u}}{Dt} = \nabla \cdot \boldsymbol{\sigma}_{ij} + \mathbf{f} \qquad (4.4)$$

$$(4.5)$$

where $\frac{D\mathbf{u}}{Dt}$ is a nonlinear operator referred to as the material derivative, $\boldsymbol{\sigma}_{ij}$ is the tensor of normal and shear stresses, and $\mathbf{f}(\mathbf{x}, t)$ represents applied body forces. When the material derivative and the stress tensor are expanded, we have the following,

$$\rho \left[\frac{\partial \mathbf{u}}{\partial t} + (\mathbf{u} \cdot \nabla)\mathbf{u} \right] = \nabla \cdot \begin{bmatrix} \sigma_{xx} & \tau_{xy} & \tau_{xz} \\ \tau_{yx} & \sigma_{yy} & \tau_{yz} \\ \tau_{zx} & \tau_{zy} & \sigma_{zz} \end{bmatrix} + \mathbf{f} \qquad (4.6)$$

Customarily, the stress tensor is split into the sum of its constituent components of volu-

metric stress (pressure or p) and deviatoric stress (shear or T) as,

$$\begin{bmatrix} \sigma_{xx} & \tau_{xy} & \tau_{xz} \\ \tau_{yx} & \sigma_{yy} & \tau_{yz} \\ \tau_{zx} & \tau_{zy} & \sigma_{zz} \end{bmatrix} = - \begin{bmatrix} p & 0 & 0 \\ 0 & p & 0 \\ 0 & 0 & p \end{bmatrix} + \begin{bmatrix} \sigma_{xx}+p & \tau_{xy} & \tau_{xz} \\ \tau_{yx} & \sigma_{yy}+p & \tau_{yz} \\ \tau_{zx} & \tau_{zy} & \sigma_{zz}+p \end{bmatrix} = -pI + T \quad (4.7)$$

After substitution we have,

$$\rho \left[\frac{\partial \mathbf{u}}{\partial t} + (\mathbf{u} \cdot \nabla)\mathbf{u} \right] = -\nabla p + \nabla \cdot T + \mathbf{f} \tag{4.8}$$

To progress further with the derivation, it is necessary to assume fluid incompressibility, a constant kinematic viscosity, and neglect the second viscosity effect and body forces. Also, it is relevant to connect fluid shear, τ_{ij}, to the deformation rate of fluid elements using the kinematic viscosity, μ, as a proportionality constant. This expression is known as Newton's law of viscosity where,

$$\tau_{ij} = \mu(\frac{\partial u_i}{\partial x_j} + \frac{\partial u_j}{\partial x_i}) = \mu \begin{bmatrix} 2\frac{\partial u}{\partial x} & \frac{\partial u}{\partial y} + \frac{\partial v}{\partial x} & \frac{\partial u}{\partial z} + \frac{\partial w}{\partial x} \\ \frac{\partial u}{\partial y} + \frac{\partial v}{\partial x} & 2\frac{\partial v}{\partial y} & \frac{\partial v}{\partial z} + \frac{\partial w}{\partial y} \\ \frac{\partial u}{\partial z} + \frac{\partial w}{\partial x} & \frac{\partial v}{\partial z} + \frac{\partial w}{\partial y} & 2\frac{\partial w}{\partial z} \end{bmatrix} \tag{4.9}$$

Now the divergence of T can be taken and the term reduces to the vector Laplacian,

$$\nabla \cdot T = \mu \nabla^2 \mathbf{u} \tag{4.10}$$

After making such simplifications and assumptions, the Navier-Stokes equations for in-

compressible, viscous flow may be expressed in expanded and expanded Cartesian form as,

$$\rho\left(\frac{\partial u}{\partial t} + u\frac{\partial u}{\partial x} + v\frac{\partial u}{\partial y} + w\frac{\partial u}{\partial z}\right) = -\frac{\partial p}{\partial x} + \rho g_x + \mu\left(\frac{\partial^2 u}{x^2} + \frac{\partial^2 u}{y^2} + \frac{\partial^2 u}{z^2}\right)$$

$$\rho\left(\frac{\partial v}{\partial t} + u\frac{\partial v}{\partial x} + v\frac{\partial v}{\partial y} + w\frac{\partial v}{\partial z}\right) = -\frac{\partial p}{\partial y} + \rho g_y + \mu\left(\frac{\partial^2 v}{x^2} + \frac{\partial^2 v}{y^2} + \frac{\partial^2 v}{z^2}\right)$$

$$\rho\left(\frac{\partial w}{\partial t} + u\frac{\partial w}{\partial x} + v\frac{\partial w}{\partial y} + w\frac{\partial w}{\partial z}\right) = -\frac{\partial p}{\partial z} + \rho g_z + \mu\left(\frac{\partial^2 w}{x^2} + \frac{\partial^2 w}{y^2} + \frac{\partial^2 w}{z^2}\right)$$

$$\rho\left[\frac{\partial \mathbf{u}}{\partial t} + (\mathbf{u} \cdot \nabla)\mathbf{u}\right] = -\nabla p + \rho\mathbf{g} + \mu\nabla^2\mathbf{u} \tag{4.11}$$

where g is the gravitational acceleration constant.

With today's computational processing capabilities, it is common practice to perform design and analysis of fluid systems with time-averaged velocity fields. Therefore to discuss time-averaged quantities, it is important to introduce the Reynolds decomposition proposed by Reynolds (1884). The technique separates the instantaneous fluid velocity into mean (time-averaged) and fluctuating components as,

$$\mathbf{u}(t) = \overline{\mathbf{u}} + \mathbf{u}'(t) \tag{4.12}$$

where $\overline{\mathbf{u}}$ denotes the time-average of $\mathbf{u}(t)$ and $\mathbf{u}'(t)$ denotes the fluctuation about the time-averaged component. The time average of the velocity in a statistically steady flow may be expressed as,

$$\overline{\mathbf{u}}(\mathbf{x}) = \frac{1}{T}\int_0^T \mathbf{u}(\mathbf{x}, t)dt \tag{4.13}$$

As is the case for all experimental fluid dynamics studies, only a subset of the total chaotic flow behavior may be sampled. Therefore, a differentiation between the full time-averaged population and the subset ensemble-averaged sample is made by defining an

ensemble-average as,

$$\overline{\mathbf{u}} = \frac{1}{N} \sum_{n=1}^{N} \mathbf{u}^n \tag{4.14}$$

where N is defined as the number of instantaneous velocity fields measured by an exper-
iment. Therefore, it is important to demonstrate that the N-sized subset of experimental
velocity fields is a sufficiently large sample such that its difference from the full population
set is statistically insignificant. This demonstration is presented in Section 5 by visualizing
the residual convergence of fluid flow variables as a function of subset size for each mea-
surement location.

Now, the definition of Equation 4.12 may be substituted into Equations 4.1 and 4.11 and
results in the Reynolds-averaged equations of mass and momentum conservation,

$$\nabla \cdot \overline{\mathbf{u}} = 0 \tag{4.15}$$

x-component (4.16a)

$$\rho \frac{\partial \overline{u}}{\partial t} + \rho \left[\frac{\partial \overline{u^2}}{\partial x} + \frac{\partial \overline{uv}}{\partial y} + \frac{\partial \overline{uw}}{\partial z} \right] = -\frac{\partial \overline{p}}{\partial x} + \mu \left[\frac{\partial^2 \overline{u}}{\partial x^2} + \frac{\partial^2 \overline{u}}{\partial y^2} + \frac{\partial^2 \overline{u}}{\partial z^2} \right] - \rho \left[\frac{\overline{u'^2}}{\partial x} + \frac{\overline{u'v'}}{\partial y} + \frac{\overline{u'w'}}{\partial z} \right]$$

y-component (4.16b)

$$\rho \frac{\partial \overline{v}}{\partial t} + \rho \left[\frac{\partial \overline{uv}}{\partial x} + \frac{\partial \overline{v^2}}{\partial y} + \frac{\partial \overline{vw}}{\partial z} \right] = -\frac{\partial \overline{p}}{\partial y} + \mu \left[\frac{\partial^2 \overline{v}}{\partial x^2} + \frac{\partial^2 \overline{v}}{\partial y^2} + \frac{\partial^2 \overline{v}}{\partial z^2} \right] - \rho \left[\frac{\overline{u'v'}}{\partial x} + \frac{\overline{v'^2}}{\partial y} + \frac{\overline{v'w'}}{\partial z} \right]$$

z-component (4.16c)

$$\rho \frac{\partial \overline{w}}{\partial t} + \rho \left[\frac{\partial \overline{uw}}{\partial x} + \frac{\partial \overline{vw}}{\partial y} + \frac{\partial \overline{w^2}}{\partial z} \right] = -\frac{\partial \overline{p}}{\partial z} + \mu \left[\frac{\partial^2 \overline{w}}{\partial x^2} + \frac{\partial^2 \overline{w}}{\partial y^2} + \frac{\partial^2 \overline{w}}{\partial z^2} \right] - \rho \left[\frac{\overline{u'w'}}{\partial x} + \frac{\overline{v'w'}}{\partial y} + \frac{\overline{w'^2}}{\partial z} \right]$$

The above component equations of momentum conservation can be simplified utilizing a notational convention suggested by Einstein (1916), where summation over a set of indices is implied by the use of subscripts. This notation introduces significant brevity and will be used henceforth. Therefore, u_i, $\overline{u_i}$, and u'_i denote the instantaneous, mean, and fluctuating velocities. The resulting Reynolds-averaged Navier Stokes (RANS) conservation equations, expressed using Einstein notation are,

$$\rho\frac{\partial \overline{u_i}}{\partial t} + \rho\overline{u_j}\frac{\partial \overline{u_i}}{\partial x_j} + \rho\frac{\partial \overline{u'_i u'_j}}{\partial x_j} = -\frac{\partial \overline{p}}{\partial x_i} + \mu\frac{\partial^2 \overline{u_i}}{\partial x_j \partial x_j} \tag{4.17}$$

These equations yield time-averaged approximate solutions to the Navier-Stokes equations. Before applying the Reynolds Decomposition, the system contained four equations (one mass conversation and three momentum conservation) and four unknowns (pressure and the velocity vector). After the decomposition, the system contains four equations, but now with the introduction of fluctuating velocities has a closure problem. CFD has addressed the closure problem with a plethora of solutions that range from 1 equation to 7 equation turbulence models with various amounts of coefficient tuning and physics-based approximations. This issue is the motivating piece for the generation of high spatiotemporal resolution experimental velocity fields such that turbulence model validation and benchmarking exercises may occur on the LMFBR fuel bundle.

4.2 Experimental Measurement Principles

The basic experimental measurement principle revolves around quantifying the displacement, Δx, of seeding particles in the fluid between consecutive images. The velocity, $\vec{u}$, may then be calculated using such displacement and the known time interval, Δt, between consecutive images. The primary components required to perform the measurement technique include: highly reflective seeding particles, a photon source, photon optics, and a photon detector. In most applications, the photon source is a monochromatic, visible wavelength laser and the photon detector is a digital charge-coupled device (CCD) / complementary metal ox-

ide semiconductor (CMOS) camera. A pulsed or continuous laser can be used to illuminate the seeding particles. Reflected light is then captured by digital camera sensors to create an image. Figure 4.1, as modified from Dynamics (2018), contains a process flow diagram of the method utilizing a dual-head pulsed laser. A collimator and beam-splitting optics are used to focus and direct the laser beam into a thin sheet, which defines the measurement volume. Only tracer particles within the laser sheet are illuminated. A series of images will then be collected and processed to generate instantaneous velocity vector fields. The three types of laser-based optical measurement techniques used in this work were PIV, SPIV, and PTV. Each technique has similar hardware setup and data acquisition requirements, but each utilizes a different processing ideology that will be briefly discussed below. For further discussion regarding these techniques, refer to the works of Westerweel (1993) and Raffel et al. (2007).

2D2C PIV is the most commonly employed laser-based optical measurement technique, as it can be performed with minimal hardware and can cover relatively large measurement regions. Additional cameras may be added to the setup to increase the measurement field of view. SPIV utilizes 2 cameras with an off-normal viewing angle relative to the laser sheet. The images of each camera can be mapped into a single plane to produce 2D3C vector fields. Yet another extension of the measurement technique is called tomographic particle image velocimetry (Tomo-PIV), where a minimum of 4 cameras and a thick laser volume are required. This method produces three-dimension three-component (3D3C) vector volumes.

4.2.1   Cross Correlation

The displacement vector between consecutive images, or image pair, is estimated by a spatial cross-correlation suggested by Keane and Adrian (1992). The process involves discretization of the images into grids of interrogation windows. Discretization criteria is based on rules of thumb specified in Section 4.2.2 and vary based on the flow fields under investigation. Inside each interrogation window of an image, the number and position of particle-images is unique. The objective is to locate the identical particle-image pattern, a
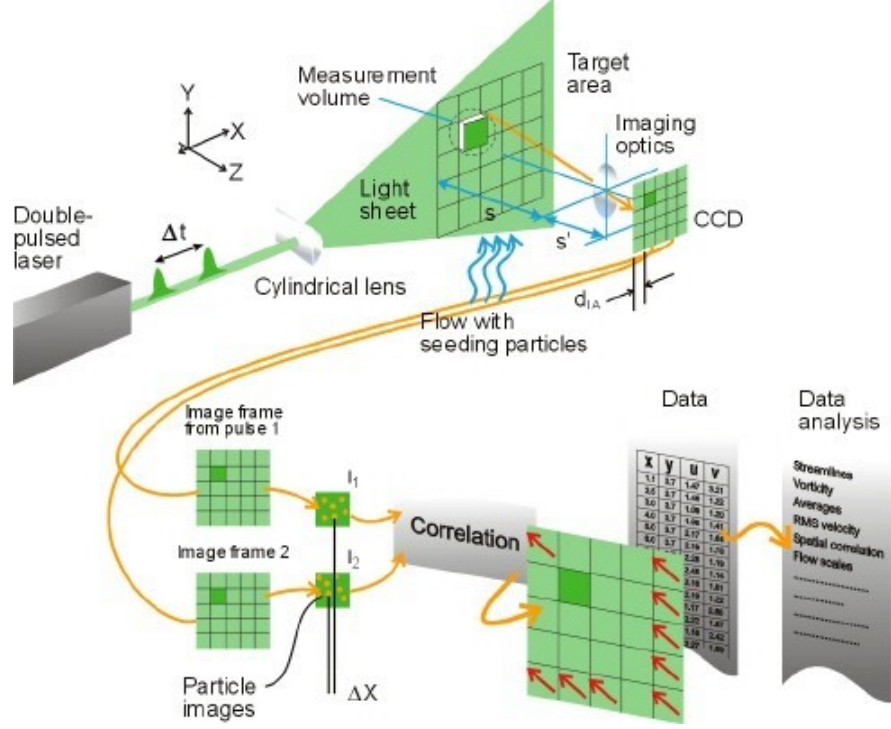
Figure 4.1: PIV measurement principles from imaginag hardware, data acquisition, discretization, cross-correlation processing, and post-processing analysis. Modified from Dynamics (2018).

fingerprint of sorts, in consecutive images. The first identification step is to interpret each image as an intensity field $I_n(x)$, where each pixel has an intensity range between 0 and $2^{bit\ depth}$ of the imaging device. The spatial cross-correlation can be represented generally by Equation 4.18, where W_1 and W_2 are the physical domains of the image pair interrogation window, I_1 and I_2 are the intensity fields of the image pair interrogation window defined by Equations 4.19 and 4.20, $\mathbf{x}$ is the interrogation window position vector, and $\mathbf{s}$ is the separation vector.

$$R(\mathbf{s}) = \int W_1(\mathbf{x})I_1(\mathbf{x})W_2(\mathbf{x}+\mathbf{s})I_2(\mathbf{x}+\mathbf{s})d\mathbf{s} \qquad (4.18)$$

$$\bar{I}_1 = \frac{1}{B_x B_y} \sum_{k=1}^{B_x} \sum_{l=1}^{B_y} I_1(k,l) \qquad (4.19)$$

34

$$\bar{I}_2 = \frac{1}{B_x B_y} \sum_{k=1}^{B_x} \sum_{l=1}^{B_y} I_2(k,l) \tag{4.20}$$

The spatial cross-correlation is typically decomposed into the three components of Equation 4.21, where $R_C(\mathbf{s})$ is the constant background correlation, $R_F(\mathbf{s})$ is the mean and random fluctuation image intensity correlation, and $R_D(\mathbf{s})$ is the displacement correlation of particle-images in the first exposure interrogation window to the second exposure interrogation window. Therefore, the field maximum of $R_D(\mathbf{s})$ occurs where $\mathbf{s} = \delta\mathbf{x}$ and corresponds to the most probable displacement of the particle-image pattern in a specific interrogation window for the current image pair. Such a search process is typically performed in the frequency domain after an fast Fourier transform (FFT) is applied.

$$R(\mathbf{s}) = R_C(\mathbf{s}) + R_F(\mathbf{s}) + R_D(\mathbf{s}) \tag{4.21}$$

It was shown by Raffel et al. (2007) that Equation 4.21 reduces to $R_D(\mathbf{s})$ when subtracting the mean image intensities from I_1 and I_2, respectively. Therefore, $R_D(\mathbf{s})$ may be represented by Equation 4.22.

$$R_D(i,j) = \frac{\sum_{k=1}^{B_x} \sum_{l=1}^{B_y} (I_a(k,l) - \bar{I}_a)(I_b(k+i,l+j) - \bar{I}_b)}{\left[\sum_{k=1}^{B_x} \sum_{l=1}^{B_y} (I_a(k,l) - \bar{I}_a)^2 \sum_{k=1}^{B_x} \sum_{l=1}^{B_y} (I_b(k+i,l+j) - \bar{I}_b)^2 \right]^{\frac{1}{2}}} \tag{4.22}$$

4.2.2 Rules of Thumb

Several aspects of the imaging hardware setup and processing parameters can influence the resulting velocity vector fields. Rules of thumb for various parameters will be discussed in this section. Their associated uncertainties will be discussed in Section 4.4. Assumptions and rules of thumb to reduce measurement uncertainty have been compiled from the the works of Westerweel (1993) and Raffel et al. (2007) and are listed below:

- Seeding particles do not perturb flow behavior

- Seeding particles do not interact or collide with each other

- Initial interrogation window size should be approximately eight times particle image displacement to avoid velocity gradients and large displacement errors

- With a negligible velocity gradient, all particle images in an interrogation window are assumed to have uniform displacement

- Final interrogation window size should be equal to or larger than four times particle image displacement

- Interrogation window particle image density should be at least 10 to ensure an adequate signal-to-noise ratio (SNR)

- Seeding particle diameter should be minimized and density similar to fluid density to ensure particle response time is equivalent to fluid response time, see Section 4.4

- 2.2 pixels is the optimal particle image diameter

- Laser sheet thickness should be minimized to reduce uncertainty of physical laser position for CFD turbulence model validation

- A minimum laser sheet thickness is also set by keeping out-of-plane motion less than 25% of the sheet thickness while having a sufficiently long Δt for detectable in-plane motion

- Camera aperture should be nearly open to shorten the depth of focus and only resolve particle images within the laser sheet

- Vector validation is crucial to eliminate spurious vectors from the field

To accurately assume that fluid element motion may be approximated by seeding particle motion, the seeding particle diameter must be minimized and density matched to the fluid

density. However as seeding particle diameter is minimized, the amount of reflected light is reduced, requiring highly reflective coatings and increased laser light intensity. In the image plane, an optimal particle image diameter exists for each phase algorithm. This optimal diameter must be known and anticipated during the imaging hardware setup, as particle image diameter is a function of both camera resolution and optical magnification. For all measurements in this work, imaging hardware setups were optimized to achieve particle image diameters between 2-3 pixels. The theoretical optimal particle image diameter is approximately 2.2 pixels per Westerweel (1993); Raffel et al. (2007).

An important justification for many assumptions of this measurement technique involves determining the difference between seeding particle response time relative to fluid element response time. The following process was used to select an appropriate seeding particle with deviation of particle motion relative to fluid element motion less than 1% as suggested by Tropea and Yarin (2007). The first step of the process is to calculate the particle Reynolds number as,

$$Re_p = \frac{\rho_f u_{rel} D_p}{\mu_f}$$
(4.23)

where ρ_f is the fluid density, u_{rel} is the relative velocity between seeding particles and fluid elements of the bulk flow far from the particle, D_p is the particle diameter, and μ_f is the fluid dynamic viscosity. If Re_p is less than unity, the particle exists in the Stokes flow regime. Once confirmed, the dimensionless Stokes number is applicable and may be calculated as,

$$Stk = \frac{\tau_p}{\tau_f}$$
(4.24)

where τ_p is the particle response time and τ_l is the fluid response time. Stokes numbers less than one represent configurations where particle response time is less than fluid response time and thus yields better tracking fidelity. The particle and fluid relaxation times

are defined as,

$$\tau_p = \frac{\rho_p D_p^2}{18\mu_f} \tag{4.25}$$

$$\tau_f = \frac{l_0}{u_{rel}} \tag{4.26}$$

where ρ_p is the particle density and l_0 is the characteristic dimension chosen as the hydraulic diameter in this application.

Many different types of phase algorithms exist to calculate the cross-correlation plane and estimate the displacement vector. Each algorithm has strengths and weaknesses for various types of fluid flow and quality of raw image. Nevertheless, the majority of phase algorithms have similar requirements to minimize uncertainty associated with the quantification of the displacement vector. The majority of processing parameters revolve around the size of the interrogation window from which the original image was discretized into.

Hence, it is also important to realize a single displacement vector is quantified per interrogation window and that multiple particle images exist per interrogation window. Therefore, it is crucial that uniform particle displacement occurs in each interrogation window. This assumption can be better met by choosing sufficiently small interrogation windows to minimize gradients of translation, rotation, or shear of the seeding particle motions.

One might consider the smallest size of interrogation window, where each window contains only one seeding particle. However, the SNR of the PIV FFT cross-correlation plane for such a small interrogation window size proves to be insufficient to accurately determine the displacement vector. The works of Keane and Adrian (1992) helped quantify an acceptable lower limit to the seeding particle concentration. To achieve a sufficiently high SNR, a minimum of 10 particle-images per interrogation window is required. The upper limit on seeding particle concentration is such that overlap, or self-shielding, between adjacent particle images does not occur and thus incorrectly influence the cross-correlation calculation. As can be seen, seeding particle density during the image acquisition step plays a major rule

in the final velocity vector field density.

Regarding the selection of interrogation window size, another competing parameter is the particle image displacement. In a multi-pass, multi-grid processing scheme (discussed further in Section 4.3.4), the initial pass (coarsest vector grid) interrogation windows must be sufficiently small to produce a quality initial guess of displacement vectors. It has been found that the initial pass window size should be no larger than eight times the particle image in-plane displacement. Also, the final pass interrogation window size should be no smaller than four times the particle image in-plane displacement. This is set to minimize the in-plane loss of particle images from the interrogation window, which could reduce the accuracy of the cross-correlation. Also, a minimum detectable in-plane displacement vector for most phase algorithms using sub-pixel estimators (Section 4.3.4) is approximately 0.2 pixels.

Out-of-plane displacement should be limited to 25% of the laser sheet thickness. Similar to maximum in-plane displacement, this rule of thumb is ensures that a sufficiently similar particle image pattern is recognizable for the cross-correlation algorithm. The uncertainty of this motion is expanded upon in Section 4.4.

4.2.3 Variations of Standard PIV

Three variations of standard PIV were utilized in this dissertation: time-resolved particle image velocimetry (TR-PIV), PTV, and SPIV. Each will be introduced in the following subsections.

4.2.3.1 Time-Resolved PIV

Typical PIV imaging hardware setups involve dual-head pulse lasers and digital cameras (CCD) with double exposure sensor capabilities. This methodology typically has short time intervals between images of a pair and long time intervals between the acquisition of subsequent image pairs. A standard setup utilizing a Nd:YAG laser may output roughly 400 mJ per pulse and operate with an image pair frequency (repetition rate) of 1-30 Hz. At these frequencies for most turbulent flows, the time interval between subsequent pairs is

sufficiently long such that pairs are nearly statistically independent. This implication limits the measurement technique to statistically steady flows. Therefore, transient or unsteady flows have been unmeasurable in the past. Technological advances in high speed lasers and cameras (CMOS) have allowed for the development of TR-PIV, where the repetition rate may approach 80 kHz or greater. These rates are approaching those required to resolve even the smallest time scales of turbulence for most flow conditions. Drawbacks of TR-PIV systems involve lower resolution images (memory bandwidth limitations) and longer laser pulse widths which may present an issue for high-speed flows.

Both standard PIV and TR-PIV methodologies were employed in this dissertation. Due to hardware availability, 1 megapixel TR-PIV setups were employed for the vertical plane measurements, which occurs chronologically first. An 8 megapixel standard PIV setup was utilized for the transverse plane 2D2C measurement. Both imaging hardware setups investigated statistically steady flows with near constant flow conditions and not transient flow conditions.

4.2.3.2 *Particle Tracking Velocimetry*

For several vertical plane measurements, standard PIV was not applicable due to the small subchannel physical size and lower particle image density. It was therefore necessary to apply the PTV post-processing methodology to the measurement locations of 5.1.2. As discussed by Adrian (1991), PTV was formerly known as low particle number density PIV. While standard PIV estimates the mean displacement of a group of particle images, PTV tracks each individual particle separately through a process involving particle identification, sizing, and tracking.

With this method, the distance between neighboring particle images should be significantly larger than mean displacement. This requirement lends to a much lower particle image density per interrogation window. With such large gaps, consistent identification of particle images in image pairs is possible. The implication of this lower particle image density is that the spatial position of displacement vectors cannot be estimated on the basis of

random choice. They must be estimated where particle images exist.

Some search criteria must be specified for particle image identification based on the im-age parameters. These typically involve thresholding of particle image radius and intensity. Once identified, particle image sizing occurs by calculating the diameter and uses sub-pixel estimation of the particle image to determine the centroid location. Thresholding can be uti-lizing on the search space to eliminate particle images with areas below a specified value. Commonly used sizing functions include: intensity weighted centroid, three-point Gaussian, four-point Gaussian, and least squares Gaussian fit.

Particle image tracking inputs are the particle image centroid, diameter, peak intensity, and ID number. Control parameters include the search radius, importance weighting of the displacement, size, and peak intensity, along with vector validation similar to PIV. Hybrid PIV-PTV can increase the computational efficiency of the particle image tracking algorithm. Standard PIV instantaneous velocity fields are generated and subsequently used as a dis-placement estimator or initial guess to bias the initial search space and inform the search radius. The result is an acceleration of the tracking algorithm. This is similar to the Discrete Window Offset (DWO) of interrogation windows for multi-pass PIV, which is discussed in Section 4.3.4.

PTV statistical analysis is typically performed by discretization of the the flow area into region of interest (ROI)s and sampling PTV vectors inside each ROI for the duration of the image set. Once samples of each ROI have been collected, ensemble-averaged statistics may be calculated.

4.3   Workflow

The workflow process of experimental PIV will be outlined in this section. The process for each measurement location began with the acquisition of data in the form of an image set of size N, which is detailed in Section 4.3.1. Next, a calibration procedure was executed to generate a mapping function between the image and object planes, as discussed in Section 4.3.2. Section 4.3.3 includes the first manipulation of the image set called pre-processing.

This manipulation includes a sequence of steps to increase the SNR of the particles images from the background noise of scattered light from nearby structures. The use of interrogation window pass schemes, cross-correlation algorithm, and displacement vector estimation occur in the PIV processing step (Section 4.3.4), which generates a set of N-1 instantaneous vector fields. Finally, post-processing of the instantaneous vector field set involves calculating derived quantities and analysis of flow behavior (Section 4.3.5).

4.3.1   Data Acquisition

Laser-based optical imaging systems for measuring fluid motion typically consist of a laser, reflective seeding particle, camera, and synchronizer. Various laser sheet and camera setups are possible to measure two-component or three-component velocity vectors. The measurement regions can consist of 2D fields or 3D volumes. Several different imaging setups were utilized for this work. Therefore, each setup will be discussed in each relevant Imaging Settings subsection of Section 5.

All but one measurements in this dissertation utilized TR-PIV methodology. This data acquisition process used high speed CMOS cameras that operated in the single-exposure mode. Based on on-board random access memory (RAM) limitations, the Phantom Miro M310 TR-PIV camera is able to acquire approximately 8,300 images at a resolution of 1280×800, maximum sample frequency of 3200 Hz, and bit depth of 12. To ensure residual convergence of the measurement, more than 8,300 images is required for flow condition inside the 61-pin fuel bundle. Therefore, multiple runs per measurement were required. Specifically, three runs were needed. Refer to the corresponding residual convergence subsection for each measurement location of Section 5 for discussion. After a run, the images were transferred from the full on-board RAM to the on-board solid state drive (SSD). This process took approximately 1 minute. Afterwards, the subsequent runs would be performed until a sufficient number of images was captured. The monochromatic collimated light source for this technique is typically a single head continuously wave laser.

Standard PIV operation was performed for the Transverse Plane 1 measurement, Sec-

tion 5.2.1. This data acquisition process require CCD cameras that operated in the double-exposure mode. The Imperx Bobcat M3340 does not have an on-board RAM and instead immediately transfers the double-exposure information to a frame buffer (PCI-e interface) or the RAM / SSD / hard disk drive (HDD) of the control computer running the acquisition software. The camera is able to acquire images up to the available control computer memory specifications at a resolution of 3312 × 2488, maximum double-exposure frequency of 8 Hz, and bit depth of 12. The monochromatic collimated light source for this technique is typically a dual head pulsed Q-switch laser.

As each measurement setup was unique, a series of parameters were optimized for each condition. To achieve an optimal particle image diameter of roughly 2 pixels, various lenses were required to adjust the magnification for the given working distance. The most commonly used lenses were the 50 mm Zeiss Makro-Planarf/2 ZF lens and 100 mm Zeiss Makro-Planarf/2 ZF lens. The use of the aperture on these lenses for PIV is typically f/4 or f/5.6, as these settings decrease the depth of focus, ensuring that only particles within the laser sheet are captured in the image, while avoiding the slight vignetting can occurs with the largest aperture. An optimum exposure is a function of the laser light intensity, aperture setting, and relative velocity of seeding particles one is trying to photograph.

Beam shaping with cylindrical lenses is necessary to convert the laser beam into what is typically referred to as the laser sheet. The first step is to collimate the raw beam output, which may be elliptical due to the laser diode, into a circular beam. Next, the circular beam must be expanded in a single dimension, which is where cylindrical lenses are advantageous for this application. A plano-convex cylindrical lens placed downstream of the collimator expands the circular beam at the half angle relative to the circular beam radius and focal length of the plano-concex cylindrical lens. A second plano-convex cylindrical lens placed yet again downstream and rotated 90 degrees from the first cylindrical lens yields the desired manipulation and generates the laser sheet. The focal length of the upstream cylindrical lens determines the expansion angle from collimated beam to sheet. The focal length of the

downstream cylindrical lens determines the distance of thinnest possible sheet. A thin sheet is extremely important if the goal to use the experimental data to make comparisons with CFD simulation results. Figure 4.2, as modified from EdmundOptics (2018), displays the collimation and expansion steps.

(a) Collimation of the raw ellipsoidal beam.

(b) Expansion of the collimated circular beam into the laser sheet
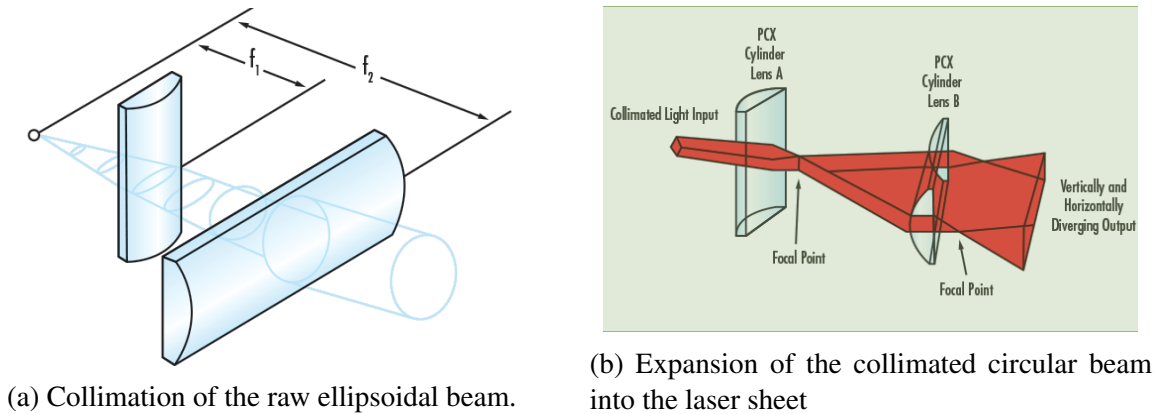
Figure 4.2: Beam shaping ray diagrams using cylindrical lenses for laser sheets. Modified from EdmundOptics (2018).

Intra-frame time delay between images is defined by ensuring out-of-plane particle displacement is less than 25% of the laser sheet thickness, while also allowing for sufficient in-plane particle displacement, which should be greater than 1 pixel. These recommendations were given by Adrian (1991) and Raffel et al. (2007). Based on the optimizations discussed, the resulting measurement FOV is defined. Additional cameras may be placed adjacent to one another with overlapping views. The resulting vector fields from each camera can be combined to increase the total FOV of the measurement.

Seeding particle usage was consistent for all measurement locations. Potters Industries Conduct-O-Fil SH400S20 silver-coated hollow glass spheres were selected as the ideal seeding particle based on an optimization of the reflectivity, diameter, and density. The selected particles had a mean diameter of 16 µm and a density of 1.6 g cm^{-3}. The Stokes number can be used to estimate seeding particle fidelity with fluid element motion and select an

appropriate seeding particle given a few parameters regarding the experiment. This calculation is discussed in Section 4.4. The seeding particles were injected into the primary loop downstream the primary pump via the particle injection manifold, Figure 4.3 .

Figure 4.3: Seeding particle injection manifold can be operated with the facility online to ensure a well-mixed distribution and allow for real-time concentration control

When applicable for vertical laser plane measurements, correction boxes were utilized to achieve orthogonal alignment for the laser sheet and cameras. Because of the hexagonal duct geometry, the most commonly used correction boxes were 30-60-90 triangular prisms constructed from PMMA. Placement of such optical prisms can be seen in Figures 5.4, 5.16, and 5.21.

A data acquisition process involved the following steps:

1. At the beginning of each test, written procedures were followed to verify equipment functionality.

2. The primary pump VFD was configured to achieve the desired volumetric flow rate for the given test.

3. Initial conditions of temperature and volumetric flow rate were established and recorded after maintaining pump speed for a sufficiently long period of time to guarantee statistically-steady flow conditions.

4. While maintaining pump speed and recording temperature and volumetric flow rate at 10 Hz, three consecutive runs fluid velocity measurements were performed at various frequencies that will be defined later.

4.3.2 Calibration

Calibration is defined as the mapping of the image space to an object space. This process allows a relevant scale to be applied to the images, such that the displacement vector, initially in pixels, can be convert to a unit of length based on some object. Both linear and nonlinear mapping functions can be applied. For all PIV measurements, linear mapping functions were generated. For all SPIV measurements, nonlinear mapping functions were generated using the reconstruction technique suggested by Soloff et al. (1997). For all measurements, a single-sided, dual level calibration plate from LaVision, model 106-10-SSDP, assisted in the mapping process. Dimensions of the plate are listed in Table 4.1

Table 4.1: LAVision dual level calibration plate model 106-16-SSDP dimensions

	Value (mm)	Tolerance ($\pm$ mm)
plate height	106	0.02
plate width	106	0.02
dot diameter	2.2	N/A
dot spacing	10	0.02
level separation	2	0.01

4.3.3 Pre-Processing

Before processing an image set, noise reducing pre-processing steps were always employed. The first step of pre-processing involved calculating the mean image intensity for a given image set. Once quantified, the mean intensity field was then subtracted from each image in the given image set. The result is a background-subtracted image set with a drastically improved SNR. Figure 4.4 presents a raw intensity image, the mean background intensity image, and a background subtracted image of Transverse Plane 1 to demonstrate the result of pre-processing to increase the SNR. Appendix E and Appendix F contain example scripts to calculate the mean image intensity of an image and also pre-processing for both single channel B&W and triple channel RBG images. The final step of pre-processing is to define the ROI relevant to processing by defining a static or dynamic mask that delineates each image into active areas considered for PIV processing and inactive areas ignored for PIV processing. Static masking in this dissertation always defined the physical boundary between solid and fluid structures.

(a) Raw image

(b) Mean background subtracted image
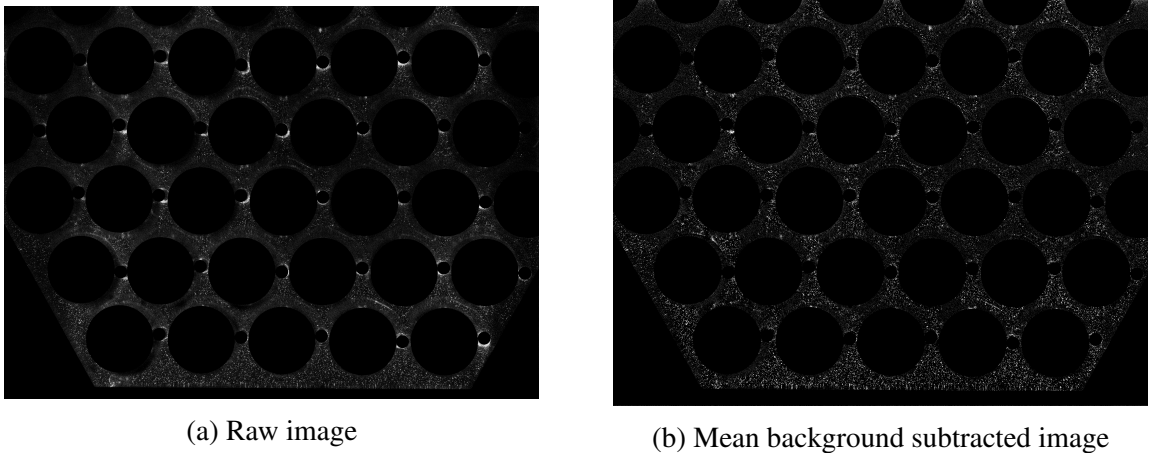
Figure 4.4: Pre-processing result by subtracting the mean image intensity from a raw image to increase the SNR of particle images.

4.3.4 Processing

The PTV, PIV, and SPIV PRANA codes developed by Eckstein and Vlachos (2009a,b) were the primary PIV processing algorithms for this dissertation. PRANA is an open-source, GUI-based, MATLAB program developed for calculating instantaneous velocity fields. The latest release may be found at the Github repository, `https://github.com/aether-lab/prana`. Each measurement location utilized the advanced multi-pass, multi-grid processing scheme with the DWO robust phase correlation (RPC) algorithms of Westerweel et al. (1997) and Eckstein and Vlachos (2009b). The increased efficiency of the window offset allows for the initial pass to be quite coarse relative to the final pass, which greatly reduces the computational cost. Three interrogation window passes were performed for each location. The interrogation window size overlap fraction were specific to each measurement and are therefore defined in the relevant subsections of Section 5. Pass 1 generated the coarsest vector field, while Passes 2 and 3 were refined fields. The Pass 1 coarse field was operated on by a bi-cubic interpolation scheme to generate an initial guess vector field for Pass 2. This guess is used by the DWO algorithm to increase computational efficiency of the search space and can lead to accuracy improvement by increasing the probability of selecting the most appropriate correlation peak. The process was also repeated for Pass 3. The RPC algorithm of Eckstein and Vlachos (2007) functions by operating on each interrogation window with an FFT to transform into the spectral domain. To increase the SNR of the correlation plane, a phase transform filter is utilized. Next, the cross-correlation is performed and followed by an inverse FFT. Afterwards, sub-pixel resolution of the correlation peak centroid is achieved using a three-point Gaussian estimator in both X and Y directions.

After each pass, the UOD method of Westerweel and Scarano (2005) was utilized to detect and eliminate spurious vectors via vector validation before moving to the next pass. The method compares each displacement vector to the median value of the adjacent eight vectors in a 3×3 grid. If the first correlation peak displacement vector is outside the residual threshold criteria, it is replaced by the second correlation peak displacement vector. If the

second peak is again outside the residual median threshold criteria, it is replacement by the third peak. Finally, if the third peak is again outside the residual median threshold criteria, the vector is replaced by the median of the adjacent eight vectors in the surrounding 3×3 grid.

An output file is generated for each correlated image pair. By defining the total number of images as N, standard PIV processing would result in $N/2$ output files, while TR-PIV would result in N-1 output files. The output container from PRANA PIV is a MATLAB file structure containing arrays of the two in-plane coordinates of the vector field (X,Y), the two in-plane components of instantaneous velocity(U,V), the statistical validation and vector replacement results (Eval), the primary peak cross-correlation plane (C), and, if specified, secondary and tertiary peak cross-correlation planes.

4.3.5 Analysis

After generating PRANA output files, post-processing and subsequent analysis was performed on the set of instantaneous velocity fields. The first step of analysis was to determine an overall level of confidence in the dataset. To do so, the first PRANA output parameter to investigate was $Eval$, which is included with each instantaneous velocity field output. This array tracks the results of the UOD vector validation success. It is therefore easy to calculate a mean field to shows the validation failure and subsequent vector replacement. The simplest of the fields to analyze is the mean replacement field. The interpretation is simply the replacement frequency for each vector. In this instance, replacement was defined any instance a validation threshold was not met, either by correlation peak 1 failure, correlation peak 2 failure, or correlation peak 3 failure. Visualization regions with low seeding density, shadows, and extraneous scattered light produce regions of high vector replacement and thus regions of lower confidence. In this dissertation, vectors with replacement frequencies above 40% were deemed questionable and discarded.

Now with modified instantaneous velocity fields, flow characterization began. The first task was to split the instantaneous datasets into ensemble-averaged and fluctuating compo-

nents by performing the Reynolds decomposition specified in Equation 4.12. This results in a single ensemble-average field and a number of fluctuating velocity fields equal to the size of the dataset. Next, it is customary to calculate an RMS field from the set fluctuating fields. It is important to note the RMS of the fluctuating component is equivalent to the standard deviation of the ensemble-average. A mean Reynolds shear stress field can be generated from the instantaneous fluctuating velocity fields. For 2D2C PIV, single component instantaneous and ensemble-averaged vorticity fields and may be calculated. For 2D3C SPIV, all three components of vorticity can be determined. Appendix G and Appendix H contain example scripts to calculate these quantities from the instantaneous velocity fields.

Turbulent kinetic energy, two-point spatiotemporal and spatial velocity-velocity cross-correlations, integral length scales, and vortical reconstruction are but a few of the quantities that can be derived from each experimental measurement location for each Reynolds number.

4.4 Measurement Uncertainties

Sources of velocity vector field uncertainty come from six primary categories, which are: magnification factor, displacement vector estimation, laser sheet positioning, as-built dimensions, experimental conditions, and intra-pair time delay. Sources within each of these categories will be discussed further. Methodologies for PIV uncertainty quantification are presented in thorough detail in the works of Sciacchitano and Wieneke (2016) and Sabharwall et al. (2013).

When employing best practices of imaging hardware setup, the magnification factor typically accounts for 10% of the total measurement uncertainty. Magnification factor sources of uncertainty include:

- Image plane distance of calibration dot positions

- Camera sensor distortion

- Optical lensing configuration distortion

- Orientation angle between camera and laser sheet

- Orientation angle between camera and calibration plate

When employing best practices of noise reduction and cross-correlation algorithm selection, the displacement vector typically accounts for 90% of the total measurement uncertainty. Displacement vector estimation sources of uncertainty include:

- Particle image diameter

- Particle image density

- Particle image uniformity

- Particle response time relative to fluid response time

- Laser light intensity fluctuation

- Phase cross-correlation algorithm of displacement vector

- Sub-pixel correlation peak estimation

- Convergence of residuals related to size to image set

Laser sheet positioning sources of uncertainty include:

- Goodness of refractive index matching of solid / fluid pair

- Laser sheet thickness

- Zero position of laser sheet

- Traversal equipment

As-built dimensional sources of uncertainty include:

- Tolerance of rod diameter

- Tolerance of wire spacer diameter

- Tolerance of wire spacer clocking angle

- Tolerance of hexagonal duct test section

Experimental condition sources of uncertainty include:

- Fluid temperature

- Fluid density

- Fluid viscosity

Intra-pair time delay includes all of the analog and digital timing hardware of the camera, laser, and synchronizer. The uncertainty of this categories is typically deemed as negligible.

4.5 Bundle-Averaged Reynolds Number

At each measurement location, image sets were collected for various bundle-averaged Reynolds numbers. The bundle-averaged Reynolds number, Re_B is defined by,

$$Re_B = \frac{\rho_f \overline{w} D_h}{\mu_f} \qquad (4.27)$$

where ρ_f is the fluid density, $\overline{w}$ is the bulk axial velocity, D_h is the hydraulic diameter, and μ_f is the fluid dynamic viscosity. The bulk axial velocity was estimated for each measurement by,

$$\overline{w} = \frac{Q}{A_{flow}} \qquad (4.28)$$

where Q is the volumetric flow rate recorded by the volumetric flowmeter and A_{flow} is the flow area of the bundle.

5. MEASUREMENTS*

This section includes discussion regarding all performed measurement setups and locations. A total of 9 different measurement locations were investigated to quantify the turbulent behavior of the bulk swirl and local swirl around pins in the corner, edge, and interior subchannels of the 61-pin hexagonal fuel bundle. Figure 5.1 highlights the 7 vertical plane and 2 transverse plane measurement locations of this dissertation. For each location, flow behavior at 3-5 different Re_B was captured. In total, 50 unique datasets were generated from this work. Table A.1 of Appendix A contains an experimental test matrix of completed measurements. Figure 5.2 displays the flow regime map of Cheng and Todreas (1986) overlaid with experimental runs completed in this study for the fuel bundle's P/D of 1.189. Most measurements have been performed in the turbulent regime, along with a few measurements in the laminar and transition flow regimes. The following measurement locations will be discussed in further detail in this dissertation: PIV Vertical Plane 1, PIV Vertical Plane 2, PIV Vertical Plane 6, and PIV Transverse Plane 1.

This section is organized first by the measurement plane orientation, which was either vertical or transverse, then by the physical location of the measurement plane (exterior, interior, or central subchannels), and finally by the Re_B of the experimental test.

5.1 Vertical Plane Measurements

Vertical plane measurements are highlighted in Figure 5.1. All PIV vertical plane measurements utilized 2 synchronized high speed cameras with overlapping FOVs. This configuration nearly doubles the measurement window for a given experimental test. Vertical plane

---

Vertical Planes   **Horizontal Planes**

■ **PIV (2D2C)**   ■ **Stereoscopic PIV (2D3C)**

Figure 5.1: Planned vertical and transverse (horizontal) plane measurement locations for both 2D2C PIV and 2D3C SPIV imaging techniques.

measurement windows span roughly a vertical distance of 0.25 wire pitches. Measurement planes in this section include PIV Vertical Plane 1, PIV Vertical Plane 2, and PIV Vertical Plane 6.

5.1.1   PIV Vertical Plane 1 (Exterior-1) (2D2C)

PIV Vertical Plane 1 (Exterior-1) is the measurement plane nearest and parallel to hexagonal duct wall F and parallel to the axial flow. Figure 5.3 shows a computer-aided design (CAD) rendering of a typical 2D2C PIV vertical plane measurement setup for the fuel bundle. Three-axis traversing systems were used to align the cameras and laser. Beam combination optics formed the laser sheet. A 30-60-90 optical prism was utilized to guide the laser sheet into the test section to achieve the normal viewing orientation between laser and camera. For further flow behavior analysis on this measurement location, please refer to the
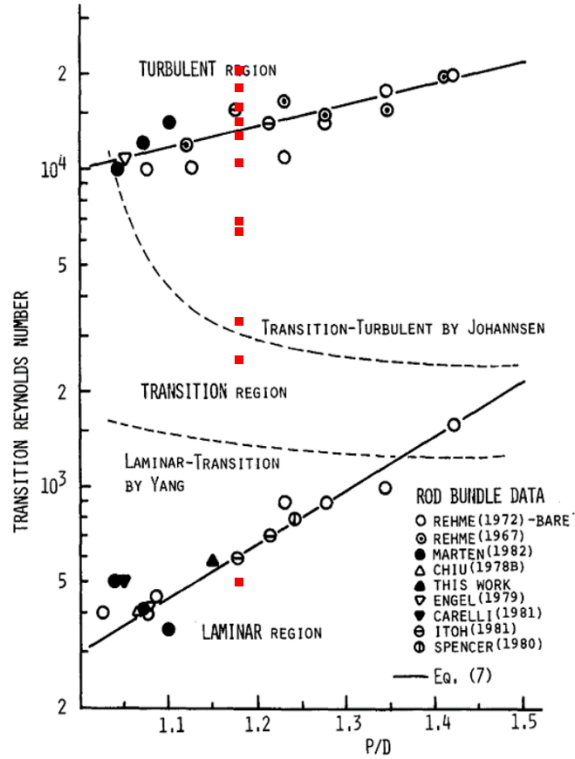
Figure 5.2: Flow regime map by Cheng and Todreas (1986) with experimental runs completed in this study denoted along P/D = 1.189.

works of Nguyen et al. (2017).

Shown in Figure 5.4, the measurement was performed on the set of exterior subchannels formed by the exterior row of pins 1-5 and hexagonal duct wall on Face F. The partial wrap of the helical wire spacer denotes the wire's path from the bottom of the measurement window FOV to the top. This is also highlighted by areas 1 and 2 for each camera. The height of the total measurement region is 0.25 wire pitches. The physical gap size between the pins or wires and hexagonal duct wall varied between 0.75 mm and 3.75 mm. An X-Y coordinate system was defined to represent the horizontal (transversal) and vertical (axial) directions, respectively. The system origin is at the intersection of the laser sheet and inner surface of the hexagonal duct wall and at the elevation of 2.25 wire pitches from the test section entrance.

Experimental results for a total of five different Re_B are presented in this section. The set of Re_B include 3410, 10410, 12370, and 19760. For each Re_B, three measurement runs

55
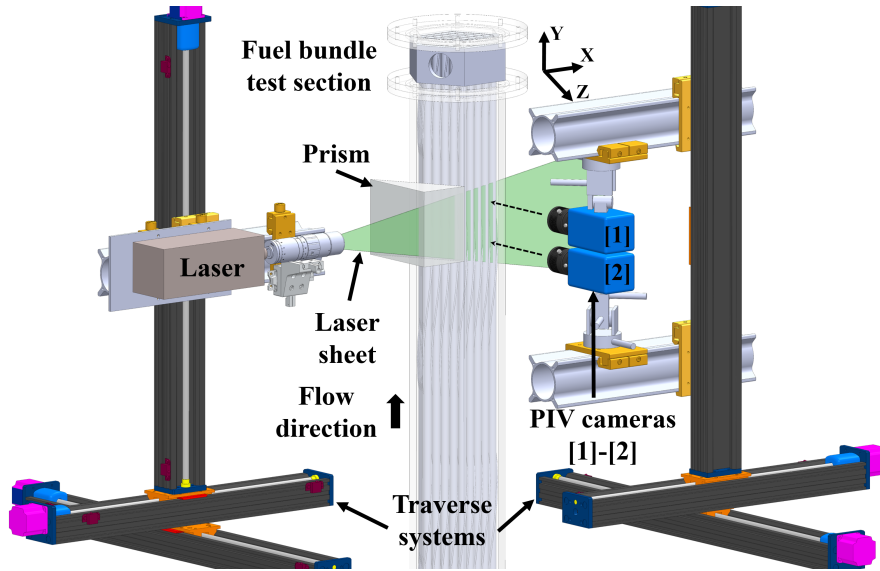
Figure 5.3: Imaging setup for the 2D2C Vertical Plane 1 PIV measurement containing test section, laser, camera, and traverse systems

were performed generating total image set sizes of 24,927 images.

5.1.1.1 *Imaging Settings*

The monochromatic collimated light source was generated using a 10 W continuous wave laser at 532 nm. Beam combination optics included a focusable collimator, 15 mm cylindrical plano-concave lens, and 25 mm cylindrical plano-convex lens. The resulting laser sheet had a thickness of 1.5 mm ± 0.5 mm. Two Phantom Miro M310 cameras captured the laser light with a resolution of 1280×800 and bit depth of 12. Each camera was paired to a 100 mm Zeiss Makro-Planarf/2 ZF lens with the aperture set to f/4. The camera image sample rate and exposure were unique for each Re_B being investigated and is defined locally in the following subsections.

Laser alignment consisted of first revolving the laser base until the sheet was parallel with the inner surface of the wall forming Face F. A parallel orientation was achieved by revolving the based until equal light intensity was achieved for the two corners of Face F. Next, the laser sheet was laterally traversed until the vertical sheet's inner wall began intersecting the exterior row of rods. The parallel orientation was checked again by visual inspection,
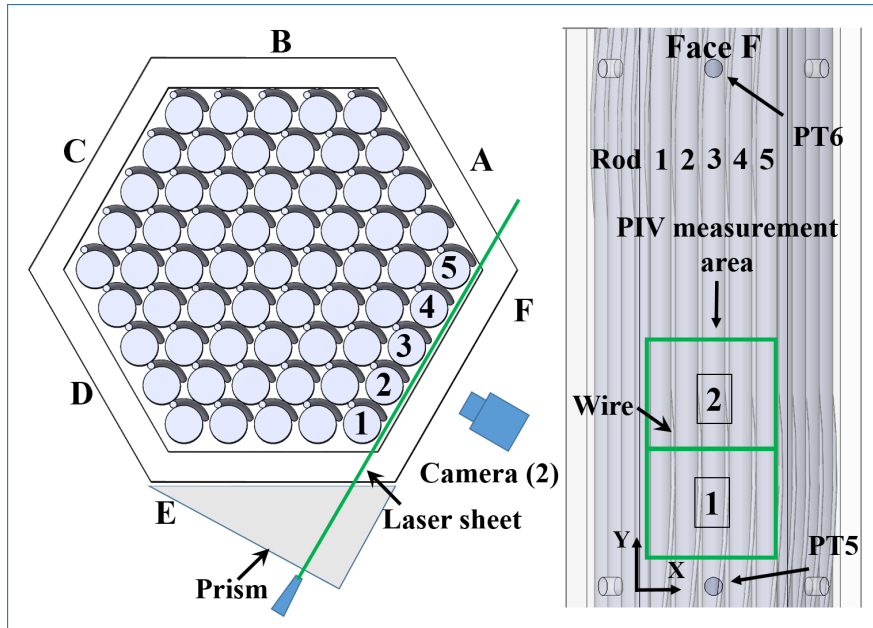
Figure 5.4: (*Left*) Top-down cross section of the fuel bundle denoting wire position and laser sheet illuminating the set of exterior subchannels. (*Right*) Side view showing the measurement window FOV and wire spacers intersecting the laser sheet from adjacent pins.

as the laser sheet would simultaneous illumination rods 1-5 as the sheet began to intersect them. Finally, the laser sheet was laterally traversed back into the exterior subchannels. The distance of the laser sheet center from the tangent plane along the exterior rods was 1.125 mm ± 0.5 mm.

5.1.1.2 PIV Processing Settings

PIV images were processing using the PRANA code introduced in Section 4.3.4. More information regarding processing settings can be found there. Table 5.1 contains the PIV processing parameters for Vertical Plane 1.

5.1.1.3 Vector Validation and Residual Convergence

This section included the discussion regarding UOD vector validation results and residual convergence of first and second order flow statistics for Re_B = 19,760 only. As can be seen in Figure 5.5, an approximate four vector thickness of high replacement occurs at the FOV edge. These regions are not compared when performing CFD comparisons. The values

Table 5.1: PIV processing settings for PIV Vertical Plane 1

Parameter	Pass 1	Pass 2	Pass 3
Multigrid method	Bi-cubic	Bi-cubic	Bi-cubic
Searching window size (pix)	128 × 128	64 × 64	32 × 32
Interrogation window size (pix)	64 × 64	32 × 32	16 × 16
Interrogation window overlap	50%	50%	50%
Grid buffer	8 × 8	8 × 8	8 × 8
Correlation type	RPC	RPC	RPC
Subpixel peak location	3 Pt. Gaussian	3 Pt. Gaussian	3 Pt. Gaussian
Vector Validation	UOD median	UOD median	UOD median

have been incorrectly modified by the UOD process, where the edge-most vectors had an insufficient number of neighbors to perform an acceptable nearest neighbor median comparison. This is also typical when near the edge of any solid structures, such as the hexagonal duct wall, pin, or helical wire spacer.

(a) Camera 1 replacement frequency heatmap from UOD vector validation checks

(b) Camera 2 replacement frequency heatmap from UOD vector validation checks
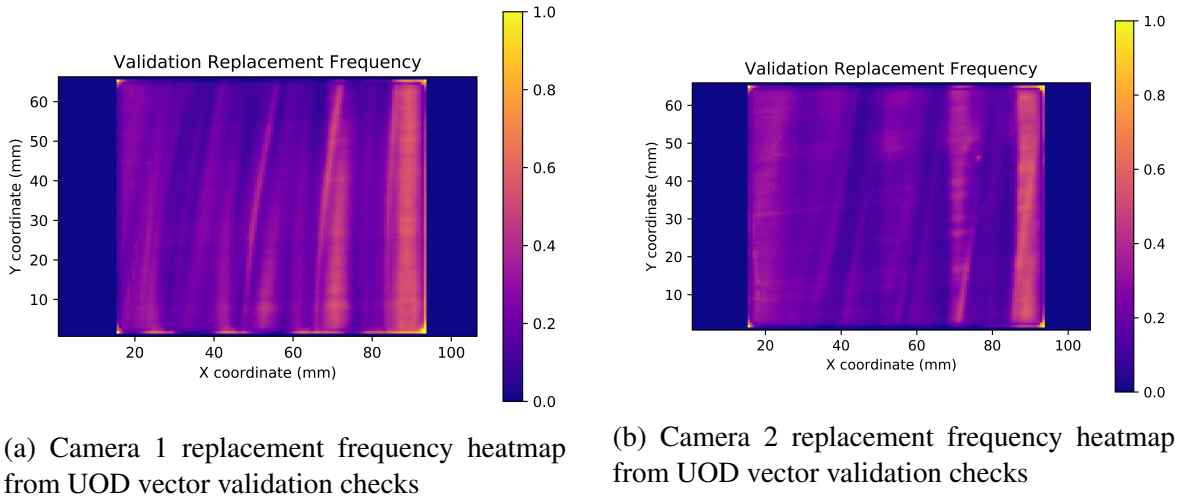
Figure 5.5: Vector replacement frequency

A 40% replacement threshold from the UOD vector validation was chosen as delineate between easier and more difficult regions for the PIV cross-correlation. Figure 5.6 highlights

each vector location with a replacement frequency greater than 40%.

(a) PIV Vertical Plane 1 Camera 1 specific vectors above the 40% of frames replacement threshold

(b) PIV Vertical Plane 1 Camera 2 specific vectors above the 40% of frames replacement threshold
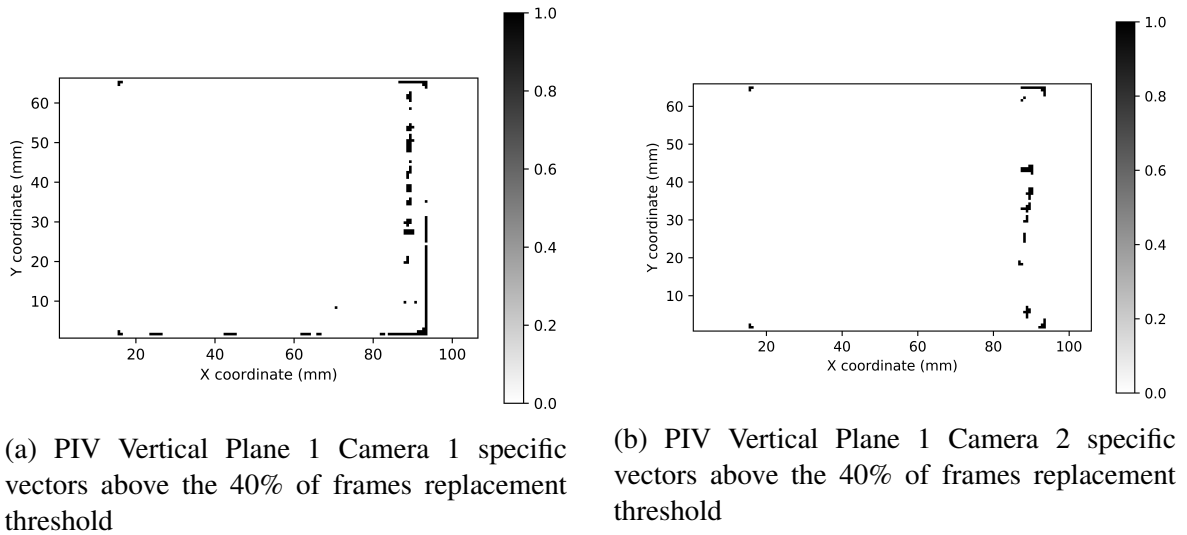
Figure 5.6: Bad vectors identified via UOD validation check threshold

For all analyzed statistical quantities, the residual convergence of the absolute relative difference was calculated comparing various subsets of the total image set. A total of 40 subsets were generated by randomly selecting instantaneous velocity vector fields from 5% of the total dataset and increasing logarithmically until the total dataset was selected. Presented in Figure 5.7 are the residual convergence plots for seven first and second order statistical quantities of interest. Absolute relative differences were averaged over two vertical and two horizontal lines spanning the measurement FOV.

5.1.1.4 Results at Re_B = 19,760

Experimental conditions for this measurement are defined in Table 5.2. The calibration scale for this measurement was equal to 0.0837 mm/pixel. The vector spacing for this measurement was equal to 0.6695 mm/vector.

Note only Camera 1 FOV is presented for the ensemble-averaged and RMS fluctuating components of velocity for PIV Vertical Plane 1 at Re_B = 19,760. Note the helical wire

59
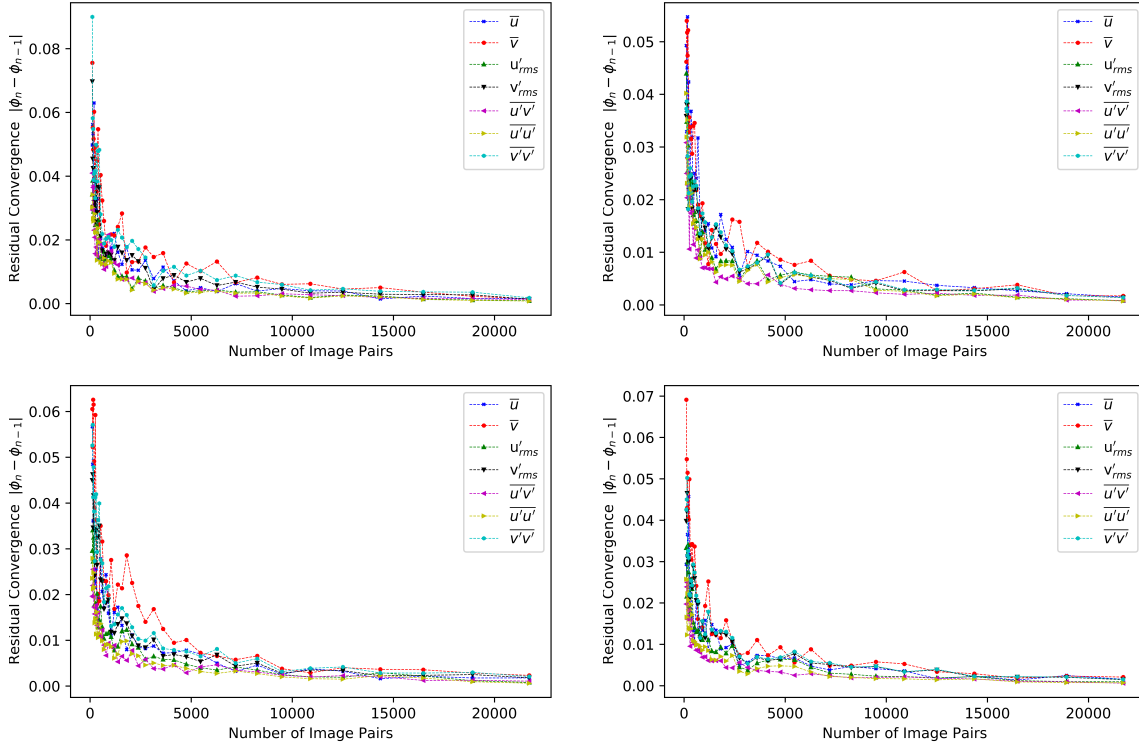
Figure 5.7: PIV Vertical Plane 1 residual convergence along two vertical and two horizontal lines spanning the measurement FOV

spacer position is on the right side of each pin at the bottom of the field. It then curls behind the pin in the positive Y-direction. Flow pattern streamlines occur at an angle within 1 to 2 degrees of the helix angle of the wire spacer. Note a positive gradient in the X-direction exists, capturing the bulk flow in a low pressure region immediately downstream the wire spacer.

The Ensemble-averaged $\overline{u}$ component contour displays bands of positive and negative transverse velocity. The negative bands are positioned immediately in the positive X-direction to each pin. The angle of such bands is 8 degrees off-vertical, coinciding exactly with the helix angle of the wire spacer. The $\overline{v}$ component contour highlights the flow restrictive regions where lower velocity regions along the Y-direction spatially match where the exterior subchannel flow area is reduced between the exterior row of pins and the hexagonal duct wall. Peaks of $v'_r ms$ occur at the elevation where the helical wire spacer has revolved and

60

Table 5.2: PIV Vertical Plane 1 experimental conditions for $Re_B = 19{,}760$

Variable	Value	Uncertainty	Unit
Temperature	24.7	0.6	°C
Viscosity	790	50	$\mu\mathrm{Pa\,s}$
Density	853.0	3.8	$\mathrm{kg\,m^{-3}}$
Flow rate	1133	19	$\mathrm{L\,min^{-1}}$
Bulk velocity	2.368	0.06	$\mathrm{m\,s^{-1}}$
Re_B	19,760	350	N/A
Intra-frame time delay	357	N/A	$\mu\mathrm{s}$

closed the gap between adjacent pins, thus blocking flow in the exterior subchannel from moving toward the interior. The single component Z-vorticity, $\overline{\omega_z}$, contour showed that the near-wall flow contains vortical structures with a very similar elongated shape, width, and off-vertical orientation to that of the helical wire spacers.
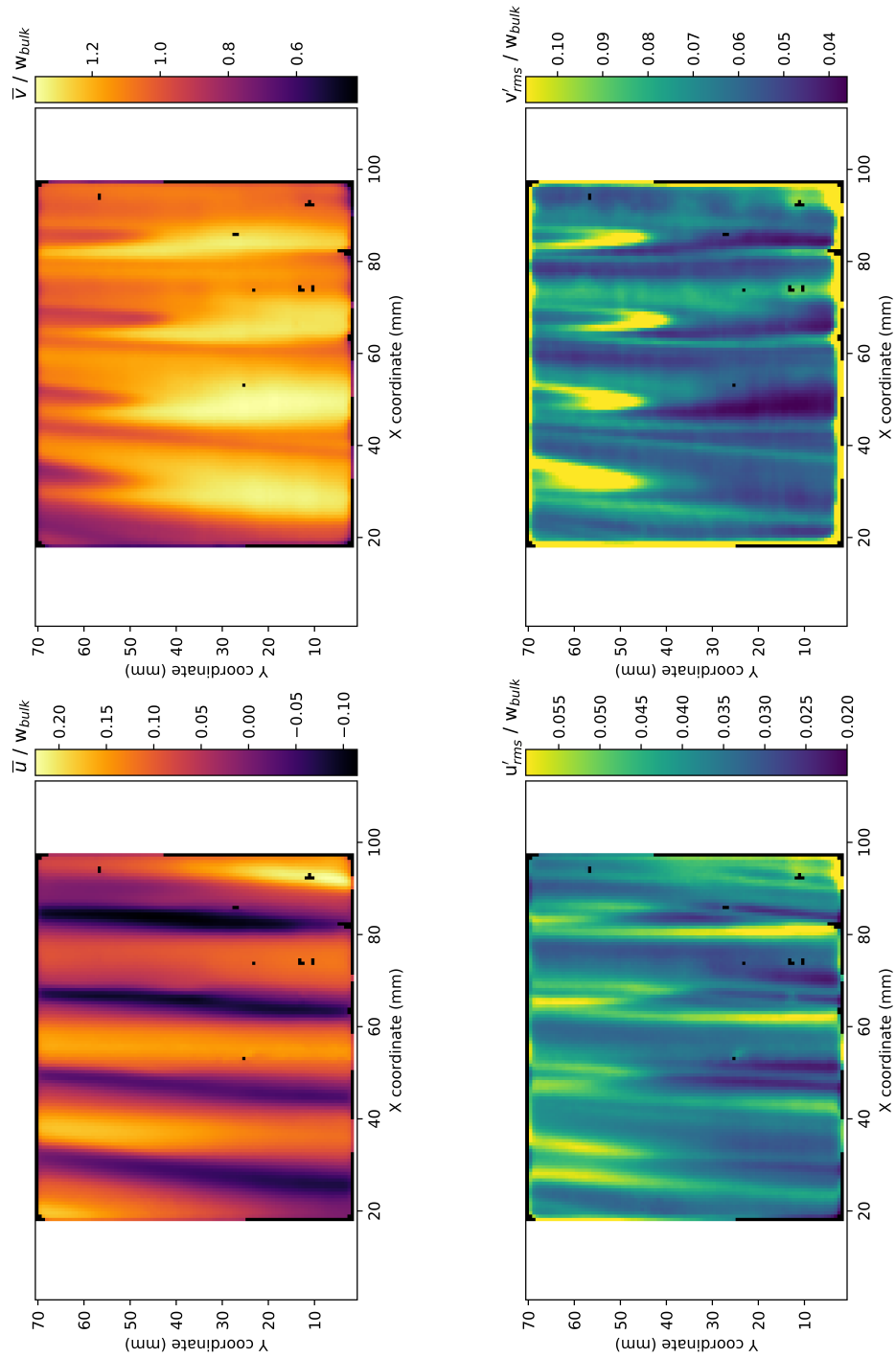
Figure 5.8: Ensemble-averaged and RMS fluctuating components of velocity for PIV Vertical Plane 1 at $Re_B = 19{,}760$.
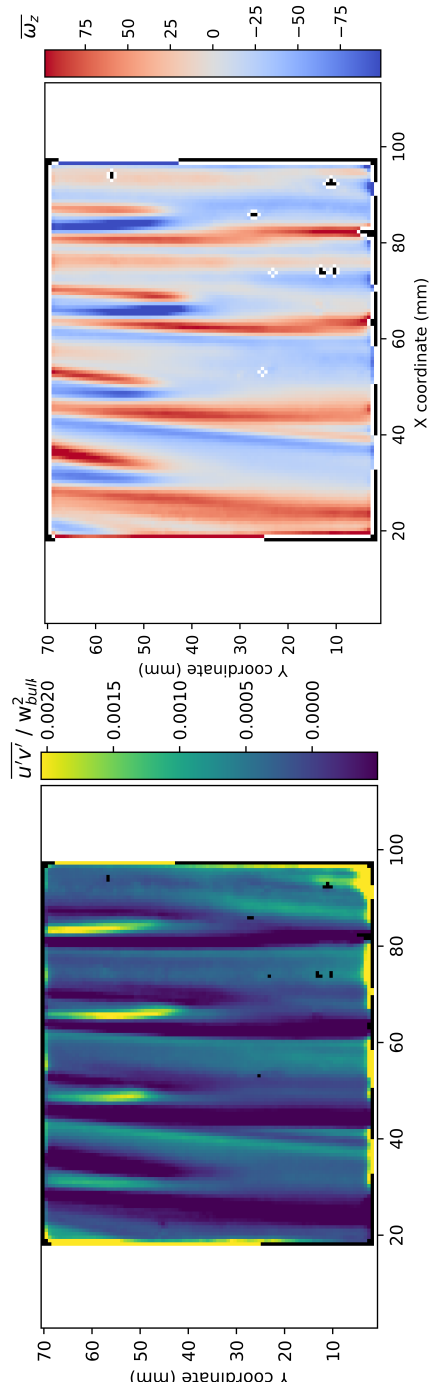
Figure 5.9: Reynolds shear stress $\overline{u'v'}$ and single vorticity component $\overline{\omega_z}$ for PIV Vertical Plane 1 at $Re_B = 19{,}760$.

Experimental conditions for this measurement are defined in Table 5.3. The calibration
scale for this measurement was equal to 0.0837 mm/pixel. The vector spacing for this
measurement was equal to 0.6695 mm/vector.

Table 5.3: PIV Vertical Plane 1 experimental conditions for Re_B = 12,370

Variable	Value	Uncertainty	Unit
Temperature	22.3	0.6	°C
Viscosity	820	50	$\mu\mathrm{Pa\,s}$
Density	854.9	3.8	$\mathrm{kg\,m^{-3}}$
Flow rate	735	12	$\mathrm{L\,min^{-1}}$
Bulk velocity	1.536	0.03	$\mathrm{m\,s^{-1}}$
Re_B	12,370	220	N/A
Intra-frame time delay	526	N/A	μs

Figure 5.10: Ensemble-averaged and RMS fluctuating components of velocity for PIV Vertical Plane 1 at $Re_B = 12{,}370$.
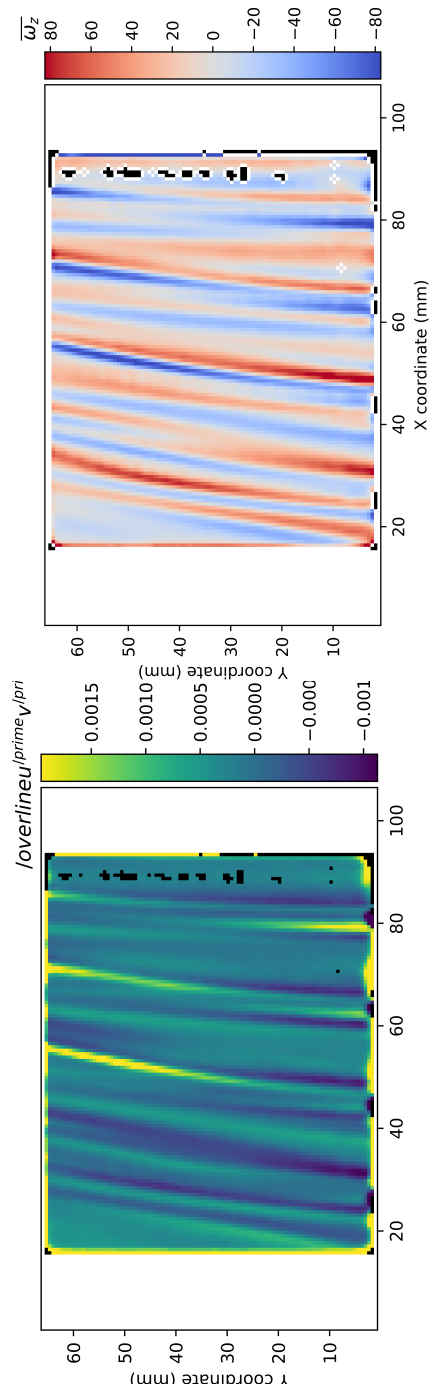
Figure 5.11: Reynolds shear stress $\overline{u'v'}$ and single vorticity component $\overline{\omega}_z$ for PIV Vertical Plane 1 at $Re_B = 12,370$

5.1.1.6 Results at Re_B = 10,410

Experimental conditions for this measurement are defined in Table 5.4. The calibration scale for this measurement was equal to 0.0837 mm/pixel. The vector spacing for this measurement was equal to 0.6695 mm/vector.

Table 5.4: PIV Vertical Plane 1 experimental conditions for Re_B = 10,410

Variable	Value	Uncertainty	Unit
Temperature	21.7	0.6	°C
Viscosity	820	50	$\mu\mathrm{Pa\,s}$
Density	854.4	3.8	$\mathrm{kg\,m^{-3}}$
Flow rate	618	10	$\mathrm{L\,min^{-1}}$
Bulk velocity	1.292	0.02	$\mathrm{m\,s^{-1}}$
Re_B	10,410	166	N/A
Intra-frame time delay	625	N/A	μs
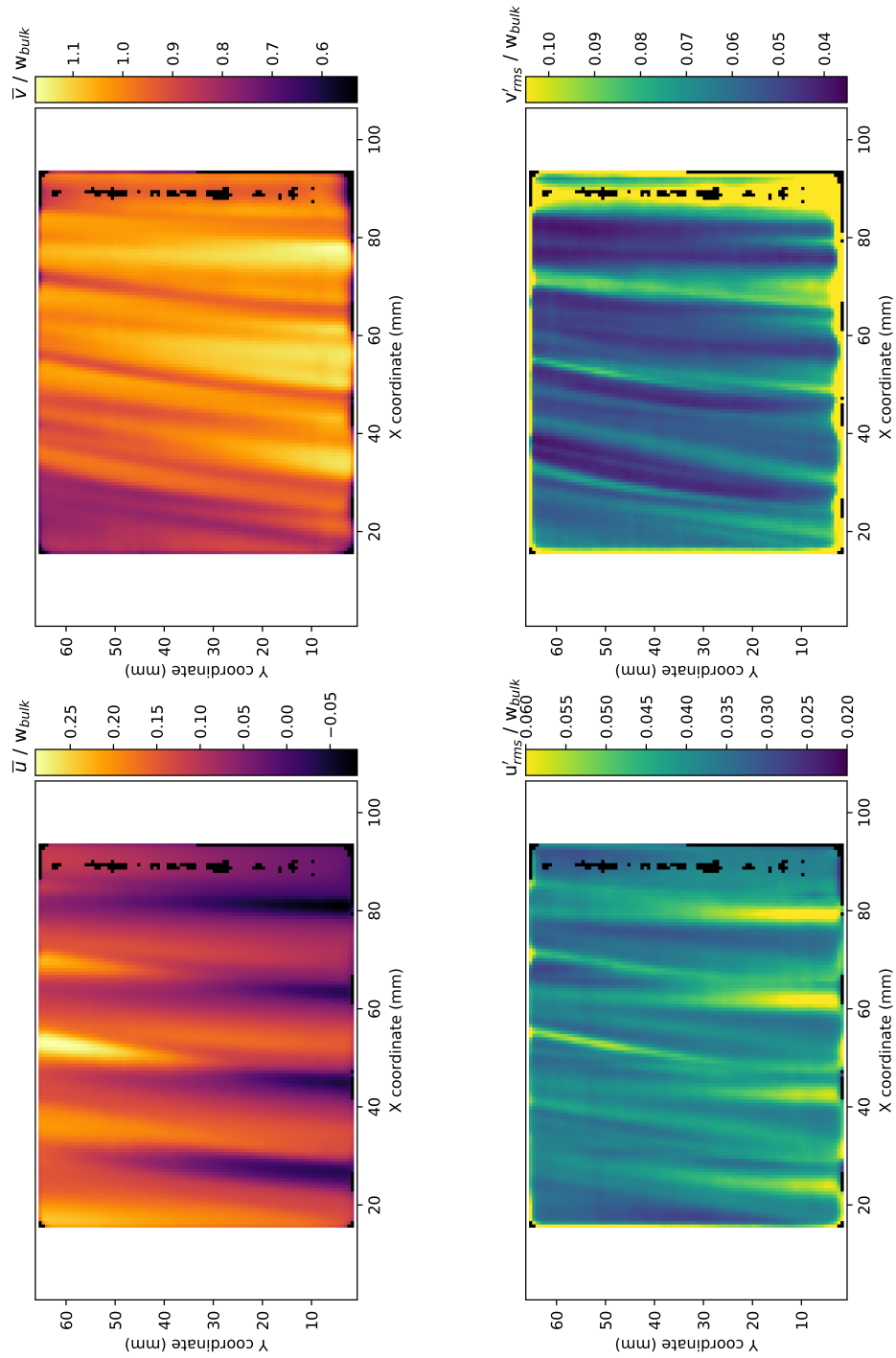
Figure 5.12: Ensemble-averaged and RMS fluctuating components of velocity for PIV Vertical Plane 1 at $Re_B = 10{,}410$.
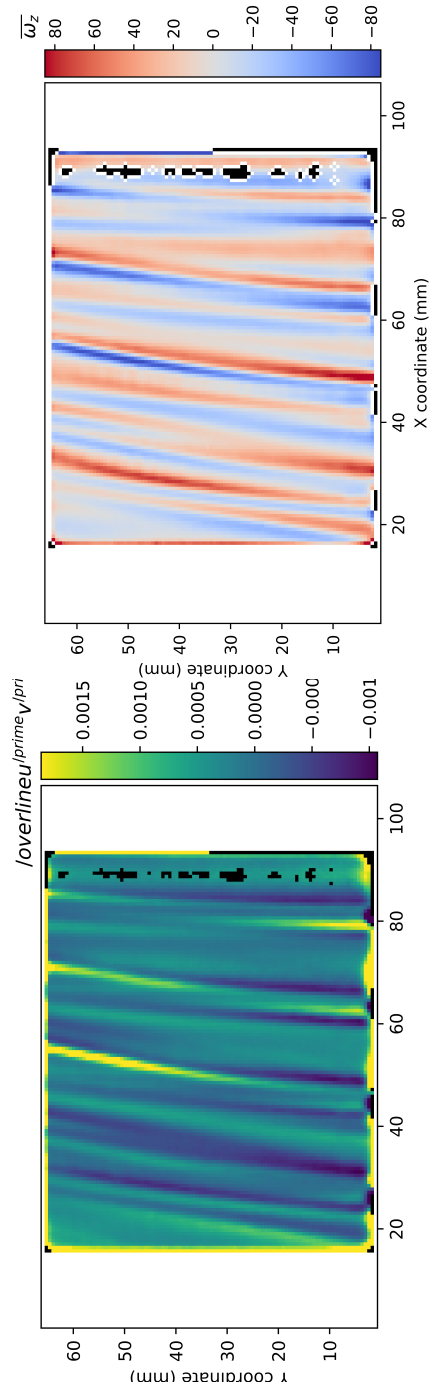
Figure 5.13: Reynolds shear stress $\overline{u'v'}$ and single vorticity component $\overline{\omega_z}$ for PIV Vertical Plane 1 at $Re_B = 10{,}410$.

5.1.1.7   Results at Re_B = 3,410

Experimental conditions for this measurement are defined in Table 5.5. The calibration scale for this measurement was equal to 0.0837 mm/pixel. The vector spacing for this measurement was equal to 0.6695 mm/vector.

Table 5.5: PIV Vertical Plane 1 experimental conditions for Re_B = 3,410

| Variable	Value	Uncertainty	Unit
Temperature	20.8	0.6	°C
Viscosity	830	50	μPa s
Density	856.1	3.8	$\mathrm{kg\,m^{-3}}$
Flow rate	205	3	$\mathrm{L\,min^{-1}}$
Bulk velocity	0.428	0.01	$\mathrm{m\,s^{-1}}$
Re_B	3,410	50	N/A
Intra-frame time delay	2000	N/A	μs
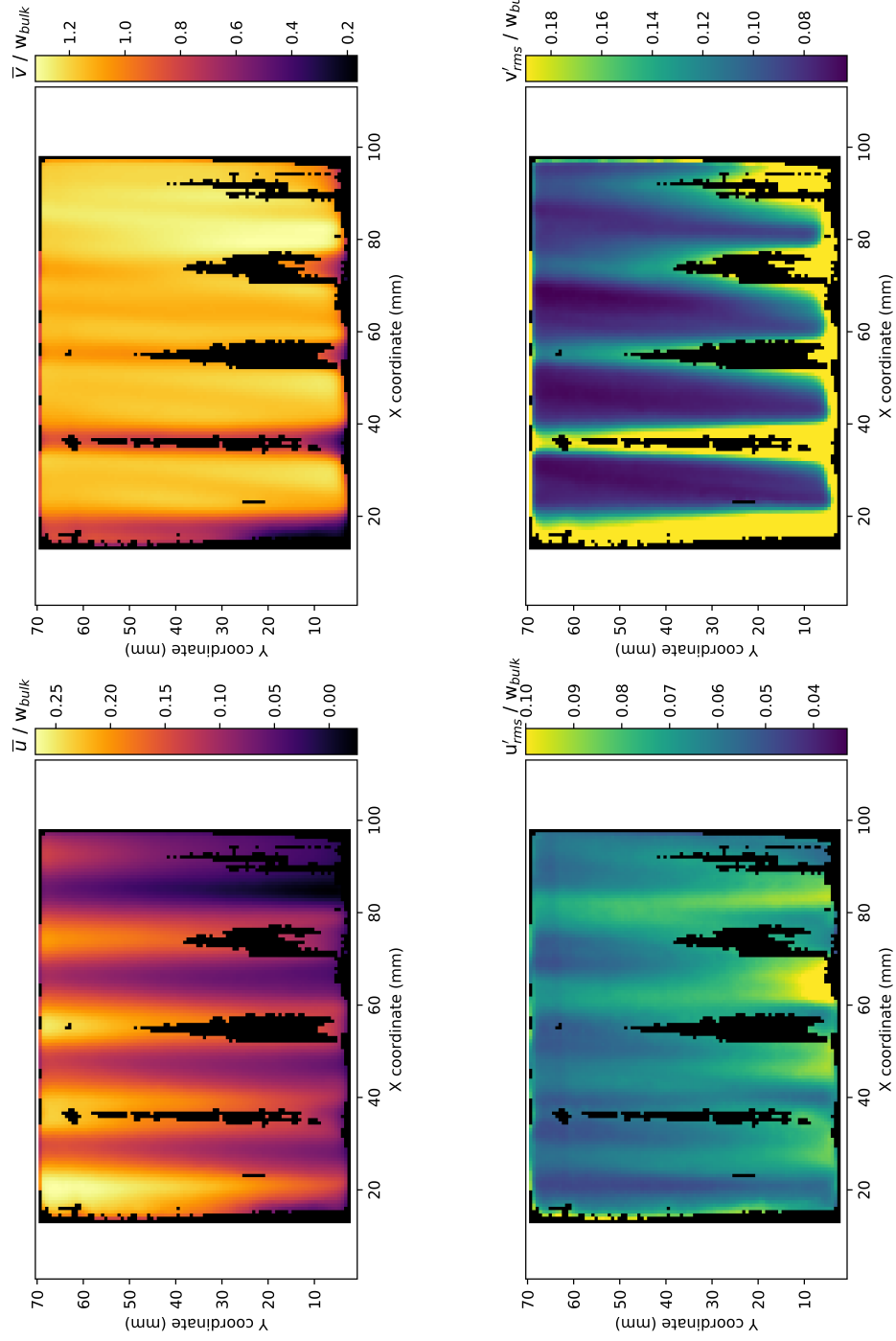
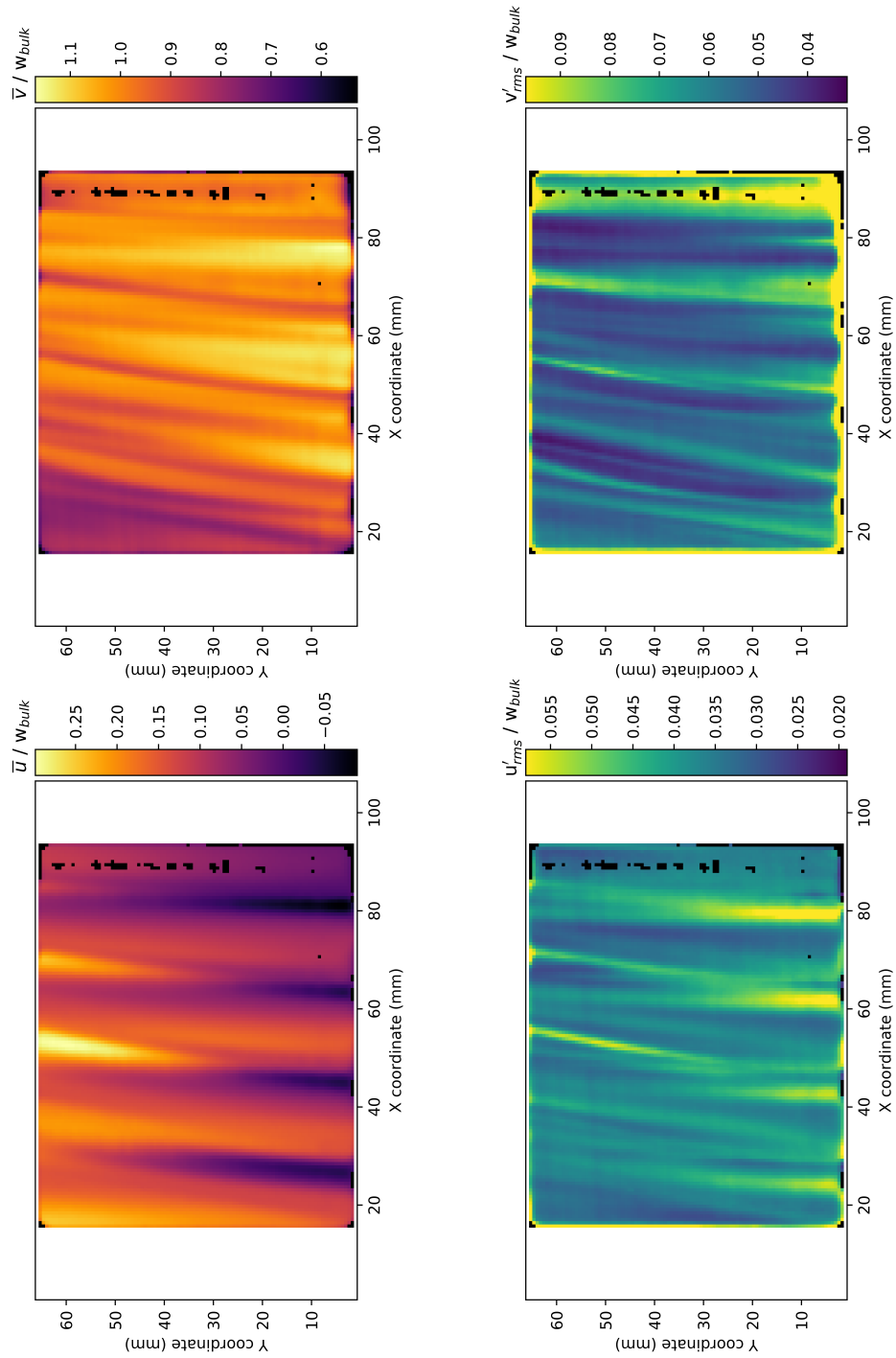Figure 5.14: Ensemble-averaged and RMS fluctuating components of velocity for PIV Vertical Plane 1 at $Re_B = 3{,}410$.
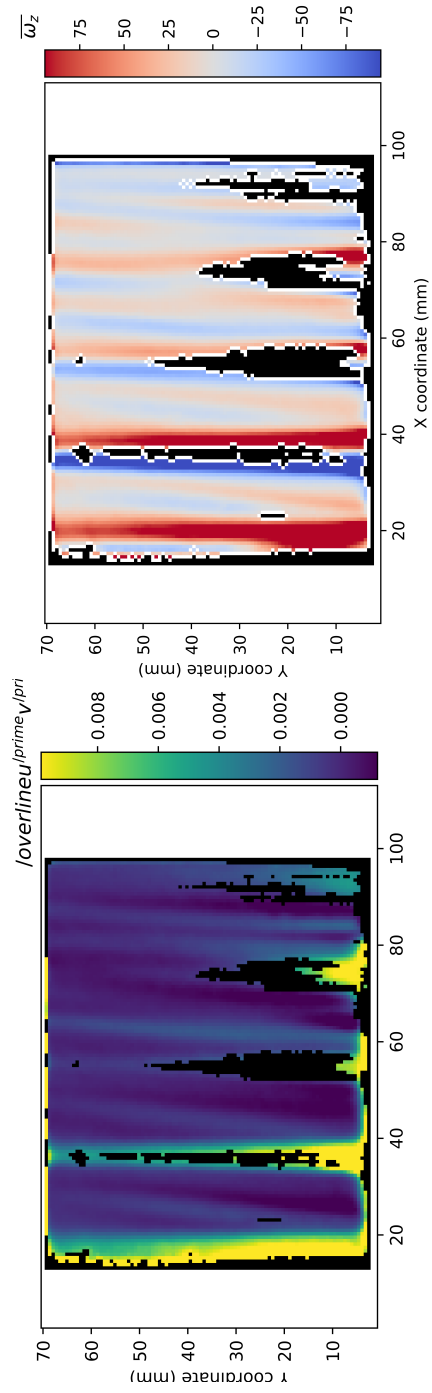
Figure 5.15: Reynolds shear stress $\overline{u'v'}$ and single vorticity component $\overline{\omega_z}$ for PIV Vertical Plane 1 at $Re_B = 3{,}410$.

5.1.2 PTV Vertical Plane 2-4 (Interior-1 to 3) (2D2C)

The PTV Vertical Plane 2 measurement was executed on four interior subchannels (ISC1-ISC4). The subchannels were between the row of pins closest to Face F. A vertical light sheet illuminated seeding particles, and it is denoted by a green line crossing the row of pins near the hexagonal duct wall. This configuration is show in Figure 5.16. The wrap of the wire spacer in the figure highlights the spacer's sweep from the bottom of the measurement window to the top. An X-Y coordinate system was assigned to each subchannel (ISC1-4). The X-origin of each subchannel was set at the right edge of the corresponding pin (1-4). The Y-origin of each subchannel was defined as the elevation where the wire spacer faces directly into the corner formed by hexagonal duct faces A and F. The domain size for each subchannel was 3 mm × 132 mm. The wire position at the bottom of the measurement window was 19° revolved counter-clockwise (CCW) relative to the wire position at the origin. The origin for ISC1 is shown in Figure 5.16.

5.1.2.1 Imaging Settings

Imaging settings were identical to the description given in Section 5.1.1.1. PTV instantaneous velocity vector fields were calculated by diving the measurement FOV into spatial regions of 5×50 pixels (0.44×4.4 mm). The vector spacing for the last pass of the hybrid PIV-PTV method was equal to 2.5 pixels (0.22 mm) in the X-direction and 5 pixels (0.44 mm) in the Y-direction.

5.1.2.2 PTV Processing Settings

The hybrid PIV-PTV approach was employed to improve the tracking efficiency of the PTV algorithm. Table 5.6 contains the PIV processing parameters for Vertical Planes 2-4 that were used to generate initial fields for PTV. The selected PTV algorithms were based on the multi-parametric particle tracking techniques of Cardwell et al. (2011). These methods have been implemented in the PRANA code discussed in Section 4.3.4. The algorithm utilized the particle intensity, particle size, prior approximate position, and current approximate position

73
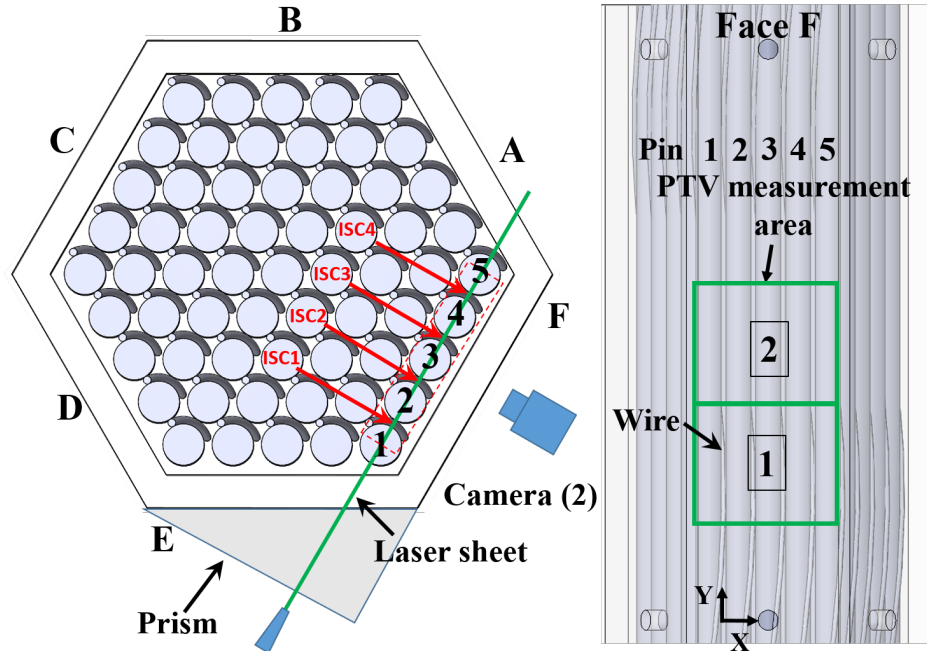
Figure 5.16: The PTV Vertical Plane 2 measurement location, with (*left*) a top-down cross section of the fuel bundle denoting wire position and laser sheet illuminating ISC1-4, and (*right*) a side view showing the measurement window, wire position, and origin of ISC1.

to classify particle matching. Particle images were identified with a dynamic threshold of pixel intensity to 10 values greater than background. Particle image size was then approximated using a continuous Gaussian least squares method proposed by Brady et al. (2009). The technique had a minimum area of 3×3 for particle image identification. Tolerance on the particle image diameter was set to 2 standard deviations. Particle image tracking utilized a searching radius of 20 pixels and matching weight values of 0.5 for both intensity and size.

5.1.2.3 *PTV Vertical Plane 2 (Interior-1)*

This section contains parts of previously published material from the article written by Goth, Jones, Nguyen, Vaghetto, Hassan, Salpeter and Merzari (2018). Specifically, it pulls from the PTV Vertical Plane 2 (Interior-1) results at $Re_B = 19{,}200$. Experimental conditions for this measurement are defined in Table 5.7.

Flow field statistics were calculated from sets of PTV velocity vectors divided into con-

Table 5.6: Hybrid PIV-PTV processing settings for PTV Vertical Plane 2

Parameter	PIV Pass 1	PIV Pass 2	PIV Pass 3
Multigrid method	Bi-cubic	Bi-cubic	Bi-cubic
Searching window size (pix)	64×64	32×32	16×16
Interrogation window size (pix)	16×32	8×16	4×8
Interrogation window overlap	50%	50%	50%
Grid buffer	8×8	8×8	8×8
Correlation type	RPC	RPC	RPC
Subpixel peak location	3 Pt. Gaussian	3 Pt. Gaussian	3 Pt. Gaussian
Vector Validation	UOD median	UOD median	UOD median

Table 5.7: Experimental conditions of PTV Vertical Plane 2

Variable	Value	Uncertainty	Unit
Temperature	22.3	0.6	°C
Viscosity	820	50	$\mu\mathrm{Pa\,s}$
Density	854.9	3.8	$\mathrm{kg\,m^{-3}}$
Flow rate	1141	18	$\mathrm{L\,min^{-1}}$
Bulk velocity	2.383	0.06	$\mathrm{m\,s^{-1}}$
Re_B	19,200	310	N/A
Intra-frame time delay	357	N/A	μs

stant spatial regions of 5×50 pixels ($0.4 \times 4\,\mathrm{mm}$) using the full 24,930 instantaneous velocity vector field dataset. PTV was used instead of PIV in these subchannels due to the small physical width (3 mm) and subsequently low seeding particle density in the small interrogation windows required.

Velocity field statistics include ensemble-averaged and RMS fluctuating axial velocity fields generated using PTV. Figure 5.17 presents the ensemble-averaged velocity field in the axial direction for Re_B = 19,200. Velocity vectors were not quantified between Y = 60 mm and 100 mm, where helical wire spacers intersected the laser sheet and blocked seeding particles. The axial velocity decreases abruptly once the fluid is within 10 mm upstream of the wire spacer as it is forced into the interior of the bundle. The lowest axial velocity can be

found immediately downstream of the wire spacer, which agrees with the direct numerical simulation (DNS) iso-contour mean velocity results of Ranjan et al. (2011). This indicates that sufficient crossflow exists in a wire-wrapped hexagonal bundle to generate recirculation regions downstream of the wire spacer. In each subchannel, the maximum velocity was typically near the center of the subchannel, except when in close proximity of the wire spacer. A positive gradient of the axial velocity is visible in the X-direction, indicating the presence of the bulk swirl generated by the helical wire spacer. This gradient was also captured in the set of edge subchannels near the hexagonal duct wall and discussed in Nguyen et al. (2017). Figure 5.19 (*left*) presents normalized ensemble-averaged axial velocity profiles (V/V_m) along X = 1.5 mm located at the midpoint of the subchannels. Axial velocities upstream the wire spacer have similarity of ± 0.1 m s^{-1} between Y = 25 mm and 50 mm. The difference increases when downstream to ± 0.2 m s^{-1} between Y = 100 mm and 130 mm. Above 130 mm, the axial velocities are converging to a value slightly higher than the upstream value at Y = 25 mm. The deceleration of the fluid upstream the spacer is similar for each subchannel. However, the rates of fluid acceleration downstream the spacer are different, with the fluid in ISC1 accelerating the slowest, followed by ISC2 and 3, with ISC4 accelerating the fastest.

Figure 5.18 presents the RMS fluctuating velocity field in the axial direction. Axial velocity fluctuations are positive and are largest in proximity to the helical wire spacer. Peaks of the contour occur just upstream of the spacers. The X-direction positive gradient is also visible in the RMS fluctuating field. Figure 5.19 (*right*) presents normalized axial velocity fluctuations (v'_{rms}/V_m) along X = 1.5 mm located at the midpoint of the subchannels. Magnitudes and accelerations of v'_{rms}/V_m are very similar for each subchannel.

5.1.3 PIV Vertical Plane 6 (Center-2) (2D2C)

Figure 5.20 presents the PIV Vertical Plane 6 (Center-2) measurement configuration. The configuration required the 30-60-90 optical prism be mounted onto Face F of the hexagonal duct and the laser sheet was aligned normal to the exterior wall of the duct.
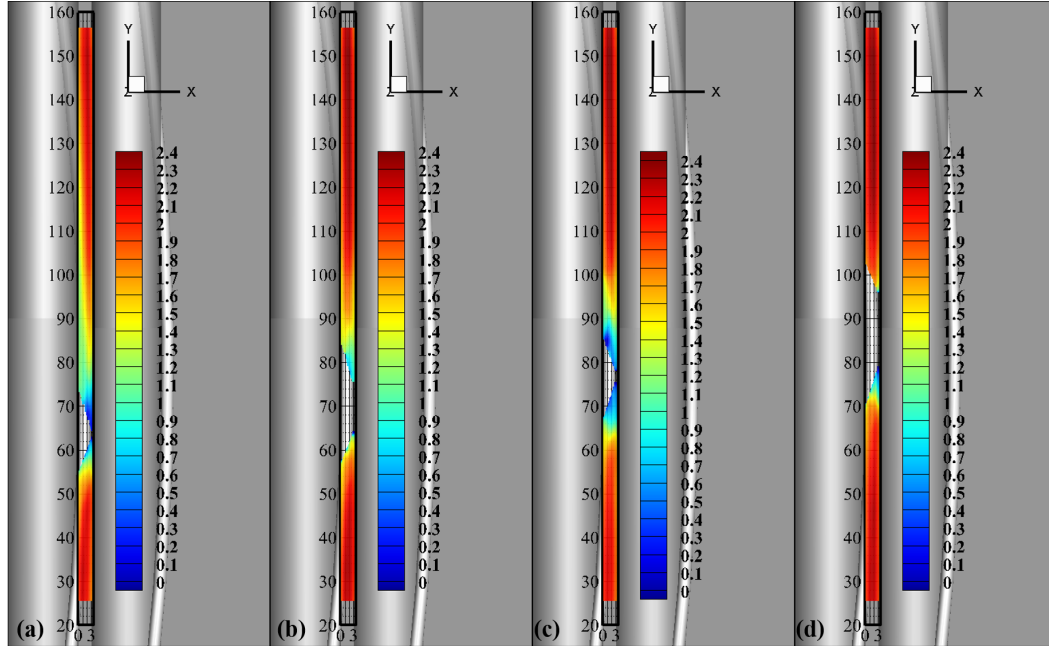
Figure 5.17: PTV Vertical Plane 2 ensemble-averaged axial velocity $(\mathrm{m\,s^{-1}})$ at $Re_B = 19{,}200$ for (*a*) ISC1, (*b*) ISC2, (*c*) ISC3, and (*d*) ISC4.

Figure 5.21 presents a cross-section highlighting the ROI, which was the set of two interior subchannels (CSC1-2) created by a pins row perpendicular to Face A. The fractional wrap of the wire spacer denoted the wire's path from the bottom of the measurement window FOV to the top. This is also highlighted by areas 1 and 2 for each camera. The height of the total measurement region was 0.25 wire pitches. A magnified view of CSC1 and CSC2 shows the wire spacers of pins 1, 2, and 3, accompanied by spacers from adjacent pins that cross into the laser sheet. These regions were denoted as dark grey arcs across the light grey subchannels. Each of the subchannels (CSC1-2) was assigned its unique X-Y coordinate system. The X-direction was in the transversal direction and the Y-direction was in the axial direction. The X-origin of each subchannel was selected to be the right surface of the corresponding pin (1 or 2). The Y-origin of each subchannel was selected to be the elevation where the helical wire spacer faces into the corner formed by faces F and A of the hexagonal duct. The size of the physical domain for each subchannel was 15 mm × 126 mm. The wire position at the bottom of the measurement FOV was 21° revolved CCW relative to the
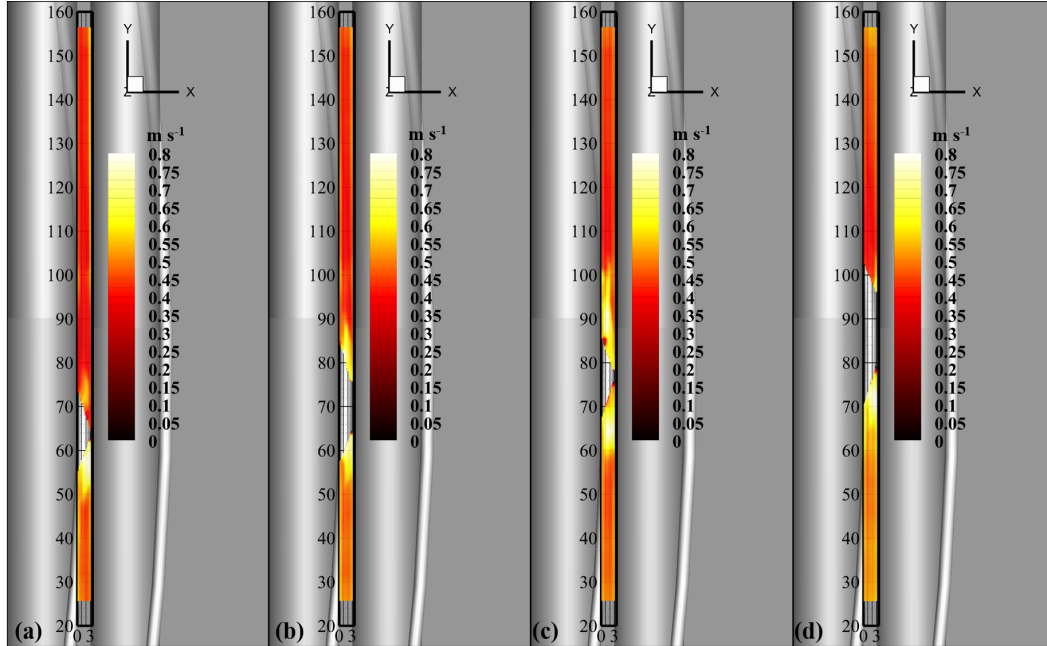
Figure 5.18: PTV Vertical Plane 2 RMS fluctuating axial velocity ($\mathrm{m\,s^{-1}}$) at Re_B = 19,200 for (*a*) ISC1, (*b*) ISC2, (*c*) ISC3, and (*d*) ISC4.

position at the origin. The origin for CSC1 is shown in Figure 5.21.

5.1.3.1 Imaging Hardware

Imaging hardware was identical that used in Section 5.1.1.1 for the PIV Vertical Plane 1 measurement. A 10 W continuous wave laser at 532 nm with laser sheet thickness of 1.5 mm ± 0.5 mm and two Phantom Miro M310 cameras were the primary hardware components. Each camera was paired to a 100 mm Zeiss Makro-Planarf/2 ZF lens. The camera image sample rate and exposure were unique for each Re_B being investigated and is defined locally in the following subsections. After calibration, the resulting magnification factor was equal to 0.084 mm/pixel

5.1.3.2 PIV Processing Settings

PIV images were processing using the PRANA code. Table 5.8 contains the PIV processing settings for this measurement location. The final pass vector spacing was equal to 0.67 mm/vector. More information regarding processing settings can be found in Section
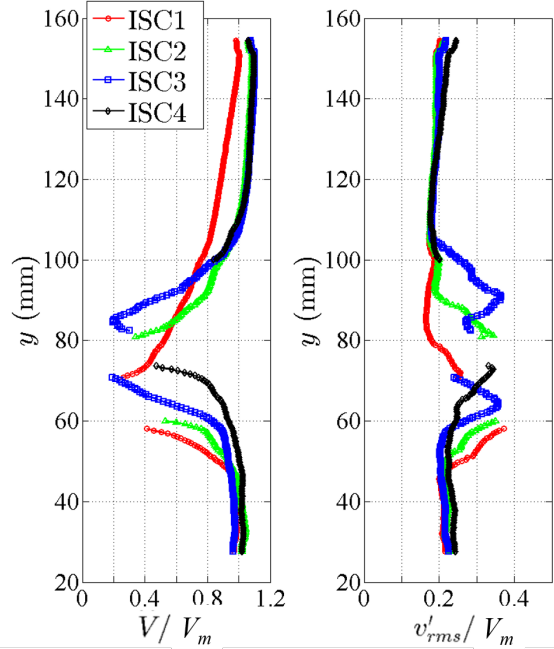
Figure 5.19: Interior-1 (PTV) (*left*) ensemble-averaged and (*right*) RMS fluctuating axial velocities $(\mathrm{m\,s^{-1}})$ at ISC1-4 midpoints along X = 1.5 mm for Re_B = 19,000

4.3.4.

5.1.3.3 *PIV Vertical Plane 6 (Center-2)*

This section contains parts of previously published materials from the analysis article of Goth, Jones, Nguyen, Vaghetto, Hassan, Salpeter and Merzari (2018) and the CFD comparison article of Goth, Jones, Nguyen, Vaghetto, Hassan, Obabko, Merzari and Fischer (2018) for Re_B = 18,810. Experimental conditions for this measurement are defined in Table 5.9.

Figure 5.22a presents the ensemble-averaged axial velocity for Re_B = 18,810 for CSC1-2. The upper zero velocity region in each subchannel was formed by the intersection of the laser sheet and wire spacer, such that no seeding particles could exist in that space and no PIV post-processing could occur. The lower left zero velocity region in each subchannel was from the laser sheet intersecting the wire spacer of the central pin of the bundle. The lower right zero velocity region is due to excessive reflection of the laser light. Therefore, it is a non-physical zero velocity region where PIV post-processing could not be performed.
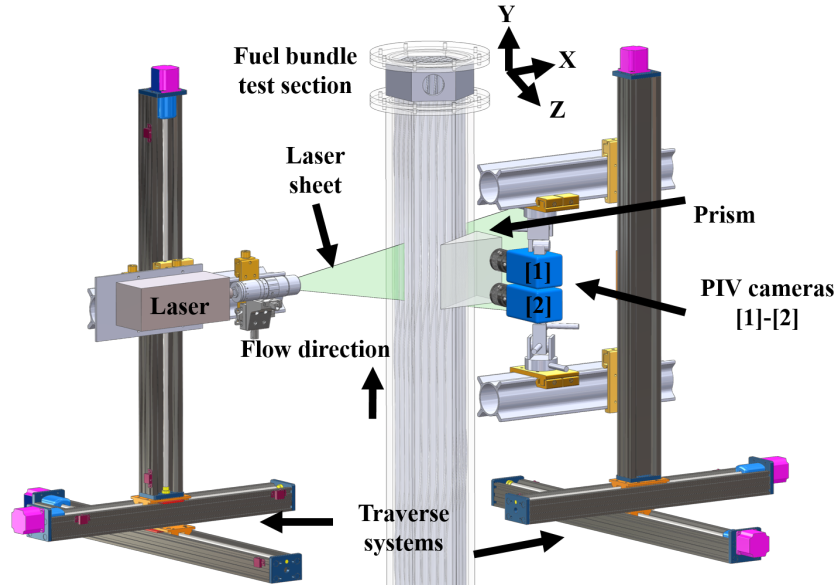
Figure 5.20: Imaging setup for the 2D2C Vertical Plane 6 PIV measurement containing test section, laser, camera, and traverse systems

At any XY-coordinate, the magnitude of the axial velocity is smaller in CSC1 than CSC2, indicating lower velocities in the central region of the bundle relative to the periphery. Figure 5.23 (*middle*) shows the normalized ensemble-averaged axial velocity profiles ($v/\overline{v}$) across the subchannel along Y = 75 and 110 mm. Comparing CSC1 and CSC2 at Y = 75 mm, axial velocities are greater than the bulk mean velocity and increase as the distance from the recirculating region increases. Comparing CSC1 and CSC2 at Y = 110 mm, axial velocities decrease below the bulk mean velocity in the center of the subchannel. $v/\overline{v}$ in CSC2 is always larger than in CSC1, presenting the amount of preferential flow toward the exterior of the fuel bundle.

Figure 5.22b presents the RMS fluctuating velocity field in the axial direction for CSC1-2. Maximum fluctuation velocities are within 10% of maximum ensemble-averaged values. Similar to PTV Vertical Plane 2, peaks in the axial velocity fluctuation are found nearby the helical wire spacers. Figure 5.23 (*right*) shows the normalized $v'_{rms}/\overline{w}$ across the subchannel along Y = 75 and 110 mm. Fluctuations are always less at Y = 75 mm and the relative magnitude of $v'_{rms}/\overline{v}$ is 5% of $v/\overline{v}$ in both subchannels.
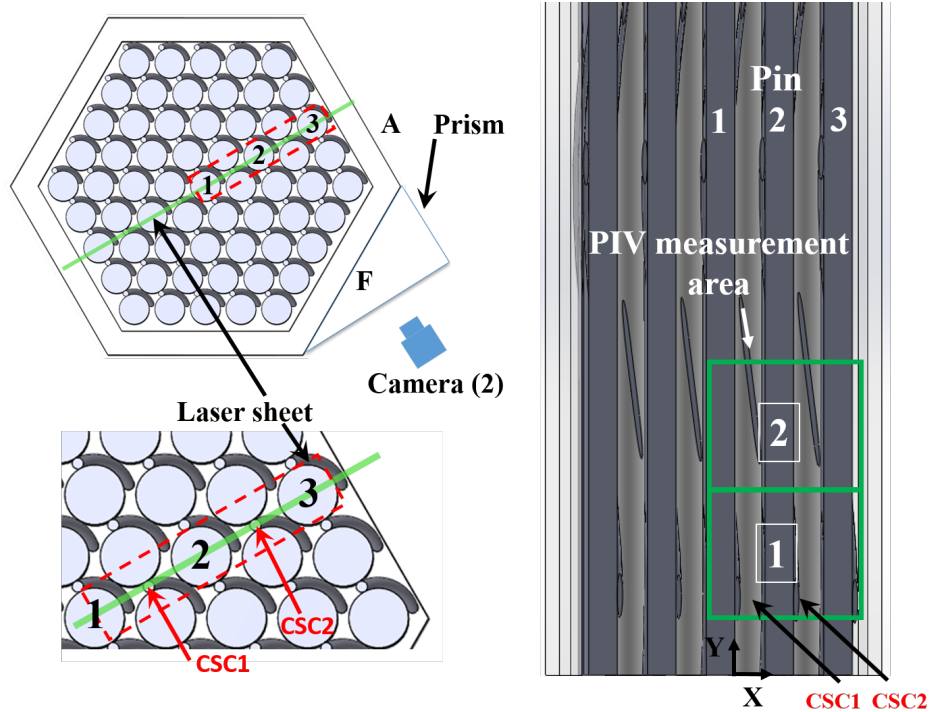
Figure 5.21: PIV Vertical Plane 6 measurement location, with (*left*) a top-down cross section of the fuel bundle denoting wire position and laser sheet illuminating CSC1-2, and (*right*) a side view showing the measurement FOV and wire spacers crossing the region from adjacent pins.

Figure 5.24a presents the ensemble-averaged transverse velocity ($U/\overline{v}$) for $Re_B = 18,810$ for CSC1-2. Similar to Figure 5.22a, three zero velocity regions exist that are due to the intersection of the laser sheet with wire spacers. The transverse velocity is an order of magnitude less than the axial velocity with a maximum value of 25% the bulk mean velocity. Between Y = 30 mm and 70 mm, the transverse velocity is primarily toward the bundle periphery, with the magnitude of the crossflow in CSC1 being approximately double that in CSC2. A region with physical dimensions similar to the wire spacer diameter and negative transverse velocity exists between Y = 70 mm and 130 mm, indicating the presence of a flow structure that continues axially after the wire spacer sweeps out of the subchannel on its helical path around the pin. These regions highlight the complex flow in subchannels containing wire spacers of adjacent pins forming the subchannel. The profiles from Figure 5.23 (*left*)

Table 5.8: PIV processing settings for PIV Vertical Plane 6

Parameter	Pass 1	Pass 2	Pass 3	Pass 4
Multigrid method	Bi-cubic	Bi-cubic	Bi-cubic	Bi-cubic
Search window	128×128	64×64	32×32	32×32
Interrogation window	64×64	32×32	16×16	16×16
Interrogation overlap	50%	50%	50%	75%
Grid buffer	8×8	8×8	8×8	8×8
Correlation type	RPC	RPC	RPC	RPC
Subpixel estimator	3 Pt. Gauss	3 Pt. Gaussi	3 Pt. Gauss	3 Pt. Gauss
Vector Validation	UOD	UOD	UOD	UOD

Table 5.9: Experimental conditions for the Vertical Plane 6 measurement

Variable	Value	Uncertainty	Unit
Temperature	20.1	0.6	°C
Viscosity	830	50	$\mu\mathrm{Pa\,s}$
Density	855.9	3.8	$\mathrm{kg\,m^{-3}}$
Flow rate	1143	22	$\mathrm{L\,min^{-1}}$
Bulk velocity	2.387	0.05	$\mathrm{m\,s^{-1}}$
Re_B	18,810	335	N/A
Intra-frame time delay	357	N/A	$\mu\mathrm{s}$

are similar in shape but present CSC2 with larger negative values just downstream the wire spacer at Y = 75 mm and with larger positive values for CSC1 at Y = 110 mm.

Figure 5.24b presents the RMS velocity field in the transverse direction. Maximum fluctuation velocities are within 40% of maximum ensemble-averaged values. Peaks in the contour appear near the helical wire spacers and adjacent pins which form the subchannels, where local maxima and minima exist.

Figure 5.25 presents the Reynolds stress, $u'v'$, for $Re_B = 18{,}810$ for CSC1-2. For these subchannels, the momentum transfer is positive downstream the wire spacer between Y = 140 mm and Y = 160 mm and where axial fluctuations are greatest. These high shear regions highlight the effectiveness of the helical wire spacer to assist in fluid mixing and thus

(a) Ensemble-averaged axial velocity

(b) RMS of the fluctuating axial velocity
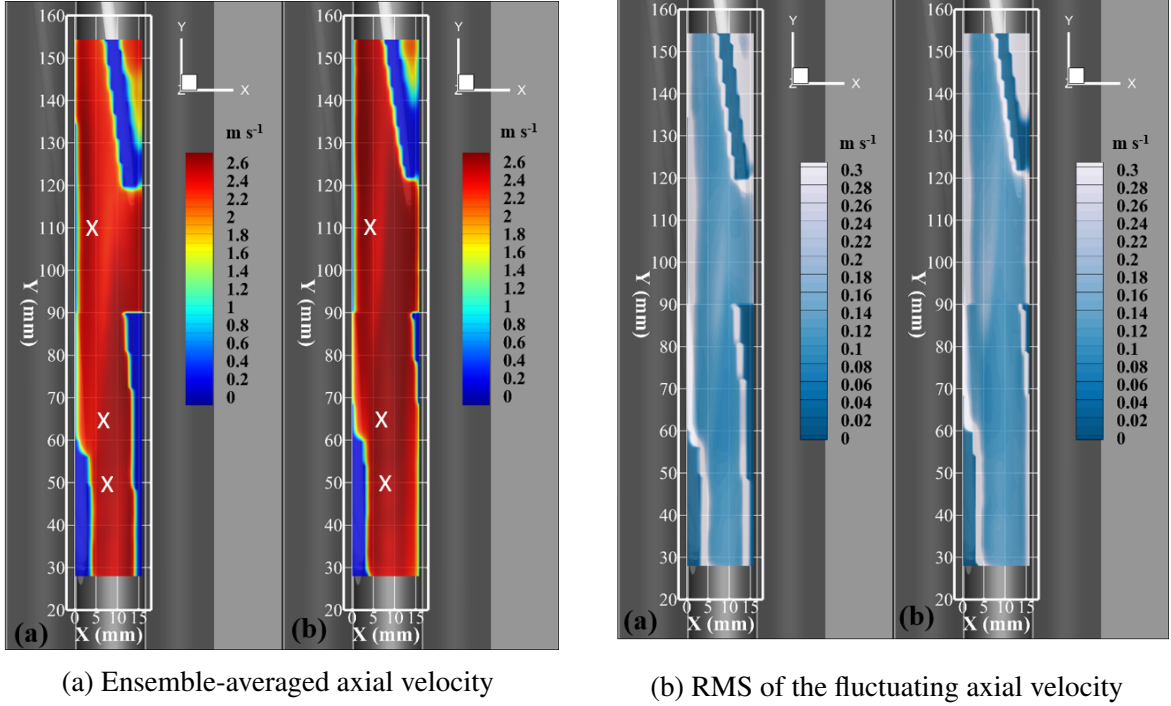
Figure 5.22: PIV Vertical Plane 6 velocity fields in the axial direction at $Re_B = 18{,}810$ for (*a*) CSC1 and (*b*) CSC2.

heat transfer in the fuel bundle. Another region of significant momentum transfer is along the shear layers of high and low axial and transverse velocities, which is especially visible between Y = 90 mm and 130 mm before the fluid impinges upon the wire spacer near the top of the visualization window.

A two-point spatiotemporal velocity-velocity cross-correlations is defined by Equation 5.1. The ensemble-averaged operator is denoted with $\langle \rangle$ and the fluctuating velocity component is u_i', the difference between the instantaneous and ensemble-averaged velocity. The spatial reference points are $\boldsymbol{x_r}$, the spatial separation between reference points is η, the time is t, and the time delay is τ. When $\tau = 0$, the two-point spatial velocity-velocity cross-correlations can be calculated as suggested by Kerhervé and Fitzpatrick (2011). This cross-correlation is defined as R_{ij0}.
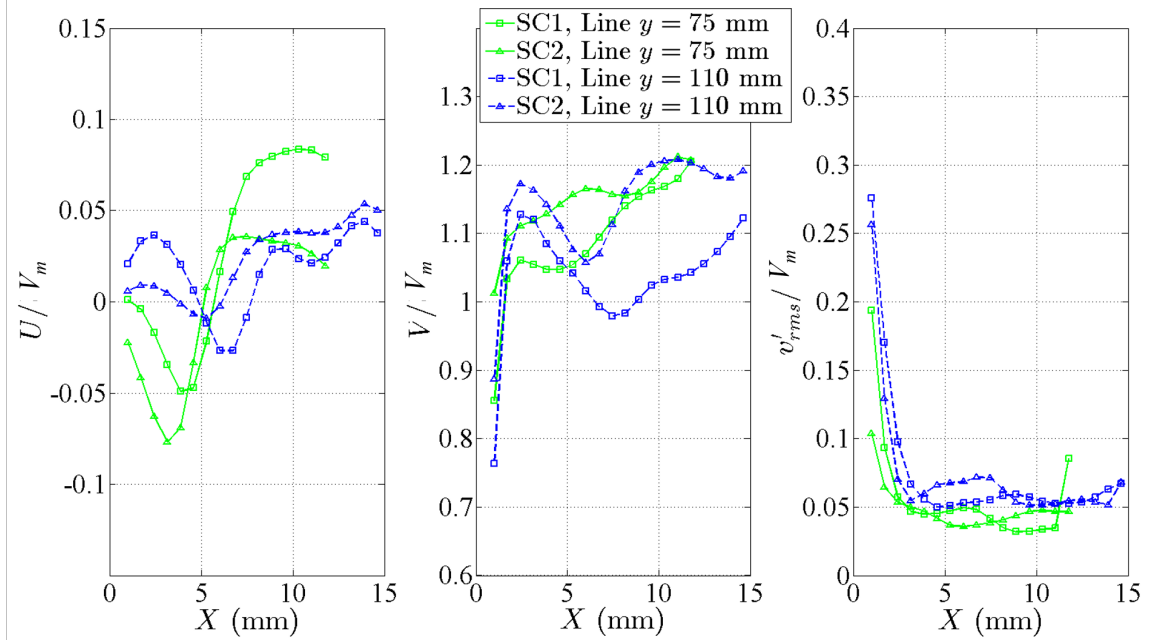
Figure 5.23: Center-2 (PIV) (*left*) ensemble-averaged transverse, (*middle*) ensemble-averaged axial, and (*right*) RMS fluctuating axial velocities at CSC1-2 midpoints for Re = 18,810 along lines Y = 75 and 110 mm.

$$R_{ij}(\boldsymbol{x}_r, \boldsymbol{\eta}, \tau) = \frac{\left\langle u_i'(\boldsymbol{x}_r, t) u_j'(\boldsymbol{x}_r + \boldsymbol{\eta}, t + \tau) \right\rangle}{\sqrt{\left\langle u_i'^2(\boldsymbol{x}_r, t) \right\rangle} \sqrt{\left\langle u_j'^2(\boldsymbol{x}_r, t) \right\rangle}}, \tag{5.1}$$

From R_{vv0} and R_{uu0}, the integral length scales may be calculated using Equations 5.2 and 5.3, where L_y and L_x are the axial and transverse integral length scales, respectively. L_y and L_x represent the characteristic length scales of turbulent eddies when the separation lengths of R_{vv0} and R_{uu0} is equal to $1/e \approx 0.37$, as suggested by Falchi and Romano (2009).

R_{vv0} and R_{uu0} were calculated at four points in each subchannel and then averaged to condense the result for $Re_B = 18,810$. The coordinates of the selected points were X = 2.9, 5.0, 7.2, and 9.3 mm along the line Y = 110.6 mm. These points were selected due to the number of interesting phenomena occurring along the line Y = 110.6 mm, such as the shear layers visible in Figure 5.22a around X = 7.2 mm and mixing highlighted by positive and negative velocities in Figure 5.24a. As shown in Figure 5.26, the R_{vv0} longitudinal spatial
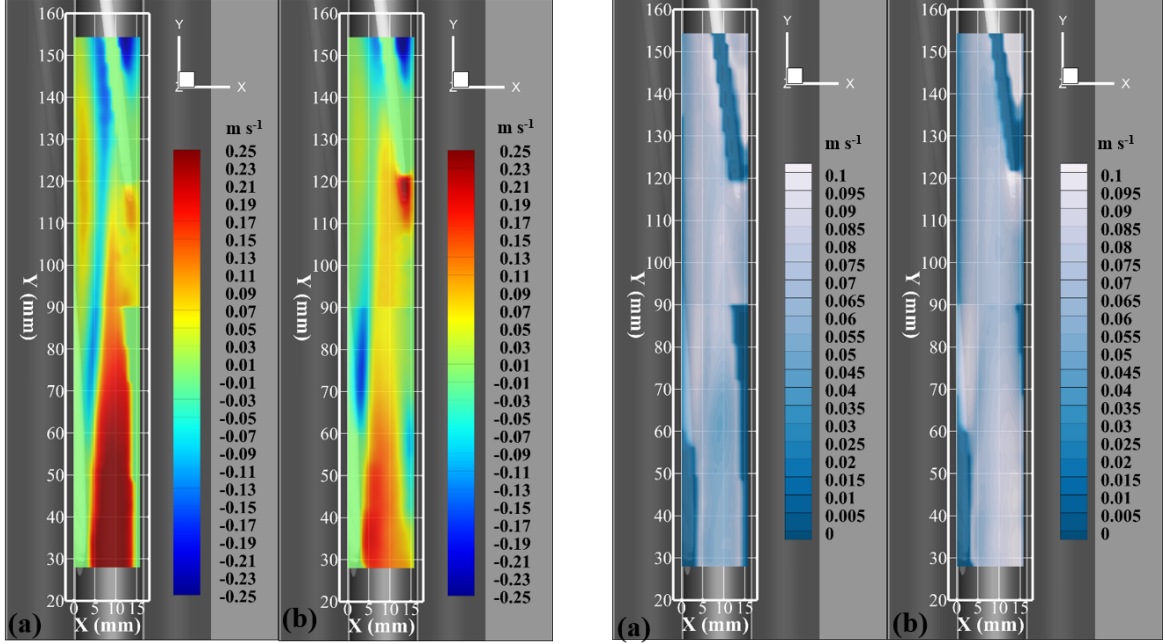
(a) Ensemble-averaged transverse velocity

(b) RMS of the fluctuating transverse velocity

Figure 5.24: PIV Vertical Plane 6 velocity fields in the transverse direction at Re_B = 18,810 for (*a*) CSC1 and (*b*) CSC2.

cross-correlations have longer separation distances over which the fluctuating velocity field is correlated for both CSC1 and CSC2. Comparing R_{vv0} and R_{uu0} between subchannels yields that longitudinal cross-correlations are nearly identical with CSC1 having a slightly longer separation distance than CSC2. It is noted that negative minima exist in CSC1 of a larger magnitude than CSC2. It is important to note the triangular shape of R_{vv0} and R_{uu0} near zero, as this indicates future results will benefit from the use of higher resolution imaging equipment to achieve higher resolution instantaneous velocity vector fields.

$$L_y = \int_0^\infty R_{vv}(\boldsymbol{x}_r, \boldsymbol{\eta}, 0)d\eta. \tag{5.2}$$

$$L_x = \int_0^\infty R_{uu}(\boldsymbol{x}_r, \boldsymbol{\eta}, 0)d\eta, \tag{5.3}$$

The axial integral length scale ranged from 1.9 mm in CSC2 to 2.3 mm in CSC1. The
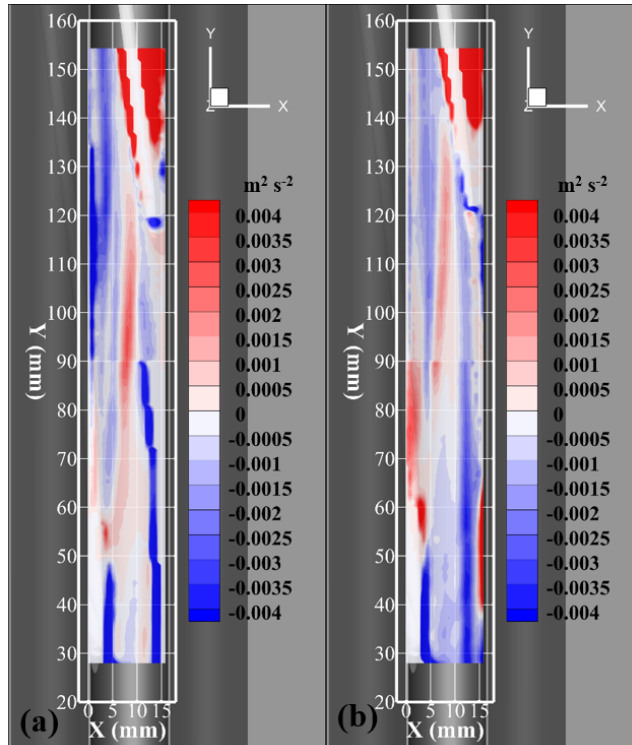
Figure 5.25: PIV Vertical Plane 6 Reynolds shear stress at Re_B = 18,810

transverse integral length scale was equal to 1.5 mm in both CSC1 and CSC2. Near-wall region integral length scales presented by Nguyen et al. (2017) state axial scales of 1.7 to 2.8 mm and transversal scales of 1.2 to 1.5 mm. When comparing PIV Vertical Plane 6 sub-channel integral length scales to the near-wall region, integral length scales are very similar.

5.2 Transverse Plane Measurements

5.2.1 PIV Transverse Plane 1 (2D2C)

PIV Transverse Plane is a measurement plane perpendicular to the axial flow. Several complications arose when attempting flow visualization on the transverse plane that were not encountered during the vertical plane measurements. The 2D2C PIV technique requires a top-down viewpoint normal to the fuel bundle cross section.

A total of three imaging configurations were tested to achieve optimal results. Each configuration and results of such will be discussed in Sections 5.2.1.1, 5.2.1.2, 5.2.1.3, re-
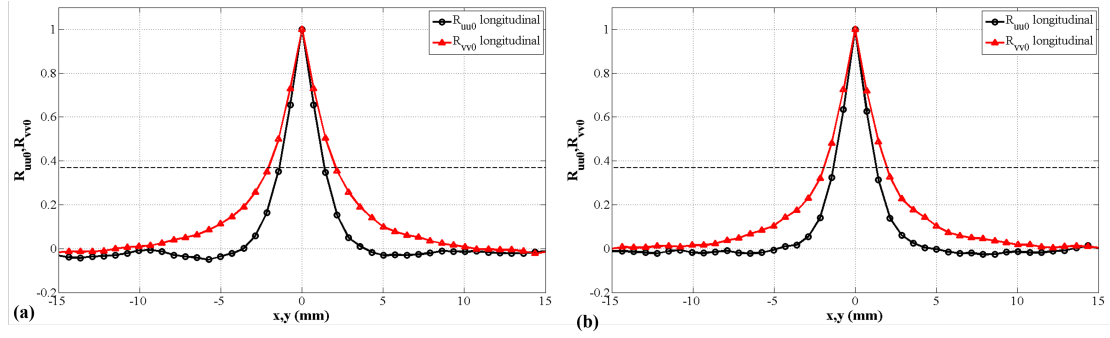
Figure 5.26: PIV Vertical Plane 6 (*a*) CSC1 and (**b**) CSC2 two-point spatial velocity-velocity cross-correlations, R_{vv0} and R_{uu0}, averaged over 4 spatial points (X = 2.9, 5.0, 7.2, and 9.3 mm along Y = 110.6 mm) for Re_B = 18,810

spectively. The only constants throughout the testing of these imaging configurations were the traversing system and camera leveling system. The traversing system consisted of four motorized Velmex BiSlide linear stages. The two parallel and vertical linear stages were configured to operate simultaneously to increase or decrease the distance between camera and measurement plane. This made for convenient testing of various conventional planar lenses when optimizing the measurement FOV and particle image size. Horizontal axis movements for alignment with the fuel bundle were made using two perpendicular linear stages. These provided the ability to quickly view different regions of the transverse plane, as none of the imaging configurations had wide enough fields of view for the entire bundle cross section. Newport three-axis finely tunable dovetail stages acted as the leveling system to minimize error associated with off-normal viewing of the laser sheet. Figure 5.27 shows a CAD rendering of the second imaging configuration, which was the selected configuration for the presented measurements of Section 5.2.1.7.

As outlined in Section 4.4, out-of-plane particle motion must be limited to 25% of the laser sheet thickness. With nuclear fuel bundles, the axial velocity component will be significantly larger than the two transverse components. Therefore, it can be difficult to capture transverse particle image displacement (in-plane motion) when the axial velocity component (out-of-plane motion) is nearly an order of magnitude larger, as is the case in the wire-
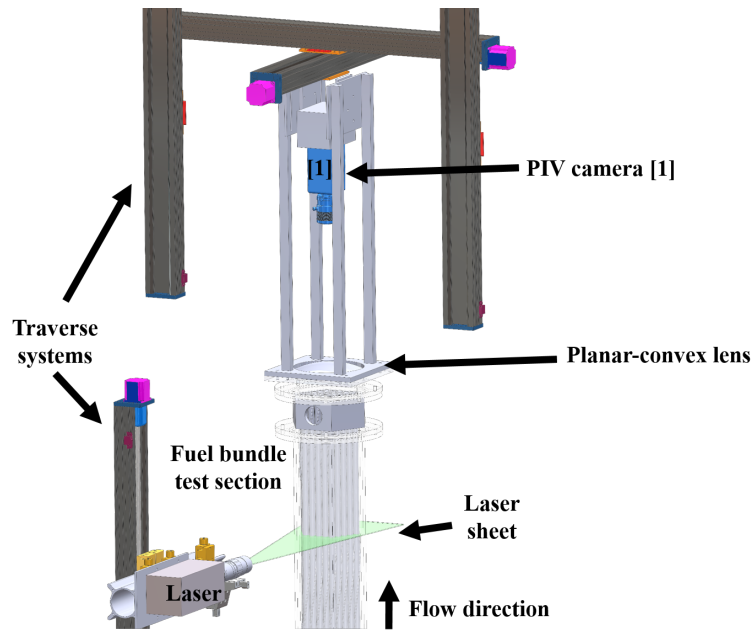
Figure 5.27: Imaging setup for the 2D2C Transverse Plane 1 PIV measurement containing test section, laser, camera, and traverse systems

wrapped fuel bundle. A small increase in the volumetric flowrate yields a significant increase of the camera capture frame rate to limit out-of-plane particle displacement. An increased camera capture frame rate also decreases the in-plane displacement, of which is there a lower limit that PIV cross-correlation algorithms cannot detect.

5.2.1.1 *Transverse Imaging Configuration 1 (Conventional Lens)*

Imaging configuration 1 consisted of all hardware visible in Figure 5.27 minus the planar-convex lens and four aluminum support beams. A single digital CMOS Phantom M310 camera was utilized and operated in single-frame mode with a full resolution of 1280×800 pixels and 12-bit image depth. It was not possible to position two Phantom M310 cameras adjacent to one another and maintain a perpendicular alignment with the laser sheet, because of the thickness of the camera housing. Three types of conventional lenses were tested. They were a 50 mm Zeiss Makro-Planarf/2 ZF lens, a 100 mm Zeiss Makro-Planarf/2 ZF lens, and a 200 mm Nikon f/4 ED-IF AF Micro-NIKKOR lens.

Perspective error, or parallax, was anticipated prior to this measurement. Therefore, the

first parameter of interest was to determine the maximum depth into the test section that could imaged. The conclusion of this effort was simple. The maximum FOV with a conventional lens was approximately equal to 2 rod diameters. This limitation would require a massive experimental effort to scan and measurement an appreciable fraction of the entire bundle cross section. The maximum working distance into the bundle was less than 100 mm. This working distance placed the laser sheet within the last 0.25 wire pitches of the test section, which is an unacceptable region classified as a no-measurement zone due to the expectation of downstream effects from the outlet plenum.

The lazing system consisted of a 20 W continuous wave 532 nm laser, focusable collimator, 15 mm cylindrical plano-convex lens, and 25 mm cylindrical plano-convex lens. The resulting laser sheet had a thickness of 2 mm. For high Re_B flow conditions (above 10,000), the camera capture rate needed to be a greater than 5000 Hz. At this rate, exposure setting, and lens setup, the 10 W continuous wave laser was insufficient to appropriately illuminate the seeding particles.

Figure 5.28 shows sample images using the 200 mm Nikon Micro-NIKKOR lens at a Re_B of 4,000. The left image is taken at 3.25 wire pitches into the test section (pressure tap 7), which is a working distance of 0.46 wire pitches deep into the rod bundle from the top. The right image is taken at 3.5 wire pitches into the test section (flange interface with the outlet plenum), corresponding to a working distance of 0.21 wire pitches deep into the rod bundle from the top. The imaging quality increases substantially as the working distance through the bundle is decreased. This is attributed to less perspective error and smaller fraction of incident laser light being attenuated by the bundle. Therefore, it was clear that the necessary steps forward were to:

- Minimize perspective error

- Increase laser light intensity

- Increase FOV if possible, but would require higher resolution camera
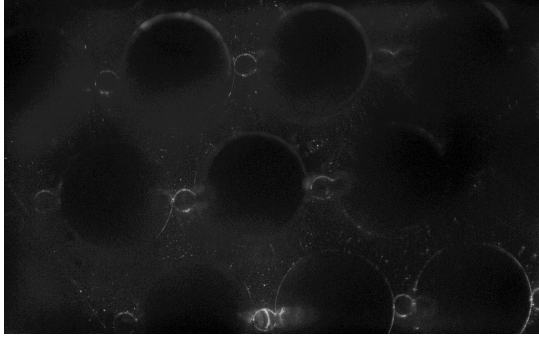
(a) Working distance of 220 mm or 0.46 wire pitches (PT 7)
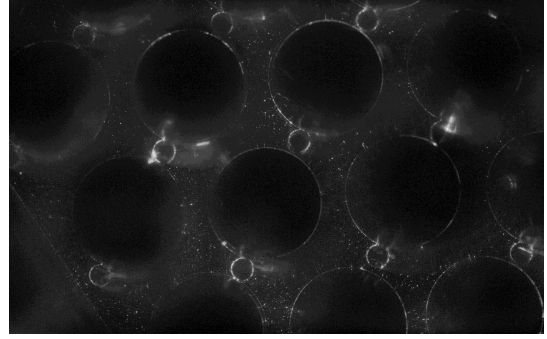
(b) Working distance of 100 mm or 0.21 wire pitches (test section upper flange)

Figure 5.28: Raw result of imaging configuration 1 with conventional lens setup

5.2.1.2 *Transverse Imaging Configuration 2 (Conventional Lens + Planar-Convex Lens)*

Imaging configuration 2 involved a different camera, lens, and laser hardware than imaging configuration 1. Also, modifications to the fuel rod tops and upper support plate were made.

The first improvement focused on minimizing the perspective error, or parallax. The optical configuration that achieves this effect is know as a telecentric configuration. The effect results in constant magnification regardless of the distance. Per ThorLabs (2018), all chiefs rays must be parallel to the optical axis for either (object- only or image- only) or both the object- or image-space. Most commercial products are configured for both and call the setup a bi-telecentric lens. The goal is to set the front lens focal plane at the aperture stop. The result is an image only using the chief rays parallel to the optical axis and sets the entrance pupil and infinity, as can be seen in Figure 5.29 for conventional, object-telecentric, and bi-telecentric lenses provided by ThorLabs (2018).

Figure 5.30 highlights the magnification differences between a conventional lens setup and a telecentric lens setup provided by ThorLabs (2018). Figure 5.31 highlights the perspective differences between a conventional lens setup and a telecentric lens setup provided by OptoEngineering (n.d.).
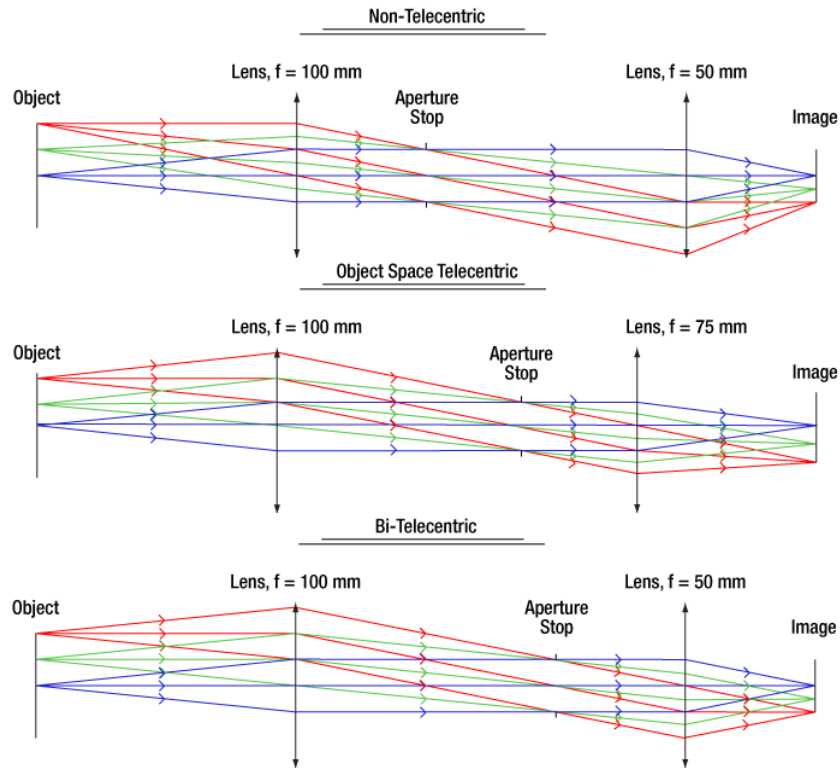
Figure 5.29: Ray diagrams of conventional, objective space telecentric, and bi-telecentric lenses.

Several optical manufacturers offer these types of lenses, such as Edmund Optics, Thor-Labs, Moritex, and Opto. However, most products in their catalogs had very short working distances (less than 100 mm) and very small fields of view (less than 50 mm x 50 mm). A few companies offered products that would meet the FOV and working distance requirement for the Transverse Plane 1 measurement, but cost approximately $10,000 and were custom built with 60 to 100 day lead times. Both of these issues resulted in an in-house investigation of ray diagrams and subsequent development of the telecentric apparatus (Figure 5.32).

Four aluminum support beams and a lens holder were added to the initial configuration. An additional lens was added between the conventional lens setup and the laser sheet. The additional lens was a 200 mm diameter, 400 mm effective focal length (EFL), spherical plano-convex condensing lens. The diameter was selected based on the size of the bundle cross section of 178 mm and off-the-shelf availability. A large lens is required, because the
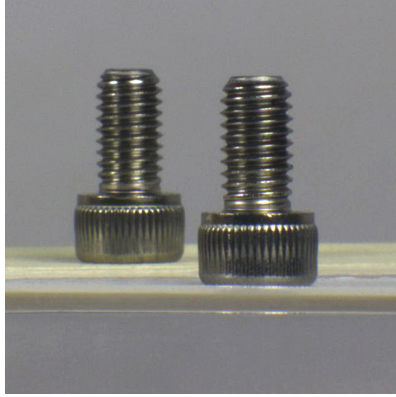
(a) Conventional setup at 45 mm depth offset   (b) Telecentric setup at 45 mm depth offset
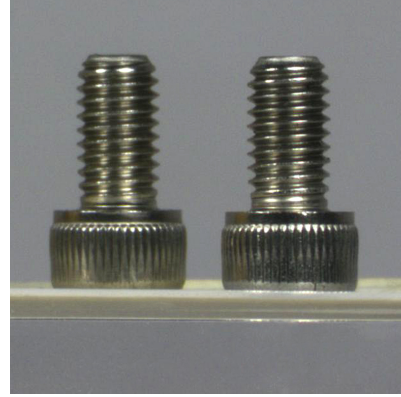
Figure 5.30: Comparison of conventional and telecentric lens setups to highlight the constant magnification.

maximum FOV a telecentric lens can achieve is no larger than the largest diameter lens furthest from the aperture. Also, it was expected that the spherical plano-convex condensing lens would have a non-zero magnification, thus reducing the final FOV further. The telecentric apparatus also consisted of a mounting system to attach to standard linear traversing stages, a camera holder that is easily adjustable to fit various camera enclosure sizes, and a Newport three-axis finely tunable dovetail stage to not only align the perpendicular orientation of camera and laser sheet, but also align coaxially the conventional lens setup with the 200 mm plano-convex lens at the end of the apparatus.

The working distance, or distance between camera sensor and laser sheet, of configuration 1 was approximately 220 mm. With the additional lens, the new working distance was expected to be nearly 620 mm. This increased distance meant the particle images would be too small based on the methodology of Section 4.4. Therefore, an 8 megapixel Imperx Bobcat B3340 was installed. The Bobcat had a maximum resolution of 3312×2488 and maximum capture rate of 17 Hz single-exposure or 8 Hz double-exposure.

The next optimization from configuration 1 involved switching to a Spectra-Physics Quanta Ray PIV-400 dual head pulsed laser with 300 mJ per pulse per head output at 532 nm. After maintenance, mirror alignment, and constructing a mobile cart, the laser system

(a) Conventional lens setup normal to extruded aluminum rail
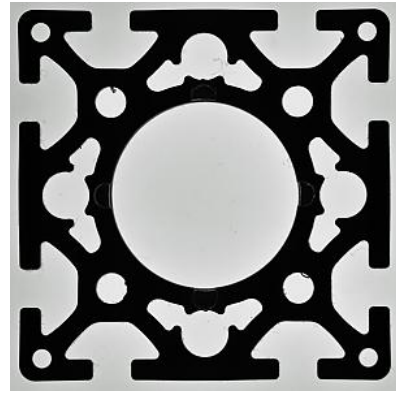
(b) Telecentric lens setup normal to extruded aluminum rail

Figure 5.31: Comparison of conventional and telecentric lens setups to highlight the elimination of perspective error or parallax.

was installed with identical beam combination optics for the laser sheet. One aspect of this older model laser was a fixed repetition rate of 30 Hz, which would not be suitable for the Bobcat B3340. Therefore, a bypass jumper inside the Quanta Ray PIV-400 was relocated and the final solution involves pulsing the lamps at the fixed 30 Hz while only triggering the Q-gate switches at the desired integer divisor of 30.

Two final modifications to the facility were the polishing of machined surfaces on the upper support plate and rod end at the top of test section. These two steps were not required but performed for good measure, as the test section was drained and open during this optimization process.

This imaging setup effectively minimizes parallax and the pin shadow, while maintaining excellent light transmission and a large field of view that is difficult to achieve with commercial telecentric lenses. The improvement can be seen in Figure 5.34 when comparing the imaging configuration 1 to imaging configuration 2.

Nevertheless, minor radial pincushion distortion was detected during the calibration procedure. This distortion was the result of a spherical lens being used instead of an aspherical lens for the forward lens. The spherical lens was procured first for two reasons. One, the
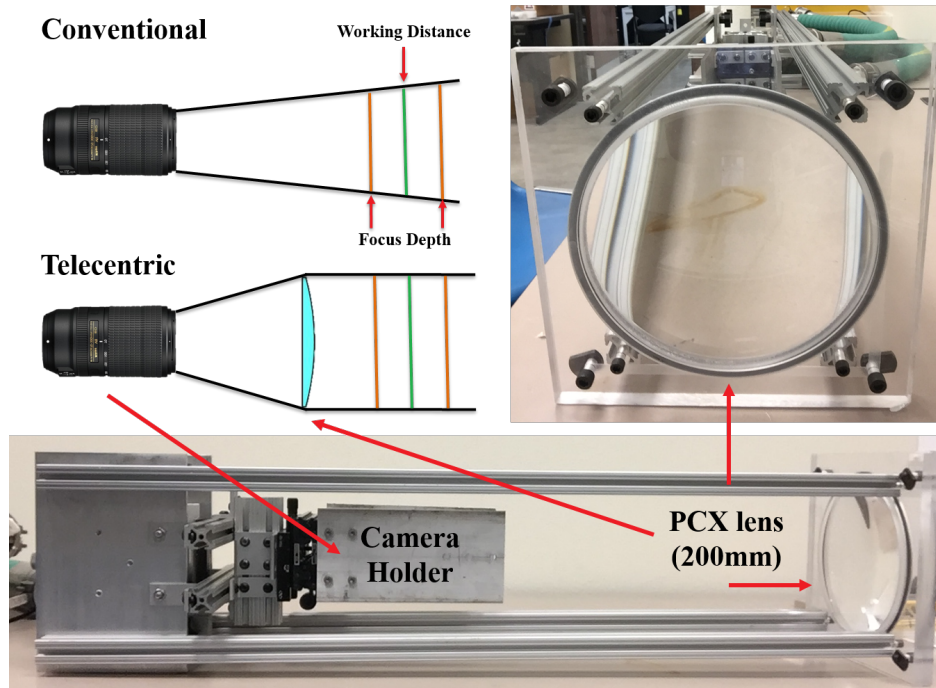
Figure 5.32: Simplified ray diagram with the telecentric apparatus made to mount to existing 3D traversing systems while position conventional camera setups coaxial to the 200 mm planar convex lens

telecentric apparatus had not been proven as a working concept. Two, no off-the-shelf large diameter (>100 mm) aspherical lens with a 400 mm EFL could be procured.

Two undistortion techniques were applied to the calibration image. Both require a set of object points, detect image points based on the supplied inputs, and calculation non-linear mapping functions to undistort or reconstruct the original image. The first method utilized the OpenCV library, developed by Bradski (2000), and its camera calibration workflow to calculate distortion coefficients, intrinsic parameters of the imaging setup, and extrinsic parameters relative to a specific calibration image. The OpenCV developers suggest using multiple calibration images at various camera / plate orientations, as seen in Figure 5.35. However, a single image calibration was the only option for the telecentric apparatus, due to the constant magnification eliminating the depth perception required to generate the optimal multi-image calibration.

Figure 5.33: Mobile cart for the Spectra-Physics laser, controller, and air-cooled chiller
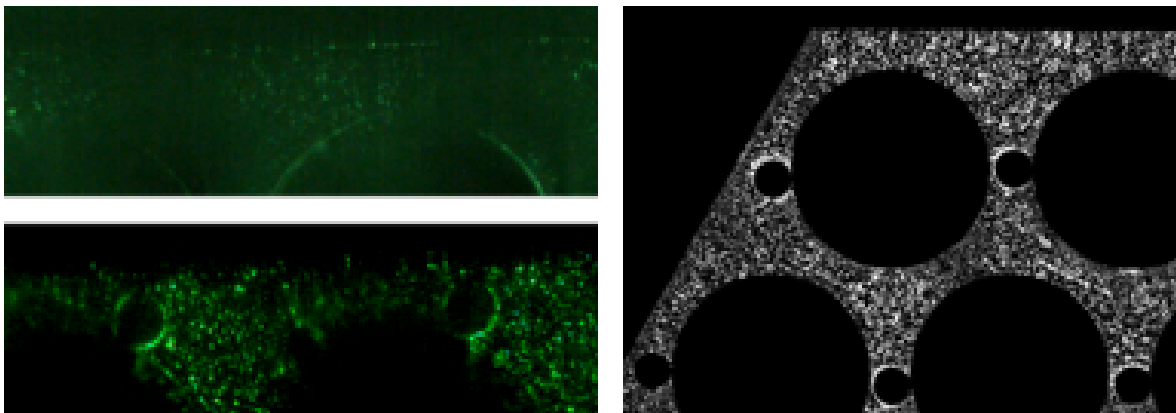
Figure 5.34: Top-down view of the fuel bundle utilizing (*left top*) conventional lens and (*left bottom*) conventional lens + plano-convex lens configurations. The pin shadow and parallax are effectively minimized and image quality of the seeding particles in the subchannels is greatly improved. *right* Background subtracted image ready for PIV processing.

To improve the single-image calibration, a 17×19 object points checkerboard grid was employed. Figure 5.36 presents the original distorted image and subsequent undistorted image. The increased grid density allowed for a better mapping function and undistortion. A better mapping function was determined using two criteria applied to the undistorted, or reconstructed, image. The first criteria was to calculate the adjacent dot-to-dot spacing distance and determine the standard deviation of the entire grid. The second criteria was to calculate the R^2 value for the linear regression of each rod and column of the grid. Example
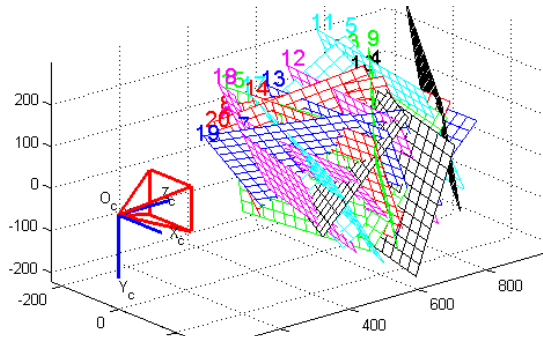
Figure 5.35: Example of the OpenCV multi-image camera calibration procedure.

scripts can be found in Appendix I. Results of the OpenCV single-image calibration are presented in Table 5.10.
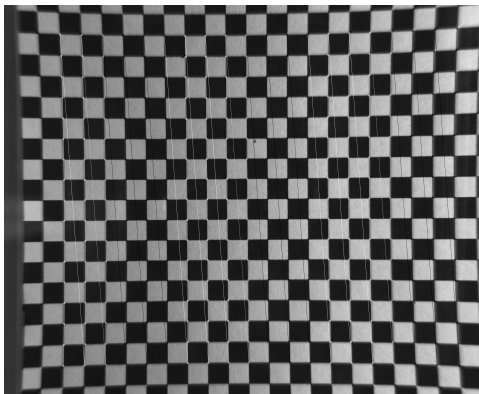
(a) Raw distorted image with corner detection grid overlay
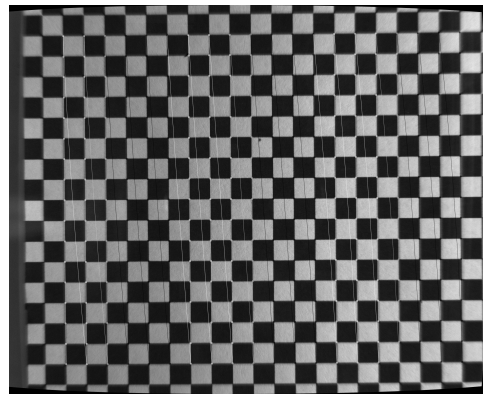
(b) Undistorted image with corner detection grid overlay

Figure 5.36: Original and undistorted images of a checkerboard pattern using camera parameters determined through OpenCV's single-image calibration process.

The second undistortion method utilized the geometric reconstruction built into the PRANA SPIV package which uses the Willert (1997) method and includes additional angle calculations recommended by Scarano et al. (2005). The same two quantifying criteria were applied to this method's undistorted image output, as well. Table 5.10 contains a comparison of the standard deviation of adjacent grid point distances and mean R^2 value for rows and columns

of the grid for four images: (1) the raw calibration image without the spherical plano-convex forward lens, (2) the raw radial pincushion distorted image, (3) the undistorted image using OpenCV radial distortion coefficients, (4) and the undistorted image using the PRANA SPIV Willert and Scarano dewarping algorithms. The first image contains none of the radial distortion that was attempted to be eliminated by the two undistortion methods. Results of the PRANA SPIV calibration are presented in Table 5.10. The PRANA SPIV Willert and Scarano dewarping best achieves the raw undistorted grid. Therefore, this method was selected to reconstruct the images of Transverse Plane 1.
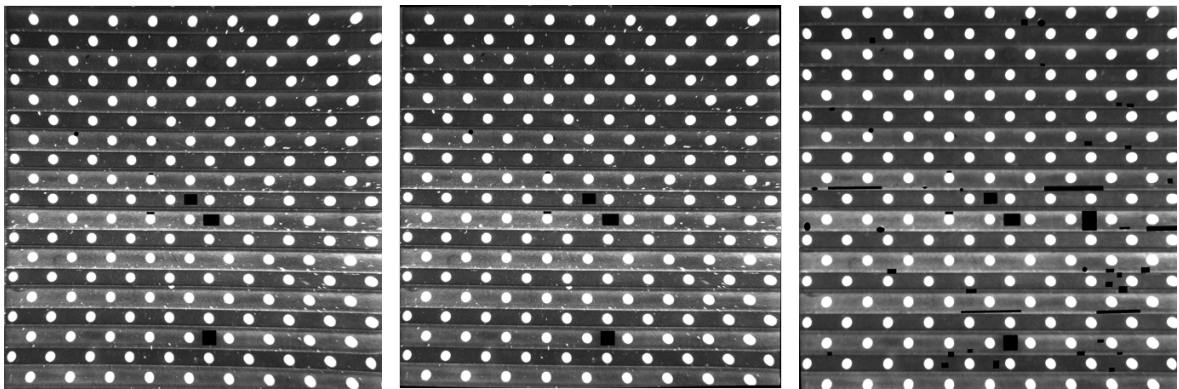
Figure 5.37: Original, OpenCV undistorted, and Willert dewarped images of an LA Vision calibration target.

Table 5.10: Summary of undistortion results achieved using OpenCV and PRANA Willert methods relative to the conventional lens setup (minimal radial distortion) and the telecentric lens setup (with radial distortion).

Image	Std. Dev. (pixel)	R^2
Imaging Configuration 1	0.9	0.996
Imaging Configuration 2	4.7	0.764
Config 1 + OpenCV Undistort	2.1	0.970
Config 1 + Willert Dewarp	1.2	0.989

5.2.1.3   Transverse Imaging Configuration 3 (Telecentric Lens)

Imaging configuration 3 initially started as replacing the spherical plano-convex forward lens with an identical aspherical design. However, this product could not be procured in a reasonable time frame (100 days) and would have cost approximately $2000 - $2500. Considering the expense of the single aspherical lens, the commercial telecentric products were not far off. Therefore, Imaging configuration 3 involved replacing the spherical plano-convex forward lens with a commercial telecentric product. The Edmund Optics TECHSPEC TitanTL model 34-012 was selected due to its off-the-shelf availability. The lens had an FOV of 146 mm horizontal, a working distance of 286 mm, and a depth of field of ± 73 mm. Figure 5.38 presents the lens installation on the end of the telecentric apparatus.

The initial concern with the TitanTL model 34-012 was a lack of sufficient laser light intensity for quality images. However, the Spectra-Physics Quanta Ray PIV-400 was sufficient. The resulting images showed no measurable radial distortion compared to the raw undistorted results of Table 5.10. One overlooked aspect of this configuration was the depth of field and its implications for PIV. The extremely deep depth of field allows for reflected light both upstream and downstream the laser sheet to be in focus and therefore part of the measurement. This differs from configurations 1 and 2, where the depth of field is less than the laser sheet thickness.

In conclusion, this commercial product was not applicable for PIV. Therefore, a custom-built apsherical plano-convex forward lens is currently being constructed for the telecentric apparatus. A 200 mm diameter lens was not practical for many lens manufacturers. Therefore, a 140 mm diameter lens was selected. Results taken with it will be compared to the results produced using the spherical forward lens of imaging configuration 2. However, that comparison is not part of the scope of this dissertation.
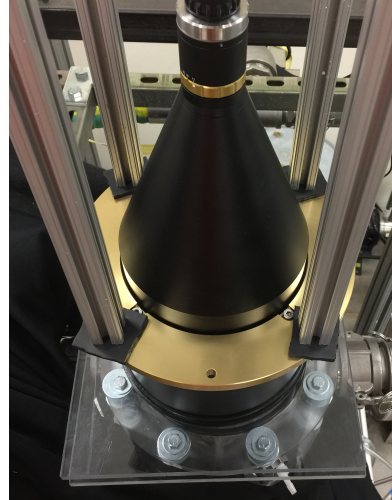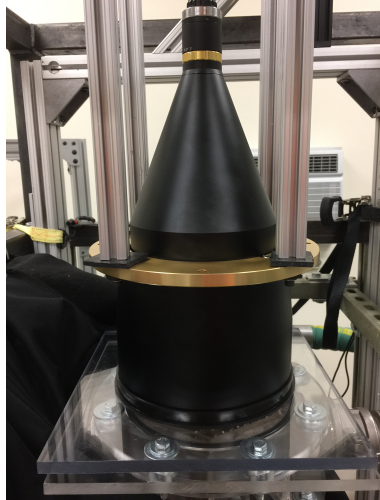
Figure 5.38: Edmund Optics TECHSPEC TitanTL model 34-012 mounted to the telecentric apparatus

5.2.1.4 Imaging Settings

Imaging configuration 2 was used to produce the following results. The monochromatic collimated light source was generated using a Spectra-Physics Quanta Ray PIV-400 dual head pulsed laser with 300 mJ per pulse per head output at 532 nm. Beam combination optics included a focusable collimator, 15 mm cylindrical plano-concave lens, and 25 mm cylindrical plano-convex lens. The resulting laser sheet had a thickness of 2 mm. An Imperx Bobcat M3340 captured the laser light with a resolution of 3312 × 2488 and bit depth of

12. It was paired to a 50 mm Zeiss Makro-Planarf/2 ZF lens with the aperture set to f/4. The intra-frame time delay, Δt, was set to 332 μs to meet the average desired particle image displacement of 4 pixels while ensuring the out-of-plane displacement remained less than 25% of the 2 mm thickness of the laser sheet. Pairs of images were collected at a frequency of 6 Hz. The calibration scale for this measurement was equal to 0.039 mm/pixel. The vector spacing for this measurement was equal to 0.157 mm/vector.

5.2.1.5 PIV Processing Settings

PIV images were processing using the PRANA code introduced in Section 4.3.4. Table 5.11 contains the PIV processing parameters for Transverse Plane 1.

Table 5.11: PIV processing settings for PIV Transverse Plane 1

Parameter	Pass 1	Pass 2	Pass 3
Multigrid method	Bi-cubic	Bi-cubic	Bi-cubic
Searching window size (pix)	64×64	32×32	32×32
Interrogation window size (pix)	32×32 pixels	16×16	16×16
Interrogation window overlap	50%	50%	75%
Grid buffer	8×8	8×8	8×8
Correlation type	RPC	RPC	RPC
Subpixel peak location	3 Pt. Gaussian	3 Pt. Gaussian	3 Pt. Gaussian
Vector Validation	UOD median	UOD median	UOD median

5.2.1.6 Vector Replacement and Residual Convergence of Datasets

This section included the discussion regarding UOD vector validation results and residual convergence of first and second order flow statistics for Re_B = 13,500 only. As can be seen in Figure 5.39a, an approximate four vector thickness of high replacement occurs at the FOV edge and near the pin and wire solid surfaces. These regions are not compared when performing CFD comparisons. The values have been incorrectly modified by the UOD process, where the edge-most vectors had an insufficient number of neighbors to perform an

100

acceptable nearest neighbor median comparison. This is also typical when near the edge of any solid structures, such as the hexagonal duct wall, pin, or helical wire spacer.

A 40% replacement threshold from the UOD vector validation was chosen as delineate between easier and more difficult regions for the PIV cross-correlation. Figure 5.39b highlights each vector location with a replacement frequency greater than 40%.

(a) Replacement frequency heatmap from UOD vector validation checks

(b) Highlighting specific vectors above the 40% of frames replacement threshold
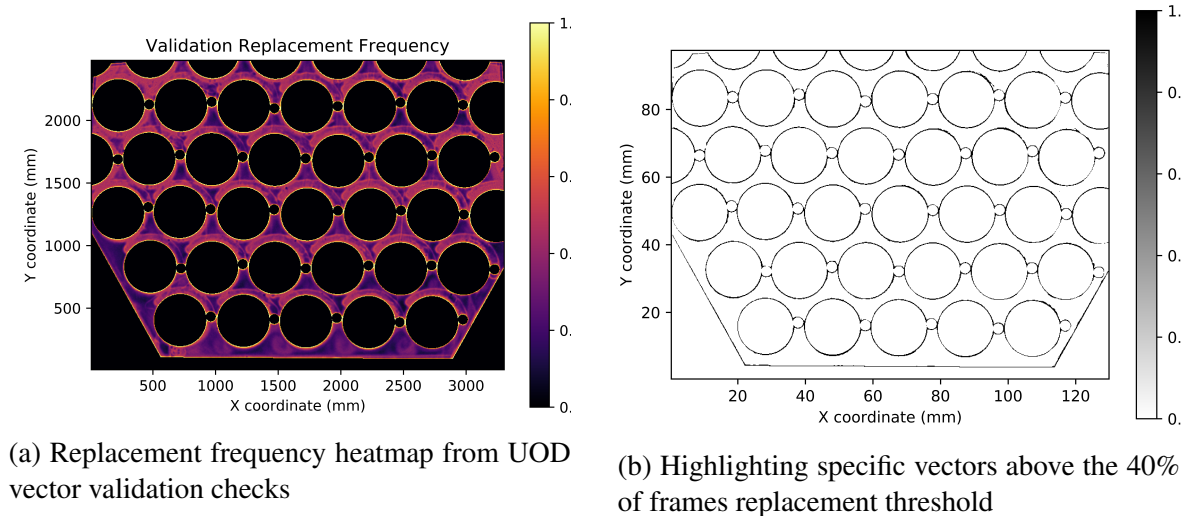
Figure 5.39: Vector validation checks

For all analyzed statistical quantities, the residual convergence of the absolute relative difference was calculated comparing various subsets of the total image set. A total of 40 subsets were generated by randomly selecting instantaneous velocity vector fields from 5% of the total dataset and increasing logarithmically until the total dataset was selected. Presented in Figure 5.40 are the residual convergence plots for five first and second order statistical quantities of interest for the exterior, corner, and central interior subchannel types. Absolute relative differences were averaged over lines spanning each subchannel.

5.2.1.7 Results at Reynolds Number = 13,500

Experimental results are presented on a transverse plane perpendicular to the axial flow of the fuel bundle at Re_B = 13,500. This Reynolds number corresponds to the turbulent flow regime. These results were generated using imaging configuration 2. Experimental conditions for this measurement are defined in Table 5.12.

Table 5.12: Experimental conditions for the Transverse Plane 1 measurement

Variable	Value	Uncertainty	Unit
Temperature	19.3	0.6	°C
Viscosity	840	50	$\mu\mathrm{Pa\,s}$
Density	857.3	3.8	$\mathrm{kg\,m^{-3}}$
Flow rate	838	16	$\mathrm{L\,min^{-1}}$
Bulk velocity	1.739	0.04	$\mathrm{m\,s^{-1}}$
Re_B	13,500	240	N/A
Intra-frame time delay	332	N/A	$\mu\mathrm{s}$

The direction of the wire wrap is clockwise (CW) when viewed from the top-down perspective. The wire position of an upstream plane would be rotated CW from the present wire position. The wire position of a downstream plane would be rotated CCW from the present wire position. Two observed phenomena were a bulk swirl around the bundle and a local swirl around each pin. Each statistical quantity will be discussed in the following order: corner subchannel behavior, exterior subchannel behavior, and interior subchannel behavior.

Figure 5.41 presents the ensemble-averaged and RMS fluctuating components of velocity in both the X- and Y-direction. For $\overline{u}$, the corner subchannels contain very little motion. The exterior subchannels are not restricted by the helical wire spacer and therefore present a flow path for the bulk swirl. However, slight expansions and restrictions occur as the distance between the pins and hexagonal duct wall change. These restrictions assist in generating four high shear regions. Also, negative gradients of $\overline{u}$ exist for both periphery-to-center and left-to-right flow paths, with the latter highlighting the propensity of fluid flow toward the bundle periphery. For $\overline{v}$, the corner subchannels contain very little motion. The exterior subchannels also highlight the four high shear regions. Again, a negative gradient exists for the periphery-to-center flow paths. However, a positive gradient highlighting the bulk swirl encountering the right hexagonal duct wall and reorienting as required. For u'_{rms} and v'_{rms}, field values are nearly identical for both components. Fluctuations are largest in the four high shear regions and also at 10:30 relative to each pin. These fluctuations occur approximately 120° CCW of the wire spacer. Each fluctuating region has a unique shape.
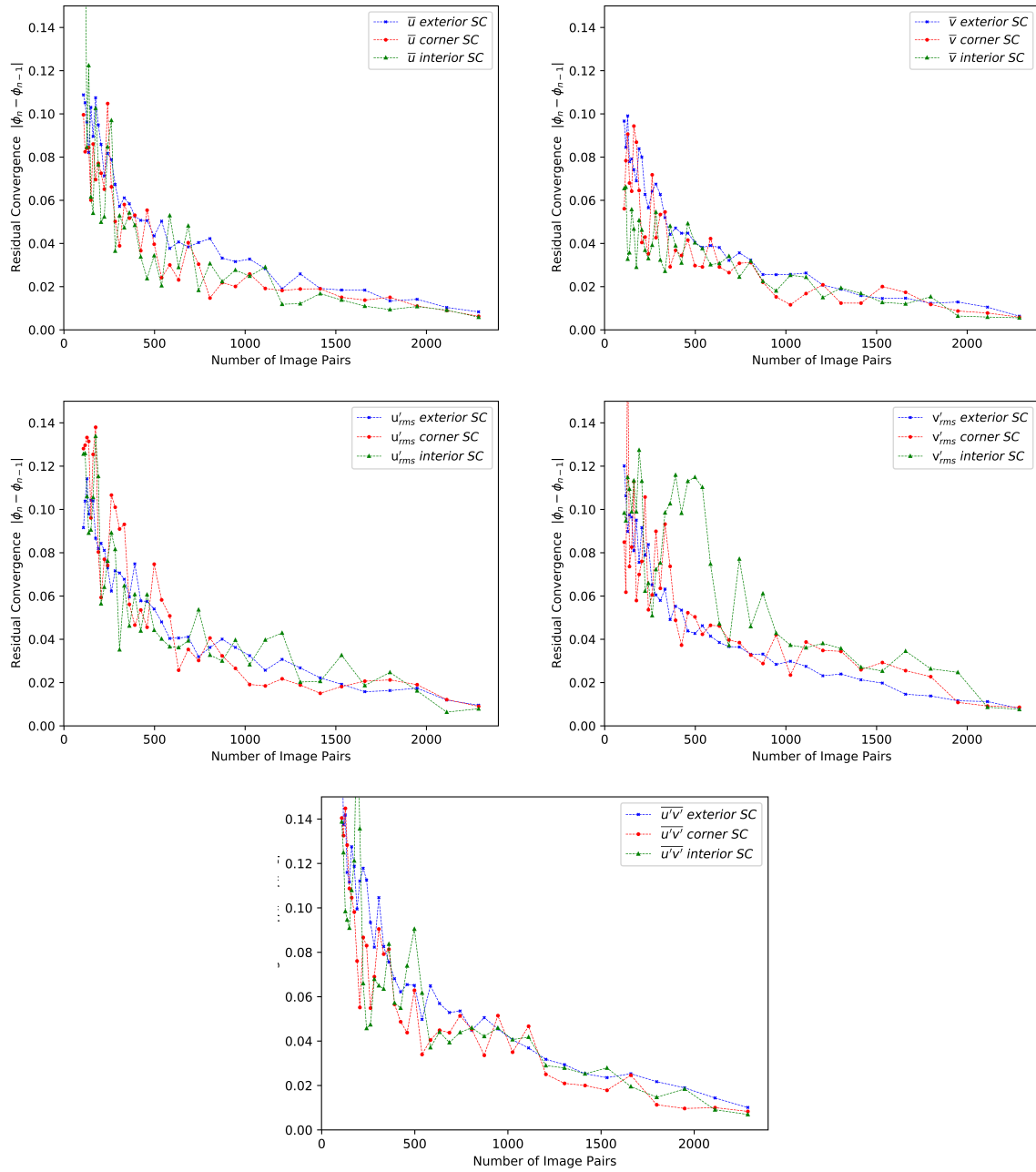
Figure 5.40: PIV Transverse Plane 1 residual convergence in the exterior, corner, and central interior subchannels.
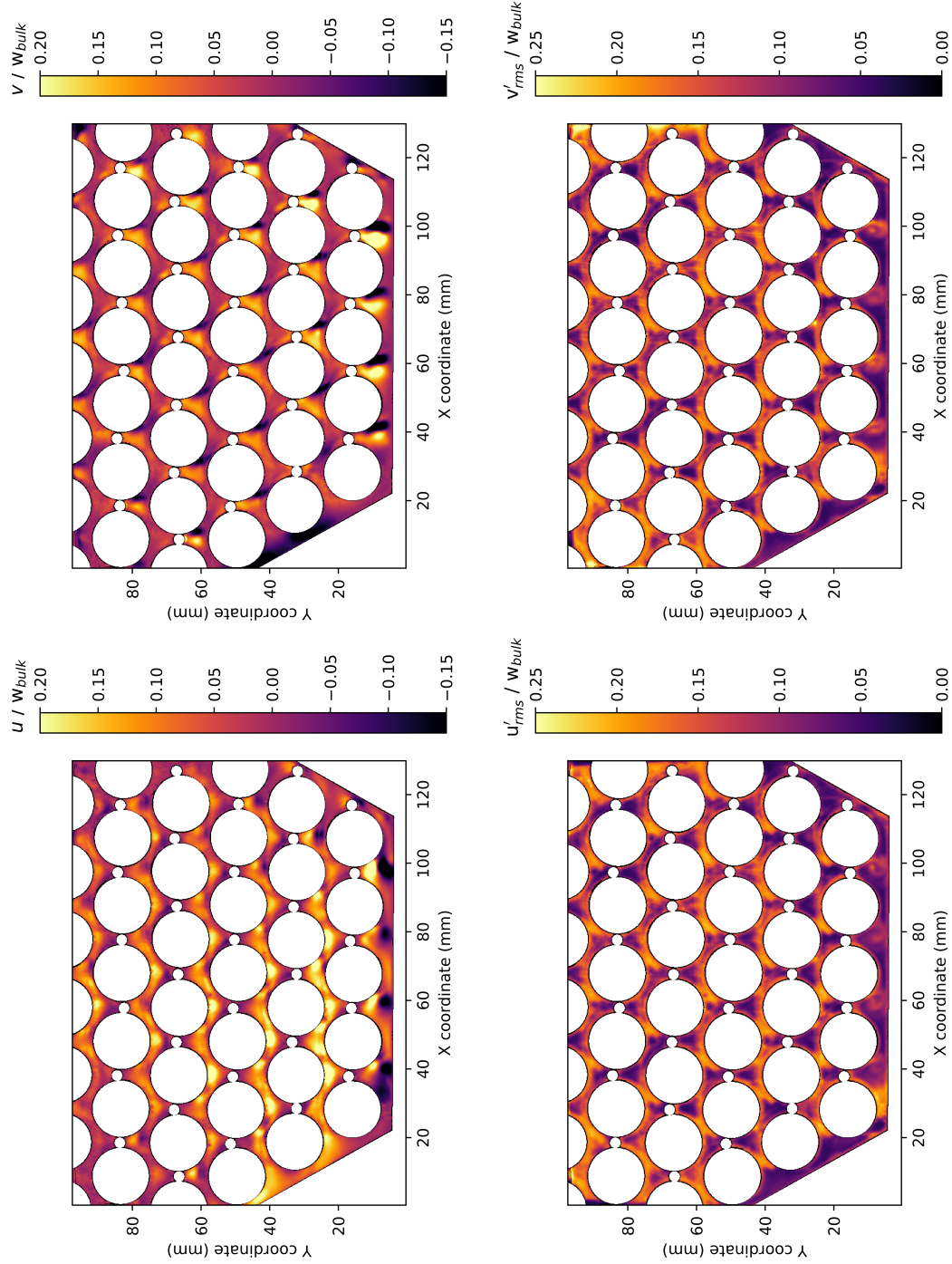
Figure 5.41: PIV Transverse Plane 1 ensemble-averaged and RMS fluctuating components of velocity in both the X- and Y-direction for $Re_B = 13,500$.
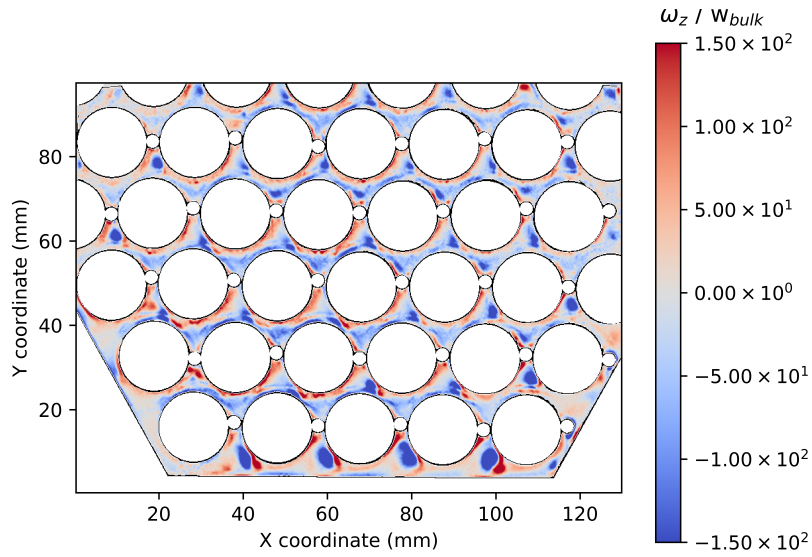
Figure 5.42: PIV Transverse Plane 1 ensemble-averaged single component z-vorticity for $Re_B = 13{,}500$.

Figures 5.43 and 5.44 present vertical and horizontal profiles through the center of the 22 subchannels. Most subchannel behavior exists within a band of 50% the mean value for both $\overline{u}$ and $\overline{v}$. However, subchannels 1-8 deviate significantly from this band. These eight subchannels represent the exterior two rows of the 61-pin, 5 row, bundle. Their unique behavior supports the conclusions of Brockmeyer et al. (2017), where a 37-pin, 4 row, bundle or larger is necessary to mitigate the exterior subchannel wall effects on the bundle central subchannel.

Figures 5.45, 5.46, and 5.47 are included to display the magnitude of the ensemble-averaged vector fields for the exterior, corner, and central subchannel types.
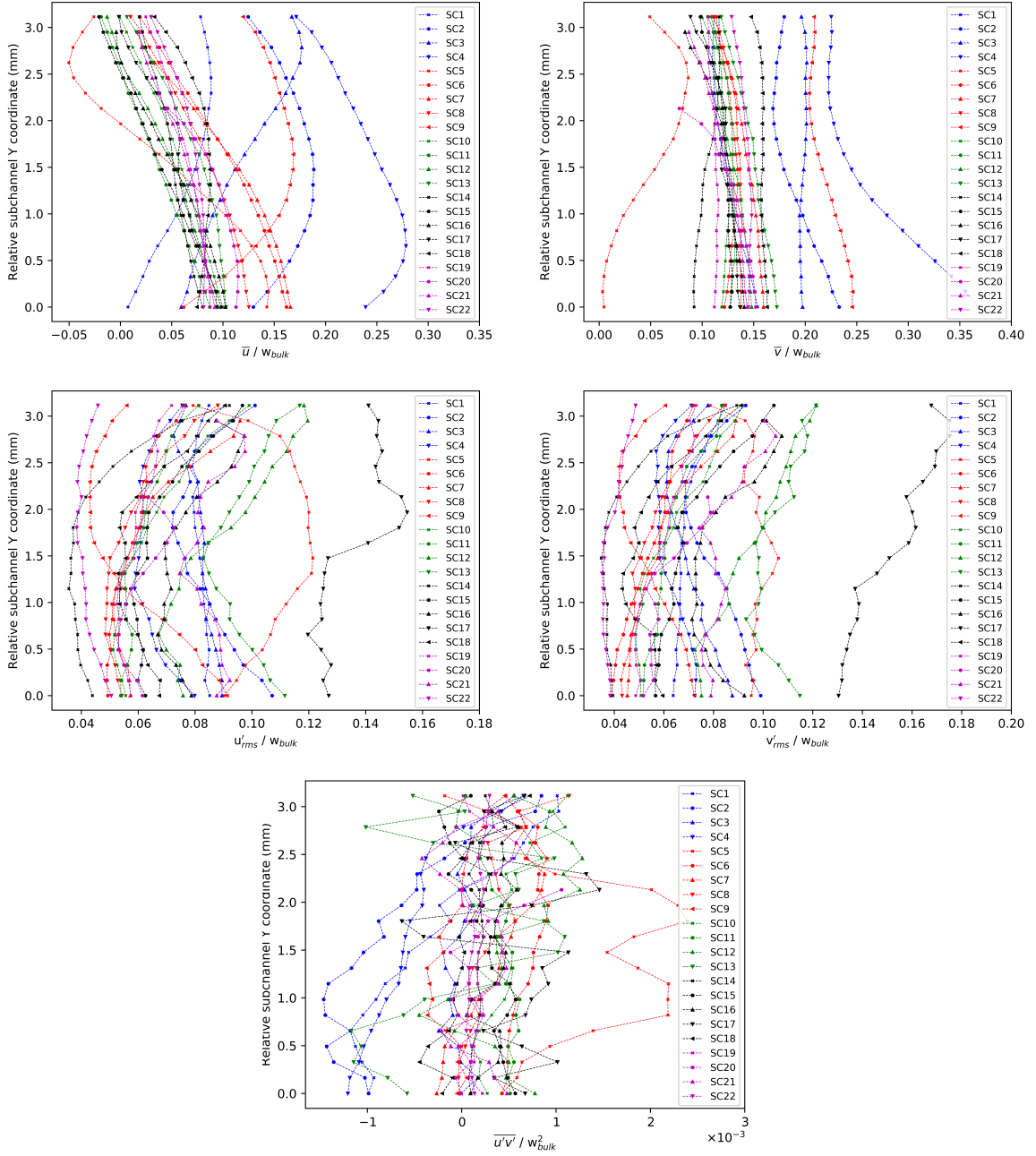
Figure 5.43: Vertical profiles of $\overline{u}$ and $\overline{v}$ through each of the 22 subchannels
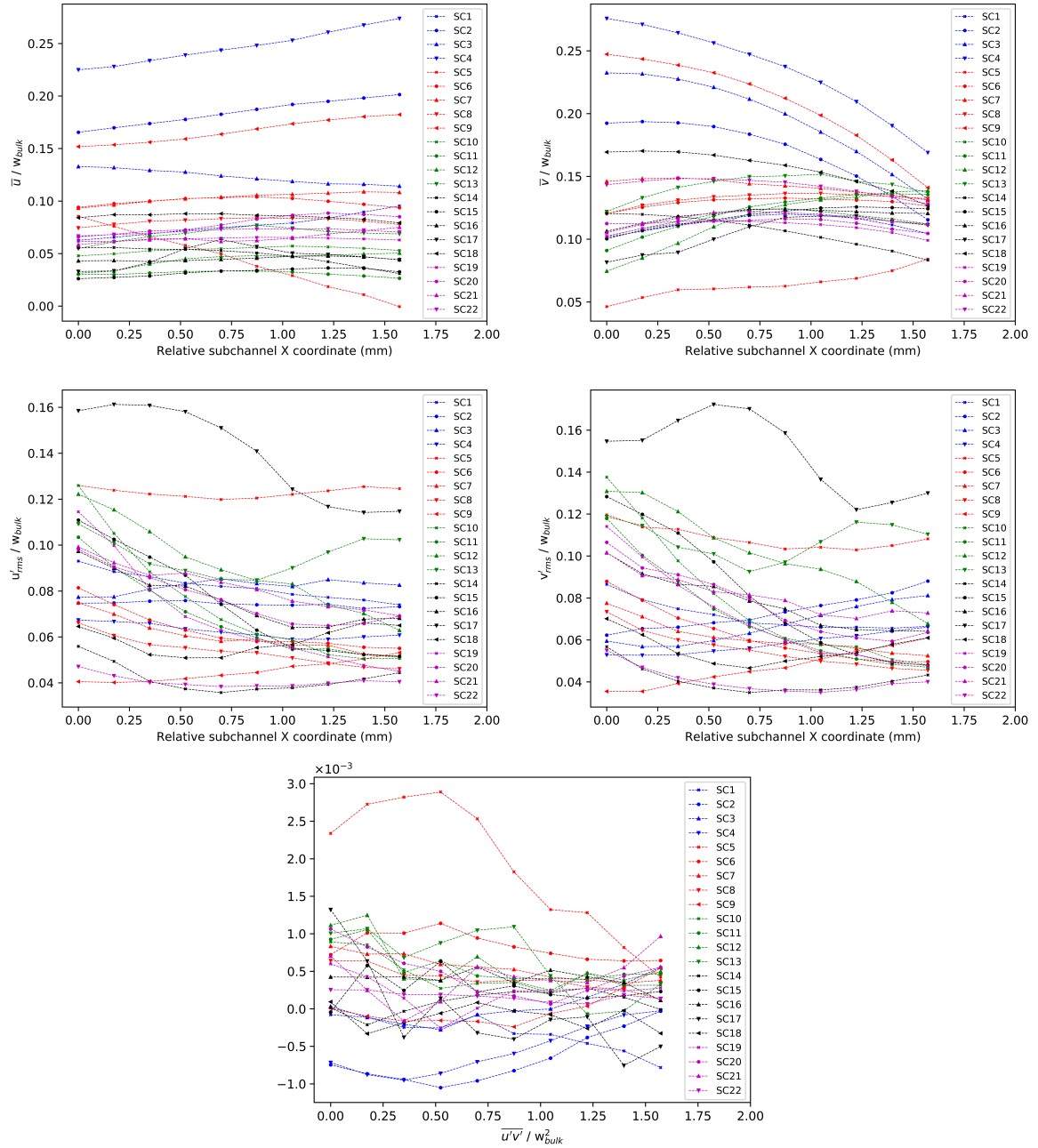
Figure 5.44: Horizontal profiles of $\overline{u}$ and $\overline{v}$ through each of the 22 subchannels
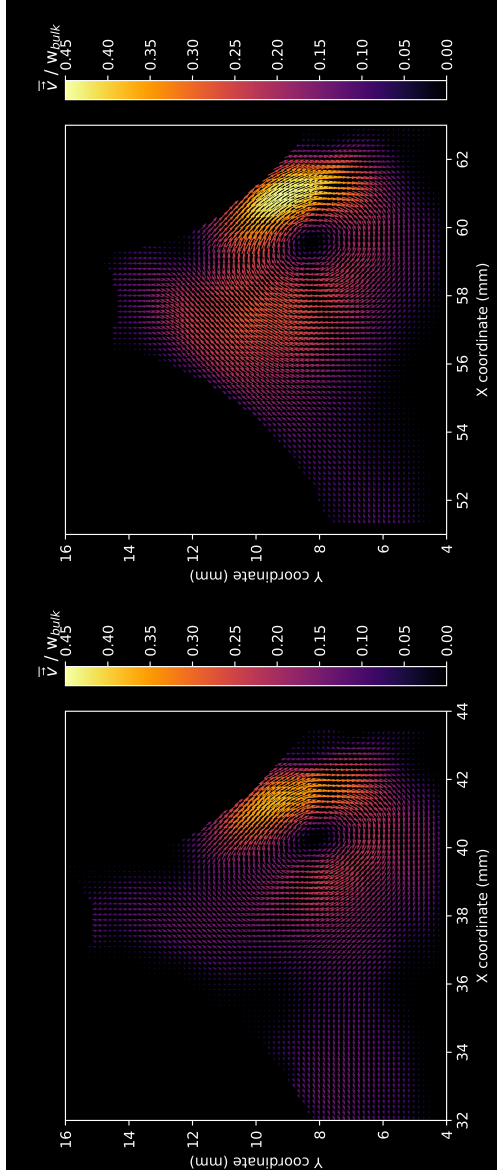
(a) ESC1

(b) ESC2
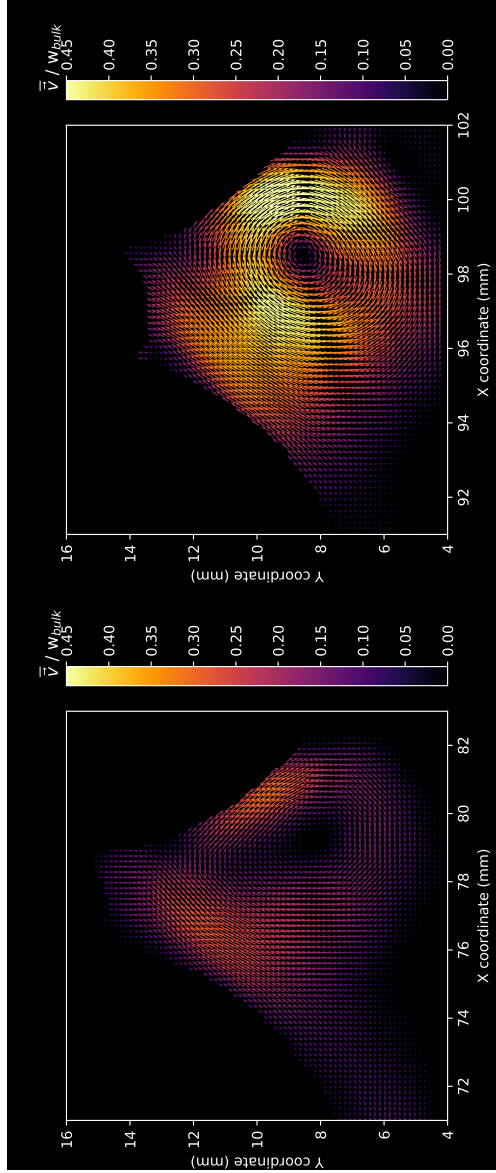
(c) ESC3

(d) ESC4

Figure 5.45: 100% sample density of the ensemble-averaged vector fields of each exterior subchannel near the hexagonal duct wall
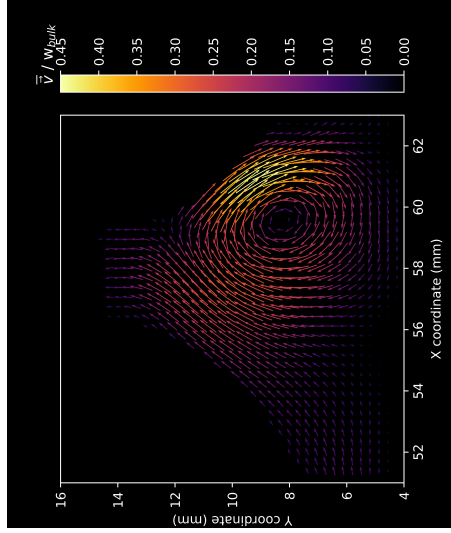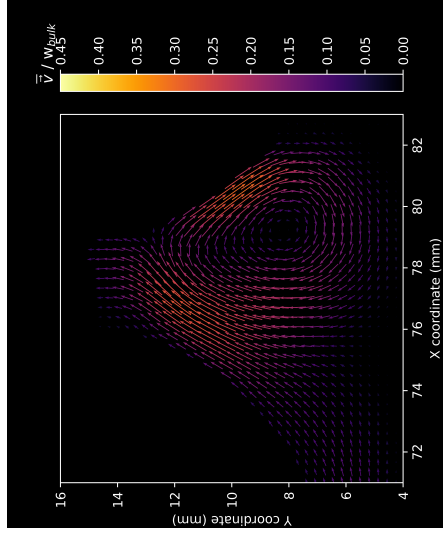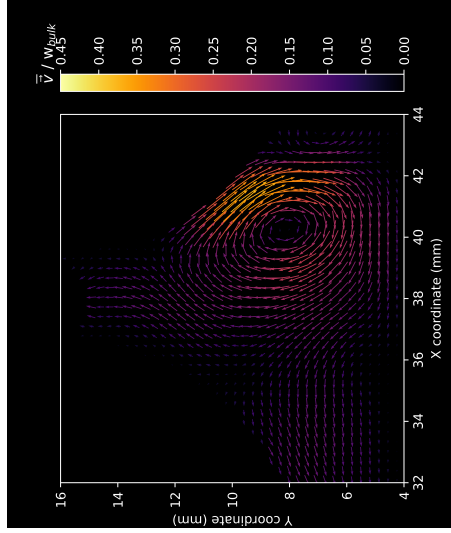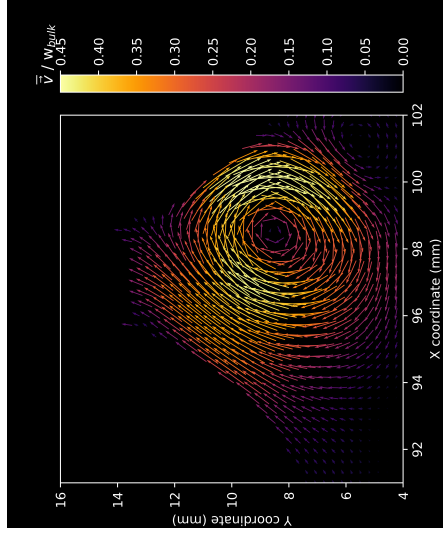
Figure 5.46: 50% sample density of the ensemble-averaged vector fields of each exterior subchannel near the hexagonal duct wall
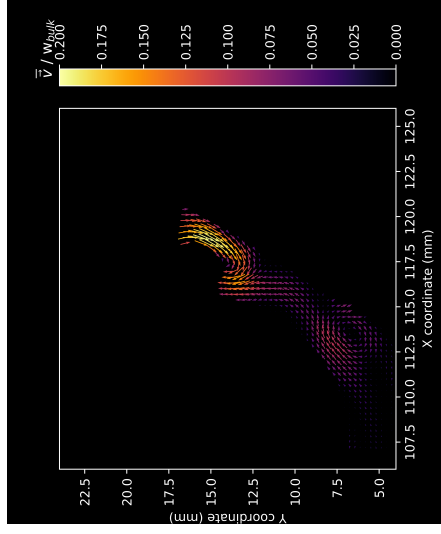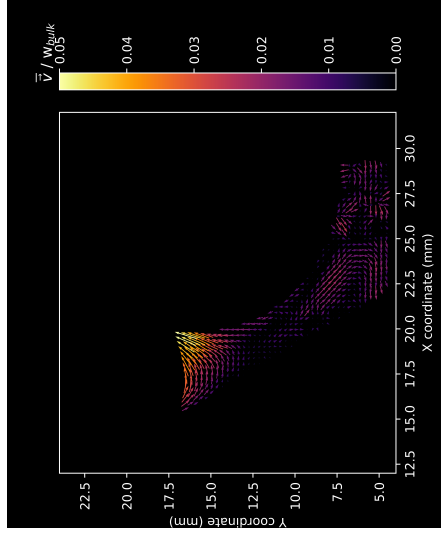
(a) Corner left

(b) Corner right
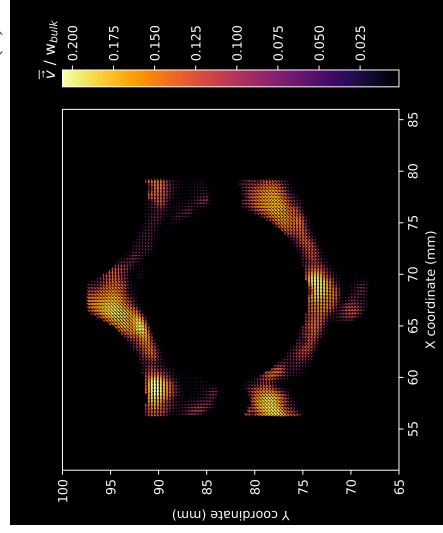
(c) Central pin

Figure 5.47: 50% sample density of the ensemble-averaged vector fields of the corner subchannel near the hexagonal duct wall and central subchannel around the central pin.

5.2.2 SPIV Transverse Plane 2(2D3C)

SPIV Transverse Plane 2 is another measurement plane perpendicular to the axial flow using 2D3C SPIV. The 2D3C SPIV technique does not require a top-down viewpoint normal to the fuel bundle cross section. Instead, it utilized the configuration of Figure 5.48. The measurement region FOV is smaller than Transverse Plane 1, but capturing the third velocity component provided significantly more information and analytical paths. However, due to imaging hardware limitations, the maximum Re_B achieved with this technique was 6,300. The results of this measurement effort can be found in the works of Nguyen et al. (2018).
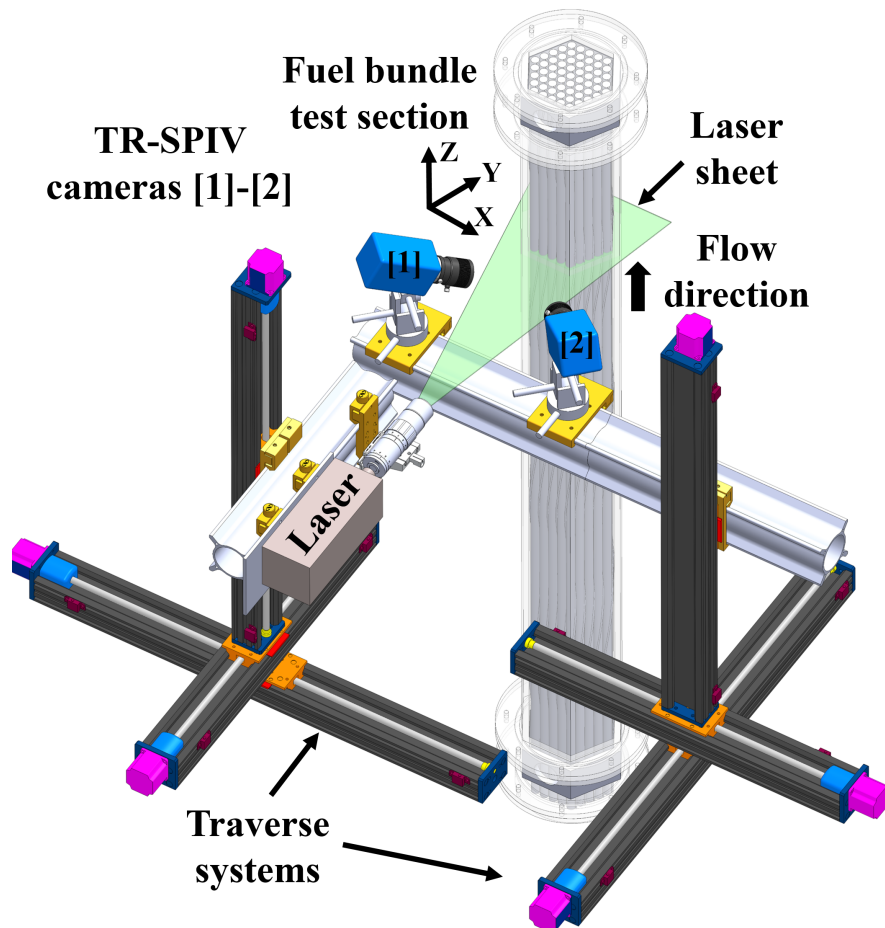
Figure 5.48: Imaging setup for the SPIV 2D3C Transverse Plane 2 measurement containing test section, laser, camera, and traverse systems

6. CONCLUSIONS

The primary objective of this research was to produce experimental velocity field data on a 61-pin wire-wrapped hexagonal fuel bundle such that commercial SFR core design and CFD turbulence model validation may be performed. The primary phenomena of interest are the bulk swirl, local swirl, subchannel mixing, and bypass flow. Flow statistics such as ensemble-averaged velocity, RMS fluctuating velocity, Reynolds stresses, and Z-vorticity were presented. Contours of these statistical quantities were utilized to understand the flow behavior in the corner, exterior, and interior subchannels. Of interest was the flow behavior around the restriction caused by the wire spacer and hexagonal duct wall.

The methodology to meet the primary objective was the utilization of a MIR experimental flow facility with laser-based optical measurement techniques such as 2D2C PIV/PTV and 2D3C SPIV. A total of 9 different measurement locations at various bundle-averaged Reynolds numbers have been investigated to generate a total of 50 unique datasets. The small subset of that data, specifically PIV Vertical Plane 1, PIV Vertical Plane 2, PIV Vertical Plane 6, and PIV Transverse Plane 1 were discussed in this dissertation.

The scientific value of this work is twofold. It benefits the grand effort of CFD turbulence modeling validation by providing new high spatiotemporal resolution experimental data for which benchmark activities may be performed. It also furthers the research and development of LMFBR core thermal hydraulics to progress the U.S DOE's advanced reactor development agenda.

REFERENCES

Adrian, R. J. (1991). Particle-imaging techniques for experimental fluid mechanics, *Annual review of fluid mechanics* **23**(1): 261–304.

Arce, A., Marchiaro, A. and Soto, A. (2004). Liquid–liquid equilibria of linalool+ ethanol+ water, water+ ethanol+ limonene, and limonene+ linalool+ water systems, *Journal of solution chemistry* **33**(5): 561–569.

Bardet, P. M., Fu, C. D., Sickel, C. E. and Weichselbaum, N. A. (2014). Refractive index and solubility control of para-cymene solutions, *2014 International Symposium on Applications of Laser Techniques to Fluid Mechanics, Instituto Superior Tecnico, Lisbon, Portugal*.

Bradski, G. (2000). The OpenCV Library, *Dr. Dobb's Journal of Software Tools* .

Brady, M. R., Raben, S. G. and Vlachos, P. P. (2009). Methods for digital particle image sizing (DPIS): comparisons and improvements, *Flow Measurement and Instrumentation* **20**(6): 207–219.

Brockmeyer, L., Carasik, L. B., Merzari, E. and Hassan, Y. (2017). Numerical simulations for determination of minimum representative bundle size in wire wrapped tube bundles, *Nuclear Engineering and Design* **322**: 577–590.

Campagnole dos Santos, A. A., Childs, M., Nguyen, D. and Hassan, Y. (2018). Matched refractive index rod bundle and space grid testing facility.

Cardwell, N. D., Vlachos, P. P. and Thole, K. A. (2011). A multi-parametric particle-pairing algorithm for particle tracking in single and multiphase flows, *Measurement Science and Technology* **22**(10): 105406.

Chang, Y.-I. (2007). Technical rationale for metal fuel in fast reactors, *Nuclear Engineering and Technology* **39**(3): 161–170.

Cheng, S.-K. and Todreas, N. E. (1986). Hydrodynamic models and correlations for bare and wire-wrapped hexagonal rod bundles—bundle friction factors, subchannel friction factors

and mixing parameters, *Nuclear engineering and design* **92**(2): 227–251.

Collingham, R., Thorne, W. and McCormack, J. (1973). Coolant mixing in a fuel pin assembly utilizing helical wire wrap spacers, *Nuclear Engineering and Design* **24**(3): 393–409.

Dynamics, D. (2018). Measurement principles of PIV, *Technical report*, Dantec Dynamics.

Eckstein, A. and Vlachos, P. (2007). A robust phase correlation dpiv processing algorithm for time resolved measurements, *Proceedings of the Seventh International PIV Symposium*.

Eckstein, A. and Vlachos, P. P. (2009a). Assessment of advanced windowing techniques for digital particle image velocimetry (dpiv), *Measurement Science and Technology* **20**(7): 075402.

Eckstein, A. and Vlachos, P. P. (2009b). Digital particle image velocimetry (dpiv) robust phase correlation, *Measurement Science and Technology* **20**(5): 055401.

EdmundOptics (2018). Introduction to cylinder lenses, *Technical report*, Edmund Optics Inc.

Einstein, A. (1916). The foundation of the general theory of relativity, *Annalen Phys.* **14**: 769–822.

Falchi, M. and Romano, G. P. (2009). Evaluation of the performance of high-speed PIV compared to standard PIV in a turbulent jet, *Experiments in Fluids* **47**(3): 509–526.

Goth, N. (2017). *Design and PIV measurements on a wire-wrapped 61-rod hexagonal fuel assembly experimental facility*, Master's thesis, Texas A&M University.

Goth, N., Jones, P., Nguyen, D., Vaghetto, R., Hassan, Y., Obabko, A., Merzari, E. and Fischer, P. (2018). Comparison of experimental and simulation results on interior subchannels of a 61-pin wire-wrapped hexagonal fuel bundle, *Nuclear Engineering and Design* **338**: 130–136.

Goth, N., Jones, P., Nguyen, T. D., Vaghetto, R., Hassan, Y., Salpeter, N. and Merzari, E. (2018). Ptv/piv measurements of turbulent flows in interior subchannels of a 61-pin wire-wrapped hexagonal fuel bundle, *International Journal of Heat and Fluid Flow* **71**: 295–304.

Grant, I. (1994). *Selected papers on particle image velocimetry*, Vol. 99, Society of Photo Optical.

Hassan, Y. A. and Dominguez-Ontiveros, E. (2008). Flow visualization in a pebble bed reactor experiment using piv and refractive index matching techniques, *Nuclear Engineering and Design* **238**(11): 3080–3085.

Keane, R. D. and Adrian, R. J. (1992). Theory of cross-correlation analysis of piv images, *Applied scientific research* **49**(3): 191–215.

Kerhervé, F. and Fitzpatrick, J. (2011). Measurement and analysis of the turbulent length scales in jet flows, *Experiments in Fluids* **50**(3): 637–651.

Kim, T., Grandy, C., Natesan, K., Sienicki, J. and Hill, R. (2017). Research and development roadmaps for liquid metal cooled fast reactors, *Technical report*, Argonne National Lab.(ANL), Argonne, IL (United States).

Lorenz, J. and Ginberg, T. (1977). Coolant mixing and subchannel velocities in an LMFBR fuel assembly, *Nuclear Engineering and Design* **40**(2): 315–326.

Lourenco, L., Krothapalli, A. and Smith, C. (1989). Particle image velocimetry, *Advances in fluid mechanics measurements*, Springer, pp. 127–199.

McCreery, G. E., McIlroy, H. M., Hamman, K. D. and Zhang, H. (2008). Design of wire-wrapped rod bundle matched index-of-refraction experiments, *16th International Conference on Nuclear Engineering*, American Society of Mechanical Engineers, pp. 595–605.

Nguyen, T., Goth, N., Jones, P., Lee, S., Vaghetto, R. and Hassan, Y. (2017). PIV measurements of turbulent flows in a 61-pin wire-wrapped hexagonal fuel bundle, *International Journal of Heat and Fluid Flow* **65**: 47–59.

Nguyen, T., Goth, N., Jones, P., Vaghetto, R. and Hassan, Y. (2018). Stereoscopic piv measurements of near-wall flow in a tightly packed rod bundle with wire spacers, *Experimental Thermal and Fluid Science* **92**: 420–435.

Nishimura, M., Sato, H., Kamide, H., Ohshima, H., Nagasawa, K. and Imai, Y. (2012). Investigation on velocity distribution around the wrapping wire in an inner subchannel

of fuel pin bundle, *2012 20th International Conference on Nuclear Engineering and the ASME 2012 Power Conference*, American Society of Mechanical Engineers, pp. 299–308.

OECD-NEA (2008). Nuclear energy outlook, *Technical Report ISBN 978-92-64-05410-3*, OECD-NEA.

OECD-NEA (2010). Uranium 2009: Resources, production, and demand, *Technical Report NEA 6891*, OECD NEA and IAEA.

OptoEngineering (n.d.). Tc1mhr-tc4mhr series bi-telecentric lens, *Technical report*, Opto-Engineering.

Planchon, H., Sackett, J., Golden, G. and Sevy, R. (1987). Implications of the ebr-ii inherent safety demonstration test, *Nuclear Engineering and Design* **101**(1): 75–90.

Raffel, M., Willert, C. E., Kompenhans, J. et al. (2007). *Particle image velocimetry: a practical guide*, Springer Science & Business Media.

Ranjan, R., Pantano, C. and Fischer, P. (2011). Direct simulation of turbulent heat transfer in swept flow over a wire in a channel, *International Journal of Heat and Mass Transfer* **54**(21): 4636–4654.

Reckley, W. (2012). Draft report assessment of the adequacy of metallic fuel qualification to support the licensing of small modular sodium-cooled fast spectrum reactors, *Technical report*, Nuclear Regulatory Commission.

Reynolds, O. (1884). On the two manners of motion of water, *Proc. R. Instn Gt Brit*, Vol. 11, pp. 44–52.

Sabharwall, P., Skifton, R., Stoots, C., Kim, E. S. and Conder, T. (2013). Piv uncertainty methodologies for cfd code validation at the mir facility, *Technical report*, Idaho National Lab.(INL), Idaho Falls, ID (United States).

Sanchez, R. (2011). Doe g 413.3-4a chg 1, technology readiness assessment guide, *Technical report*, U.S. Department of Energy.

Sato, H., Kobayashi, J., Miyakoshi, H. and Kamide, H. (2008). Study on velocity field in a deformed fuel pin bundle: Influence of pin deformation and wrapping wire on velocity

distribution, *16th International Conference on Nuclear Engineering*, American Society of Mechanical Engineers, pp. 831–839.

Scarano, F., David, L., Bsibsi, M. and Calluaud, D. (2005). S-piv comparative assessment: image dewarping+ misalignment correction and pinhole+ geometric back projection, *Experiments in fluids* **39**(2): 257–266.

Sciacchitano, A. and Wieneke, B. (2016). Piv uncertainty propagation, *Measurement Science and Technology* **27**(8): 084006.

Soloff, S. M., Adrian, R. J. and Liu, Z.-C. (1997). Distortion compensation for generalized stereoscopic particle image velocimetry, *Measurement science and technology* **8**(12): 1441.

Stokes, G. G. (1851). *On the effect of the internal friction of fluids on the motion of pendulums*, Vol. 9, Pitt Press Cambridge.

Strydom, G., Petti, D. A. and Gougar, H. D. (2017). Advanced demonstration and test reactor options study, *Technical report*, Idaho National Laboratory (INL), Idaho Falls, ID (United States).

Temam, R. (2001). *Navier-Stokes equations: theory and numerical analysis*, Vol. 343, American Mathematical Soc.

ThorLabs (2018). Bi-telecentric lenses for machine vision tutorial, *Technical report*, Thor-Labs.

Tropea, C. and Yarin, A. L. (2007). *Springer handbook of experimental fluid mechanics*, Vol. 1, Springer Science & Business Media.

Waltar, A., Todd, D. and Tsvetkov, P. (2011). *Fast Spectrum Reactors*, Vol. 1, Springer.

Westerweel, J. (1993). *Digital particle image velocimetry: theory and application*, PhD thesis, TU Delft, Delft University of Technology.

Westerweel, J. (1994). Efficient detection of spurious vectors in particle image velocimetry data, *Experiments in Fluids* **16**(3): 236–247.

Westerweel, J., Dabiri, D. and Gharib, M. (1997). The effect of a discrete window offset on

the accuracy of cross-correlation analysis of digital piv recordings, *Experiments in fluids* **23**(1): 20–28.

Westerweel, J. and Scarano, F. (2005). Universal outlier detection for piv data, *Experiments in fluids* **39**(6): 1096–1100.

Willert, C. (1997). Stereoscopic digital particle image velocimetry for application in wind tunnel flows, *Measurement science and technology* **8**(12): 1465.

Willert, C. E. and Gharib, M. (1991). Digital particle image velocimetry, *Experiments in fluids* **10**(4): 181–193.

Woodhams, F. (1980). The laser doppler technique, *Journal of Modern Optics* **27**(11): 1501–1501.

Works, C. (1987). Pyrex glass code 7740 - material properties, *Technical report*, Corning Glass WOrks.

APPENDIX A

EXPERIMENTAL TEST MATRIX

Table A.1 contains the job name, date, temperature, and flow conditions of all MIR experiments performs as part of this dissertation.

Table A.1: Experimental test matrix containing all vertical and transverse measurements performed as of December 2018.

Location	Job	Date	Temp ($^\circ$C)	Flowrate (H$_2$O) (Lmin^{-1})	Flowrate (PCY) (Lmin^{-1})	Reynolds Number	Bulk Velocity (ms^{-1})	Camera Freq (Hz)	Camera Exposure (μs)
Exterior1 (PIV)	PCM1	040916	N/A	189.3	N/A	N/A	N/A	500	500
	PCM2	041216	20.8	189.3	204.8	3400	0.428	500	500
	PCM4	041516	N/A	567.8	N/A	N/A	N/A	1600	400
	PCM11	062716	21.7	567.8	618.5	10414	1.292	1600	200
	PCM11	062716	22.3	681.4	735.1	12373	1.536	1900	200
	PCM11	062716	22.8	832.8	898.7	15131	1.877	2200	200
	PCM11	062716	23.2	946.4	1024.3	17437	2.140	2500	200
	PCM11	062716	23.7	1059.9	1136.0	19574	2.373	2800	200
	PCM13	062916	24.7	681.4	735.9	12826	1.54	1900	400
	PCM13	062916	24.3	1059.9	1133.4	19764	2.368	2800	150
	PCM14	080216	22.0	1059.9	1139.0	19180	2.380	2800	100
Exterior2 (SPIV)	N/A	112316	20.5	196.8	214.3	3528	0.448	800	N/A
	N/A	112316	20.6	378.5	412.2	6866	0.861	1200	N/A
	N/A	112816	21.1	189.3	204.0	3395	0.426	800	1000

Continued on next page

Table A.1 – Continued

Location	Job	Date	Temp (°C)	Flowrate (H$_2$O) (Lmin^{-1})	Flowrate (PCY) (Lmin^{-1})	Reynolds Number	Bulk Velocity (ms^{-1})	Camera Freq (Hz)	Camera Exposure (μs)
	N/A	112816	21.3	378.5	413.0	6875	0.863	1200	600
	N/A	112916	21.2	567.8	618.9	10300	1.293	1600	600
	N/A	112916	21.7	757.1	820.7	13818	1.714	2000	490
	N/A	112916	22.4	1059.9	1140.2	19422	2.38	2800	300
Exterior3 (SPIV)	N/A	113016	21.5	196.8	214.3	3609	0.448	800	800
	N/A	113016	22.0	378.5	411.9	6934	0.860	1200	600
	N/A	113016	22.2	567.8	618.5	10413	1.292	1600	400
	N/A	113016	22.6	757.1	821.4	13991	1.716	2000	300
	N/A	113016	23.1	1059.9	1140.9	19423	2.38	2800	200
Interior1 (PTV)	PCM2	041216	N/A	189.3	N/A	N/A	N/A	500	500
	PCM4	041516	20.9	567.8	618.5	10298	1.292	1600	400
	PCM14	080216	22.3	1059.9	1140.5	19195	2.383	2800	250
Interior2 (PTV)	PCM3	041416	N/A	189.3	N/A	N/A	N/A	600	500
	PCM4	041516	21.1	567.8	620.1	10323	1.295	1600	400
	PCM14	080216	22.7	1059.9	1140.2	19421	2.382	2800	250
Interior3 (PTV)	PCM3	041416	N/A	189.3	N/A	N/A	N/A	600	500
	PCM4	041516	21.3	567.8	618.9	10319	1.293	1600	400
	PCM15	080316	20.5	1059.9	1142.4	19030	2.387	2800	250
Center1 (PTV)	PCM4	041516	21.3	189.3	205.9	3429	0.430	600	500
	PCM4	041516	21.5	567.8	618.2	10411	1.291	1600	400
	PCM13	062916	22.2	567.8	619.3	10425	1.294	1600	400
	PCM13	062916	22.3	681.4	734.7	12341	1.534	1900	350
	PCM13	062916	22.8	832.8	900.9	16348	1.882	2200	250
	PCM13	062916	23.1	946.4	1022.4	17417	2.136	2500	200

Continued on next page

Table A.1 – Continued

Location	Job	Date	Temp (°C)	Flowrate (H₂O) (Lmin⁻¹)	Flowrate (PCY) (Lmin⁻¹)	Reynolds Number	Bulk Velocity (ms⁻¹)	Camera Freq (Hz)	Camera Exposure (μs)
	PCM13	062916	23.6	1059.9	1136.0	19575	2.373	2800	200
	PCM15	080316	20.2	1059.9	1142.4	18808	2.387	2800	250
Center2 (PIV)	PCM5	041816	20.8	189.3	204.8	3408	0.428	600	600
	PCM5	041816	21.5	567.8	618.2	10411	1.291	1600	500
	PCM16	080416	20.6	681.4	741.9	12357	1.550	1900	350
	PCM16	080416	20.5	832.8	903.2	15041	1.886	2200	350
	PCM16	080416	20.1	1059.9	1142.8	18815	2.387	2800	200
Transverse ROI (PIV)	PCM-23	041318	19.3	844.1	837.7	13498	1.739	6	N/A

APPENDIX B

EXTERIOR SUBCHANNEL TEST SUMMARY

This appendix summarizes the conditions of the experimental test PCM-11-E, and provides instructions for reading the associated pressure and velocity data produced by the experimental test. This test summary was produced as part of the work under Project DE-NE0008321.

TECHNICAL DOCUMENT COVER PAGE

Document No:	TAMU-WW-TEST-PCM-11-E	Revision: Rev.2.0	Page 1 of 22
Doc Title: TAMU Wire-Wrapped Test Summary of Test PCM-11 at the Exterior Subchannel			
Projects No:	DE-NE0008321		
Project Name:	Toward a Longer Life Core: Thermal-Hydraulic CFD Simulations and Experimental Investigation of Deformed Fuel Assemblies		
Document Purpose/Summary: This document summarizes the conditions of the experimental test PCM-11-E, and provides instructions for reading the associated pressure and velocity data produced by the experimental test. Total Page Count: 22 pages.			

Document No:	TAMU-WW-TEST-PCM-11-E		Revision: Rev.2.0	Page 2 of 22

TAMU Prepared By:	Nolan Goth		
	Printed/Typed Name	Signature	Date
	Philip Jones		
	Printed/Typed Name	Signature	Date
TAMU Reviewed By:	Thien Nguyen		
	Printed/Typed Name	Signature	Date
	Rodolfo Vaghetto		
	Printed/Typed Name	Signature	Date
Approved By:			
	Printed/Typed Name	Signature	Date

REVISION HISTORY LOG

Document Number: TAMU-WW-TEST-PCM-11-E   Revision: Rev.2.0

Document Title: TAMU Wire-Wrapped Test Summary of Test PCM-11 at the Exterior Subchannel

REVISION	DATE	DESCRIPTION
Draft	10/04/16	Initial draft for review.
Rev.1	11/02/2016	Comments from TerraPower incorporated
Rev.1.1	11/21/2016	Included discussion on PIV error estimation and calibration (Appendix III)
Rev.2.0	12/12/2016	Changed reference coordinate system (Section 2.3) and updated file naming (Section 3.1)

Table of Contents

Acronyms and Definitions

Acronym	Definition
TAMU	The Texas A&M University
CAD	computer-aided-design
CFD	computational fluid dynamics
DP	differential pressure
FS	full scale
FTF	flat-to-flat
GPM	gallon per minute
PIV	particle image velocimetry
RMS	root-mean-square
RTD	resistance thermometer detector
VFD	variable frequency drive

1.0   INTRODUCTION AND SCOPE

This test summary provides information about the experimental setup, boundary conditions, and data sets for the experimental test PCM-11 performed on June 27, 2016. The experimental setup describes the data acquisition, temperature, flow rate, pressure, and imaging hardware utilized to collect data. The boundary conditions are the fluid temperature, centrifugal pump rotational frequency, and volumetric flow rate during the experimental test. The data sets contain the instantaneous and time-averaged flow rate, pressure (axial and azimuthal), and velocity measurements, along with the particle image velocimetry (PIV) statistical analysis.

2.0   TEST DESCRIPTION

An isothermal experimental flow test was conducted utilizing the 61-pin Hexagonal Wire-Wrapped Flow Facility. The test was performed to generate high spatial and temporal resolution data sets of the velocity in a vertical plane and wall pressures through the fuel bundle. The working fluid in the experimental test was p-Cymene. The bundle utilized in this test was the Second Non-Deformed Bundle, with geometric parameters defined in [1]. The measurement process was repeated three times, generating three sets of data. Each set contains time-synchronized PIV and gauge pressure measurements, along with a unique set differential pressure measurements that were not time-synchronized. Both of the PIV and gauge pressure measurements can be averaged over all three sets. The differential pressure measurements in each set correspond to a unique lineup as described in Section 3.3. The measurement length and frequency of each set is provided in section 3.0.

2.1   Experimental Setup

The experimental facility contains two loops. Figure 1 displays a computer-aided design (CAD) model of the experimental facility. The primary loop performs the experimental function. The primary loop includes the following components:

- The hexagonal test section containing the 61-pin wire-wrapped experimental fuel bundle
- The primary tank is used as storage between experiments and as an inline surge volume. The primary pump and associated variable frequency drive (VFD) to control the flow rate in the test section
- An inline turbine flow meter
- A resistance temperature detector (RTD)
- Nine pressure transducers and two differential pressure transducers

The secondary loop performs volume control, temperature control, and filtration. The secondary loop contains the following components:

- The secondary tank
- The secondary pump and associated VFD

129

- A heat exchanger supplied with chilled water to control the primary loop temperature
- A filtration system

 The test section can be divided into three distinct sections can be identified in the test bundle:

- The lower (inlet) plenum located at the bottom of the bundle
- The central section (test section) where the flow measurements will be conducted
- The upper (outlet) plenum located at the top of the bundle.

Figure 1. CAD rendering of the experimental facility

2.1.1   Data Acquisition Hardware

The data acquisition hardware consisted of equipment manufactured by National Instruments. The chassis used was a 4-slot model SCXI-1000. The input cards were 32-channel analog input modules, with model numbers of SCXI-1100 and SCXI-1102.

2.1.2   Temperature Hardware

An RDF Corporation resistance temperature device (RTD) was utilized to measure the temperature of the p-Cymene during the experiment. The accuracy of the device is ±0.3°C at 0°C with an operating range of -196 °C to 480°C.

2.1.3   Flow Rate Hardware
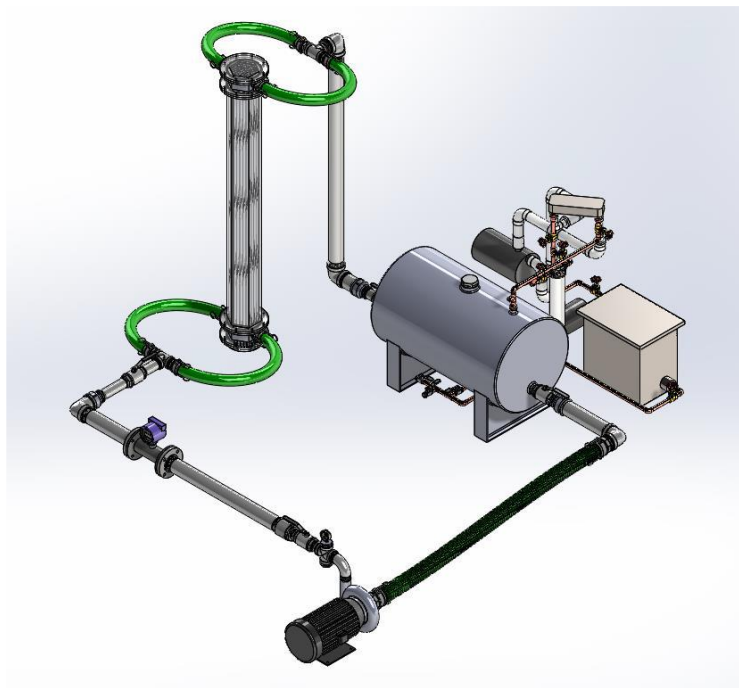
A Sponsler in-line precision turbine flowmeter was utilized to measure the volumetric flow rate of the working fluid. The Sponsler flowmeter used was a SP3-MB-PHL-D-4X. The uncertainty of the flowmeter analog output is 0.025% of full scale at 20 °C. The full scale reading is 600 gallons per minute (GPM). A Sponsler IT400 totalizer recorded the analog output from the flowmeter with a digital uncertainty of ±1 GPM.

2.1.4   Pressure Hardware

High accuracy pressure transducers were utilized to measure the wall pressure on Face F at various axial locations. Specifications can be found in Table 1.

Table 1. Pressure hardware used in the experimental test

Position In Facility	Model Number	Device Description	Accuracy
0F	PX309-030G5V	30 psi Gauge Pressure	< 4% FS
1F	PX309-030G5V	30 psi Gauge Pressure	< 4% FS
2F	PX419-030G5V	30 psi Gauge Pressure	< 0.1% FS
3F	PX419-030G5V	30 psi Gauge Pressure	< 0.1% FS
4F	PX419-030G5V	30 psi Gauge Pressure	< 0.1% FS
5F	MMG015V5P1D0T4A6CEPS	15 psi Gauge Pressure	<0.1% F.S
6F	PX419-030G5V	30 psi Gauge Pressure	< 0.1% FS
7F	MMG015V5P1D0T4A6CEPS	15 psi Gauge Pressure	<0.1% F.S
8A	PX309-015G5V	15 psi Gauge Pressure	< 1% FS
5 D/E/F/A	P55D-4-N-20-S-5-A	5 inch H_2O Differential Pressure	< 4.28% FS
6 D/E/F/A	MMDWB10WBIV5P2D0T2A2CE	10 inch H_2O Differential Pressure	< 0.1% FS

2.1.5   Imaging Hardware

The PIV system consisted of a 10 W continuous laser at a wavelength of 527 nm and two digital CMOS Phantom M310 cameras. The laser beam was adjusted by beam combination optics to form a 1.5 mm thick laser sheet for the PIV measurements. The laser position was adjusted with three motorized linear

translation stages. The high-speed Phantom M310 cameras have a full resolution of 1280 x 800 pixels, a pixel size of 20×20 μm^2 and 12-bit depth image capturing. Seeding particles were silver-coated hollow glass spheres with a mean diameter of 16 μm and a density of 1.6 g cm^{-3}.

2.2   Pressure Measurement Location

The locations of the pressure measurements are defined in [1].

2.3   Velocity Measurement Location

The location of velocity measurements was in the set of exterior subchannels near the wall of Face F, Figure 2. The vertical laser sheet used to illuminate particles for the PIV measurements is represented by the green line (a) (data will be on the plane x-y). The PIV measurement window for each camera is represented by the green rectangles (b). An X-Y coordinate system was assigned to represent horizontal and vertical directions in the laser sheet. The origin of the X-Y coordinate system is shown in Figure 2. The origin is selected as follow:

- $x = 0$ at the midpoint of face F (inner side)
- $y = 0$ at centerline of PT#5 (corresponding to the axial location of 2.25 pitches, as defined in [1, 2])
- $z = 0$ at face F (inner side)

The positive direction of each axis is also shown in Figure 2.

The minimum and maximum X-Y coordinates of the visualization region are X_{min} = -35.50 mm, X_{max} = 40.35 mm, Y_{min} = 107.70 mm, and Y_{max} = 229.18 mm. The x-y plane is located at a z = -1.88 mm.
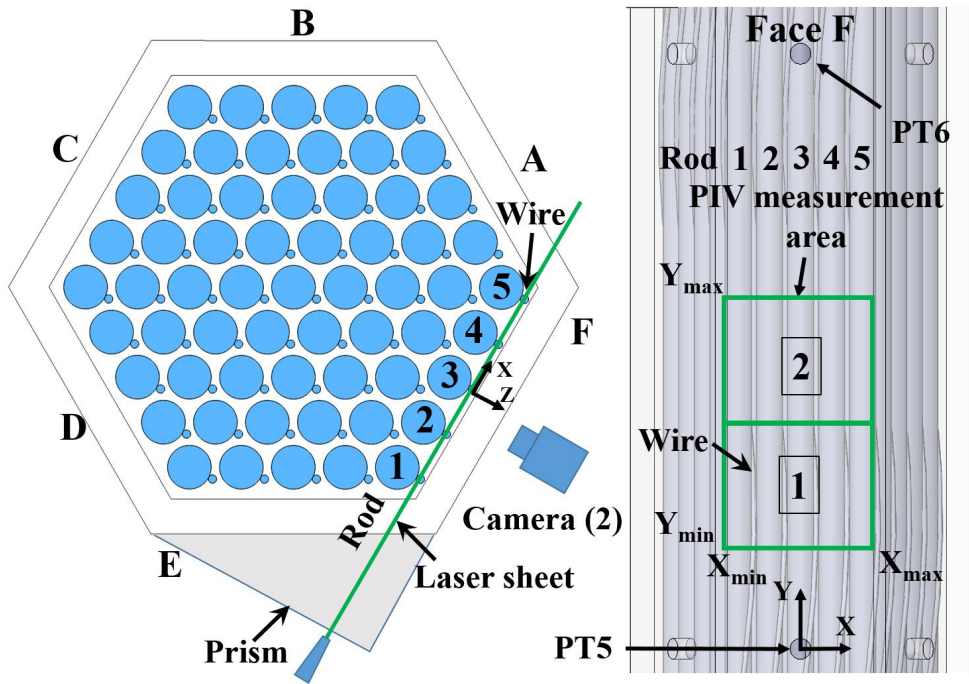
Figure 2. (a) Top view of the fuel bundle denoting the laser and camera positions. (b) Side view of the PIV measurement windows for Camera 1 and 2.

2.3.1   Laser Alignment

A three-dimensional traversing system was utilized to perform fine spatial adjustments of the laser sheet within the test section. The laser alignment process started by adjusting the base of the laser until the laser sheet was parallel with the inner surface of the wall forming Face F. A parallel orientation was confirmed by visual inspection. The relative intensity of the laser sheet in the two corners of Face F was monitored until equal. Next, the laser sheet was laterally traversed until it intersected the exterior row of rods. Again, by visual inspection, the laser sheet was confirmed to simultaneous intersect each rod in

the plane parallel to face F. The laser sheet had a thickness of 1.5 mm ±0.5mm[1]. The distance of the laser sheet from the tangent to the exterior rods was 1.88 mm ±0.5mm[2].

2.4   Boundary Conditions

This section describes the environmental conditions that existed during the experimental test. The quantities of interest were the fluid temperature, the pump frequency, the volumetric flow rate, and the Reynolds number.

2.4.1   Temperature

The temperature was monitored near the pump outlet using a resistance thermometer detector (RTD). The RTD had an uncertainty of ± 0.3 °C. Table 2 contains the temperature of the working fluid measured at the beginning of each data set.

Table 2. Working fluid temperature measured at the beginning of each run

	Fluid Temp (°C)
Set 1	23.3 ± 0.3
Set 2	23.7 ± 0.3
Set 3	24.2 ± 0.3

2.4.2   Pump

The centrifugal pump driving the working fluid was operated at a frequency of 51.5 Hz for all three data sets. The frequency was controlled by a variable frequency drive (VFD)

2.4.3   Volumetric Flow Rate

The average volumetric flow rate for the three sets recorded by the flowmeter for each data set is presented in Table 3. This average is the arithmetic average of the data points recorded during each set. More information is provided in Appendix I.

---

[1] The thickness of the laser sheet was estimated by measuring the thickness of the projected laser sheet on a flat surface using a ruler of 0.5 mm precision.
[2] Error in the laser sheet location is based on the precision of the ruler used to identify the laser sheet position on the traversing system

Table 3. Averaged volumetric flow rate of each run

	Flow Rate (gal min-1)
Set 1	300.06 ± 1.3
Set 2	300.15 ± 1.3
Set 3	300.37 ± 1.3

2.4.4   Reynolds Number

The bundle-averaged Reynolds number for each set was calculated and shown in Table 4. The bundle-averaged Reynolds number was calculated based on the bulk velocity, along with the as-built bundle hydraulic diameter. The pin diameter, wire diameter, and flat-to-flat dimensions used in the hydraulic diameter calculation are the average values from the 61-rod, 61-wire, and 3 enclosure FTF characterizations provided in [1]. The bulk velocity was defined by the averaged volumetric flow rate. Appendix II shows the equations used to calculate the as-built flow area, hydraulic diameter, and wetted perimeter.

The bundle averaged Re number was calculated from Equation 1. Temperature-dependent density and viscosity values of the fluid were linearly interpolated based on the measured temperature of each set, Section 2.4.1 [3]. These values are presented in Table 4.

$$Re = \frac{\rho U_m D_H}{\mu} \tag{1}$$

Table 4. Bundle-averaged Reynolds number

	Fluid Temperature (°C)	Density (kg m-3)	Bulk Velocity (m s-1)	Hydraulic Diameter (m)	Dynamic Viscosity (Pa sec)	Reynolds Number
Set 1	23.3	854.58	2.358	7.728 E-3	8.094 E-4	19,239
Set 2	23.7	854.18	2.359	7.728 E-3	8.040 E-4	19,362
Set 3	24.2	853.86	2.360	7.728 E-3	7.999 E-4	19,471

3.0   DATA SETS

This section provides information on the contents of the data files and instruction on how to read them. Three data sets were generated for this experimental test. Each set contains associated flow rate, pressure, and velocity files. Further description of each subset is provided in Sections 3.2, 3.3, and 3.4, respectively. A list of electronic attachments is included in Section 3.1

Table 5 defines the measurement duration and sampling frequency of each measurement in the following data sets.

Table 5. Measurement duration and sampling frequency for each data set

	PIV		Gauge Pressure		Differential Pressure	
	Measurement Duration (sec)	Sampling Frequency (Hz)	Measurement Duration (sec)	Sampling Frequency (Hz)	Measurement Duration (sec)	Sampling Frequency (Hz)
Set1 F-E	~ 3	2800	5.36	2800	9.90	1000
Set2 F-D	~ 3	2800	5.99	2800	10	1000
Set3 F-A	~ 3	2800	4.67	2800	10	1000

3.1   List of Electronic Attachments

The following files are submitted as electronic attachments. The files are archived into a .zip file named REV2-TAMU-WW-TEST-PCM-11-E-DATA.zip. The file is uploaded into the TerraPower ftp server under the folder *DOE Grant 1163/TAMU/PCM-11-E.*

The file contains the following data (time stamp is reported next to the file name).

Volumetric Flow Rate Data

REV2-TAMU-WW-TEST-PCM-11-E-FLOWRATE-SET1.csv 12/12/2016 10:05AM

REV2-TAMU-WW-TEST-PCM-11-E-FLOWRATE-SET2.csv 12/12/2016 10:06AM

REV2-TAMU-WW-TEST-PCM-11-E-FLOWRATE-SET3.csv 12/12/2016 10:07AM

REV2-TAMU-WW-TEST-PCM-11-E-FLOWRATE-AVERAGE.csv   12/12/2016 10:04AM

Pressure Data

REV2-TAMU-WW-TEST-PCM-11-E-PRESSURE-SET1-F-E.csv 11/21/2016 2:15PM

REV2-TAMU-WW-TEST-PCM-11-E-PRESSURE-SET2-F-D.csv 11/21/2016 2:16PM

REV2-TAMU-WW-TEST-PCM-11-E-PRESSURE-SET3-F-A.csv   11/21/2016 2:14PM

REV2-TAMU-WW-TEST-PCM-11-E-PRESSURE-AVERAGE.csv   12/12/2016 9:44AM

<u>Velocity (PIV) Data</u>

REV2-TAMU-WW-TEST-PCM-11-E_Inst_Vel-SET1.zip (all files with time stamp 12/07/2016 5:16PM to 10:39PM)

REV2-TAMU-WW-TEST-PCM-11-E_Vel_Stats_Mean-SET1.dat 12/11/2016 2:59PM

REV2-TAMU-WW-TEST-PCM-11-E_Vel_Stats_RMS-SET1.dat 12/11/2016 2:59PM

REV2-TAMU-WW-TEST-PCM-11-E_Vel_Stats_UV-SET1.dat 12/11/2016 2:59PM

REV2-TAMU-WW-TEST-PCM-11-E_Inst_Vel-SET2.zip (all files with time stamp 12/07/2016 5:17PM to 10:42PM)

REV2-TAMU-WW-TEST-PCM-11-E_Vel_Stats_Mean-SET2.dat 12/11/2016 3:46PM

REV2-TAMU-WW-TEST-PCM-11-E_Vel_Stats_RMS-SET2.dat 12/11/2016 3:46PM

REV2-TAMU-WW-TEST-PCM-11-E_Vel_Stats_UV-SET2.dat 12/11/2016 3:46PM

REV2-TAMU-WW-TEST-PCM-11-E_Inst_Vel-SET3.zip (all files with time stamp 12/07/2016 5:18PM to 10:44PM)

REV2-TAMU-WW-TEST-PCM-11-E_Vel_Stats_Mean-SET3.dat 12/11/2016 3:49PM

REV2-TAMU-WW-TEST-PCM-11-E_Vel_Stats_RMS-SET3.dat 12/11/2016 3:49PM

REV2-TAMU-WW-TEST-PCM-11-E_Vel_Stats_UV-SET3.dat 12/11/2016 3:49PM

REV2-TAMU-WW-TEST-PCM-11-E_Vel_Stats_Mean-combined.dat 12/11/2016 4:00PM

REV2-TAMU-WW-TEST-PCM-11-E_Vel_Stats_RMS-combined.dat 12/11/2016 4:00PM

REV2-TAMU-WW-TEST-PCM-11-E_Vel_Stats_UV-combined.dat 12/11/2016 4:00PM

3.2   Volumetric Flow Rate Data

Three files are provided containing the instantaneous volumetric flow rate for each set:

REV2-TAMU-WW-TEST-PCM-11-E-FLOWRATE-SET1.csv

REV2-TAMU-WW-TEST-PCM-11-E-FLOWRATE-SET2.csv

REV2-TAMU-WW-TEST-PCM-11-E-FLOWRATE-SET3.csv

A summary file is included, which contains the arithmetic average, standard deviation, and k-factor conversion for each set.

REV2-TAMU-WW-TEST-PCM-11-E-FLOWRATE-AVERAGE.xlsx

The summary file contains the calculation to convert the raw flow meter output (working fluid = water) into the actual flow rate (working fluid = p-Cymene). More information on data conversion is provided in Appendix II.

137

3.3   Pressure Data

Three files are provided containing the instantaneous pressures for each set:

REV2-TAMU-WW-TEST-PCM-11-E-PRESSURE-SET1-F-E.csv

REV2-TAMU-WW-TEST-PCM-11-E-PRESSURE-SET2-F-D.csv

REV2-TAMU-WW-TEST-PCM-11-E-PRESSURE-SET3-F-A.csv

Each file contains a unique pair of letters at the end of the filename. This corresponds to the two faces being measured by the azimuthal differential pressure (DP) transducers. Set 1 contains the DP data between faces F and E. Set 2 contains the DP data between faces F and D. Set 3 contains the DP data between faces F and A.

The pressure data from PT0 – PT8 were recorded during the same time interval as the velocity measurements using an electronic pulse to trigger the start of the data acquisition. The DP data was recorded immediately after recording the data from PT0 – PT8.

The signal output from the DP transducers was factory calibrated in inches of water. The provided files contain the raw DP data in inches of water, along with a column containing the conversion into psi using the following conversion factors from [4] in Equation 3.

$$Pressure\ (inch\ water) = \left[\frac{2.4884\times10^2\ Pa}{1\ inch\ water\ at\ 60\ °F}\right]\left[\frac{1\ psi}{6.894757\times10^3\ Pa}\right] \tag{3}$$

A summary file is included, which contains the arithmetic average and standard deviation for each set.

REV2-TAMU-WW-TEST-PCM-11-E-PRESSURE-AVERAGE.xlsx

NOTE: PT5, PT7, and PT8 were off-scale for this test, as the maximum reading of these transducers is 15 psig.

3.4   Velocity (PIV) Data: Instantaneous, Mean, rms, and Reynolds stress.

The velocity data provided represents a two dimensional array, but is presented in a one dimensional vector. The vector field consists of 114 point on x-direction, and 178 points on y-direction. Notes on calibration and error estimation are provided in Appendix III.

All data are stored in .dat format. These files contain multiple columns without headers.

Each set is identified in the file name (SET1, SETE2, SET3). File naming is consistent within the sets. As an example, contain for SET1 is described below:

REV2-TAMU-WW-TEST-PCM-11-E_Inst_Vel-SET1.zip:

This file contains 8308 .dat files of the instantaneous velocity. The structure of each file is described in Table 5.

Table 6. Instantaneous Velocity .dat File Structure

Column #	1	2	3	4	5	6
Parameter	X	Y	Z	u	v	w
Unit	mm	mm	mm	m/s	m/s	m/s

REV2-TAMU-WW-TEST-PCM-11-E_Vel_Stats_Mean-SET1.dat:

This file contains the time-averaged velocity for set 1. The structure of the file is shown in Table 6.

Table 7. Mean Velocity .dat File Structure

Column #	1	2	3	4	5	6
Parameter	X	Y	Z	u	v	w
Unit	mm	mm	mm	m/s	m/s	m/s

REV2-TAMU-WW-TEST-PCM-11-E_Vel_Stats_RMS-SET1.dat:

This file contains the root mean square (rms) fluctuating velocity. The file structure is described in Table 7.

Table 8. rms File Structure

Column #	1	2	3	4	5	6
Parameter	X	Y	Z	u'_rms	v'_rms	w'_rms
Unit	mm	mm	mm	m/s	m/s	m/s

REV2-TAMU-WW-TEST-PCM-11-E_Vel_Stats_UV-SET1.dat

This file contains the Reynold Stress $\overline{u'v'}$. The file structure is described in Table 8.

Table 9. Reynolds Stress File Structure

Column #	1	2	3	4
Parameter	X	Y	Z	$\overline{u'v'}$
Unit	mm	mm	mm	$m^2 \, s^{-2}$

NOTE: in all .dat files, z is constant and equal to the laser sheet location (1.88 mm). The velocity component along the z-direction and all related parameters are 0.

The .dat files marked as "combined" contain the same information and structure of the files described above for set 1. However, the statistical values are computed based on the total number of instantaneous velocities (3 x 8308 = 24924).

139

4.0   REFERENCES

1. TAMU-WW-AS Rev.1, TAMU Wire-Wrapped As-Built Geometry (Non-Deformed Bundle)
2. TWRP-31-TSPEC-0010 Rev. 1 , TAMU Fuel Assembly Flow Visualization Test Specification,
3. P-Cymene Chemical Information Sheet. Cameo Chemicals, Database of Hazard Materials, June 1999.
4. Appendix B.9 Factors for units listed by kind of quantity or field of science, NIST Guide, https://www.nist.gov/pml/nist-guide-si-appendix-b9-factors-units-listed-kind-quantity-or-field-science
5. S.-K. CHENG and N. E. TODREAS, "Hydrodynamic Models and Correlations for Bare and Wire-Wrapped Hexagonal Rod Bundles — Bundle Friction Factors, Subchannel Friction Factors and Mixing Parameters," Nucl. Eng. Des., 92, , 227–251 (1986).

APPENDIX I: TURBINE FLOW METER CALIBRATION FOR P-CYMENE

Since the flow meter was originally calibrated with water as the working fluid, the data presented in the output file is the flow rate of the fluid if it was water. Because the working fluid, p-Cymene, has a different density and viscosity than water, it was required to generate a new calibration of the turbine flow meter with p-Cymene as the working fluid.

This was achieved using an Omega FPT-6130 high accuracy pitot tube with an Omega high accuracy differential pressure transducer. The Omega FPT-6130 high accuracy Pitot tube had an accuracy of < 1% of the volumetric flow rate. Three different Omega differential pressure transducers were utilized, because the range of DP measured by each transducer is small relative to the total span of DP required to fully calibrate the turbine flow meter. Each Omega differential pressure transducer had the following maximum pressure reading, associated accuracy, and flow meter frequency range in which each differential pressure transducer was used, Table 109.

Table 10. Differential pressure transducers utilized in the p-Cymene k-factor calibration

Differential Pressure Transducer	Maximum Pressure (psi)	Accuracy (% Full Scale)	Flow Meter Frequency Range (Hz)
Omega MMDWB10WBIV5P2D0T2A2CE	0.36	< 0.1% FS	0-100
Omega MMDWB001BIV5P2D0T2A2CE	1.0	< 0.1% FS	100-160
Omega MMDWB005BIV5P2D0T2A3CE	5.0	< 0.1% FS	160-300

The rate meter determined the volumetric flow rate by multiplying the turbine rotational frequency by a multiplication factor, the factory calibrated k-factor. A new p-Cymene k-factor was calculated from the pitot flow, turbine meter output, and the factory k-factor. Presented in Figure 3 is a plot of the p-Cymene k-factor as a function of turbine flow meter frequency. The factory calibrated k-factor for water was 43.2411. The p-Cymene volumetric flow rate is calculated by Equation 4.

$$Flow\ Rate_{pcy} = Indicated\ Flow\ Rate\left(\frac{k_{H2O}}{k_{pcy}}\right) \tag{4}$$

141

Figure 3. p-Cymene k-factor plotted versus the turbine flow meter rotational frequency

APPENDIX II: BUNDLE GEOMETRY CALCULATION

From [5], the following expressions describe the variables used in the bundle geometry calculation. The subscripts one, two, and three correspond to the interior, wall, and corner sub channels respectively. P is the rod pitch, D is the pin diameter, D_{wire} is the wire spacer diameter, D_h is the hydraulic diameter, W is the edge pitch, N_i is the number of each sub channel, and H is the wire spacer lead or axial distance required for the spacer to complete one revolution around the pin. D, D_{wire}, and W are from the rod, wire and flat-to-flat characterization performed in [1]. The cosine term takes into account the elliptical projected area of the wire due to it not being parallel to the flow.

Parameter	Value	Unit
N_1	96	n/a
N_2	24	n/a
N_3	6	n/a
P	1.8878 E-2	m
D	1.5880 E-2	m
D_{wire}	3.0000 E-3	m
W	1.9548 E-2	m
$FTF_{enclosure}$	1.5400 E-1	m
FTF_{bundle}	1.5266 E-1	m
A_1	5.1747 E-5	m²
A_2	1.1661 E-4	m²
A_3	4.3637 E-5	m²
A_{Bundle}	8.0281 E-3	m²
$P_{wet,1}$	2.9688 E-2	m
$P_{wet,2}$	4.8564 E-2	m
$P_{wet,3}$	2.3302 E-2	m
$P_{wet,bundle}$	4.1554	m
H	4.7625 E-1	m

$$W = D + G_{wall}$$

$$G_{wall} = FTF_{enclosure} - FTF_{bundle}$$

$$FTF_{bundle} = \frac{8P\sqrt{3}}{2} + D + 2D_{wire}$$

$$A_1 = \left(\frac{\sqrt{3}}{4}\right)P^2 - \frac{\pi D^2}{8} - \frac{\pi D_{wire}^2}{8\cos(\theta)}$$

$$A_2 = \left(W - \frac{D}{2}\right)P - \frac{\pi D^2}{8} - \frac{\pi D_{wire}^2}{8\cos(\theta)}$$

$$A_3 = \frac{\left(W - \frac{D}{2}\right)^2}{\sqrt{3}} - \frac{\pi D^2}{24} - \frac{\pi D_{wire}^2}{24\cos(\theta)}$$

$$A_{Bundle} = N_1 A_1 + N_2 A_2 + N_3 A_3$$

$$P_{wet,1} = \frac{\pi D}{2} + \frac{\pi D_{wire}}{2\cos(\theta)}$$

$$P_{wet,2} = P + \frac{\pi D}{2} + \frac{\pi D_{wire}}{2\cos(\theta)}$$

$$P_{wet,3} = \frac{\pi D}{6} + \frac{2\left(W - \frac{D}{2}\right)}{\sqrt{3}} + \frac{\pi D_{wire}}{6\cos(\theta)}$$

$$P_{wet,Bundle} = N_1 P_{wet,1} + N_2 P_{wet,2} + N_3 P_{wet,3}$$

$$D_h = \frac{4\,A_{Bundle}}{P_{wet,Bundle}}$$

$$\cos(\theta) = \frac{H}{\sqrt{H^2 + \left(\pi(D + D_w)\right)^2}}$$

144

APPENDIX III: NOTES ON PIV SYSTEM CALIBRATION AND ERROR ESTIMATION

The system was calibrated using LaVision ® calibration plates. The methodology adopted followed the guidelines published and described in [A-III-1].

The software used for the PIV imaging post-processing is the PRANA code developed by Virginia Tech. Performance and uncertainty of the PRANA RPC algorithm have been previously accessed (A-III-2, A-III-3, A-III-4, and A-III-5).

The analysis described in this report analysis was limited to estimate the overall uncertainty in the PIV velocity measurements. This was estimated to be approximately 0.1 pixels which yields to an uncertainty of less than 3% of the mean axial velocity.

[A-III-1]. Wieneke, B. "Stereo-PIV using self-calibration on particle images". Experiments in Fluids (2005) 39: 267–280 DOI 10.1007/s00348-005-0962-z

[A-III-2]. Timmins, B. H., Wilson, B. W., Smith, B. L. and Vlachos, P. P. ,"A method for automatic estimation of instantaneous local uncertainty in particle image velocimetry measurements". Experiments in Fluids 53(4): 1133–1147.

[A-III-3]. Wilson, B. M. and Smith, B. L., "Uncertainty on PIV mean and Fluctuating velocity due to Bias and Random Errors", Measurement Science and Technology 24(3): 035302.

[A-III-4]. Charonko, J. J. and Vlachos, P. P.,"Estimation of Uncertainty Bounds for Individual Particle Image Velocimetry Measurements from Cross-Correlation Peak Ratio". Measurement Science and Technology 24(6): 065301.

[A-III-5]. Boomsma, A., Bhattacharya, S., Troolin, D., Pothos, S. and Vlachos, P., "A Comparative Experimental Evaluation of Uncertainty Estimation Methods for Two-Component PIV". Measurement Science and Technology 27(9): 094006.

APPENDIX C

INTERIOR SUBCHANNEL TEST SUMMARY

This appendix summarizes the conditions of the experimental test PCM-14-INT1, and provides instructions for reading the associated flowrate and velocity data produced by the experimental test. This test summary was produced as part of the work under Project DE-NE0008321.
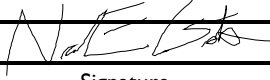
TECHNICAL DOCUMENT COVER PAGE

Document No:	TAMU-WW-TEST-PCM-14-INT1	Revision: Rev.0	Page 1 of 19
Doc Title: TAMU Wire-Wrapped Test Summary of Test PCM-14-INT1 at Interior Subchannel One			
Projects No:	DE-NE0008321		
Project Name:	Toward a Longer Life Core: Thermal-Hydraulic CFD Simulations and Experimental Investigation of Deformed Fuel Assemblies		
Document Purpose/Summary: This document summarizes the conditions of the experimental test PCM-14-INT1, and provides instructions for reading the associated flowrate and velocity data produced by the experimental test. Total Page Count: 19 pages.			

TECHNICAL DOCUMENT COVER PAGE

TAMU Prepared By:	Nolan Goth		
	Printed/Typed Name	Signature	Date
	Philip Jones		
	Printed/Typed Name	Signature	Date
TAMU Reviewed By:	Thien Nguyen		
	Printed/Typed Name	Signature	Date
	Rodolfo Vaghetto		
	Printed/Typed Name	Signature	Date
Approved By:			
	Printed/Typed Name	Signature	Date

REVISION HISTORY LOG

Document Number: TAMU-WW-TEST-PCM-14-INT1   Revision: Rev.0

Document Title: TAMU Wire-Wrapped Test Summary of Test PCM-14-INT1 at Interior Subchannel One

REVISION	DATE	DESCRIPTION
Rev.0	12/19/2016	First release

Table of Contents

Acronyms and Definitions

Acronym	Definition
TAMU	The Texas A&M University
CAD	computer-aided-design
CFD	computational fluid dynamics
DP	differential pressure
FS	full scale
FTF	flat-to-flat
GPM	gallon per minute
PTV	particle tracking velocimetry
RMS	root-mean-square
RTD	resistance thermometer detector
VFD	variable frequency drive

1.0   INTRODUCTION AND SCOPE

This test summary provides information about the experimental setup, boundary conditions, and data sets for the experimental test PCM-14-INT1 performed on August 2nd, 2016. The experimental setup describes the data acquisition, temperature, flow rate, and imaging hardware utilized to collect data. The boundary conditions are the fluid temperature, centrifugal pump rotational frequency, and volumetric flow rate during the experimental test. The data sets contain the instantaneous and time-averaged flow rate, instantaneous velocity measurements, along with the particle tracking velocimetry (PTV) statistical analysis.

2.0   TEST DESCRIPTION

An isothermal experimental flow test was conducted utilizing the 61-pin Hexagonal Wire-Wrapped Flow Facility. The test was performed to generate high spatial and temporal resolution data sets of the velocity in a vertical plane. Pressure measurements were not recorded during this test. The working fluid in the experimental test was p-Cymene. The bundle utilized in this test was the Second Non-Deformed Bundle, with geometric parameters defined in [1]. The measurement process was repeated three times, generating three sets of flowrate and velocity data. The PTV measurements can be averaged over all three sets. The measurement length and frequency of each set is provided in section 3.0.

2.1   Experimental Setup

The experimental facility contains two loops. Figure 1 displays a computer-aided design (CAD) model of the experimental facility. The primary loop performs the experimental function. The primary loop includes the following components:

- The hexagonal test section containing the 61-pin wire-wrapped experimental fuel bundle
- The primary tank is used as storage between experiments and as an inline surge volume. The primary pump and associated variable frequency drive (VFD) to control the flow rate in the test section
- An inline turbine flow meter
- A resistance temperature detector (RTD)
- Nine pressure transducers and two differential pressure transducers

The secondary loop performs volume control, temperature control, and filtration. The secondary loop contains the following components:

- The secondary tank
- The secondary pump and associated VFD
- A heat exchanger supplied with chilled water to control the primary loop temperature
- A filtration system

The test section can be divided into three distinct sections can be identified in the test bundle:

152

- The lower (inlet) plenum located at the bottom of the bundle
- The central section (test section) where the flow measurements will be conducted
- The upper (outlet) plenum located at the top of the bundle.

Figure 1. CAD rendering of the experimental facility

2.1.1 Data Acquisition Hardware

The data acquisition hardware consisted of equipment manufactured by National Instruments. The chassis used was a 4-slot model SCXI-1000. The input cards were 32-channel analog input modules, with model numbers of SCXI-1100 and SCXI-1102.

2.1.2 Temperature Hardware

An RDF Corporation resistance temperature device (RTD) was utilized to measure the temperature of the p-Cymene during the experiment. The accuracy of the device is ±0.3°C at 0°C with an operating range of -196 °C to 480°C.

2.1.3   Flow Rate Hardware

A Sponsler in-line precision turbine flowmeter was utilized to measure the volumetric flow rate of the working fluid. The Sponsler flowmeter used was a SP3-MB-PHL-D-4X. The uncertainty of the flowmeter analog output is 0.025% of full scale at 20 °C. The full scale reading is 600 gallons per minute (GPM). A Sponsler IT400 totalizer recorded the analog output from the flowmeter with a digital uncertainty of ±1 GPM.

2.1.4   Imaging Hardware

The PTV system consisted of a 10 W continuous laser at a wavelength of 527 nm and two digital CMOS Phantom M310 cameras. The laser beam was adjusted by beam combination optics to form a 1.5 mm thick laser sheet for the PTV measurements. The laser position was adjusted with three motorized linear translation stages. The high-speed Phantom M310 cameras have a full resolution of 1280 x 800 pixels, a pixel size of 20 x 20 μm^2 and 12-bit depth image capturing. Seeding particles were silver-coated hollow glass spheres with a mean diameter of 16 μm and a density of 1.6 g cm^{-3}.

2.2   Velocity Measurement Location

The location of velocity measurements was in the set of interior subchannels formed by the row of pins nearest to Face F, Figure 2. The vertical laser sheet used to illuminate particles for the PTV measurements is represented by the green line (a). The PTV measurement window for each camera is represented by the green rectangles (b). An X-Y coordinate system was assigned to represent horizontal and vertical directions in the laser sheet. The coordinate system is identical to the coordinate system used in [6]. The origin of the coordinate system is shown in Figure 2. The origin is selected as follow:

- x = 0 at the midpoint of face F (inner side)
- y = 0 at centerline of PT#5 (corresponding to the axial location of 2.25 pitches, as defined in [1, 2])
- z = 0 at face F (inner side)

Subchannel 1 (SC1)

X_{min} = -29.7 mm, and X_{max} = -26.7 mm.

Y_{min} = 25.7 mm, Y_{max} = 156.5 mm

Subchannel 2 (SC2)

X_{min} = -10.8 mm, and X_{max} = -7.8 mm.

Y_{min} = 25.7 mm, Y_{max} = 156.5 mm

154

Subchannel 3 (SC3)

X_{min} = 8.0 mm, and X_{max} = 11.0 mm.

Y_{min} = 25.7 mm, Y_{max} = 156.5 mm

Subchannel 4 (SC4)

X_{min} = 26.9 mm, and X_{max} = 29.9 mm.

Y_{min} = 25.7 mm, Y_{max} = 156.5 mm

The x-y plane is located at a z = -11.69 mm.

Figure 2. (a) Top view of the fuel bundle denoting the laser and camera positions. (b) Side view of the PTV measurement windows for Camera 1 and 2.

2.2.1   Laser Alignment

A three-dimensional traversing system was utilized to perform fine spatial adjustments of the laser sheet within the test section. The laser alignment process started by adjusting the base of the laser until the laser sheet was parallel with the inner surface of the wall forming Face F. A parallel orientation was confirmed by visual inspection. The relative intensity of the laser sheet in the two corners of Face F was monitored until equal. Next, the laser sheet was laterally traversed until it intersected the exterior row of rods. Again, by visual inspection, the laser sheet was confirmed to simultaneous intersect each rod in the plane parallel to face F. Finally, the laser sheet was traversed until equally bisecting rods of the first row. The laser sheet had a thickness of 1.5 mm ±0.5mm[1].

2.3   Boundary Conditions

This section describes the environmental conditions that existed during the experimental test. The quantities of interest were the fluid temperature, the pump frequency, the volumetric flow rate, and the Reynolds number.

2.3.1   Temperature

The temperature was monitored near the pump outlet using a resistance thermometer detector (RTD). The RTD had an uncertainty of ± 0.3 °C. Table 1 contains the temperature of the working fluid measured at the beginning of each data set.

Table 1. Working fluid temperature measured at the beginning of each run

	Fluid Temp (°C)
Set 1	22.0 ± 0.3
Set 2	22.4 ± 0.3
Set 3	22.5 ± 0.3

2.3.2   Pump

The centrifugal pump driving the working fluid was operated at a frequency of 51.5 Hz for all three data sets. The frequency was controlled by a variable frequency drive (VFD)

---

[1] The thickness of the laser sheet was estimated by measuring the thickness of the projected laser sheet on a flat surface using a ruler of 0.5 mm precision.

2.3.3   Volumetric Flow Rate

The average volumetric flow rate for the three sets recorded by the flowmeter for each data set is presented in Table 2. This average is the arithmetic average of the data points recorded during each set. More information is provided in Appendix I.

Table 2. Averaged volumetric flow rate of each run

	Flow Rate (gal min⁻¹)
Set 1	301.32 ± 1.3
Set 2	301.07 ± 1.3
Set 3	301.08 ± 1.3

2.3.4   Reynolds Number

The bundle-averaged Reynolds number for each set was calculated and shown in Table 4. The bundle-averaged Reynolds number was calculated based on the bulk velocity, along with the as-built bundle hydraulic diameter. The pin diameter, wire diameter, and flat-to-flat dimensions used in the hydraulic diameter calculation are the average values from the 61-rod, 61-wire, and 3 enclosure FTF characterizations provided in [1]. The bulk velocity was defined by the averaged volumetric flow rate. Appendix II shows the equations used to calculate the as-built flow area, hydraulic diameter, and wetted perimeter.

The bundle averaged Re number was calculated from Equation 1. Temperature-dependent density and viscosity values of the fluid were linearly interpolated based on the measured temperature of each set, Section 2.3.1 [3]. These values are presented in Table 3.

$$Re = \frac{\rho U_m D_H}{\mu} \tag{1}$$

Table 3. Bundle-averaged Reynolds number

	Fluid Temperature (°C)	Density (kg m⁻³)	Bulk Velocity (m s⁻¹)	Hydraulic Diameter (m)	Dynamic Viscosity (Pa sec)	Reynolds Number
Set 1	22.0	855.63	2.368	7.728 E-3	8.234 E-4	19,014
Set 2	22.4	855.31	2.366	7.728 E-3	8.191 E-4	19,091
Set 3	22.5	855.22	2.366	7.728 E-3	8.175 E-4	19,127

3.0   DATA SETS

This section provides information on the contents of the data files and instruction on how to read them. Three data sets were generated for this experimental test. Each set contains associated flow rate and velocity files. Further description of each subset is provided in Sections 3.2 and 3.3. A list of electronic attachments is included in Section 3.1

Table 4 defines the measurement duration and sampling frequency of each measurement in the following data sets.

Table 4. Measurement duration and sampling frequency for each data set

	PTV	
	Measurement Duration (sec)	Sampling Frequency (Hz)
Set 1	~ 3	2800
Set 2	~ 3	2800
Set 3	~ 3	2800

3.1   List of Electronic Attachments

The following files are submitted as electronic attachments. The files are archived into a .zip file named REV0-TAMU-WW-TEST-PCM-14-INT1-DATA.zip. The file is uploaded into the TerraPower ftp server under the folder *DOE Grant 1163/TAMU/PCM-14-INT1.*

Volumetric Flow Rate Data

REV0-TAMU-WW-TEST-PCM-14-INT1-FLOWRATE-SET1.csv 11/22/2016 2:54PM

REV0-TAMU-WW-TEST-PCM-14-INT1-FLOWRATE-SET2.csv 11/22/2016 2:54PM

REV0-TAMU-WW-TEST-PCM-14-INT1-FLOWRATE-SET3.csv 11/22/2016 2:54PM

REV0-TAMU-WW-TEST-PCM-14-INT1-FLOWRATE-AVERAGE.csv 11/22/2016 2:54PM

Velocity (PTV) Data

REV0-TAMU-WW-TEST-PCM-16-C2_SUB1_Vel_Stats-Combined.dat 12/15/2016 3:53PM

REV0-TAMU-WW-TEST-PCM-16-C2_SUB1_Vel_Stats-SET1.dat 12/15/2016 2:24PM

REV0-TAMU-WW-TEST-PCM-16-C2_SUB1_Vel_Stats-SET2.dat 12/15/2016 2:32PM

REV0-TAMU-WW-TEST-PCM-16-C2_SUB1_Vel_Stats-SET3.dat 12/15/2016 1:16PM

REV0-TAMU-WW-TEST-PCM-16-C2_SUB2_Vel_Stats-Combined.dat 12/15/2016 3:59PM

REV0-TAMU-WW-TEST-PCM-16-C2_SUB2_Vel_Stats-SET1.dat 12/15/2016 2:29PM

REV0-TAMU-WW-TEST-PCM-16-C2_SUB2_Vel_Stats-SET2.dat 12/15/2016 2:58PM

REV0-TAMU-WW-TEST-PCM-16-C2_SUB2_Vel_Stats-SET3.dat 12/15/2016 3:03PM

REV0-TAMU-WW-TEST-PCM-16-C2_SUB3_Vel_Stats-Combined.dat 12/15/2016 4:15PM

REV0-TAMU-WW-TEST-PCM-16-C2_SUB3_Vel_Stats-SET1.dat 12/15/2016 3:03PM

REV0-TAMU-WW-TEST-PCM-16-C2_SUB3_Vel_Stats-SET2.dat 12/15/2016 3:11PM

REV0-TAMU-WW-TEST-PCM-16-C2_SUB3_Vel_Stats-SET3.dat 12/15/2016 3:19PM

REV0-TAMU-WW-TEST-PCM-16-C2_SUB4_Vel_Stats-Combined.dat 12/15/2016 4:15PM

REV0-TAMU-WW-TEST-PCM-16-C2_SUB4_Vel_Stats-SET1.dat 12/15/2016 3:20PM

REV0-TAMU-WW-TEST-PCM-16-C2_SUB4_Vel_Stats-SET2.dat 12/15/2016 3:47PM

REV0-TAMU-WW-TEST-PCM-16-C2_SUB4_Vel_Stats-SET3.dat 12/15/2016 3:51PM

3.2   Volumetric Flow Rate Data

Three files are provided containing the instantaneous volumetric flow rate for each set:

REV0-TAMU-WW-TEST-PCM-14-INT1-FLOWRATE-SET1.csv

REV0-TAMU-WW-TEST-PCM-14-INT1-FLOWRATE-SET2.csv

REV0-TAMU-WW-TEST-PCM-14-INT1-FLOWRATE-SET3.csv

A summary file is included, which contains the arithmetic average, standard deviation, and k-factor conversion for each set.

REV0-TAMU-WW-TEST-PCM-14-INT1-FLOWRATE-AVERAGE.xlsx

The summary file contains the calculation to convert the raw flow meter output (working fluid = water) into the actual flow rate (working fluid = p-Cymene). More information on data conversion is provided in Appendix II.

3.3   Velocity (PTV) Data: Mean, rms, and Reynolds stress.

The velocity data provided represents a two dimensional array, but is presented in a one dimensional vector. The vector field consists of 16 point on x-direction, and 328 points on y-direction. Notes on calibration and error estimation are provided in Appendix III.

All data are stored in .dat format. These files contain multiple columns without headers.

Each set is identified in the file name (SET1, SETE2, SET3). File naming is consistent within the sets. As an example, content for SET1 is described below:

REV0-TAMU-WW-TEST-PCM-16-C2_SUB1_Vel_Stats-SET1.dat:

This file contains all velocity statistics for set 1 on sub-channel 1. The structure of the file is shown in Table 5.

Table 5. Velocity Statistics .dat File Structure

Column #	1	2	3	4	5	6	7	8	9	10
Parameter	X	Y	Z	u	v	w	u_rms	v_rms	w_rms	uv
Unit	mm	mm	mm	m/s	m/s	m/s	m/s	m/s	m/s	m^2/s^2

NOTE: in all .dat files, z is constant and equal to the laser sheet location (-11.69 mm). The velocity component along the z-direction and all related parameters are 0.

The .dat files marked as "combined" contain the same information and structure of the files described above for set 1. However, the statistical values are computed based on the total number of instantaneous velocities (3 x 8308 = 24924).

4.0   REFERENCES

1. TAMU-WW-AS Rev.1, TAMU Wire-Wrapped As-Built Geometry (Non-Deformed Bundle)
2. TWRP-31-TSPEC-0010 Rev. 1 , TAMU Fuel Assembly Flow Visualization Test Specification,
3. P-Cymene Chemical Information Sheet. Cameo Chemicals, Database of Hazard Materials, June 1999.
4. Appendix B.9 Factors for units listed by kind of quantity or field of science, NIST Guide, https://www.nist.gov/pml/nist-guide-si-appendix-b9-factors-units-listed-kind-quantity-or-field-science
5. S.-K. CHENG and N. E. TODREAS, "Hydrodynamic Models and Correlations for Bare and Wire-Wrapped Hexagonal Rod Bundles — Bundle Friction Factors, Subchannel Friction Factors and Mixing Parameters," Nucl. Eng. Des., 92, , 227–251 (1986).
6. TAMU-WW-TEST-PCM-11-E-rev2.0, TAMU Wire-Wrapped Test Summary of Test PCM-11 at the Exterior Subchannel.

APPENDIX I: TURBINE FLOW METER CALIBRATION FOR P-CYMENE

Since the flow meter was originally calibrated with water as the working fluid, the data presented in the output file is the flow rate of the fluid if it was water. Because the working fluid, p-Cymene, has a different density and viscosity than water, it was required to generate a new calibration of the turbine flow meter with p-Cymene as the working fluid.

This was achieved using an Omega FPT-6130 high accuracy pitot tube with an Omega high accuracy differential pressure transducer. The Omega FPT-6130 high accuracy Pitot tube had an accuracy of < 1% of the volumetric flow rate. Three different Omega differential pressure transducers were utilized, because the range of DP measured by each transducer is small relative to the total span of DP required to fully calibrate the turbine flow meter. Each Omega differential pressure transducer had the following maximum pressure reading, associated accuracy, and flow meter frequency range in which each differential pressure transducer was used, Table 69.

Table 6. Differential pressure transducers utilized in the p-Cymene k-factor calibration

Differential Pressure Transducer	Maximum Pressure (psi)	Accuracy (% Full Scale)	Flow Meter Frequency Range (Hz)
Omega MMDWB10WBIV5P2D0T2A2CE	0.36	< 0.1% FS	0-100
Omega MMDWB001BIV5P2D0T2A2CE	1.0	< 0.1% FS	100-160
Omega MMDWB005BIV5P2D0T2A3CE	5.0	< 0.1% FS	160-300

The rate meter determined the volumetric flow rate by multiplying the turbine rotational frequency by a multiplication factor, the factory calibrated k-factor. A new p-Cymene k-factor was calculated from the pitot flow, turbine meter output, and the factory k-factor. Presented in Figure 3 is a plot of the p-Cymene k-factor as a function of turbine flow meter frequency. The factory calibrated k-factor for water was 43.2411. The p-Cymene volumetric flow rate is calculated by Equation 4.

$$Flow\ Rate_{pcy} = Indicated\ Flow\ Rate \left(\frac{k_{H2O}}{k_{pcy}}\right) \tag{4}$$

Figure 3. p-Cymene k-factor plotted versus the turbine flow meter rotational frequency

APPENDIX II: BUNDLE GEOMETRY CALCULATION

From [5], the following expressions describe the variables used in the bundle geometry calculation. The subscripts one, two, and three correspond to the interior, wall, and corner sub channels respectively. P is the rod pitch, D is the pin diameter, D_{wire} is the wire spacer diameter, D_h is the hydraulic diameter, W is the edge pitch, N_i is the number of each sub channel, and H is the wire spacer lead or axial distance required for the spacer to complete one revolution around the pin. D, D_{wire}, and W are from the rod, wire and flat-to-flat characterization performed in [1]. The cosine term takes into account the elliptical projected area of the wire due to it not being parallel to the flow.

Parameter	Value	Unit
N_1	96	n/a
N_2	24	n/a
N_3	6	n/a
P	1.8878 E-2	m
D	1.5880 E-2	m
D_{wire}	3.0000 E-3	m
W	1.9548 E-2	m
$FTF_{enclosure}$	1.5400 E-1	m
FTF_{bundle}	1.5266 E-1	m
A_1	5.1747 E-5	m^2
A_2	1.1661 E-4	m^2
A_3	4.3637 E-5	m^2
A_{Bundle}	8.0281 E-3	m^2
$P_{wet,1}$	2.9688 E-2	m
$P_{wet,2}$	4.8564 E-2	m
$P_{wet,3}$	2.3302 E-2	m
$P_{wet,bundle}$	4.1554	m
H	4.7625 E-1	m

$$W = D + G_{wall}$$

$$G_{wall} = FTF_{enclosure} - FTF_{bundle}$$

$$FTF_{bundle} = \frac{8P\sqrt{3}}{2} + D + 2D_{wire}$$

$$A_1 = \left(\frac{\sqrt{3}}{4}\right)P^2 - \frac{\pi D^2}{8} - \frac{\pi D_{wire}^2}{8\cos(\theta)}$$

$$A_2 = \left(W - \frac{D}{2}\right)P - \frac{\pi D^2}{8} - \frac{\pi D_{wire}^2}{8\cos(\theta)}$$

$$A_3 = \frac{\left(W - \frac{D}{2}\right)^2}{\sqrt{3}} - \frac{\pi D^2}{24} - \frac{\pi D_{wire}^2}{24\cos(\theta)}$$

$$A_{Bundle} = N_1 A_1 + N_2 A_2 + N_3 A_3$$

$$P_{wet,1} = \frac{\pi D}{2} + \frac{\pi D_{wire}}{2\cos(\theta)}$$

$$P_{wet,2} = P + \frac{\pi D}{2} + \frac{\pi D_{wire}}{2\cos(\theta)}$$

$$P_{wet,3} = \frac{\pi D}{6} + \frac{2\left(W - \frac{D}{2}\right)}{\sqrt{3}} + \frac{\pi D_{wire}}{6\cos(\theta)}$$

$$P_{wet,Bundle} = N_1 P_{wet,1} + N_2 P_{wet,2} + N_3 P_{wet,3}$$

$$D_h = \frac{4\, A_{Bundle}}{P_{wet,Bundle}}$$

$$\cos(\theta) = \frac{H}{\sqrt{H^2 + \left(\pi(D + D_w)\right)^2}}$$

165

APPENDIX D

CENTER-2 SUBCHANNEL TEST SUMMARY

This appendix summarizes the conditions of the experimental test PCM-16-C2, and provides instructions for reading the associated flowrate and velocity data produced by the experimental test. This test summary was produced as part of the work under Project DE-NE0008321.

TECHNICAL DOCUMENT COVER PAGE

Document No:	TAMU-WW-TEST-PCM-16-C2		Revision: Rev.1	Page 1 of 21
Doc Title:	TAMU Wire-Wrapped Test Summary of Test PCM-16-C2 (Center plane - 30° offset)			
Projects No:	DE-NE0008321			
Project Name:	Toward a Longer Life Core: Thermal-Hydraulic CFD Simulations and Experimental Investigation of Deformed Fuel Assemblies			

Document Purpose/Summary: This document summarizes the conditions of the experimental test PCM-16-C2, and provides instructions for reading the associated flowrate and velocity data produced by the experimental test.

Total Page Count: 21 pages.

TECHNICAL DOCUMENT COVER PAGE

Document No:	TAMU-WW-TEST-PCM-16-C2	Revision: Rev.1	Page 2 of 21

TAMU Prepared By:	Nolan Goth		
	Printed/Typed Name	Signature	Date
	Philip Jones		
	Printed/Typed Name	Signature	Date
TAMU Reviewed By:	Thien Nguyen		
	Printed/Typed Name	Signature	Date
	Rodolfo Vaghetto		
	Printed/Typed Name	Signature	Date
Approved By:			
	Printed/Typed Name	Signature	Date

REVISION HISTORY LOG

Document Number: TAMU-WW-TEST-PCM-16-C2   Revision: Rev.1

Document Title: TAMU Wire-Wrapped Test Summary of Test PCM-16-C2 (Center plane - 30° offset)

REVISION	DATE	DESCRIPTION
Rev.0	11/23/16	First Release.
Rev.1	12/14/16	Changed reference coordinate system (Section 2.2) and updated file naming (Section 3.1)

Table of Contents

Acronyms and Definitions

Acronym	Definition
TAMU	The Texas A&M University
CAD	computer-aided-design
CFD	computational fluid dynamics
DP	differential pressure
FS	full scale
FTF	flat-to-flat
GPM	gallon per minute
PIV	particle image velocimetry
RMS	root-mean-square
RTD	resistance thermometer detector
VFD	variable frequency drive

1.0   INTRODUCTION AND SCOPE

This test summary provides information about the experimental setup, boundary conditions, and data sets for the experimental test PCM-16-C2 performed on August 04, 2016. The experimental setup describes the data acquisition, temperature, flow rate, and imaging hardware utilized to collect data. The boundary conditions are the fluid temperature, centrifugal pump rotational frequency, and volumetric flow rate during the experimental test. The data sets contain the instantaneous and time-averaged flow rate, instantaneous velocity measurements, along with the particle image velocimetry (PIV) statistical analysis.

2.0   TEST DESCRIPTION

An isothermal experimental flow test was conducted utilizing the 61-pin Hexagonal Wire-Wrapped Flow Facility. The test was performed to generate high spatial and temporal resolution data sets of the velocity in a vertical plane. Pressure measurements were not recorded during this test. The working fluid in the experimental test was p-Cymene. The bundle utilized in this test was the Second Non-Deformed Bundle, with geometric parameters defined in [1]. The measurement process was repeated three times, generating three sets of flowrate and velocity data.

2.1   Experimental Setup

The experimental facility contains two loops. Figure 1 displays a computer-aided design (CAD) model of the experimental facility. The primary loop performs the experimental function. The primary loop includes the following components:

- The hexagonal test section containing the 61-pin wire-wrapped experimental fuel bundle
- The primary tank is used as storage between experiments and as an inline surge volume. The primary pump and associated variable frequency drive (VFD) to control the flow rate in the test section
- An inline turbine flow meter
- A resistance temperature detector (RTD)
- Nine pressure transducers and two differential pressure transducers

The secondary loop performs volume control, temperature control, and filtration. The secondary loop contains the following components:

- The secondary tank
- The secondary pump and associated VFD
- A heat exchanger supplied with chilled water to control the primary loop temperature
- A filtration system

The test section can be divided into three distinct sections can be identified in the test bundle:

172

- The lower (inlet) plenum located at the bottom of the bundle
- The central section (test section) where the flow measurements will be conducted
- The upper (outlet) plenum located at the top of the bundle.

Figure 1. CAD rendering of the experimental facility

2.1.1   Data Acquisition Hardware

The data acquisition hardware consisted of equipment manufactured by National Instruments. The chassis used was a 4-slot model SCXI-1000. The input cards were 32-channel analog input modules, with model numbers of SCXI-1100 and SCXI-1102.

2.1.2   Temperature Hardware

An RDF Corporation resistance temperature device (RTD) was utilized to measure the temperature of the p-Cymene during the experiment. The accuracy of the device is ±0.3˚C at 0˚C with an operating range of -196 ˚C to 480˚C.

2.1.3 Flow Rate Hardware

A Sponsler in-line precision turbine flowmeter was utilized to measure the volumetric flow rate of the working fluid. The Sponsler flowmeter used was a SP3-MB-PHL-D-4X. The uncertainty of the flowmeter analog output is 0.025% of full scale at 20 °C. The full scale reading is 600 gallons per minute (GPM). A Sponsler IT400 totalizer recorded the analog output from the flowmeter with a digital uncertainty of ±1 GPM.

2.1.4 Imaging Hardware

The PIV system consisted of a 10 W continuous laser at a wavelength of 527 nm and two digital CMOS Phantom M310 cameras. The laser beam was adjusted by beam combination optics to form a 1.5 mm thick laser sheet for the PIV measurements. The laser position was adjusted with three motorized linear translation stages. The high-speed Phantom M310 cameras have a full resolution of 1280 x 800 pixels, a pixel size of 20 x 20 μm^2 and 12-bit depth image capturing. Seeding particles were silver-coated hollow glass spheres with a mean diameter of 16 μm and a density of 1.6 g cm^{-3}.

2.2 Velocity Measurement Location

The location of velocity measurements was in the set of interior subchannels denoted in Figure 2. The vertical laser sheet used to illuminate particles for the PIV measurements is represented by the green line (a). The figure also shows the location of the prism used during the experiment. A closeup of the subchannels of interest (SC1 and SC2) can be seen in (c). The PIV measurement window for each camera is represented by the green rectangles (b). In (b), pins are dark grey and the subchannels are light grey. The wires of neighboring pins cross into SC1 and SC2 at various axial locations. These wires are visible as dark grey sweeps across the subchannels. An Y-Z coordinate system was assigned to represent horizontal and vertical directions in the laser sheet. The origin of the Y-Z coordinate system is shown in Figure 2. The origin is selected as follow:

- x = 0 at the midpoint of face A (inner side)
- y = 0 at centerline of PT#5 (corresponding to the axial location of 2.25 pitches, as defined in [1, 2])
- z = 0 at face A (inner side)

The positive direction of each axis is also shown in Figure 2.

The minimum and maximum Y-Z coordinates of the visualization region are listed below:

Subchannel 1 (SC1)

Y_{min} = 28.0 mm, Y_{max} = 154.4 mm

Z_{min} = -69.0 mm, and Z_{max} = -53.2 mm.

Subchannel 2 (SC2)

Y_{min} = 28.0 mm, Y_{max} = 154.4 mm

Z_{min} = -36.3 mm, and Z_{max} = -20.5 mm.

The y-z plane is located at a x = 0 mm.
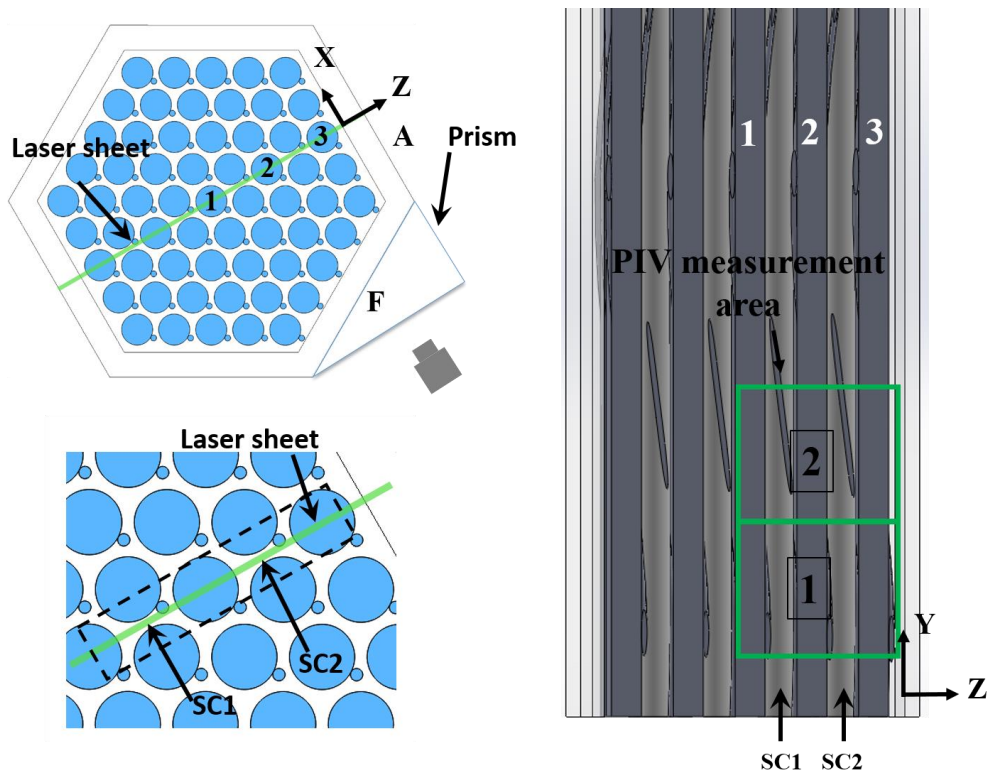
Figure 2. (a) Top view of the fuel bundle denoting the laser and camera positions. (b) Side view of the PIV measurement windows for Camera 1 and 2. (c) Top view close-up of SC1 and SC2.

2.2.1   Laser Alignment

A three-dimensional traversing system was utilized to perform fine spatial adjustments of the laser sheet within the test section. The laser alignment process started by placing the laser perpendicular Face D and Face A (opposite sides of the hexagonal enclosure). The laser sheet was then moved laterally until the laser sheet intersected the horizontal midpoints of Face D and Face A simultaneously. The midpoints of Face D and Face A were located using two rulers with 0.03125 inch markings. The laser sheet had a thickness of 1.5 mm ±0.5mm[1].

2.3   Boundary Conditions

This section describes the environmental conditions that existed during the experimental test. The quantities of interest were the fluid temperature, the pump frequency, the volumetric flow rate, and the Reynolds number.

2.3.1   Temperature

The temperature was monitored near the pump outlet using a resistance thermometer detector (RTD). The RTD had an uncertainty of ± 0.3 °C. Table 1 contains the temperature of the working fluid measured at the beginning of each data set.

Table 1. Working fluid temperature measured at the beginning of each run

	Fluid Temp (°C)
Set 1	19.8 ± 0.3
Set 2	20.0 ± 0.3
Set 3	20.3 ± 0.3

2.3.2   Pump

The centrifugal pump driving the working fluid was operated at a frequency of 51.5 Hz for all three data sets. The frequency was controlled by a variable frequency drive (VFD)

---

[1] The thickness of the laser sheet was estimated by measuring the thickness of the projected laser sheet on a flat surface using a ruler of 0.5 mm precision.

2.3.3   Volumetric Flow Rate

The average volumetric flow rate for the three sets recorded by the flowmeter for each data set is presented in Table 2. This average is the arithmetic average of the data points recorded during each set. More information is provided in Appendix I.

Table 2. Averaged volumetric flow rate of each run

	Flow Rate (gal min⁻¹)
Set 1	301.96 ±1.3
Set 2	302.09 ±1.3
Set 3	301.81 ±1.3

2.3.4   Reynolds Number

The bundle-averaged Reynolds number for each set was calculated and shown in Table 3. The bundle-averaged Reynolds number was calculated based on the bulk velocity, along with the as-built bundle hydraulic diameter. The pin diameter, wire diameter, and flat-to-flat dimensions used in the hydraulic diameter calculation are the average values from the 61-rod, 61-wire, and 3 enclosure FTF characterizations provided in [1]. The bulk velocity was defined by the averaged volumetric flow rate. Appendix II shows the equations used to calculate the as-built flow area, hydraulic diameter, and wetted perimeter.

The bundle averaged Re number was calculated from Equation 1. Temperature-dependent density and viscosity values of the fluid were linearly interpolated based on the measured temperature of each set, Section 2.3.1 [3]. These values are presented in Table 3.

$$Re = \frac{\rho U_m D_H}{\mu} \tag{1}$$

Table 3. Bundle-averaged Reynolds number

	Fluid Temperature (°C)	Density (kg m⁻³)	Bulk Velocity (m s⁻¹)	Hydraulic Diameter (m)	Dynamic Viscosity (Pa sec)	Reynolds Number
Set 1	19.8	857.41	2.373	7.728 E-3	8.472 E-4	18,558
Set 2	20.0	857.24	2.374	7.728 E-3	8.450 E-4	18,610
Set 3	20.3	857.00	2.372	7.728 E-3	8.405 E-4	18,688

3.0   DATA SETS

This section provides information on the contents of the data files and instruction on how to read them. Three data sets were generated for this experimental test. Each set contains associated flow rate and velocity files. Further description of each subset is provided in Sections 3.2 and 3.3. A list of electronic attachments is included in Section 3.1

Table 4 defines the measurement duration and sampling frequency of each measurement in the following data sets.

Table 4. Measurement duration and sampling frequency for each data set

	PIV	
	Measurement Duration (sec)	Sampling Frequency (Hz)
Set 1	~ 3	2800
Set 2	~ 3	2800
Set 3	~ 3	2800

3.1   List of Electronic Attachments

The following files are submitted as electronic attachments. The files are archived into a .zip file named REV1-TAMU-WW-TEST-PCM-16-C2-DATA.zip. The file is uploaded into the TerraPower ftp server under the folder *DOE Grant 1163/TAMU/PCM-16-C2.*

The file contains the following data (time stamp is reported next to the file name).

Volumetric Flow Rate Data

REV1-TAMU-WW-TEST-PCM-16-C2-FLOWRATE-SET1.csv 10/21/2016 1:19PM

REV1-TAMU-WW-TEST-PCM-16-C2-FLOWRATE-SET2.csv 10/21/2016 1:19PM

REV1-TAMU-WW-TEST-PCM-16-C2-FLOWRATE-SET3.csv 10/21/2016 1:19PM

REV1-TAMU-WW-TEST-PCM-16-C2-FLOWRATE-AVERAGE.xlsx 10/21/2016 1:19PM

Velocity (PIV) Data – Subchannel 1

REV1-TAMU-WW-TEST-PCM-16-C2_SUB1_Inst_Vel-SET1.zip 12/14/2016 6:57PM

REV1-TAMU-WW-TEST-PCM-16-C2_SUB1_Vel_Stats_Mean-SET1.dat 12/14/2016 11:46AM

REV1-TAMU-WW-TEST-PCM-16-C2_SUB1_Vel_Stats_RMS-SET1.dat 12/14/2016 11:46AM

REV1-TAMU-WW-TEST-PCM-16-C2_SUB1_Vel_Stats_VW-SET1.dat 12/14/2016 11:46AM

REV1-TAMU-WW-TEST-PCM-16-C2_SUB1_Inst_Vel-SET2.zip 12/14/2016 8:34PM
REV1-TAMU-WW-TEST-PCM-16-C2_SUB1_Vel_Stats_Mean-SET2.dat 12/14/2016 11:50AM
REV1-TAMU-WW-TEST-PCM-16-C2_SUB1_Vel_Stats_RMS-SET2.dat 12/14/2016 11:50AM
REV1-TAMU-WW-TEST-PCM-16-C2_SUB1_Vel_Stats_VW-SET2.dat 12/14/2016 11:50AM
REV1-TAMU-WW-TEST-PCM-16-C2_SUB1_Inst_Vel-SET3.zip 12/14/2016 8:35PM
REV1-TAMU-WW-TEST-PCM-16-C2_SUB1_Vel_Stats_Mean-SET3.dat 12/14/2016 11:50AM
REV1-TAMU-WW-TEST-PCM-16-C2_SUB1_Vel_Stats_RMS-SET3.dat 12/14/2016 11:50AM
REV1-TAMU-WW-TEST-PCM-16-C2_SUB1_Vel_Stats_VW-SET3.dat 12/14/2016 11:50AM
REV1-TAMU-WW-TEST-PCM-16-C2_SUB1_Vel_Stats_Mean-combined.dat 12/14/2016 12:07PM
REV1-TAMU-WW-TEST-PCM-16-C2_SUB1_Vel_Stats_RMS-combined.dat 12/14/2016 12:07PM
REV1-TAMU-WW-TEST-PCM-16-C2_SUB1_Vel_Stats_VW-combined.dat 12/14/2016 12:07PM

Velocity (PIV) Data – Subchannel 2
REV1-TAMU-WW-TEST-PCM-16-C2_SUB2_Inst_Vel-SET1.zip 12/14/2016 8:35PM
REV1-TAMU-WW-TEST-PCM-16-C2_SUB2_Vel_Stats_Mean-SET1.dat 12/14/2016 11:53AM
REV1-TAMU-WW-TEST-PCM-16-C2_SUB2_Vel_Stats_RMS-SET1.dat 12/14/2016 11:53AM
REV1-TAMU-WW-TEST-PCM-16-C2_SUB2_Vel_Stats_VW-SET1.dat 12/14/2016 11:53AM
REV1-TAMU-WW-TEST-PCM-16-C2_SUB2_Inst_Vel-SET2.zip 12/14/2016 8:36PM
REV1-TAMU-WW-TEST-PCM-16-C2_SUB2_Vel_Stats_Mean-SET2.dat 12/14/2016 11:56AM
REV1-TAMU-WW-TEST-PCM-16-C2_SUB2_Vel_Stats_RMS-SET2.dat 12/14/2016 11:56AM
REV1-TAMU-WW-TEST-PCM-16-C2_SUB2_Vel_Stats_VW-SET2.dat 12/14/2016 11:56AM
REV1-TAMU-WW-TEST-PCM-16-C2_SUB2_Inst_Vel-SET3.zip 12/14/2016 7:59PM
REV1-TAMU-WW-TEST-PCM-16-C2_SUB2_Vel_Stats_Mean-SET3.dat 12/14/2016 11:57AM
REV1-TAMU-WW-TEST-PCM-16-C2_SUB2_Vel_Stats_RMS-SET3.dat 12/14/2016 11:57AM
REV1-TAMU-WW-TEST-PCM-16-C2_SUB2_Vel_Stats_VW-SET3.dat 12/14/2016 11:57AM
REV1-TAMU-WW-TEST-PCM-16-C2_SUB2_Vel_Stats_Mean-combined.dat 12/14/2016 12:11PM
REV1-TAMU-WW-TEST-PCM-16-C2_SUB2_Vel_Stats_RMS-combined.dat 12/14/2016 12:11PM
REV1-TAMU-WW-TEST-PCM-16-C2_SUB2_Vel_Stats_VW-combined.dat 12/14/2016 12:11PM

3.2   Volumetric Flow Rate Data

Three files are provided containing the instantaneous volumetric flow rate for each set:

REV1-TAMU-WW-TEST-PCM-16-C2-FLOWRATE-SET1.csv

REV1-TAMU-WW-TEST-PCM-16-C2-FLOWRATE-SET2.csv

REV1-TAMU-WW-TEST-PCM-16-C2-FLOWRATE-SET3.csv

A summary file is included, which contains the arithmetic average, standard deviation, and k-factor conversion for each set.

REV1-TAMU-WW-TEST-PCM-16-C2-FLOWRATE-AVERAGE.xlsx

The summary file contains the calculation to convert the raw flow meter output (working fluid = water) into the actual flow rate (working fluid = p-Cymene). More information on data conversion is provided in Appendix I.

3.3   Velocity (PIV) Data: Instantaneous, Mean, rms, and Reynolds stress.

The velocity data provided represents a two dimensional array, but is presented in a one dimensional vector. For each subchannel, the vector field consists of 23 point in the x-direction, and 177 points in the y-direction. Notes on calibration and error estimation are provided in Appendix III.

All data are stored in .dat format. These files contain multiple columns without headers.

Each set is identified in the file name (SET1, SETE2, SET3). File naming is consistent within the sets. As an example, content for SET1 of subchannel 1 is described below:

REV1-TAMU-WW-TEST-PCM-16-C2_SUB1_Inst_Vel-SET1.zip:

This file contains 8309 .dat files of the instantaneous velocity. The structure of each file is described in Table 5

Table 5. Instantaneous Velocity .dat File Structure

Column #	1	2	3	4	5	6
Parameter	X	Y	Z	u	v	w
Unit	mm	mm	mm	m/s	m/s	m/s

REV1-TAMU-WW-TEST-PCM-16-C2_SUB1_Vel_Stats_Mean-SET1.dat:

This file contains the time-averaged velocity for set 1. The structure of the file is shown in Table 6.

Table 6. Mean Velocity .dat File Structure

Column #	1	2	3	4	5	6
Parameter	X	Y	Z	u	v	w
Unit	mm	mm	mm	m/s	m/s	m/s

REV1-TAMU-WW-TEST-PCM-16-C2_SUB1_Vel_Stats_RMS-SET1.dat:

This file contains the root mean square (rms) fluctuating velocity. The file structure is described in Table 7.

Table 7. rms File Structure

Column #	1	2	3	4	5	6
Parameter	X	Y	Z	u'_rms	v'_rms	w'_rms
Unit	mm	mm	mm	m/s	m/s	m/s

REV1-TAMU-WW-TEST-PCM-16-C2_SUB1_Vel_Stats_VW-SET1.dat

This file contains the Reynolds Stress $\overline{u'v'}$. The file structure is described in Table 8.

Table 8. Reynolds Stress File Structure

Column #	1	2	3	4
Parameter	X	Y	Z	$\overline{u'v'}$
Unit	mm	mm	mm	$m^2 s^{-2}$

NOTE: in all .dat files, z is constant and set to zero. The velocity component along the z-direction and all related parameters are 0.

The .dat files marked as "combined" contain the same information and structure of the files described above for set 1. However, the statistical values are computed based on the total number of instantaneous velocities (3 x 8309 = 24927).

4.0   REFERENCES

1. TAMU-WW-AS Rev.1, TAMU Wire-Wrapped As-Built Geometry (Non-Deformed Bundle)
2. TWRP-31-TSPEC-0010 Rev. 1 , TAMU Fuel Assembly Flow Visualization Test Specification,
3. P-Cymene Chemical Information Sheet. Cameo Chemicals, Database of Hazard Materials, June 1999.
4. Appendix B.9 Factors for units listed by kind of quantity or field of science, NIST Guide, https://www.nist.gov/pml/nist-guide-si-appendix-b9-factors-units-listed-kind-quantity-or-field-science
5. S.-K. CHENG and N. E. TODREAS, "Hydrodynamic Models and Correlations for Bare and Wire-Wrapped Hexagonal Rod Bundles — Bundle Friction Factors, Subchannel Friction Factors and Mixing Parameters," Nucl. Eng. Des., 92, 227–251 (1986).

APPENDIX I: TURBINE FLOW METER CALIBRATION FOR P-CYMENE

Since the flow meter was originally calibrated with water as the working fluid, the data presented in the output file is the flow rate of the fluid if it was water. Because the working fluid, p-Cymene, has a different density and viscosity than water, it was required to generate a new calibration of the turbine flow meter with p-Cymene as the working fluid.

This was achieved using an Omega FPT-6130 high accuracy pitot tube with an Omega high accuracy differential pressure transducer. The Omega FPT-6130 high accuracy Pitot tube had an accuracy of < 1% of the volumetric flow rate. Three different Omega differential pressure transducers were utilized, because the range of DP measured by each transducer is small relative to the total span of DP required to fully calibrate the turbine flow meter. Each Omega differential pressure transducer had the following maximum pressure reading, associated accuracy, and flow meter frequency range in which each differential pressure transducer was used, Table 99.

Table 9. Differential pressure transducers utilized in the p-Cymene k-factor calibration

Differential Pressure Transducer	Maximum Pressure (psi)	Accuracy (% Full Scale)	Flow Meter Frequency Range (Hz)
Omega MMDWB10WBIV5P2D0T2A2CE	0.36	< 0.1% FS	0-100
Omega MMDWB001BIV5P2D0T2A2CE	1.0	< 0.1% FS	100-160
Omega MMDWB005BIV5P2D0T2A3CE	5.0	< 0.1% FS	160-300

The rate meter determined the volumetric flow rate by multiplying the turbine rotational frequency by a multiplication factor, the factory calibrated k-factor. A new p-Cymene k-factor was calculated from the pitot flow, turbine meter output, and the factory k-factor. Presented in Figure 3 is a plot of the p-Cymene k-factor as a function of turbine flow meter frequency. The factory calibrated k-factor for water was 43.2411. The p-Cymene volumetric flow rate is calculated by Equation 4.

$$Flow\ Rate_{pcy} = Indicated\ Flow\ Rate\left(\frac{k_{H2O}}{k_{pcy}}\right) \quad\quad (4)$$

Figure 3. p-Cymene k-factor plotted versus the turbine flow meter rotational frequency

APPENDIX II: BUNDLE GEOMETRY CALCULATION

From [5], the following expressions describe the variables used in the bundle geometry calculation. The subscripts one, two, and three correspond to the interior, wall, and corner sub channels respectively. P is the rod pitch, D is the pin diameter, D_{wire} is the wire spacer diameter, D_h is the hydraulic diameter, W is the edge pitch, N_i is the number of each sub channel, and H is the wire spacer lead or axial distance required for the spacer to complete one revolution around the pin. D, D_{wire}, and W are from the rod, wire and flat-to-flat characterization performed in [1]. The cosine term takes into account the elliptical projected area of the wire due to it not being parallel to the flow.

Parameter	Value	Unit
N_1	96	n/a
N_2	24	n/a
N_3	6	n/a
P	1.8878 E-2	m
D	1.5880 E-2	m
D_{wire}	3.0000 E-3	m
W	1.9548 E-2	m
$FTF_{enclosure}$	1.5400 E-1	m
FTF_{bundle}	1.5266 E-1	m
A_1	5.1747 E-5	m²
A_2	1.1661 E-4	m²
A_3	4.3637 E-5	m²
A_{Bundle}	8.0281 E-3	m²
$P_{wet,1}$	2.9688 E-2	m
$P_{wet,2}$	4.8564 E-2	m
$P_{wet,3}$	2.3302 E-2	m
$P_{wet,bundle}$	4.1554	m
H	4.7625 E-1	m

$$W = D + G_{wall}$$

$$G_{wall} = FTF_{enclosure} - FTF_{bundle}$$

$$FTF_{bundle} = \frac{8P\sqrt{3}}{2} + D + 2D_{wire}$$

$$A_1 = \left(\frac{\sqrt{3}}{4}\right)P^2 - \frac{\pi D^2}{8} - \frac{\pi D_{wire}^2}{8\cos(\theta)}$$

185

$$A_2 = \left(W - \frac{D}{2}\right)P - \frac{\pi D^2}{8} - \frac{\pi D_{wire}^2}{8\cos(\theta)}$$

$$A_3 = \frac{\left(W - \frac{D}{2}\right)^2}{\sqrt{3}} - \frac{\pi D^2}{24} - \frac{\pi D_{wire}^2}{24\cos(\theta)}$$

$$A_{Bundle} = N_1 A_1 + N_2 A_2 + N_3 A_3$$

$$P_{wet,1} = \frac{\pi D}{2} + \frac{\pi D_{wire}}{2\cos(\theta)}$$

$$P_{wet,2} = P + \frac{\pi D}{2} + \frac{\pi D_{wire}}{2\cos(\theta)}$$

$$P_{wet,3} = \frac{\pi D}{6} + \frac{2\left(W - \frac{D}{2}\right)}{\sqrt{3}} + \frac{\pi D_{wire}}{6\cos(\theta)}$$

$$P_{wet,Bundle} = N_1 P_{wet,1} + N_2 P_{wet,2} + N_3 P_{wet,3}$$

$$D_h = \frac{4\,A_{Bundle}}{P_{wet,Bundle}}$$

$$\cos(\theta) = \frac{H}{\sqrt{H^2 + \left(\pi(D + D_w)\right)^2}}$$

APPENDIX III: NOTES ON PIV SYSTEM CALIBRATION AND ERROR ESTIMATION

The system was calibrated using LaVision ® calibration plates. The methodology adopted followed the guidelines published and described in [A-III-1].

The software used for the PIV imaging post-processing is the PRANA code developed by Virginia Tech. Performance and uncertainty of the PRANA RPC algorithm have been previously accessed (A-III-2, A-III-3, A-III-4, and A-III-5).

The analysis described in this report analysis was limited to estimate the overall uncertainty in the PIV velocity measurements. This was estimated to be approximately 0.1 pixels which yields to an uncertainty of less than 3% of the mean axial velocity.

[A-III-1]. Wieneke, B. "Stereo-PIV using self-calibration on particle images". Experiments in Fluids (2005) 39: 267–280 DOI 10.1007/s00348-005-0962-z

[A-III-2]. Timmins, B. H., Wilson, B. W., Smith, B. L. and Vlachos, P. P. ,"A method for automatic estimation of instantaneous local uncertainty in particle image velocimetry measurements". Experiments in Fluids 53(4): 1133–1147.

[A-III-3]. Wilson, B. M. and Smith, B. L., "Uncertainty on PIV mean and Fluctuating velocity due to Bias and Random Errors", Measurement Science and Technology 24(3): 035302.

[A-III-4]. Charonko, J. J. and Vlachos, P. P.,"Estimation of Uncertainty Bounds for Individual Particle Image Velocimetry Measurements from Cross-Correlation Peak Ratio". Measurement Science and Technology 24(6): 065301.

[A-III-5]. Boomsma, A., Bhattacharya, S., Troolin, D., Pothos, S. and Vlachos, P., "A Comparative Experimental Evaluation of Uncertainty Estimation Methods for Two-Component PIV". Measurement Science and Technology 27(9): 094006.

187

APPENDIX E

MEAN BACKGROUND INTENSITY SCRIPT

This appendix contains the mean background intensity script used during the pre-processing step of the experimental method workflow. The output is a single image of either 1 (black and white image set) or 3 channels (RBG image set). This script can be adjusted for either 8-bit depth or 16-bit depth images. It are currently configured for 16-bit depth images.

```python
# -*- coding: utf-8 -*-
"""
Created on Fri Sep  7 12:37:37 2018

@author: negcm7

REQUIREMENTS:
Files of type TIF must only be the raw images due to *.tif wildcard
"""
#---------------------------------------------------------------------#
import os
import glob
import numpy as np
import re
from skimage import io

# manually define the list of paths for each background subtract
# PATHS USE '/' (linux forward slash) NOT '\' (windows back slash)
```

```python
file_dir      = [
              ]

for active_dir in range(0,len(file_dir)):

    bg_subtract_dir = file_dir[active_dir] + 'bg_subtract'

    if not os.path.exists(bg_subtract_dir):
        os.makedirs(bg_subtract_dir)

    # generate list of images
    active_file_list = sorted(glob.glob(file_dir[active_dir]+"*.tif"))
    # replace \\ windows path with / for cv2.imread to function properly
    active_file_list = [active_file_list[item].replace('\\','/') for item in range(0,len(
    ↪ active_file_list) ) ]

    #initialize image_bgd
    image_temp = ( io.imread(active_file_list[0]) ).astype(np.float64)
    image_bgd = np.zeros_like(image_temp)

    # sum raw images
    counter=0
    for image in active_file_list:
        print('Image number = ', counter)
        counter += 1

        image_active = ( io.imread(image) ).astype(np.float64)
        image_bgd = image_bgd + image_active

    # calculate mean background image
```

```python
image_bgd = ( image_bgd / len (active_file_list) ).astype(np.uint16)

# setup bg_mean filename
bg_mean_filename = re.sub('.00001.tif$', '_bg_mean.tif', os.path.split(
    ↪ active_file_list[0])[1] )

# save mean image to (directory,data)
io.imsave( bg_subtract_dir + bg_mean_filename , image_bgd)
```

APPENDIX F

MEAN BACKGROUND SUBTRACTION SCRIPT

This appendix contains two mean background subtraction scripts used during the pre-processing step of the experimental method workflow. The first script is appropriate for a single channel (black and white) image set. The second script is appropriate for a RBG (color) image set, as it contains color coefficients provided by the camera sensor manufacturer. These scripts can be adjusted for either 8-bit depth or 16-bit depth images. They are currently configured for 16-bit depth images.

```
# -*- coding: utf-8 -*-
"""
Created on Mon Sep 10 11:52:18 2018

@author: negcm7
"""

import os
import glob
import numpy as np
from skimage import io

# manually define the list of paths for each background subtract directory
# PATHS USE '/' (linux forward slash) NOT '\' (windows back slash)
file_dir = [
    ]
```

```python
for active_dir in range(0, len(file_dir)):

    bg_subtract_dir = file_dir[active_dir] + 'bg_subtract/'

    # create bg_subtract directory if it does not exist
    if not os.path.exists(bg_subtract_dir):
        os.makedirs(bg_subtract_dir)

    # generate list of images for active directory
    active_file_list = sorted(glob.glob(file_dir[active_dir]+"*.tif"))

    # replace \\ windows path with / for cv2.imread or io.imread to function properly
    active_file_list = [active_file_list[item].replace('\\','/') for item in range(0,len(
    ↪ active_file_list) ) ]

    # find path of background mean image and load it
    bg_mean_dir = glob.glob(bg_subtract_dir + '*bg_mean.tif' )

    # replace \\ windows path with / for cv2.imread or io.imread to function properly
    bg_mean_dir = [bg_mean_dir[item].replace('\\','/') for item in range(0,len(bg_mean_dir
    ↪ ) ) ]

    # load background mean image as float64
    image_bgd =  (io.imread(bg_mean_dir[0])).astype(np.float64)

    # loop through all images and write all background subtracted images
    counter=0
    for image in active_file_list:
        print('Image number = ', counter)
```

```python
counter += 1

image_active = ( io.imread(image) ).astype(np.float64)
image_active = image_active - image_bgd

# scale array to avoid having negative values
image_active = image_active - np.min(image_active)

# lookup path for naming structure
active_image_path = os.path.split(image)

# save bg subtracted image
io.imsave( bg_subtract_dir + active_image_path[1][:-10]+'_bg_subtract'+
    active_image_path[1][-10:],
(image_active).astype(np.uint16) )
```

The 3 channel RBG color image background subtract script begins here.

```python
# -*- coding: utf-8 -*-
"""
Created on Mon Sep 10 11:52:18 2018

@author: negcm7
"""

import os
import glob
import numpy as np
import re
```

```python
from skimage import io

# manually define the list of paths for each background subtract directory
# PATHS USE '/' (linux forward slash) NOT '\' (windows back slash)
file_dir = [
    ]

for active_dir in range(0, len(file_dir)):

    # define the directory to write backgorund subtracted images
    bg_subtract_dir = file_dir[active_dir] + 'bg_subtract/'

    # create bg_subtract directory if it does not exist
    if not os.path.exists(bg_subtract_dir):
        os.makedirs(bg_subtract_dir)

    # generate list of images for active directory
    active_file_list = sorted(glob.glob(file_dir[active_dir]+"*.tif"))

    # replace \\ windows path with / for cv2.imread or io.imread to function properly
    active_file_list = [active_file_list[item].replace('\\','/') for item in range(0, len(
    ↪ active_file_list) ) ]

    # find path of bg_mean image and load
    bg_mean_dir = glob.glob(bg_subtract_dir + '*bg_mean.tif' )

    # replace \\ windows path with / for cv2.imread or io.imread to function properly
    bg_mean_dir = [bg_mean_dir[item].replace('\\','/') for item in range(0, len(bg_mean_dir
    ↪ ) ) ]
```

```python
# load background mean image as float64
image_bgd_3_channel = (io.imread(bg_mean_dir[0])).astype(np.float64)

# define color cone coefficients for the camera sensor used in the experiment
red_coeff    = 0.3
green_coeff  = 0.59
blue_coeff   = 0.11

# scale the image intensities for each channel by the color coefficient (3rd dimension
↪ index order = Red, Green Blue)
image_bgd = image_bgd_3_channel[:,:,0] * red_coeff + image_bgd_3_channel[:,:,1] *
↪ green_coeff + image_bgd_3_channel[:,:,2] * blue_coeff

# loop through all images and write all background subtracted images
counter=0
for image in active_file_list:
    print('Image number = ', counter)
    counter += 1

    image_active = ( io.imread(image) ).astype(np.float64)
    image_active = image_active[:,:,0] * red_coeff + image_active[:,:,1] * green_coeff +
    ↪ image_active[:,:,2] * blue_coeff
    image_active = image_active - image_bgd
    image_active = image_active - np.min(image_active)

    # lookup path for naming structure
    active_image_path = os.path.split(image)

    # save bg subtracted image
```

```
io.imsave( bg_subtract_dir + active_image_path[1][:-10]+'_bg_subtract'+
↪ active_image_path[1][-10:],
(image_active).astype(np.uint16) )
```

APPENDIX G

EXAMPLE INPUT DECK

This appendix contains an example input deck that calls the primary statistical calculation function defined in Appendix H.

```python
#!/usr/bin/env python3
# -*- coding: utf-8 -*-
"""
Created on Thu Aug 23 16:56:18 2018

@author: nol
"""
import os
from IPython import get_ipython
ipython = get_ipython()

#%% INPUTS FOR STATISTICAL CALCULATION

# define file directory, PIV output file name, and desired name for plots
file_dir     = [
                ]

filename     = 'PIV_pass3_'
plotname     = 'ext1_080216_280_cam2_'
plot_dir     = 'C:/example_dir'
if not os.path.exists(plot_dir):
```

```python
os.makedirs(plot_dir)

# define the time interval between laser pulses / images
dt = 0.000357143   #(2800Hz)
# define the conversion from (pixels/frame) to (m/s) with 'meter/pixel' input
scaling = 0.089335145 * ( 10**(-3) ) / 1
# define the bulk mean velocity from flowmeter (meter / second)
v_bulk =  2.380
# define the vector spacing in meter
vec_space_dx = 0.7147 * 10**-3
vec_space_dy = 0.7147 * 10**-3
# residual convergence
# define the coordnate points for 2 horizontal and 2 vertical lines
horzline_1_x1 = 40
horzline_1_x2 = 60
horzline_1_y  = 25
horzline_2_x1 = 40
horzline_2_x2 = 60
horzline_2_y  = 40
vertline_1_x  = 80
vertline_1_y1 = 20
vertline_1_y2 = 40
vertline_2_x  = 80
vertline_2_y1 = 40
vertline_2_y2 = 60
#%%

import stats_time_resolved as stats_time_resolved
```

```
stats_time_resolved.stats_time_resolved( file_dir, filename, plotname, plot_dir, dt,
↪ scaling, v_bulk, vec_space_dx, vec_space_dy, horzline_1_x1, horzline_1_x2,
↪ horzline_1_y, horzline_2_x1, horzline_2_x2, horzline_2_y, vertline_1_x,
↪ vertline_1_y1, vertline_1_y2, vertline_2_x, vertline_2_y1, vertline_2_y2 )

#%reset -f
#ipython.magic('reset -f')
```

APPENDIX H

STATISTICS CALCULATION SCRIPT

This appendix contains the script used to manipulate the instantaneous velocity fields from the PRANA processing workflow step output. **add more discussion here**

```python
# -*- coding: utf-8 -*-
"""
Created on Thu May 31 12:59:22 2018

@author: negcm7
"""

import numpy as np
import numpy.ma as ma
import scipy.io as sio
import glob
import matplotlib.pyplot as plt
import random
import matplotlib
import h5py

#plt.rcParams.update(plt.rcParamsDefault)

# set plotting fonts
```

```python
# for regular text to look like the mathtext text, you can change everything to Stix.
↪ This will affect labels, titles, ticks, etc:
#matplotlib.rcParams['mathtext.fontset'] = 'stix'
#matplotlib.rcParams['font.family'] = 'STIXGeneral'
#matplotlib.pyplot.title(r'ABC123 vs $\mathrm{ABC123}^{123}$')

# for tex-style/mathtext text look like the regular text:
#matplotlib.rcParams['mathtext.fontset'] = 'custom'
#matplotlib.rcParams['mathtext.rm'] = 'Bitstream Vera Sans'
#matplotlib.rcParams['mathtext.it'] = 'Bitstream Vera Sans:italic'
#matplotlib.rcParams['mathtext.bf'] = 'Bitstream Vera Sans:bold'
#matplotlib.pyplot.title(r'ABC123 vs $\mathrm{ABC123}^{123}$')
def stats_time_resolved( file_dir, filename, plotname, plot_dir, dt, scaling, v_bulk,
↪ vec_space_dx, vec_space_dy,
horzline_1_x1, horzline_1_x2, horzline_1_y, horzline_2_x1, horzline_2_x2, horzline_2_y
↪ ,
vertline_1_x, vertline_1_y1, vertline_1_y2, vertline_2_x, vertline_2_y1, vertline_2_y2
↪ ):

# Initialize structures for script
number_files = [None]*len(file_dir)
number_files = [ len(glob.glob(file_dir[i] + filename + '*')) for i in range(0,len(
↪ file_dir)) ]
load_temp_mat = sio.loadmat(file_dir[0] + filename + '00001')
num_rows    = np.size (load_temp_mat['X'],0)
num_cols    = np.size (load_temp_mat['X'],1)
#%% calculate average eval field from total image set
eval_replace_count = np.zeros([ len(load_temp_mat['U']), len(load_temp_mat['U'][1]) ])
eval_sum = 0
```

```python
unique     = 0
vector_counts = 0
eval_pass_count = 1

for active_dir in range(0,len(file_dir)):
    active_file_list = sorted(glob.glob(file_dir[active_dir]+filename+"*.mat"))
    #       for pass_number in range(1,number_files[active_dir]+1):
    for pass_number in active_file_list:
        print("eval array pass ",eval_pass_count)
        #       active_file = sio.loadmat(file_dir[active_dir] + filename + '%05d' %
        ↪ pass_number + '.mat')
        active_file = sio.loadmat(pass_number)
        eval_instantaneous = active_file['Eval']

        # count vector replacement for current pass
        unique_temp, vector_counts_temp = np.unique(eval_instantaneous, return_counts=True)
        unique = unique + unique_temp
        vector_counts = vector_counts + vector_counts_temp

        # count individual vector replacements for each pass
        for i in range(0,num_rows):
            for j in range(0,num_cols):
                if eval_instantaneous[i,j] == 1 or eval_instantaneous[i,j] == 2:
                    eval_replace_count[i,j] += 1

        # calculate eval sum matrix
        eval_sum = eval_sum + eval_instantaneous
        eval_pass_count += 1

    # calculate fraction of vector replacement in field
```

```python
# Eval    -1 = mask
#          0 = no validation fail
#          1 = failed validation on tight and loose threshold, vector replaced
#          2 = failed validation on tight but not loose threshold, vector replaced
fraction_replaced_vectors = ( vector_counts[2] + vector_counts[3] ) / (vector_counts
↪ [1] + vector_counts[2] + vector_counts[3])

# list of locations of high frequency vector replacement
high_freq_replace                = np.argwhere( ( eval_replace_count / np.sum(
↪ number_files) ) >= 0.4)
fraction_replaced_vectors_final  = fraction_replaced_vectors - ( len(high_freq_replace
↪ ) / ( np.size(active_file['Eval'],0) * np.size(active_file['Eval'],1) ) )
print("fraction of replaced vectors =",fraction_replaced_vectors_final)

#%% generate velocity component arrays
u_instantaneous_tot = np.zeros([ len(load_temp_mat['U']), len(load_temp_mat['U'][1]),
↪ np.sum(number_files) ])
v_instantaneous_tot = np.zeros([ len(load_temp_mat['U']), len(load_temp_mat['U'][1]),
↪ np.sum(number_files) ])
bad_vectors         = np.zeros([ len(load_temp_mat['U']), len(load_temp_mat['U'][1])
↪ ])
image_counter = 1

for active_dir in range(0,len(file_dir)):
active_file_list = sorted(glob.glob(file_dir[active_dir]+filename+"*.mat"))
#       for pass_number in range(1,number_files[active_dir]+1):
for pass_number in active_file_list:
print("velocity array pass ", image_counter)
#       active_file = sio.loadmat(file_dir[active_dir] + filename + '%05d' %
↪ pass_number + '.mat')
```

```python
active_file = sio.loadmat(pass_number)
u_instantaneous = active_file['U']
v_instantaneous = active_file['V']

# subtract high frequency replacement vectors before statistical calculations
for i in range(0,len(high_freq_replace)):
    u_instantaneous[ high_freq_replace[i,:][0], high_freq_replace[i,:][1] ] = np.nan
    v_instantaneous[ high_freq_replace[i,:][0], high_freq_replace[i,:][1] ] = np.nan


if image_counter == 1:
    u_instantaneous_tot[:,:,0] = u_instantaneous
    v_instantaneous_tot[:,:,0] = v_instantaneous
    image_counter +=1

else:
    u_instantaneous_tot[:,:,image_counter-1] = u_instantaneous
    v_instantaneous_tot[:,:,image_counter-1] = v_instantaneous
    image_counter +=1

for i in range (0,len(high_freq_replace)):
    bad_vectors[ high_freq_replace[i,:][0], high_freq_replace[i,:][1] ] = 1

#%% mean, rms, and uv stress calc from 100% image set
u_mean  = np.mean(u_instantaneous_tot,2)
v_mean  = np.mean(v_instantaneous_tot,2)

u_rms   = np.std(u_instantaneous_tot, 2, dtype=np.float64, ddof=0)
v_rms   = np.std(v_instantaneous_tot, 2, dtype=np.float64, ddof=0)
```

204

```python
u_prime = np.subtract(u_instantaneous_tot, u_mean[:,:,None])
v_prime = np.subtract(v_instantaneous_tot, v_mean[:,:,None])

uv_prime_mean = np.mean ( np.multiply (u_prime, v_prime),2 )
uu_prime_mean = np.mean ( np.multiply (u_prime, u_prime),2 )
vv_prime_mean = np.mean ( np.multiply (v_prime, v_prime),2 )

#

# clear RAM
del u_prime,v_prime

#%% Convert velocity arrays from pixel / frame to meter / second

# convert axis to millimeter, can offset based on local coordinate system (see old
� matlab script)

x_phys = active_file['X'] * scaling * 1000
y_phys = active_file['Y'] * scaling * 1000

# scale velocity fields
u_mean = (u_mean * scaling / dt ) / v_bulk
v_mean = (v_mean * scaling / dt ) / v_bulk
u_rms  = (u_rms  * scaling / dt ) / v_bulk
v_rms  = (v_rms  * scaling / dt) / v_bulk

uv_prime_mean = (uv_prime_mean * scaling**2 / dt**2) / v_bulk**2
uu_prime_mean = (uu_prime_mean * scaling**2 / dt**2) / v_bulk**2
vv_prime_mean = (vv_prime_mean * scaling**2 / dt**2) / v_bulk**2

u_mean[u_mean==0] = np.nan
```

```python
v_mean[v_mean==0]  = np.nan
u_rms [ u_rms==0]  = np.nan
v_rms [ v_rms==0]  = np.nan

uv_prime_mean[uv_prime_mean==0]  = np.nan
uu_prime_mean[uu_prime_mean==0]  = np.nan
vv_prime_mean[vv_prime_mean==0]  = np.nan

#%% 1-Component Vorticity for 2D2C plane

# first array stands for the gradient along each column and the second along each row
# The returned gradient hence has the same shape as the input array
du_dy,  du_dx = np.gradient(u_mean,  vec_space_dx )
dv_dy,  dv_dx = np.gradient(v_mean,  vec_space_dy )

z_vorticity_mean = dv_dx - du_dy

#%% RESIDUAL CONVERGENCE
# non-linear step method to select datasets
# specify number of fractional data sets
number_rel_converge_pts = 41
# specify start and stop numbers for fractional datasets
rel_size_start = 100
rel_size_stop  = np.sum(number_files)
# In linear space, the sequence starts at base ** start and ends with base ** stop
rel_size = np.logspace(np.log(rel_size_start)/np.log(10),np.log(rel_size_stop)/np.log
↪ (10),number_rel_converge_pts ,dtype=int)

# initialize arrays
random_u_mean  = np.zeros([ len(load_temp_mat['U']), len(load_temp_mat['U'][1]), len(
```

```
                                                     ↪ rel_size) ])
random_v_mean      = np.zeros([ len(load_temp_mat['U']), len(load_temp_mat['U'][1]), len(
↪ rel_size) ])
random_u_prime     = np.zeros([ len(load_temp_mat['U']), len(load_temp_mat['U'][1]), len(
↪ rel_size) ])
random_v_prime     = np.zeros([ len(load_temp_mat['U']), len(load_temp_mat['U'][1]), len(
↪ rel_size) ])
random_u_rms       = np.zeros([ len(load_temp_mat['U']), len(load_temp_mat['U'][1]), len(
↪ rel_size) ])
random_v_rms       = np.zeros([ len(load_temp_mat['U']), len(load_temp_mat['U'][1]), len(
↪ rel_size) ])
random_uv_prime    = np.zeros([ len(load_temp_mat['U']), len(load_temp_mat['U'][1]), len(
↪ rel_size) ])
random_uu_prime    = np.zeros([ len(load_temp_mat['U']), len(load_temp_mat['U'][1]), len(
↪ rel_size) ])
random_vv_prime    = np.zeros([ len(load_temp_mat['U']), len(load_temp_mat['U'][1]), len(
↪ rel_size) ])

residual_u_mean    = np.zeros([ len(load_temp_mat['U']), len(load_temp_mat['U'][1]),
↪ len(rel_size) -1 ])
residual_v_mean    = np.zeros([ len(load_temp_mat['U']), len(load_temp_mat['U'][1]),
↪ len(rel_size) -1 ])
residual_u_rms     = np.zeros([ len(load_temp_mat['U']), len(load_temp_mat['U'][1]),
↪ len(rel_size) -1 ])
residual_v_rms     = np.zeros([ len(load_temp_mat['U']), len(load_temp_mat['U'][1]),
↪ len(rel_size) -1 ])
residual_uv_prime  = np.zeros([ len(load_temp_mat['U']), len(load_temp_mat['U'][1]),
↪ len(rel_size) -1 ])
residual_uu_prime  = np.zeros([ len(load_temp_mat['U']), len(load_temp_mat['U'][1]),
↪ len(rel_size) -1 ])
```

```python
residual_vv_prime = np.zeros([ len(load_temp_mat['U']), len(load_temp_mat['U']), len(load_temp_mat['U'][1]),
↪ len(rel_size) -1 ])

residual_u_mean_horzline_1       = np.zeros([len(rel_size) -1 ])
residual_v_mean_horzline_1       = np.zeros([len(rel_size) -1 ])
residual_u_rms_horzline_1        = np.zeros([len(rel_size) -1 ])
residual_v_rms_horzline_1        = np.zeros([len(rel_size) -1 ])
residual_uv_prime_horzline_1     = np.zeros([len(rel_size) -1 ])
residual_uu_prime_horzline_1     = np.zeros([len(rel_size) -1 ])
residual_vv_prime_horzline_1     = np.zeros([len(rel_size) -1 ])

residual_u_mean_horzline_2       = np.zeros([len(rel_size) -1 ])
residual_v_mean_horzline_2       = np.zeros([len(rel_size) -1 ])
residual_u_rms_horzline_2        = np.zeros([len(rel_size) -1 ])
residual_v_rms_horzline_2        = np.zeros([len(rel_size) -1 ])
residual_uv_prime_horzline_2     = np.zeros([len(rel_size) -1 ])
residual_uu_prime_horzline_2     = np.zeros([len(rel_size) -1 ])
residual_vv_prime_horzline_2     = np.zeros([len(rel_size) -1 ])

residual_u_mean_vertline_1       = np.zeros([len(rel_size) -1 ])
residual_v_mean_vertline_1       = np.zeros([len(rel_size) -1 ])
residual_u_rms_vertline_1        = np.zeros([len(rel_size) -1 ])
residual_v_rms_vertline_1        = np.zeros([len(rel_size) -1 ])
residual_uv_prime_vertline_1     = np.zeros([len(rel_size) -1 ])
residual_uu_prime_vertline_1     = np.zeros([len(rel_size) -1 ])
residual_vv_prime_vertline_1     = np.zeros([len(rel_size) -1 ])

residual_u_mean_vertline_2       = np.zeros([len(rel_size) -1 ])
residual_v_mean_vertline_2       = np.zeros([len(rel_size) -1 ])
residual_u_rms_vertline_2        = np.zeros([len(rel_size) -1 ])
```

```python
residual_v_rms_vertline_2        = np.zeros([len(rel_size)  -1  ])
residual_uv_prime_vertline_2     = np.zeros([len(rel_size)  -1  ])
residual_uu_prime_vertline_2     = np.zeros([len(rel_size)  -1  ])
residual_vv_prime_vertline_2     = np.zeros([len(rel_size)  -1  ])

# Random image pair selection for each fractional dataset
for i in range(0,len(rel_size)-1):
    print("Fractional Dataset Selection ",i)
    selection_list = random.sample(range(0, np.sum(number_files)), rel_size[i])

    # pre-allocate and re-zero arrays for each J loop
    random_u_instantaneous_tot = np.zeros([ len(load_temp_mat['U']), len(load_temp_mat['U'
    ↪ ][1]), rel_size[i] ])
    random_v_instantaneous_tot = np.zeros([ len(load_temp_mat['U']), len(load_temp_mat['U'
    ↪ ][1]), rel_size[i] ])

    for j in range(0, rel_size[i]):
        random_u_instantaneous_tot[:,:,j] = u_instantaneous_tot[:,:,selection_list[j]]
        random_v_instantaneous_tot[:,:,j] = v_instantaneous_tot[:,:,selection_list[j]]

    random_u_mean[:,:,i]  = np.mean( random_u_instantaneous_tot, 2 )
    random_v_mean[:,:,i]  = np.mean( random_v_instantaneous_tot, 2 )
    random_u_rms [:,:,i]  = np.std ( random_u_instantaneous_tot, 2, dtype=np.float64)
    random_v_rms [:,:,i]  = np.std ( random_v_instantaneous_tot, 2, dtype=np.float64)

    random_u_prime = np.subtract(random_u_instantaneous_tot, random_u_mean[:,:,i,None] )
    random_v_prime = np.subtract(random_v_instantaneous_tot, random_v_mean[:,:,i,None] )

    random_uv_prime[:,:,i] = np.mean(np.multiply (random_u_prime, random_v_prime),2 )
    random_uu_prime[:,:,i] = np.mean(np.multiply (random_u_prime, random_u_prime),2 )
```

```python
random_vv_prime[:,:,i] = np.mean(np.multiply (random_v_prime, random_v_prime), 2 )

# Residual Convergence Calculation for entire vector field
#    M = num_rows*num_cols
for i in range(0,len(rel_size)-1):
print("Residual Convergence for Fractional Dataset ",i)
# random method, difference
residual_u_mean    [:,:,i] = np.abs( random_u_mean    [:,:,i+1] - random_u_mean    [:,:,i] )
residual_v_mean    [:,:,i] = np.abs( random_v_mean    [:,:,i+1] - random_v_mean    [:,:,i] )
residual_u_rms     [:,:,i] = np.abs( random_u_rms     [:,:,i+1] - random_u_rms     [:,:,i] )
residual_v_rms     [:,:,i] = np.abs( random_v_rms     [:,:,i+1] - random_v_rms     [:,:,i] )
residual_uv_prime[:,:,i] = np.abs( random_uv_prime[:,:,i+1] - random_uv_prime[:,:,i] )
residual_uu_prime[:,:,i] = np.abs( random_uu_prime[:,:,i+1] - random_uu_prime[:,:,i] )
residual_vv_prime[:,:,i] = np.abs( random_vv_prime[:,:,i+1] - random_vv_prime[:,:,i] )

# random method, residual relatve fraction
#    residual_u_mean   [:,:,i-1] = np.sqrt( ( M * np.nansum (random_u_mean   [:,:,i] -
↪ random_u_mean   [:,:,i-1] )**2) / ( np.nansum(random_u_mean   [:,:,i])**2 ))
#    residual_v_mean   [:,:,i-1] = np.sqrt( ( M * np.nansum (random_v_mean   [:,:,i] -
↪ random_u_mean   [:,:,i-1] )**2) / ( np.nansum(random_u_mean   [:,:,i])**2 ))
#    residual_u_rms    [:,:,i-1] = np.sqrt( ( M * np.nansum(random_u_rms    [:,:,i] -
↪ random_u_rms    [:,:,i-1] )**2) / ( np.nansum(random_u_rms    [:,:,i])**2 ))
#    residual_v_rms    [:,:,i-1] = np.sqrt( ( M * np.nansum(random_v_rms    [:,:,i] -
↪ random_u_rms    [:,:,i-1] )**2) / ( np.nansum(random_u_rms    [:,:,i])**2 ))
#    residual_uv_prime[:,:,i-1] = np.sqrt( ( M * np.nansum(random_uv_prime[:,:,i] -
↪ random_uv_prime[:,:,i-1] )**2) / ( np.nansum(random_uv_prime[:,:,i])**2 ))
#    residual_uu_prime[:,:,i-1] = np.sqrt( ( M * np.nansum(random_uu_prime[:,:,i] -
↪ random_uu_prime[:,:,i-1] )**2) / ( np.nansum(random_uu_prime[:,:,i])**2 ))
#    residual_vv_prime[:,:,i-1] = np.sqrt( ( M * np.nansum(random_vv_prime[:,:,i] -
↪ random_vv_prime[:,:,i-1] )**2) / ( np.nansum(random_vv_prime[:,:,i])**2 ))
```

```python
# residual calculation for horizontal line 1
residual_u_mean_horzline_1    [i-1] = np.nanmean(residual_u_mean    [horzline_1_y,
↪ horzline_1_x1:horzline_1_x2 ,i-1])
residual_v_mean_horzline_1    [i-1] = np.nanmean(residual_v_mean    [horzline_1_y,
↪ horzline_1_x1:horzline_1_x2 ,i-1])
residual_u_rms_horzline_1     [i-1] = np.nanmean(residual_u_rms     [horzline_1_y,
↪ horzline_1_x1:horzline_1_x2 ,i-1])
residual_v_rms_horzline_1     [i-1] = np.nanmean(residual_v_rms     [horzline_1_y,
↪ horzline_1_x1:horzline_1_x2 ,i-1])
residual_uv_prime_horzline_1[i-1] = np.nanmean(residual_uv_prime[horzline_1_y,
↪ horzline_1_x1:horzline_1_x2 ,i-1])
residual_uu_prime_horzline_1[i-1] = np.nanmean(residual_uu_prime[horzline_1_y,
↪ horzline_1_x1:horzline_1_x2 ,i-1])
residual_vv_prime_horzline_1[i-1] = np.nanmean(residual_vv_prime[horzline_1_y,
↪ horzline_1_x1:horzline_1_x2 ,i-1])

# residual calculation for horizontal line 1
residual_u_mean_horzline_2    [i-1] = np.nanmean(residual_u_mean    [horzline_2_y,
↪ horzline_2_x1:horzline_2_x2 ,i-1])
residual_v_mean_horzline_2    [i-1] = np.nanmean(residual_v_mean    [horzline_2_y,
↪ horzline_2_x1:horzline_2_x2 ,i-1])
residual_u_rms_horzline_2     [i-1] = np.nanmean(residual_u_rms     [horzline_2_y,
↪ horzline_2_x1:horzline_2_x2 ,i-1])
residual_v_rms_horzline_2     [i-1] = np.nanmean(residual_v_rms     [horzline_2_y,
↪ horzline_2_x1:horzline_2_x2 ,i-1])
residual_uv_prime_horzline_2[i-1] = np.nanmean(residual_uv_prime[horzline_2_y,
↪ horzline_2_x1:horzline_2_x2 ,i-1])
residual_uu_prime_horzline_2[i-1] = np.nanmean(residual_uu_prime[horzline_2_y,
↪ horzline_2_x1:horzline_2_x2 ,i-1])
```

```python
residual_vv_prime_horzline_2[i-1]     = np.nanmean(residual_vv_prime[horzline_2_y,
↪ horzline_2_x1:horzline_2_x2 ,i-1])

# residual calculation for vertical line 1
residual_u_mean_vertline_1    [i-1] = np.nanmean(residual_u_mean    [vertline_1_y1:
↪ vertline_1_y2, vertline_1_x ,i-1])
residual_v_mean_vertline_1    [i-1] = np.nanmean(residual_v_mean    [vertline_1_y1:
↪ vertline_1_y2, vertline_1_x ,i-1])
residual_u_rms_vertline_1     [i-1] = np.nanmean(residual_u_rms     [vertline_1_y1:
↪ vertline_1_y2, vertline_1_x ,i-1])
residual_v_rms_vertline_1     [i-1] = np.nanmean(residual_v_rms     [vertline_1_y1:
↪ vertline_1_y2, vertline_1_x ,i-1])
residual_uv_prime_vertline_1[i-1] = np.nanmean(residual_uv_prime[vertline_1_y1:
↪ vertline_1_y2, vertline_1_x ,i-1])
residual_uu_prime_vertline_1[i-1] = np.nanmean(residual_uu_prime[vertline_1_y1:
↪ vertline_1_y2, vertline_1_x ,i-1])
residual_vv_prime_vertline_1[i-1] = np.nanmean(residual_vv_prime[vertline_1_y1:
↪ vertline_1_y2, vertline_1_x ,i-1])

# residual calculation for vertical line 2
residual_u_mean_vertline_2    [i-1] = np.nanmean(residual_u_mean    [vertline_2_y1:
↪ vertline_2_y2, vertline_2_x ,i-1])
residual_v_mean_vertline_2    [i-1] = np.nanmean(residual_v_mean    [vertline_2_y1:
↪ vertline_2_y2, vertline_2_x ,i-1])
residual_u_rms_vertline_2     [i-1] = np.nanmean(residual_u_rms     [vertline_2_y1:
↪ vertline_2_y2, vertline_2_x ,i-1])
residual_v_rms_vertline_2     [i-1] = np.nanmean(residual_v_rms     [vertline_2_y1:
↪ vertline_2_y2, vertline_2_x ,i-1])
residual_uv_prime_vertline_2[i-1] = np.nanmean(residual_uv_prime[vertline_2_y1:
↪ vertline_2_y2, vertline_2_x ,i-1])
```

```python
    residual_uu_prime_vertline_2[i-1]   = np.nanmean(residual_uu_prime[vertline_2_y1:
    ↪ vertline_2_y2, vertline_2_x ,i-1])
    residual_vv_prime_vertline_2[i-1]   = np.nanmean(residual_vv_prime[vertline_2_y1:
    ↪ vertline_2_y2, vertline_2_x ,i-1])
#%% CLEAR RAM
del random_u_instantaneous_tot, random_u_mean, random_u_prime, random_u_rms,
    ↪ random_uu_prime, random_v_instantaneous_tot, \
    random_v_mean, random_v_prime, random_v_rms, random_vv_prime, random_uv_prime

#%% Write HDF5 files for archive and clear variables

with h5py.File(plot_dir + plotname + "stats.hdf5", "w") as f:
    # 2D coordinate mesh
    f.create_dataset("dataset_x_phys", data = x_phys)
    f.create_dataset("dataset_y_phys", data = y_phys)
    # velocity and derived quantity fields
    f.create_dataset("dataset_u_instantaneous_tot", data = u_instantaneous_tot)
    f.create_dataset("dataset_v_instantaneous_tot", data = v_instantaneous_tot)
    f.create_dataset("dataset_u_mean", data = u_mean)
    f.create_dataset("dataset_v_mean", data = v_mean)
    f.create_dataset("dataset_u_rms", data = u_rms )
    f.create_dataset("dataset_v_rms", data = v_rms )
    f.create_dataset("dataset_uv_prime_mean", data = uv_prime_mean )
    f.create_dataset("dataset_uu_prime_mean", data = uu_prime_mean )
    f.create_dataset("dataset_vv_prime_mean", data = vv_prime_mean )
    f.create_dataset("dataset_z_vorticity", data = z_vorticity_mean )
    # statistical validation
    f.create_dataset("dataset_eval", data = eval_replace_count / np.sum(number_files))
    f.create_dataset("dataset_bad_vectors", data = bad_vectors )
    # residual convergence along 4 lines
```

213

```python
f.create_dataset("dataset_residual_u_mean_horzline_1", data =
↪ residual_u_mean_horzline_1 )
f.create_dataset("dataset_residual_v_mean_horzline_1", data =
↪ residual_v_mean_horzline_1 )
f.create_dataset("dataset_residual_u_rms_horzline_1", data =
↪ residual_u_rms_horzline_1 )
f.create_dataset("dataset_residual_v_rms_horzline_1", data =
↪ residual_v_rms_horzline_1 )
f.create_dataset("dataset_residual_uv_prime_horzline_1", data =
↪ residual_uv_prime_horzline_1 )
f.create_dataset("dataset_residual_uu_prime_horzline_1", data =
↪ residual_uu_prime_horzline_1 )
f.create_dataset("dataset_residual_vv_prime_horzline_1", data =
↪ residual_vv_prime_horzline_1 )

f.create_dataset("dataset_residual_u_mean_horzline_2", data =
↪ residual_u_mean_horzline_2 )
f.create_dataset("dataset_residual_v_mean_horzline_2", data =
↪ residual_v_mean_horzline_2 )
f.create_dataset("dataset_residual_u_rms_horzline_2", data =
↪ residual_u_rms_horzline_2 )
f.create_dataset("dataset_residual_v_rms_horzline_2", data =
↪ residual_v_rms_horzline_2 )
f.create_dataset("dataset_residual_uv_prime_horzline_2", data =
↪ residual_uv_prime_horzline_2 )
f.create_dataset("dataset_residual_uu_prime_horzline_2", data =
↪ residual_uu_prime_horzline_2 )
f.create_dataset("dataset_residual_vv_prime_horzline_2", data =
↪ residual_vv_prime_horzline_2 )
```

```python
f.create_dataset("dataset_residual_u_mean_vertline_1", data =
↪ residual_u_mean_vertline_1 )
f.create_dataset("dataset_residual_v_mean_vertline_1", data =
↪ residual_v_mean_vertline_1 )
f.create_dataset("dataset_residual_u_rms_vertline_1", data =
↪ residual_u_rms_vertline_1 )
f.create_dataset("dataset_residual_v_rms_vertline_1", data =
↪ residual_v_rms_vertline_1 )
f.create_dataset("dataset_residual_uv_prime_vertline_1", data =
↪ residual_uv_prime_vertline_1 )
f.create_dataset("dataset_residual_uu_prime_vertline_1", data =
↪ residual_uu_prime_vertline_1 )
f.create_dataset("dataset_residual_vv_prime_vertline_1", data =
↪ residual_vv_prime_vertline_1 )

f.create_dataset("dataset_residual_u_mean_vertline_2", data =
↪ residual_u_mean_vertline_2 )
f.create_dataset("dataset_residual_v_mean_vertline_2", data =
↪ residual_v_mean_vertline_2 )
f.create_dataset("dataset_residual_u_rms_vertline_2", data =
↪ residual_u_rms_vertline_2 )
f.create_dataset("dataset_residual_v_rms_vertline_2", data =
↪ residual_v_rms_vertline_2 )
f.create_dataset("dataset_residual_uv_prime_vertline_2", data =
↪ residual_uv_prime_vertline_2 )
f.create_dataset("dataset_residual_uu_prime_vertline_2", data =
↪ residual_uu_prime_vertline_2 )
f.create_dataset("dataset_residual_vv_prime_vertline_2", data =
↪ residual_vv_prime_vertline_2 )
#%% LOAD HDF5 FILE USING H5PY EXAMPLE
```

```python
#   hdf5_data = h5py.File('J:/wirewrapped_DE_NE_8321/internal_data/pcymene/
↪  measurement locations/exterior1/PCM_14_080216/PIV/280GPM/Camera 1/plots/
↪  ext1_080216_280_cam1_stats.hdf5', 'r+')
#       v_mean = hdf5_data.get('dataset_v_mean').value
#       u_mean = hdf5_data.get('dataset_u_mean').value
#       u_rms = hdf5_data.get('dataset_u_rms').value
#       v_rms = hdf5_data.get('dataset_v_rms').value
#       uv_prime_mean = hdf5_data.get('dataset_uv_prime_mean').value
#       bad_vectirs = hdf5_data.get('dataset_bad_vectors').value
#%% PLOTZ
# scientific notation for plot axes
def fmt(x, pos):
    a, b = '{:.2e}'.format(x).split('e')
    b = int(b)
    return r'${} \times 10^{{{}}}$'.format(a, b)

#######################################################
# eval replacement fraction (normalized by total images)
#######################################################
plt.plot()
plt.pcolormesh(active_file['X'], active_file['Y'], eval_replace_count / np.sum(
↪ number_files), cmap='inferno', vmin= 0.0, vmax= 1.0)# shading='gouraud')
plt.title('Validation Replacement Frequency')
#plt.axis([x_phys.min(), x_phys.max(), y_phys.min(), y_phys.max()])
plt.ylabel('Y coordinate (mm)')
plt.xlabel('X coordinate (mm)')
plt.axes().set_aspect('equal')
plt.colorbar()
plt.savefig(plot_dir + plotname + 'eval_replacement.png', dpi=1000)
plt.close()
```

```python
#plt.show()

##############################################
# high replacement vectors
##############################################
# mean

plt.plot()
plt.pcolormesh(x_phys, y_phys, bad_vectors, cmap='binary') #, vmin= -0.20, vmax= 0.200)
    ↪ # shading='gouraud')
plt.axis([x_phys.min(), x_phys.max(), y_phys.min(), y_phys.max()])
plt.ylabel('Y coordinate (mm)')
plt.xlabel('X coordinate (mm)')
plt.axes().set_aspect('equal')
plt.colorbar()
plt.savefig(plot_dir + plotname + 'high_replacement_vectors.png', dpi=1000)
plt.close()
#plt.show()
#%% VELOCITY CONTOURS

##############################################
# u velocity component
##############################################
# mean

u_mean_mask = ma.masked_invalid(u_mean)
plt.plot()
plt.pcolormesh(x_phys, y_phys, bad_vectors, cmap='binary')
plt.pcolormesh(x_phys, y_phys, u_mean_mask, cmap='inferno', vmin= np.nanmin(u_mean),
    ↪ vmax= np.nanmax(u_mean) ) #, shading='gouraud' )
plt.axis([x_phys.min(), x_phys.max(), y_phys.min(), y_phys.max()])
plt.ylabel('Y coordinate (mm)')
```

```python
plt.xlabel('X coordinate (mm)')
plt.axes().set_aspect('equal')
clb = plt.colorbar()
clb.ax.set_title('                    $\overline{u}$ / w$_{bulk}$')
clb.ax.set_ylim(0,1.02)
plt.savefig(plot_dir + plotname + 'u_mean.png', dpi=1000)
plt.close()
#plt.show()

# rms of fluctuating
u_rms_mask = ma.masked_invalid(u_rms)
plt.plot()
#    plt.pcolormesh(x_phys, y_phys, bad_vectors, cmap='binary')
plt.pcolormesh(x_phys, y_phys, u_rms_mask, cmap='inferno', vmin= np.nanmean(u_rms)
↪ *0.5, vmax= np.nanmean(u_rms)*1.5 )#, shading='gouraud' )
plt.axis([x_phys.min(), x_phys.max(), y_phys.min(), y_phys.max()])
plt.ylabel('Y coordinate (mm)')
plt.xlabel('X coordinate (mm)')
plt.axes().set_aspect('equal')
clb = plt.colorbar()
clb.ax.set_title('                    u$^{\prime}_{rms}$ / w$_{bulk}$')
clb.ax.set_ylim(0,1.02)
plt.savefig(plot_dir + plotname + 'u_rms.png', dpi=1000)
plt.close()
#plt.show()

#######################################################
# v velocity component
#######################################################
# mean
```

```python
v_mean_mask = ma.masked_invalid(v_mean)
plt.plot
plt.pcolormesh(x_phys, y_phys, bad_vectors, cmap='binary')
plt.pcolormesh(x_phys, y_phys, v_mean_mask, cmap='inferno', vmin= np.nanmin(v_mean),
↪ vmax= np.nanmax(v_mean) ) #, shading='gouraud' )
plt.axis([x_phys.min(), x_phys.max(), y_phys.min(), y_phys.max()])
plt.ylabel('Y coordinate (mm)')
plt.xlabel('X coordinate (mm)')
plt.axes().set_aspect('equal')
clb = plt.colorbar()
clb.ax.set_title('                    $\overline{v}$ / w$_{bulk}$')
clb.ax.set_ylim(0,1.02)
plt.savefig(plot_dir + plotname + 'v_mean.png', dpi=1000)
plt.close()
#    plt.show()

# rms of fluctuating
v_rms_mask = ma.masked_invalid(v_rms)
plt.plot
#    plt.pcolormesh(x_phys, y_phys, bad_vectors, cmap='binary')
plt.pcolormesh(x_phys, y_phys, v_rms_mask, cmap='inferno', vmin= round(np.nanmean(
↪ v_rms)*0.5,3), vmax= round(np.nanmean(v_rms)*1.5,3 ) ) #, shading='gouraud' )
plt.axis([x_phys.min(), x_phys.max(), y_phys.min(), y_phys.max()])
plt.ylabel('Y coordinate (mm)')
plt.xlabel('X coordinate (mm)')
plt.axes().set_aspect('equal')
clb = plt.colorbar()
clb.ax.set_title('                    v$^{\prime}_{rms}$ / w$_{bulk}$')
clb.ax.set_ylim(0,1.02)
plt.savefig(plot_dir + plotname + 'v_rms.png', dpi=1000)
```

```python
plt.close()
#plt.show()

######################################
# u'v' Reynolds shear stress
######################################

uv_prime_mean_mask = ma.masked_invalid(uv_prime_mean)
plt.plot
#    plt.pcolormesh(x_phys, y_phys, bad_vectors, cmap='binary')
plt.pcolormesh(x_phys, y_phys, uv_prime_mean_mask, cmap='inferno', vmin= np.nanmin(
↪ uv_prime_mean), vmax= np.nanmax(uv_prime_mean) )#, shading='gouraud')
plt.axis([x_phys.min(), x_phys.max(), y_phys.min(), y_phys.max()])
plt.ylabel('Y coordinate (mm)')
plt.xlabel('X coordinate (mm)')
plt.axes().set_aspect('equal')
#    clb = plt.colorbar(format=matplotlib.ticker.FuncFormatter(fmt))
clb.ax.set_title('                    $\overline{u^{\prime}v^{\prime}}$ / w$_{bulk}^{2}$')
clb.ax.set_ylim(0,1.02)
plt.savefig(plot_dir + plotname + 'uv_prime_mean.png', dpi=1000)
plt.close()
#plt.show()

######################################
# Z-Vorticity
######################################

z_vorticity_mean_mask = ma.masked_invalid(z_vorticity_mean)
plt.plot
plt.pcolormesh(x_phys, y_phys, bad_vectors, cmap='binary')
plt.pcolormesh(x_phys, y_phys, z_vorticity_mean_mask, cmap='coolwarm', vmin= np.nanmin
↪ (z_vorticity_mean), vmax= np.nanmax(z_vorticity_mean) )#, shading='gouraud')
```

```python
plt.axis([x_phys.min(), x_phys.max(), y_phys.min(), y_phys.max()])
plt.ylabel('Y coordinate (mm)')
plt.xlabel('X coordinate (mm)')
plt.axes().set_aspect('equal')
clb = plt.colorbar(format=matplotlib.ticker.FuncFormatter(fmt))
clb.ax.set_title('$\overline{\omega_{z}}$ / w$_{bulk}$ ')
clb.ax.set_ylim(0,1.02)
plt.savefig(plot_dir + plotname + 'z_vorticity_mean.png', dpi=1000)
plt.close()
#plt.show()
#%% Residual Convergence
#
↪ ##############################################################################
↪

# Horzline 1
plt.plot
plt.plot(rel_size[1:40], residual_u_mean_horzline_1   [:39]  , label='$\overline{u}$'
↪                       , color='b', marker='x', markersize=2, ls='--', lw=0.5)
plt.plot(rel_size[1:40], residual_v_mean_horzline_1   [:39]  , label='$\overline{v}$'
↪                       , color='r', marker='o', markersize=2, ls='--', lw=0.5)
plt.plot(rel_size[1:40], residual_u_rms_horzline_1    [:39]  , label='u$^{\prime}_{rms}
↪ $'                    , color='g', marker='^', markersize=2, ls='--', lw=0.5)
plt.plot(rel_size[1:40], residual_v_rms_horzline_1    [:39]  , label='v$^{\prime}_{rms}
↪ $'                    , color='k', marker='v', markersize=2, ls='--', lw=0.5)
plt.plot(rel_size[1:40], residual_uv_prime_horzline_1[:39]   , label='$\overline{u^{\
↪ prime}v^{\prime}}$'   , color='m', marker='<', markersize=2, ls='--', lw=0.5)
plt.plot(rel_size[1:40], residual_uu_prime_horzline_1[:39]   , label='$\overline{u^{\
↪ prime}u^{\prime}}$'   , color='y', marker='>', markersize=2, ls='--', lw=0.5)
plt.plot(rel_size[1:40], residual_vv_prime_horzline_1[:39]   , label='$\overline{v^{\
```

```python
                                → prime}v^{\prime}}$', color='c', marker='h', markersize=2, ls='--', lw=0.5)
plt.ylabel(r'Residual Convergence $ \vert \phi_{n} - \phi_{n-1} \vert $')
plt.xlabel('Number of Image Pairs')
plt.legend()
x1,x2,y1,y2 = plt.axis()
#    plt.axis((x1,x2,0,0.15))
plt.savefig(plot_dir + plotname + 'residual_converge_horzline_1.png', dpi=1000)
plt.close()

# Horzline 2
plt.plot
plt.plot(rel_size[1:40], residual_u_mean_horzline_2   [:39] ,  label='$\overline{u}$'
                            → , color='b', marker='x', markersize=2, ls='--', lw=0.5)
plt.plot(rel_size[1:40], residual_v_mean_horzline_2   [:39] ,  label='$\overline{v}$'
                            → , color='r', marker='o', markersize=2, ls='--', lw=0.5)
plt.plot(rel_size[1:40], residual_u_rms_horzline_2   [:39] ,  label='u$^{\prime}_{rms}
                            → $', color='g', marker='^', markersize=2, ls='--', lw=0.5)
plt.plot(rel_size[1:40], residual_v_rms_horzline_2   [:39] ,  label='v$^{\prime}_{rms}
                            → $', color='k', marker='v', markersize=2, ls='--', lw=0.5)
plt.plot(rel_size[1:40], residual_uv_prime_horzline_2[:39] ,  label='$\overline{u^{\
                            → prime}v^{\prime}}$', color='m', marker='<', markersize=2, ls='--', lw=0.5)
plt.plot(rel_size[1:40], residual_uu_prime_horzline_2[:39] ,  label='$\overline{u^{\
                            → prime}u^{\prime}}$', color='y', marker='>', markersize=2, ls='--', lw=0.5)
plt.plot(rel_size[1:40], residual_vv_prime_horzline_2[:39] ,  label='$\overline{v^{\
                            → prime}v^{\prime}}$', color='c', marker='h', markersize=2, ls='--', lw=0.5)
plt.ylabel(r'Residual Convergence $ \vert \phi_{n} - \phi_{n-1} \vert $')
plt.xlabel('Number of Image Pairs')
plt.legend()
x1,x2,y1,y2 = plt.axis()
#    plt.axis((x1,x2,0,0.15))
```

```python
plt.savefig(plot_dir + plotname + 'residual_converge_horzline_2.png', dpi=1000)
plt.close()

# Vertline 1
plt.plot
plt.plot(rel_size[1:40], residual_u_mean_vertline_1  [:39]  ,  label='$\overline{u}$'
↪       ,  color='b', marker='x', markersize=2,  ls='--',  lw=0.5)
plt.plot(rel_size[1:40], residual_v_mean_vertline_1  [:39]  ,  label='$\overline{v}$'
↪       ,  color='r', marker='o', markersize=2,  ls='--',  lw=0.5)
plt.plot(rel_size[1:40], residual_u_rms_vertline_1  [:39]  ,  label='u$^{\prime}_{rms}
↪ $',  color='g', marker='^', markersize=2,  ls='--',  lw=0.5)
plt.plot(rel_size[1:40], residual_v_rms_vertline_1  [:39]  ,  label='v$^{\prime}_{rms}
↪ $',  color='k', marker='v', markersize=2,  ls='--',  lw=0.5)
plt.plot(rel_size[1:40], residual_uv_prime_vertline_1[:39]  ,  label='$\overline{u^{\
↪ prime}v^{\prime}}$',  color='m', marker='<', markersize=2, ls='--',  lw=0.5)
plt.plot(rel_size[1:40], residual_uu_prime_vertline_1[:39]  ,  label='$\overline{u^{\
↪ prime}u^{\prime}}$',  color='y', marker='>', markersize=2, ls='--',  lw=0.5)
plt.plot(rel_size[1:40], residual_vv_prime_vertline_1[:39]  ,  label='$\overline{v^{\
↪ prime}v^{\prime}}$',  color='c', marker='h', markersize=2, ls='--',  lw=0.5)
plt.ylabel(r'Residual Convergence  $ \vert \phi_{n} - \phi_{n-1} \vert $')
plt.xlabel('Number of Image Pairs')
plt.legend()
x1,x2,y1,y2 = plt.axis()
#     plt.axis((x1,x2,0,0.15))
plt.savefig(plot_dir + plotname + 'residual_converge_vertline_1.png', dpi=1000)
plt.close()

# Vertline 2
plt.plot
plt.plot(rel_size[1:40], residual_u_mean_vertline_2  [:39]   , label='$\overline{u}$'
```

```python
                , color='b', marker='x', markersize=2,   ls='--',   lw=0.5)
plt.plot(rel_size[1:40], residual_v_mean_vertline_2  [:39]  ,   label='$\overline{v}$'
↪
                , color='r', marker='o', markersize=2,   ls='--',   lw=0.5)
plt.plot(rel_size[1:40], residual_u_rms_vertline_2   [:39]  ,   label='u$^{\prime}_{rms}
↪ $'
                , color='g', marker='^', markersize=2,   ls='--',   lw=0.5)
plt.plot(rel_size[1:40], residual_v_rms_vertline_2   [:39]  ,   label='v$^{\prime}_{rms}
↪ $'
                , color='k', marker='v', markersize=2,   ls='--',   lw=0.5)
plt.plot(rel_size[1:40], residual_uv_prime_vertline_2[:39]  ,   label='$\overline{u^{\
↪ prime}v^{\prime}}$', color='m', marker='<', markersize=2,  ls='--',  lw=0.5)
plt.plot(rel_size[1:40], residual_uu_prime_vertline_2[:39]  ,   label='$\overline{u^{\
↪ prime}u^{\prime}}$', color='y', marker='>', markersize=2,  ls='--',  lw=0.5)
plt.plot(rel_size[1:40], residual_vv_prime_vertline_2[:39]  ,   label='$\overline{v^{\
↪ prime}v^{\prime}}$', color='c', marker='h', markersize=2,  ls='--',  lw=0.5)
plt.ylabel(r'Residual Convergence  $ \vert \phi_{n} - \phi_{n-1} \vert $')
plt.xlabel('Number of Image Pairs')
plt.legend()
x1,x2,y1,y2 = plt.axis()
#       plt.axis((x1,x2,0,0.15))
plt.savefig(plot_dir + plotname + 'residual_converge_vertline_2.png', dpi=1000)
plt.close()
#%% DELETE UNNECESSARY ARRAYS
del residual_u_mean, residual_u_rms, residual_v_mean, residual_v_rms,
↪ residual_uu_prime, residual_vv_prime, residual_uv_prime
#%% MORE MEMORY EFFICIENT VELOCITY ALGORITHM (SLOWER THAN ABOVE)
#%% GENERATE VELOCITY COMPONENT ARRAYS (EACH ROW IS SEQUENTIAL IMAGE CAPTURES ,COLUMNS
↪ ARE SPATIAL COORDINATES in orignal MxN array)
#for pass_number in range(1,number_files):
#    print(pass_number)
#    active_file = sio.loadmat(file_dir + filename + '%05d' % pass_number + '.mat')
#    u_instantaneous = np.reshape(active_file['U'],  ( 1,sum(len(x) for x in
```

```python
#        active_file['U']) ) )
#    v_instantaneous = np.reshape(active_file['V'],   ( 1,sum(len(x) for x in
#        active_file['V']) ) )
#
#    if pass_number == 1:
#        print("if")
#        u_instantaneous_tot = u_instantaneous
#        v_instantaneous_tot = v_instantaneous
#
#    else:
#        u_instantaneous_tot = np.concatenate( (u_instantaneous_tot,u_instantaneous),
#  axis = 0)
#        v_instantaneous_tot = np.concatenate( (v_instantaneous_tot,v_instantaneous),
#  axis = 0)
#
##%% mean, rms, and uv stress calc
#u_mean  = np.mean(u_instantaneous_tot,0)
#u_prime = u_instantaneous_tot - u_mean
#u_mean = np.reshape( u_mean ,  ( np.size(active_file['U'],0), np.size(active_file['U
#  '],1) ) )
#
#v_mean   = np.mean(v_instantaneous_tot,0)
#v_prime = v_instantaneous_tot - v_mean
#v_mean = np.reshape( u_mean ,  ( np.size(active_file['V'],0), np.size(active_file['V
#  '],1) ) )
#
#uv_prime_mean = np.reshape( np.mean ( np.multiply (u_prime, v_prime),0 ) , ( np.size(
#  active_file['U'],0), np.size(active_file['U'],1) ) )
#
#u_rms  = np.reshape( np.std(u_instantaneous_tot,0) , ( np.size(active_file['U'],0),
```

```
      ↪ np.size(active_file['U'],1) ) )
#v_rms  = np.reshape( np.std(v_instantaneous_tot,0) ,  ( np.size(active_file['V'],0),
      ↪ np.size(active_file['V'],1) ) )
```

APPENDIX I

OPENCV RADIAL UNDISTORTION SCRIPT

This appendix contains two scripts. The first script requires an input calibration image of a square checkerboard and the expected grid (object pts) for the corner detection algorithm to find. The output is a *yaml* file containing the camera calibration coefficients to correct for the radial distortion. The second script loads the camera calibration coefficients and undistorts the specified image set.

```python
# -*- coding: utf-8 -*-
"""
Created on Mon May  7 13:17:19 2018
@author: negcm7
"""

import numpy as np
import cv2
#import glob
import matplotlib.pyplot as plt
import yaml

#%%
# termination criteria
criteria = (cv2.TERM_CRITERIA_EPS + cv2.TERM_CRITERIA_MAX_ITER, 300, 0.0001)

# prepare object points, like (0,0,0), (1,0,0), (2,0,0) ....,(6,5,0)
```

```python
objp = np.zeros((4*5,3), np.float32)
objp[:,:2] = np.mgrid[0:4,0:5].T.reshape(-1,2)

# Arrays to store object points and image points from all the images.
objpoints = [] # 3d point in real world space
imgpoints = [] # 2d points in image plane.

# load chessboard image (issue with 3312x2488 images, 1656x1244 was ok.)
#img_og = cv2.imread('D:/wirewrapped/images/calibration/five_seven/
↪ calibration_plate_five_seven_sharp_8_bright_downsize1656.tif')
img_og = cv2.imread('D:/wirewrapped/images/calibration/five_seven/
↪ calibration_plate_five_seven_sharp_4_contrast_dark.tif')
img = img_og[:,:,2]
h,  w = img.shape[:2]

# specify downscale factor for high resolution images (issue with 3312x2488 images, 1656
↪ x1244 was ok (50%)
scaling = 2
img_downscale = cv2.resize(img, (0,0), fx= 1/scaling, fy= 1/scaling, interpolation=cv2.
↪ INTER_LANCZOS4)

# Find the chess board corners
ret, corners = cv2.findChessboardCorners(img_downscale, (4,5),None)

# resize corners to orignal resolution
corners = corners*scaling

# plot chessboard corners
fig, ax = plt.subplots()
ax.invert_yaxis()
```

```python
ax.xaxis.tick_top()
ax.plot(corners[:,0,0],corners[:,0,1], marker='+', color='k', linestyle='none')
#plt.savefig('D:/wirewrapped/images/calibration/five_seven/
  ↪ calibration_plate_five_seven_sharp_8_bright_downsize1656_corners.tif',dpi=300)

#%% If corners found, add object points, image points (after refining them)

if ret == True:
    objpoints.append(objp)

    corners2 = cv2.cornerSubPix(img,corners,(21,21),(-1,-1),criteria)
    imgpoints.append(corners2)

    # Draw and display the corners
    img_og = cv2.drawChessboardCorners(img_og, (4,5), corners2,ret)

    # view image with corners
    img_resize = cv2.resize(img_og[:,:,2], (1241, 700))     # Resize image for display
    cv2.imshow('img',img_resize)
    cv2.waitKey(0)
    cv2.destroyAllWindows()
    cv2.imwrite('D:/wirewrapped/images/calibration/five_seven/
      ↪ calibration_plate_five_seven_sharp_4_contrast_dark_drawn.tif', img)
#%%
# calibration (estimate distortion parameters)
ret, mtx, dist, rvecs, tvecs = cv2.calibrateCamera(objpoints, imgpoints, img.shape[::-1],
  ↪ None,None) #,flags=cv2.CALIB_RATIONAL_MODEL)
newcameramtx, roi=cv2.getOptimalNewCameraMatrix(mtx,dist,(w,h),1,(w,h))

# undistort chessboard
```

```python
dst = cv2.undistort(img, mtx, dist, None, newcameramtx)
cv2.imwrite('D:/wirewrapped/images/calibration/five_seven/undistorted/
↪ calibration_plate_five_seven_sharp_4_contrast_dark_undistort.tif',dst)

# crop the image
#x,y,w,h = roi
#dst = dst[y:y+h, x:x+w]

#%% undistort LA Vision calibration plate
cal_img = cv2.imread('D:/wirewrapped/images/calibration/four_twentyfive/
↪ calibration_plate_four_twentyfive_master_mod.tif')
cal_dst = cv2.undistort(cal_img , mtx, dist, None, newcameramtx)
cv2.imwrite('D:/wirewrapped/images/calibration/four_twentyfive/
↪ calibration_plate_four_twentyfive_master_undistort_opencv4.tif',cal_dst)


#%% reprojection error estimation
mean_error = 0
for i in range(len(objpoints)):
    imgpoints2, _ = cv2.projectPoints(objpoints[i], rvecs[i], tvecs[i], mtx, dist)
    error = cv2.norm(imgpoints[i],imgpoints2, cv2.NORM_L2)/len(imgpoints2)
    mean_error += error

print ("total error: ", mean_error/len(objpoints) )

#%% save camera calibration parameters
# It's very important to transform the matrix to list.
data = {'camera_matrix': np.asarray(mtx).tolist(), 'dist_coeff': np.asarray(dist).tolist()
↪ }
```

```python
with open("camera_calibration_opencv4.yaml", "w") as f:
    yaml.dump(data, f)

# You can use the following 4 lines of code to load the data in file "calibration.yaml"
# with open('camera_calibration.yaml') as f:
#     loadeddict = yaml.load(f)
# mtxloaded = loadeddict.get('camera_matrix')
# distloaded = loadeddict.get('dist_coeff')
```

Use this second script to load the output from above and undistort an image set.

```python
# -*- coding: utf-8 -*-
"""
Created on Fri May 11 16:15:13 2018
@author: negcm7
"""

import numpy as np
import cv2
import glob
import matplotlib.pyplot as plt
import yaml

def undistort_images(image_filename, image_path, camera_calibration_path):

    # load camera calibration parameters
    with open(camera_calibration_path) as f:
```

```python
        loadeddict = yaml.load(f)
    mtx_loaded = loadeddict.get('camera_matrix')
    newcameramtx_loaded = loadeddict.get('new_camera_matrix')
    dist_loaded = loadeddict.get('dist_coeff')

    # get image list
    image_list = glob.glob( image_path+image_filename )
    # loop through multiple image directories
    for fname in image_list:
        # load image to be undistorted
        img_og = cv2.imread(fname)
        img     = img_og[:,:,2]
        dst = cv2.undistort(img, mtx_loaded, dist_loaded, None, newcameramtx_loaded)
        save_fname = fname.replace('bgd_subtract','bgd_subtract_undistorted')
        cv2.imwrite(save_fname, dst)
        print("image complete =",fname)
    return (mtx_loaded, newcameramtx_loaded, dist_loaded)

# call function
mtx_loaded, newcameramtx_loaded, dist_loaded = undistort_images(
'roi_a_bgd_subtract_*.tif', 'D:/wirewrapped/images/roi_a/four_thirteen_eighteen/
↪ bgd_subtract/', 'D:/wirewrapped/scripts/distortion/camera_calibration_opencv8_np.
↪ yaml' )
```

APPENDIX J

POSTERS

This appendix contains various posters generated as part of this dissertation.

Toward a Longer Life Core: Thermal-Hydraulic CFD Simulations and Experimental Investigation of Deformed Fuel Assemblies

NUCLEAR ENGINEERING

PRINCIPAL INVESTIGATOR: Rodolfo Vaghetto
OTHER INVESTIGATORS/COLLABORATORS: Yassin Hassan, NK Anand, Saya Lee, Then Nguyen,

GRADUATE STUDENTS:
Nolan Goth   – PhD Candidate (Nuclear Engineering Department)
Mason Childs   – PhD Candidate (Nuclear Engineering Department)
Philip Jones   – Graduate Student (Mechanical Engineering Department)
Nicholas Quintanar   – PhD Candidate (Nuclear Engineering Department)
UNDERGRADUATE STUDENTS: Macon Heath   – Nuclear Engineering Department
William Headley   – Nuclear Engineering Department
Matthew Marciniak   – Nuclear Engineering Department
Mathew Abernathy   – Nuclear Engineering Department

WIRE-WRAPPED 61-PIN HEXAGONAL FUEL BUNDLE

MAIN FEATURES

- 61-pin wire-wrapped acrylic rods
- Full transparent acrylic enclosure
- Wide Operation Range
  - Up to 350 GPM
  - Laminar, Transition, Turbulent Regimes
- Multiple Working Fluids:
  - P-Cymene
  - Water
  - Air

INSTRUMENTATION

- 9 Axial Pressure Transducers
- 6 Azimuthal Differential Pressure Meas.
- Flow Meter and Flow Control
- Temperature Measurement and Control

STATE-OF-THE-ART FLOW MEASUREMENTS

- Matched Refractive Index (MIR)
- Particle Image Velocimetry (PIV)
- Stereoscopic PIV
- Laser Doppler Velocimetry (LDV)
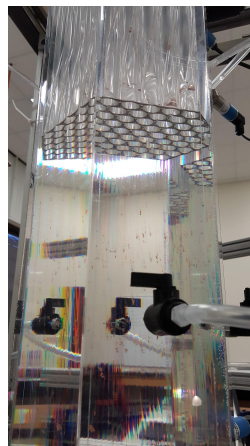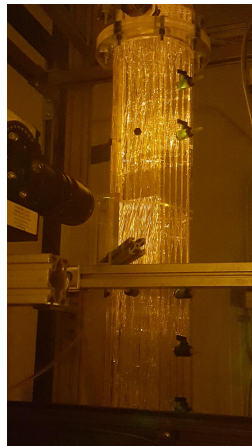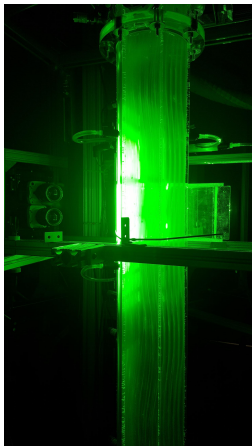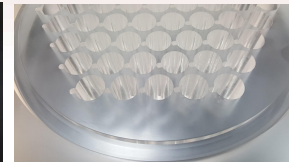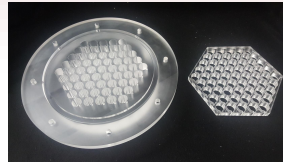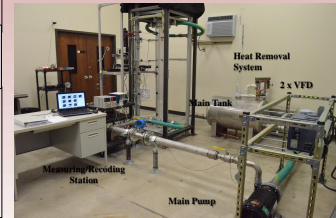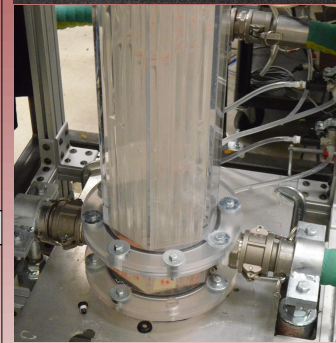
# HIGH RESOLUTION FLOW MEASUREMENTS IN A 61-PIN WIRE-WRAPPED HEXAGONAL BUNDLE

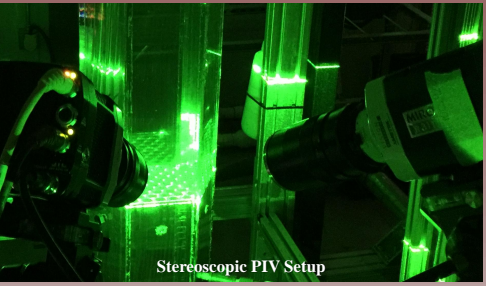**INVESTIGATORS:** Rodolfo Vaghetto, Thien Nguyen, Yassin Hassan, NK Anand, Saya Lee

GRADUATE STUDENTS:
- Nolan Goth – PhD Candidate (Nuclear Engineering Department)
- Mason Childs – PhD Candidate (Nuclear Engineering Department)
- Philip Jones – Graduate Student (Mechanical Engineering Department)
- Nicolas Quintanar – PhD Candidate (Nuclear Engineering Department)

UNDERGRADUATE STUDENTS:
- Brandon Joe – Nuclear Engineering Department
- Macon Heath – Nuclear Engineering Department
- William Headley – Nuclear Engineering Department
- Brian Hubbard – Mechanical Engineering Department
- Matthew Marciniak – Nuclear Engineering Department
- Mathew Abernathy – Nuclear Engineering Department
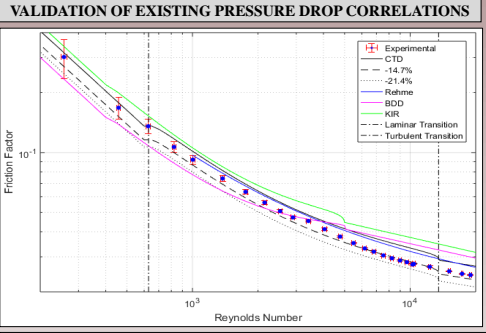
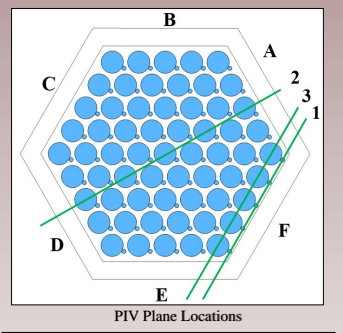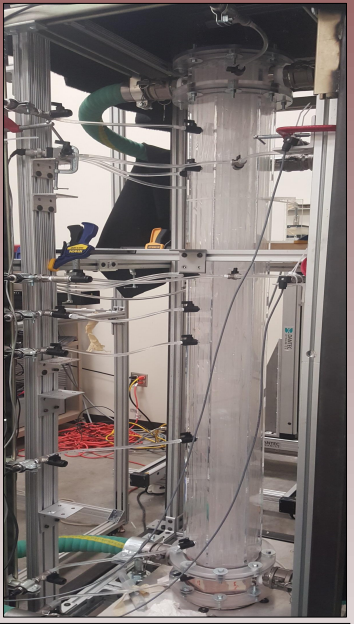## THE LARGEST WIRE-WRAPPED MIR ASSEMBLY IN THE WORLD
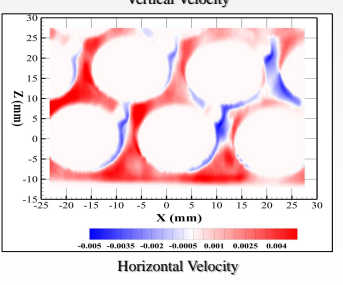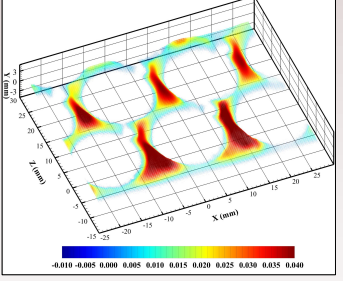
FULLY ACCESSIBLE OPTICALLY CLEAR TEST SECTION

High Speed/Resolution Cameras

Multiple Laser Sources

PIV Plane Locations
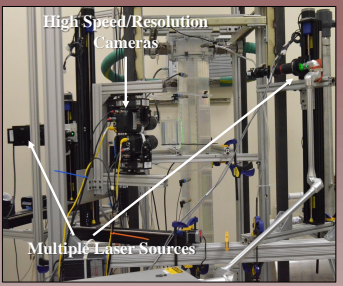
STATE-OF-THE-ART LASER-BASED TECHNIQUES FOR VELOCITY MEASUREMENTS

Stereoscopic PIV Setup

VALIDATION OF EXISTING PRESSURE DROP CORRELATIONS

AXIAL AND AZIMUTHAL PRESSURE DROP MEASUREMENTS

STEREOSCOPIC PIV

-0.010 -0.005 0.000 0.005 0.010 0.015 0.020 0.025 0.030 0.035 0.040

Vertical Velocity

-0.005 -0.0035 -0.002 -0.0005 0.001 0.0025 0.004

Horizontal Velocity

2D-PIV: TIME-AVERAGED VERTICAL VELOCITY CONTOURS

Axial velocity (m/s)
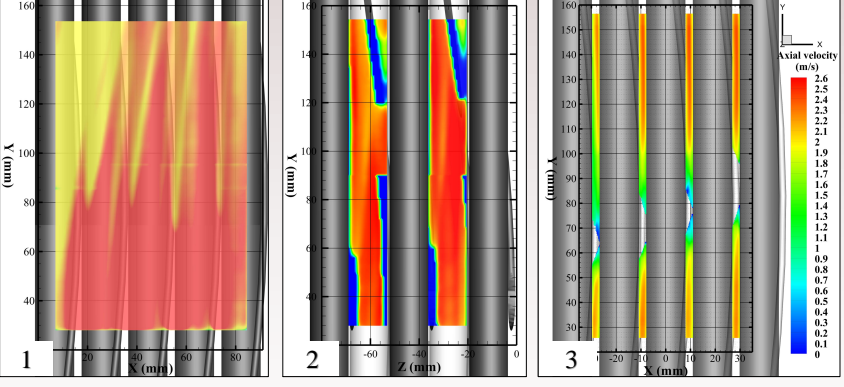
JOURNAL PUBLICATIONS:
- D.T. Nguyen, N. Goth, P. Jones, S. Lee, R. Vaghetto, Y. Hassan, "PIV Measurements of Turbulent Flows in a 61-Pin Wire-Wrapped Hexagonal Fuel Bundle." International Journal of Heat and Fluid Flow, 65 (2017) 47–59.
- R. Vaghetto, N. Goth, P. Jones, M. Childs, S. Lee, D.T. Nguyen, Y.A. Hassan, "Pressure Measurements in a Wire-Wrapped 61-Pin Fuel Bundle". Submitted to Journal of Fluids Engineering (under review).

CONFERENCE PROCEEDINGS:
- N. Goth, P. Jones, S. Lee, D.T. Nguyen, R. Vaghetto, Y.A. Hassan, "Time-Resolved PIV/PTV Measurements on Interior Subchannels of a Wire-Wrapped 61-pin Hexagonal Fuel Bundle," 2017 American Nuclear Society Annual Meeting, San Francisco, CA, June 11-15, 2017
- R. Vaghetto, N. Goth, P. Jones, M. Childs, S. Lee, D.T. Nguyen, Y.A. Hassan, "Flow Field and Pressure Measurements in a 61-Pin Wire-Wrapped Bundle". American Nuclear Society Winter meeting, Las Vegas, NV, 2016 November 6-10, 2016
- N. Goth, P. Jones, M. Childs, S. Lee, D.T. Nguyen, R. Vaghetto, Y.A. Hassan, "Pressure Measurements in a Wire-Wrapped 61-Pin Hexagonal Fuel Bundle." American Nuclear Society Winter meeting, Las Vegas, NV, 2016 November 6-10, 2016
- N. Goth, M. Childs, P. Jones, S. Lee, D.T. Nguyen, R. Vaghetto, Y.A. Hassan, "Particle Image Velocimetry Measurements in a Wire-Wrapped 61-Pin Hexagonal Fuel Bundle." American Nuclear Society Winter meeting, Las Vegas, NV, 2016 November 6-10, 2016
- N. Goth, P. Jones, S. Lee, D.T. Nguyen, R. Vaghetto, and Y.A. Hassan, "Velocity and Pressure Measurements in a Wire-Wrapped 61-Pin Hexagonal Fuel Bundle". ETMM11 – ERCOFTAC SYMPOSIUM, September 21, 2016.

235

High Resolution Temperature and Flow Measurements in Wire-Wrapped Fuel Assemblies

INVESTIGATORS: Rodolfo Vaghetto, Thien Nguyen, Yassin Hassan (TAMU)
Brian Jackson, Michael Steer (TerraPower)
Katrien Van Tichelen (SCK·CEN)

GRADUATE STUDENTS:
Nolan Goth — PhD Candidate (Nuclear Engineering)
Lance White — PhD Candidate (Nuclear Engineering)
Philip Jones — Graduate Student (Mechanical Engineering)

UNDERGRADUATE STUDENTS: Colin Guilbault — Nuclear Engineering
Matt Marciniak — Nuclear Engineering
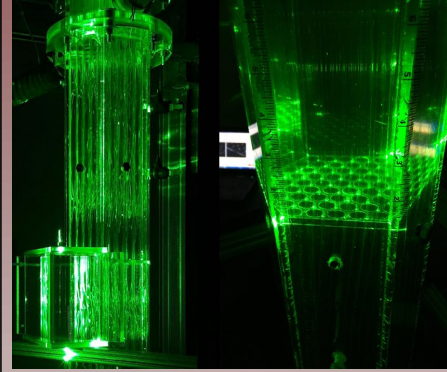Jadyn Reis — Nuclear Engineering

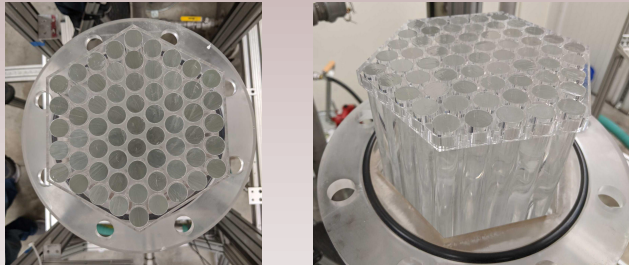## THE LARGEST HEXAGONAL WIRE-WRAPPED MIR ASSEMBLY IN THE WORLD

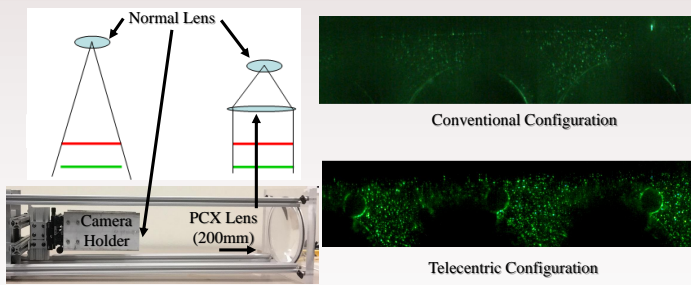### COMPARISON OF EXPERIMENTAL RESULTS WITH NEK5000 LARGE EDDY SIMULATIONS

● Experiments
— Nek5000 Simulations

PIV Measurements Location
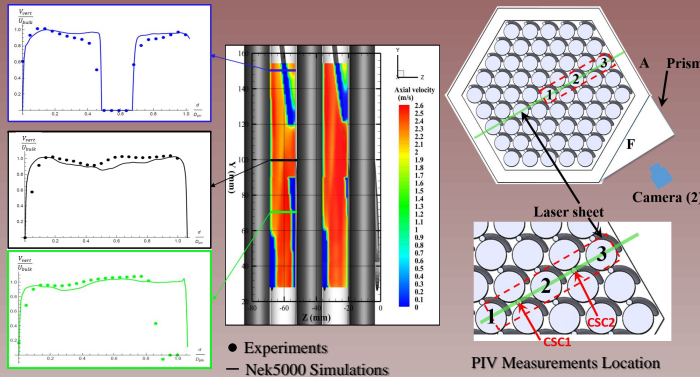
STATE-OF-THE-ART LASER-BASED VELOCITY MEASUREMENT TECHNIQUES

TELECENTRIC

New Bundle Featuring Fully Polished Pins

Conventional Configuration

Telecentric Configuration

STEREOSCOPIC PIV

Re = 6300

Normalized velocity vectors and normalized magnitude contour

Re = 6300

Reconstructed vortical structures by applying Taylor's hypothesis
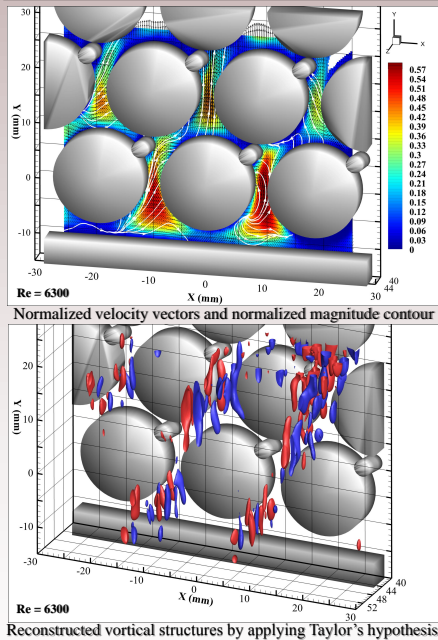
JOURNAL PUBLICATIONS:
- Thien Nguyen, Goth, Nolan, Philip Jones, Saya Lee, Rodolfo Vaghetto, and Yassin Hassan. "PIV measurements of turbulent flows in a 61-pin wire-wrapped hexagonal fuel bundle". In: *International Journal of Heat and Fluid Flow* 65 (2017), pp. 47–59.
- Thien Nguyen, Goth, Nolan, Philip Jones, Rodolfo Vaghetto, and Yassin Hassan. "Stereoscopic PIV measurements of flow in a complex geometry of a tightly packed rod bundle with wire spacers". In: *International Journal of Heat and Fluid Flow* (2017).
- Rodolfo Vaghetto, Goth, Nolan, Philip Jones, Mason Childs, Saye Lee, Duy Thien Nguyen, and Yassin A Hassan. "Pressure Measurements in a Wire-Wrapped 61-Pin Hexagonal Fuel Bundle". In: *Journal of Fluids Engineering* 140.3 (2018), p. 031104.
- Goth, Nolan, Philip Jones, Thien Nguyen, Rodolfo Vaghetto, and Yassin Hassan. "PTV/PIV Measurements of Turbulent Flows in Interior Subchannels of a 61-Pin Wire-Wrapped Hexagonal Fuel Bundle". In: *International Journal of Heat and Fluid Flow* (2018). (under review)

CONFERENCE PROCEEDINGS:
- Goth, Nolan, Mason Childs, Philip Jones, Saya Lee, D.T. Nguyen, Rodolfo Vaghetto, and Y.A. Hassan. "Particle Image Velocimetry Measurements in a Wire-Wrapped 61-pin Hexagonal Fuel Bundle". In: *American Nuclear Society Winter Meeting*. 2016.
- Goth, Nolan, Philip Jones, Saya Lee, D.T. Nguyen, Rodolfo Vaghetto, and Y.A. Hassan. "Velocity and Pressure Measurements in a Wire- Wrapped 61-Pin Hexagonal Fuel Bundle". In: *Engineering Turbulence Modeling and Measurements 11*. 2016.
- Goth, Nolan, Philip Jones, Mason Childs, Saya Lee, D.T. Nguyen, Rodolfo Vaghetto, and Y.A. Hassan. "Pressure Measurements in a Wire- Wrapped 61-Pin Hexagonal Fuel Bundle". In: *American Nuclear Society Winter Meeting*. 2016.
- Rodolfo Vaghetto, Goth, Nolan, Mason Childs, Philip Jones, Saya Lee, D.T. Nguyen, and Y.A. Hassan. "Flow Field and Pressure Measurements in a 61-Pin Wire-Wrapped Hexagonal Fuel Bundle". In: *American Nuclear Society Winter Meeting*. 2016.
- Goth, Nolan, Philip Jones, D.T. Nguyen, Rodolfo Vaghetto, Y.A. Hassan. "Time-Resolved PIV/PTV Measurements on Interior Subchannels of a Wire-Wrapped 61-pin Hexagonal Fuel Bundle". In: *American Nuclear Society Annual Meeting*. 2017.
- Goth, Nolan, Philip Jones, D.T. Nguyen, Rodolfo Vaghetto, Y.A. Hassan, Aleksandr Obabko, Elia Merzari, and Paul Fisher. "Comparison of Experimental and Simulation Results on Interior Subchannel of a 61-Pin Wire-Wrapped Hexagonal Fuel Bundle". In: *17th International Topical Meeting on Nuclear Reactor Thermal Hydraulics*. 2017.
- Goth, Nolan, Philip Jones, D.T. Nguyen, Rodolfo Vaghetto, and Y.A. Hassan. "Turbulent Transverse Plane PIV Measurements on a Wire- Wrapped 61-Pin Hexagonal Fuel Bundle". In: *26th International Conference on Nuclear Engineering*. 2018.

Nolan E. **Goth**

NUCLEAR ENGINEER

1521 Wolf Run, College Station, Texas, 77840

417-425-9810 | negcm7@tamu.edu | nolangoth | U.S. Citizen

"The glass is twice as big as it needs to be."

Education

Texas A&M University	*College Station, Texas*
PhD in Nuclear Engineering	*2018*
MS in Nuclear Engineering	

Missouri S&T	*Rolla, Missouri*
BS in Nuclear Engineering	*2012*
BA in Economics	
Minor in Mathematics	

Skills

Thermal Hydraulics (Sim)	BISON, Ansys, COBRA-TF, OpenFOAM, StarCCM+
Thermal Hydraulics (Exp)	Test Loops, Optics, Instrumentation, Sensors, LDV, PIV, SPIV, PTV
Neutronics (Sim)	Serpent, MPACT, MCNP, SCALE/ORIGEN, Homemade Diffusion/Transport/MOC Codes
Neutronics (Exp)	Shielding, Dosimetry, Directional Detectors
Reactor Operations	Senior Reactor Operator, Fuel Movement, Power Maneuver, Operator Training
Programming	Python, MATLAB, LaTeX, C++, SQL
Modeling	Solidworks, AutoCAD, Tecplot, Paraview, Gmsh

Experience

Texas A&M University — *College Station, Texas*
Graduate Researcher, Fast Reactor Fuel Assembly Flow Characterization — *2015 - PRESENT*

- Group leader of a six-person team with $1.2M budget
- Designed, procured, constructed, and operated an experimental flow facility
- Performed PIV, SPIV, and PTV laser-based measurement techniques to quantify fuel assembly flow behavior
- Collaborated with *NASA* on the design of a compact reactor module for Martian surface fission power

The Babcock & Wilcox Company, mPower SMR — *Lynchburg, Virginia*
Operations Engineer & Project Manager — *2013 - 2014*

- Performed system design reviews of mPower SMR systems
- Managed the DCD schedule for Chapter 18 – Human Factors Engineering using Primavera P6
- Developed budget trends, tracked critical paths, and formulated weekly plans

Missouri S&T — *Rolla, Missouri*
Senior Reactor Operator & Operations Instructor — *2010 - 2012*

- Conducted reactor startups, power maneuvers, and shutdowns
- Supervised fuel movements, material irradiations, and handling activities
- Taught introductory reactor operations classes

Smith-Goth Engineers, Inc. — *Springfield, Missouri*
AutoCAD Technician — *2006 - 2008*

- Designed and drafted HVAC, lighting, and fire protection systems

237

Certifications and Awards

2018	**Innovations in Nuclear Technology R&D Award - 2nd Place**, U.S. Department of Energy
2017	**Workshop and First Place Poster**, Consortium for Advanced Simulation of LWRs (CASL) Summer Institute
2012	**Magna Cum Laude**, Missour S&T
2011-12	**Senior Reactor Operator License**, Nuclear Regulatory Commission
2008-12	**Bright Flight Scholarship**, Missouri Dept of Higher Education
2008-12	**NRC Scholarship**, Nuclear Regulatory Commission

Publications

JOURNAL

[1] Thien Nguyen, **Goth, Nolan**, Philip Jones, Saya Lee, Rodolfo Vaghetto, and Yassin Hassan. "PIV measurements of turbulent flows in a 61-pin wire-wrapped hexagonal fuel bundle". In: *International Journal of Heat and Fluid Flow* 65 (2017), pp. 47–59.

[2] Thien Nguyen, **Goth, Nolan**, Philip Jones, Rodolfo Vaghetto, and Yassin Hassan. "Stereoscopic PIV measurements of flow in a complex geometry of a tightly packed rod bundle with wire spacers". In: *International Journal of Heat and Fluid Flow* (2017).

[3] Rodolfo Vaghetto, **Goth, Nolan**, Philip Jones, Mason Childs, Saye Lee, Duy Thien Nguyen, and Yassin A Hassan. "Pressure Measurements in a Wire-Wrapped 61-Pin Hexagonal Fuel Bundle". In: *Journal of Fluids Engineering* 140.3 (2018), p. 031104.

[4] **Goth, Nolan**, Philip Jones, Thien Nguyen, Rodolfo Vaghetto, and Yassin Hassan. "PTV/PIV Measurements of Turbulent Flows in Interior Subchannels of a 61-Pin Wire-Wrapped Hexagonal Fuel Bundle". In: *International Journal of Heat and Fluid Flow* (2018).

[5] **Goth, Nolan**, P Jones, DT Nguyen, R Vaghetto, YA Hassan, A Obabko, E Merzari, and PF Fischer. "Comparison of experimental and simulation results on interior subchannels of a 61-pin wire-wrapped hexagonal fuel bundle". In: *Nuclear Engineering and Design* 338 (2018), pp. 130–136.

CONFERENCE

[1] **Goth, Nolan**, Mason Childs, Philip Jones, Saya Lee, D.T. Nguyen, Rodolfo Vaghetto, and Y.A. Hassan. "Particle Image Velocimetry Measurements in a Wire-Wrapped 61-pin Hexagonal Fuel Bundle". In: *American Nuclear Society Winter Meeting*. 2016.

[2] **Goth, Nolan**, Philip Jones, Saya Lee, D.T. Nguyen, Rodolfo Vaghetto, and Y.A. Hassan. "Velocity and Pressure Measurements in a Wire-Wrapped 61-Pin Hexagonal Fuel Bundle". In: *Engineering Turbulence Modeling and Measurements 11*. 2016.

[3] **Goth, Nolan**, Philip Jones, Mason Childs, Saya Lee, D.T. Nguyen, Rodolfo Vaghetto, and Y.A. Hassan. "Pressure Measurements in a Wire-Wrapped 61-Pin Hexagonal Fuel Bundle". In: *American Nuclear Society Winter Meeting*. 2016.

[4] Rodolfo Vaghetto, **Goth, Nolan**, Mason Childs, Philip Jones, Saya Lee, D.T. Nguyen, and Y.A. Hassan. "Flow Field and Pressure Measurements in a 61-Pin Wire-Wrapped Hexagonal Fuel Bundle". In: *American Nuclear Society Winter Meeting*. 2016.

[5] **Goth, Nolan**, Philip Jones, Saya Lee, D.T. Nguyen, Rodolfo Vaghetto, and Y.A. Hassan. "Time-Resolved PIV/PTV Measurements on Interior Subchannels of a Wire-Wrapped 61-pin Hexagonal Fuel Bundle". In: *American Nuclear Society Annual Meeting*. 2017.

[6] **Goth, Nolan**, Philip Jones, D.T. Nguyen, Rodolfo Vaghetto, Y.A. Hassan, Aleksandr Obabko, Elia Merzari, and Paul Fisher. "Comparison of Experimental and Simulation Results on Interior Subchannel of a 61-Pin Wire-Wrapped Hexagonal Fuel Bundle". In: *17th International Topical Meeting on Nuclear Reactor Thermal Hydraulics*. 2017.

[7] **Goth, Nolan**, Philip Jones, D.T. Nguyen, Rodolfo Vaghetto, and Y.A. Hassan. "Turbulent Transverse Plane PIV Measurements on a Wire-Wrapped 61-Pin Hexagonal Fuel Bundle". In: *26th International Conference on Nuclear Engineering*. 2018.

[8] **Goth, Nolan**, Lance White, William Headley, D.T. Nguyen, Rodolfo Vaghetto, and Y.A. Hassan. "High Resolution Transverse Plane PIV Measurements of a 61-pin LMFBR Fuel Bundle". In: *American Nuclear Society Winter Meeting*. 2018.

THESIS & DISSERTATION

[1] **Goth, Nolan**. "Design and PIV Measurements on a Wire-Wrapped 61-Rod Hexagonal Fuel Assembly Experimental Facility". MA thesis. Texas A&M University, 2017.

Professional Service

2016	**Session Chair**, American Nuclear Society Winter Conference
2014-18	**Reviewer**, Nuclear Engineering and Design Journal
2012	**Vice President**, Alpha Nu Sigma Nuclear Honor Society
2008-18	**Member**, American Nuclear Society
2009	**Member**, Kappa Mu Epsilon Mathematics Honor Society